FINAL REPORT

Scientific Support of the Apollo Infrared Scanning Radiometer Experiment

Contract NAS9-10428

Rice University

The enclosed collection of publications constitutes the final report for Contract NAS9-10428, "Scientific Support of the Apollo Infrared Scanning Radiometer Experiment". The principal document for reference is entitled, "The Apollo 17 Infrared Scanning Radiometer" by Wendell W. Mendell. It contains a detailed discussion of the experimental objectives, instrument design and development, and radiometric calibration. In later chapters of the document the instrument performance is analyzed and the nature of the scientific results is established.

The other documents address more specific topics and generally are earlier results. The collection as a whole represents the Principal Investigator's effort for Apollo Experiment S-171.

This effort established the utility of scanning radiometry for the study of planetary surface processes. The quantitative, two-dimensional thermal "image" produced by the scanning technique permits an exchange of information between the radiometric results and photogeologic mapping. Collections of point radiometric measurements are difficult to interpret without reference to the surface geology. Thermal maps clarify the correlations. Once the geological context of the thermal data is clear, then the physical properties of the geologic units can be quantified from the thermal emission data.

The Infrared Scanning Radiometer also proved out the concept of mapping low temperature surfaces using an uncooled bolometer detector. The experience gained on Apollo can be applied directly to future orbital missions to the Moon and Mercury and to future exploration of the asteroids and the satellites of the outer planets.

The ISR was the first space borne mapper designed for far infrared radiometry. Calibration procedures had to be developed, and the experience is described in some detail in this report. Hopefully, future investigators can make use of the discussion in the design of their infrared calibration facilities.

The ISR Experiment was a complex and successful effort involving the coordinated activities of many people from Rice University, NASA, and Barnes Engineering. We are pleased to have been part of it.

RICE UNIVERSITY

THE APOLLO 17 INFRARED SCANNING RADIOMETER

by

Wendell W. Mendell

A THESIS SUBMITTED
IN PARTIAL FULFILLMENT OF THE
REQUIREMENTS FOR THE DEGREE OF

Ph.D.

Thesis Director's signature:

Frank J. Low

Houston, Texas

April 1976

THE APOLLO 17 INFRARED SCANNING RADIOMETER

Abstract

The Infrared Scanning Radiometer (ISR) was designed to map the thermal emission of the lunar surface from the Service Module of the orbiting Apollo 17 spacecraft. The principal experimental objective was the measurement of lunar surface nighttime temperatures, which are extremely difficult to map from Earth-based telescopes.

Data objectives fall into two main categories. In the first case, lunar regions can be classed according to surface properties as determined by nighttime temperatures and cooling rates. Secondly, geophysical boundaries can be established from thermal maps of the highest possible spatial resolution.

The ISR is an imaging line scanner utilizing a continuously rotating, single-sided, plane scan mirror. The detector is an uncooled thermistor bolometer bonded to a hyperhemispheric silicon immersion lens. The all-reflective Cassegrain optical system has an aperture of 17.8 cm and an instantaneous field of view of 20 milliradians. The spectral response of the ISR starts at 2 μm and extends to approximately 70 μm. A temperature measurement sensitivity of 1K is maintained over a dynamic range of 80K to 400K within the constraints of the Apollo telemetry system. A unique "space clamp" circuit provides an absolute radiometric measurement by automatically referencing each lunar scan to the "zero" signal from deep space.

A comprehensive program of acceptance testing verified the ability of the ISR to operate in the Apollo mission environment. Significant tests supporting scientific objectives included calibration in a thermal

vacuum chamber, mapping the instantaneous field of view, and characterization of the frequency response of the ISR signal processing. Discrepancies in the acceptance tests and anomalies during mission operation prompted further tests on the nonflight units.

The ISR transmitted approximately 90 hours of lunar data spread over 5 days in lunar orbit. Approximately 10^8 independent lunar temperature measurements were made with an absolute accuracy of 2K. Spatial resolution at nadir was approximately 2.2 km (depending on orbital altitude), exceeding that of Earth-based measurements by at least an order of magnitude. The data covers approximately 35% of the sphere as determined by the horizon-to-horizon scans centered on the Apollo 17 ground track.

Preliminary studies of the data reveal the highest population of thermal anomalies (or "hot spots") in Oceanus Procellarum. Very few anomalies exist on the far side of the Moon as was predicted from the association of anomalies with mare on the near side. A number of negative anomalies (or "cold spots") have also been found. It is possible that these areas represent geologically young deposits of material which is less compacted than the average lunar soil layer.

TABLE OF CONTENTS

TABLE OF CONTENTS (Continued)

I. Introduction

Project Apollo was the great adventure in planetary science of the early Seventies. More than a tour de force of engineering and technology, the program represented the first step beyond planetary reconnaissance toward a capability for intensive planetary exploration, Over a period of three and a half years the basic Apollo spacecraft was upgraded continuously to increase scientific payload, astronaut mobility, and stay time on the lunar surface.

The final spacecraft configuration, known as the J series, carried a suite of instruments dedicated to orbital science. The orbital science payload provided data on lunar surface geochemistry and the geophysical properties of the Moon as a planet. The instruments were operated primarily by the Command Module Pilot, who remained in orbit in the Command-Service Module (CSM) while the other two crew members explored the lunar surface. The instruments were installed in a sector of the Service Module called the Scientific Instrument Module (SIM) Bay.

Apollo 17, the final mission, carried the Infrared Scanning Radiometer (ISR) to lunar orbit in December, 1972. The ISR was designed to map thermal emission from the lunar surface with greater accuracy, sensitivity, and spatial resolution than could be obtained using Earth-based techniques. The principal experimental objective was the acquisition of accurate temperature measurements from the nighttime surface, particularly at local times between lunar midnight and dawn.

Theoretical considerations predict that nighttime surface temperature distributions mirror variations in the physical properties of the lunar soil from place to place. Thermal mapping from Earth-based tele-

scopes had demonstrated large scale heterogeneity in soil parameters in association with various classes of lunar features. We believed that better resolution of these thermal patterns would give insight into lunar geological processes. Additionally, analysis of the temperature data would result in quantitative estimates of soil density and structure.

Implementation of the experiment seemed straightforward at first, but it soon became clear that the instrumentation would require some "firsts". Predawn lunar temperatures fall to 90 K and lower. Earth-based detection of such low thermal flux requires cryogenically cooled detectors. The best detector available for that task was a germanium bolometer cooled by liquid helium. However, any type of cooling system, passive or active, for such a long mission (~2 weeks) required development work.

Preliminary calculations showed that an "ordinary" weather satellite radiometer using an uncooled thermistor bolometer could be modified to provide a reasonable signal to noise ratio for the measurement of a 90 K temperature (F. Malinowski, unpubl. memo). The absence of any significant absorbing and emitting atmosphere around the Moon permitted operation of the radiometer without spectral filters. The increase in flux available to the unfiltered detector, particularly at long wavelengths, compensated for the low level of emitted radiation. Proposals received from industry for construction of the ISR independently confirmed the analysis (e.g., Plakun, et al., 1969).

The use of an uncooled detector for observation of such low temperatures was a new concept, and the long wavelength response of the thermistor bolometer was largely unknown. If the ISR successfully mapped lunar nighttime temperatures, then the uncooled detector concept was

viable for scanning radiometry of Jupiter, Saturn, and Mercury where mission lifetimes are much more of a problem. The importance of the ISR development was emphasized by the failure of a cooling system for the infrared spectrometer aboard Mariner 6 (Wilson, 1971).

The dual themes of the study of the state of the lunar surface and the proof of the instrument concept occupy the remainder of this work. The next two chapters provide a basic theoretical introduction to the lunar surface thermal regime and a summary of the understanding of infrared observations at the time of the Apollo mission. These discussions should clarify the scientific goals of the ISR experiment. The following pair of chapters develop the rationale behind the design and operation of the experiment. Chapter VI analyzes the performance of the design. In Chapters VII and VIII testing and calibration of the ISR are described and analyzed. Chapter IX summarizes the actual performance of the ISR, and Chapter X presents some preliminary scientific results. A final chapter concludes and recommends.

II. Experimental Objective

The principal experimental objective of the ISR was the mapping of thermal emission from the nighttime lunar surface. The radiometer was designed with a dynamic range capable of also measuring the emission from the illuminated surface but the latter was not considered a prime objective.

The regular diurnal passage of the Sun over a spot on the Moon induces a thermal wave in the surface layer. A simple picture of the character of the wave can be obtained by consideration of Fourier's equation of heat conduction in a semi-infinite solid,

$$\rho c \frac{\partial T}{\partial t} = \frac{\partial}{\partial z}\left(k \frac{\partial T}{\partial z}\right), \tag{2.1}$$

where $T(z,t)$ is the temperature in the body as a function of depth and time, ρ is the bulk density, c is the specific heat, and k is the thermal conductivity. If the surface temperature is a simple harmonic function

$$T(0,t) = b_0 + b_1 \cos\left(\frac{2\pi t}{P} + \phi\right) \tag{2.2}$$

with period P, then the solution at all points within the body is (Carslaw and Jaeger, (1959); Wesselink, (1948))

$$T(z,t) = b_0 + b_1 \exp\left(\frac{-2\pi z}{\ell}\right)\cos\left(\frac{2\pi t}{P} - \frac{2\pi z}{\ell} + \phi\right) \tag{2.3}$$

where the thermal wavelength, ℓ, is given by

$$\ell = \sqrt{4\pi P \cdot \frac{k}{\rho c}} \tag{2.4}$$

The solution is clearly a wave, exponentially damped with depth.

If the surface temperature can be represented in a Fourier expansion

$$T = \sum_n b_n \cos\left(\frac{2\pi n t}{P} + \phi_n\right) \equiv \sum_n b_n \cos(n\Omega + \phi_n) \qquad (2.5)$$

then the linearity of the heat conduction equation implies that the general temperature field can be written as

$$T(\Omega,s) = \sum_n b_n \exp(-\sqrt{n}\, s) \cos(n\Omega - \sqrt{n}\, s + \phi_n) \qquad (2.6)$$

where the spatial frequency $s = \frac{2\pi z}{l}$. Equation (2.6) represents a sum of harmonic waves, with the higher harmonic being more severely damped.

Although this simple model illustrates the nature of the thermal response of the lunar surface layer, the subsurface temperature field is not of direct interest in the interpretation of infrared radiometric measurements. Rather, the surface temperature variation with time is the measured quantity, and the thermophysical parameters of the layer are tne inferred quantities. In order to model this relationship, one must consider the boundary condition for (2.1) at the surface.

At the surface plane ($z = 0$) the energy flux is partitioned three ways: a) some fraction of the solar insolation is absorbed; b) heat is conducted into or out of the subsurface; and c) thermal energy is radiated away from the surface to deep space. In the non-dimensional variables previously defined, this boundary condition can be written as

$$\varepsilon\sigma T^4(0,\Omega) = S(\Omega)[1-A(\Omega)] + \frac{1}{\gamma}\sqrt{\frac{\pi}{P}}\,\frac{\partial}{\partial s}T(0,\Omega), \qquad (2.7)$$

where ε is the emissivity of the lunar surface, σ is the Stefan-Boltzmann constant, S is the insolation at the surface, A is the solar albedo, and $\gamma = (k\rho c)^{-1/2}$. The insolation is a simple function of the brightness longitude (Ω) and the latitude (β).

$$S(\Omega) = \begin{cases} S_0 \cos\Omega \cos\beta & |\Omega| \leq \frac{\pi}{2} \\ 0 & \frac{\pi}{2} \leq \Omega \leq \frac{3\pi}{2} \end{cases} \tag{2.8}$$

where S_0 is the solar constant. In these coordinates, the subsolar point corresponds to $\Omega = 0$, $\beta = 0$.

The solar albedo is also a function of sun angle. This dependence has recently been incorporated into lunar models by Cremers (1974) and has been shown to have a significant effect on the temperature regime near the terminators.

Boundary conditions (2.7) and the non-dimensional form of (2.1),

$$\frac{\partial T}{\partial \Omega} = \frac{1}{2} \frac{\partial^2 T}{\partial s^2}, \tag{2.9}$$

are the basis of the calculation for the lunar surface temperature as a function of time. The left-hand side of (2.7) is nonlinear in T, and this fact precludes an analytical solution to (2.9).
Numerical solution is obtained through finite difference techniques.

Examination of (2.7) and (2.9) shows that the thermophysical properties of the surface layer appear only as the single parameter, γ. All other terms in (2.7) are well defined by the type of boundary condition (lunation or eclipse). Surface temperature curves can be calculated as a function of γ and compared with experimental data.

As will be discussed in the next section, early observations showed that the lunar value of γ was on the order of 10^3 cal^{-1} sec$^{1/2}$K cm^2. Theoretical curves calculated for a range of γ from 500 to 1500 exhibit almost indistinguishable daytime surface temperatures but rather dramatic differences in nighttime levels. The physical reason for this behavior

is quite simple. A value of γ in the above range is characteristic of a good thermal insulator. During the daytime, the lunar surface layer conducts only a small fraction of the absorbed solar energy into the subsurface. Therefore, the equilibrium surface temperature is controlled by the absorbed solar radiation as determined by local variations in albedo, slope, and roughness and is much less dependent on the range of thermal properties.

In this simple, first-order model nighttime temperature mapping provides the key to the distribution of physical properties of the lunar surface layer. Since a value for γ uniquely defines a cooling curve, the temperature of a lunar region at some given phase angle (e.g., the midnight temperature) can be compared with that of other regions to determine the relative physical states of the surface layer. A further normalization of (2.7) is required to demonstrate this point rigorously.

The goniometric character of the lunar reflectivity function is the same everywhere on the lunar surface. It follows that one may write

$$1-A(\Omega) = E_0 E(\Omega) \tag{2.10}$$

where E_0 is the normal solar emissivity which varies from place to place. We will define a normalized temperature

$$\Theta = T/T_0 \tag{2.11}$$

where $$\varepsilon\sigma T_0^4 = E_0 S_0 \cos\beta. \tag{2.12}$$

It whould be noted at this point that the lunar rotational equator lies very nearly in the ecliptic plane. Therefore, the luminance latitude is

very nearly equal to the selenographic latitude. The two latitudes shall be interchangeably denoted by β in this paper.

Equation (2.7) can now be rewritten as

$$\Theta^4 = E(\Omega)\, S(\Omega) + \frac{1}{\gamma^*}\sqrt{\frac{\pi}{P}}\frac{\partial\Theta}{\partial s} \tag{2.13}$$

where $\gamma^* = \gamma(\varepsilon\sigma)^{1/4}(S_0 E_0 \cos\beta)^{3/4}$ (2.14)

Since all the parameters of the region are now combined into γ^*, that quantity can be uniquely associated with a temperature measurement. The thermophysical quantity γ can be derived with an uncertainty approximately equal to that of the albedo value.

This simple model of the lunar surface thermal regime serves to illustrate the physical principles behind the ISR experimental objective. More detailed study of the ISR data requires more realistic models incorporating radiative transfer as part of the subsurface thermal regime. Such models are discussed elsewhere and will not be covered in detail here.

III. Historical Context of the Measurement

Current data on lunar surface temperatures comes from Earth-based observations using the techniques of infrared astronomy. The terrestrial atmosphere rather severely restricts such measurements. Water vapor, carbon dioxide, and oxygen absorb most of the radiation entering the Earth's atmosphere in the spectral band from 7 μm to 50 μm. In accordance with Kirchoff's Law, these gases also emit thermal radiation in direct proportion to their absorptivity. Atmospheric thermal emission becomes the principal source of background noise against which an infrared signal must be detected.

The majority of lunar temperature measurements have been taken in an atmospheric "window" between 8 μm and 14 μm. Sensitive infrared quantum detectors are available for this spectral band of atmospheric transparency. The thermal flux distribution peaks in or near this band for lunar daytime and lunar eclipse temperatures. Detection and measurement of these two thermal regimes has been quite successful.

Mapping of lunar nighttime temperatures has proven much more difficult. Surface temperatures typically are 90K to 100K in the lunar night, and the blackbody peak lies at approximately 30 μm. The irradiance available within the 8 - 14 μm window falls off sharply and became undetectable for many investigators (Shorthill and Saari, 1965; Murray and Wildey, 1964; Wildey et al., 1967).

Low (1965) developed an astronomical technique for observing low temperature point sources through a less transparent atmospheric window (17 μm - 25 μm). The procedure dynamically compares the signal from two adjacent resolution elements in the sky, one containing the object of

interest and one empty. However, this differential measurement is not well suited to mapping an extended object such as the Moon.

A more complete discussion of lunar observations and techniques can be found in Mendell (1971).

If the problem of detection is overcome, the variability of atmospheric transmissivity still precludes an absolute radiometric measurement of lunar thermal emission. The value of the lunar radiance must be inferred from a contemporaneous observation of a "known" extraterrestrial source. The planet Venus was used as a calibration source for the dark side measurements made by Mendell and Low (1970). Saari and Shorthill (1967) referenced their measurements to the Moon's subsolar point, the temperature of which was computed using the solar constant, the local albedo, and a correction for conduction into the surface. The accuracies of these calibrations are no better than 10% to 15%.

The lunar cooling curve has been studied by scanning the telescope across the sunset terminator. Post-sunset nighttime temperatures are relatively high and readily detectable. On a typical scan, the surface temperature falls below the detection threshold before the telescope reaches the antisolar meridian. Cooling curves derived from these scans by various investigators exhibit significant differences. The disagreement has been attributed to regional variation in thermal properties or to drifts in the sky background. Equatorial scans were used by Saari (1964) to estimate the lunar midnight temperature at 104 K.

Estimation of a typical midnight temperature has been important in the absence of dark side thermal maps. Although evidence exists for large scale regional variations in thermophysical properties (Mendell and Low, 1972; Wildey et al., 1967), models of the surface thermal regime

are frequently based on a single parameter keyed to the midnight temperature (e.g., Linsky, 1973; Winter and Saari, 1968). The lunar soil is simply characterized as geophysically the same everywhere, varying only in the distribution of rocks.

The foregoing discussion makes clear the advantages of lunar orbit radiometry. The absence of an intervening atmosphere eliminates the major noise source and makes an absolute measurement possible. The global nature of the measurement allows the intercomparison of soil properties in different classes of lunar features. True cooling curves and the subsequent inference of thermophysical properties are possible. The entire thermal spectrum is available for radiometry. The data base can be extended to the far side of the Moon. Finally, the high spatial resolution makes it possible to study in detail the thermal structure in "thermal anomalies" discovered from Earth-based work.

Infrared measurements of the eclipse of March 12-13, 1960, revealed that several large rayed craters remained warmer than their environs during totality (Shorthill et al., 1960). The existence of thermal anomalies was soon verified by other workers (Sinton, 1962; Saari and Shorthill, 1963). During the eclipse of December 19, 1964, Shorthill and Saari (1969) completed nine infrared maps of the complete lunar disk. The telescopic field of view, 10 arc seconds, translated to a surface resolution element of 17 kilometers at the center of the disk. Approximately 1000 local anomalies were detected.

Many models have been put forward to explain the thermophysical heterogeneity of the lunar surface. The first anomalies detected were large rayed craters, geologically the youngest features on the Moon. It was hypothesized that the ubiquitous dust layer was thinner there than

in older, more eroded regions. However, other effects (volcanism, radioactivity, emissivity variations) were not ruled out. In general, models for anomalous thermal behavior fall into four categories: a) subsurface heat sources; b) unusual soil properties; c) geometrical effects on both large and/or small scales; and d) a large rock population.

A. Subsurface heat sources

Non-solar heating is the most intriguing explanation from a scientific point of view. Volcanic or subsurface magmatic activity is only a remote possibility in view of the Moon's seismic quiescence and the extreme age of even the youngest lunar samples.

The gamma ray spectrometer experiment flown on Apollos 15 and 16 has found local concentrations of radioactivity in the Aristarchus Plateau, the Fra Mauro formation, and Van de Graaff (Adler et al., 1973). However, the local variability in heat flow attributable to variations in KREEP* abundance has been estimated at less than a factor of two over the heat flow measured by the Apollo Heat Flow Experiment (Toksoz and Solomon, 1973). Such an enhancement of the heat flow would elevate lunar nighttime temperatures less than 0.5 K. While this enhancement is marginally detectable by the ISR, it is too small to explain the vast majority of thermal anomalies.

B. Unusual soil properties

Buettner (1962) suggested that lunar surface material might be partially transparent to thermal infrared radiation. During an eclipse,

*KREEP is an acronym for a lunar rock type containing a high concentration of radioactive elements.

large thermal gradients exist near the surface. If thermal emission from warm subsurface layers could escape through the surface, a radiometric temperature higher than the actual surface temperature would result.

Lunar soils have been found to consist predominantly of pyroxenes, olivines, anorthosites, and glasses. None of these are particularly transparent at infrared wavelengths. Surface particle sizes are on the order of the wavelength of the radiation ($\sim$10 μm). As effective scatterers of subsurface emission, the soil particles tend to thermalize the radiation field.

If the measured thermal emission is primarily a surface process, then variations in emissivity of the soil is a possible reason for thermal contrasts. Relative to a "blackbody" soil, a low emissivity surface reaches a higher equilibrium temperature to compensate for the reduced radiating efficiency. The spectral distribution of the emission will be shifted to shorter wavelengths. The net effect on the measured temperature will depend on the details of the spectral response of the sensor.

Saari and Shorthill (1963) discussed the effects of reduced surface emissivity on eclipse temperatures and measurements. For an umbral temperature of 200 K, they demonstrated actual enhancements ranging from +6.7 K (ε = 0.9) to +34.5 K (ε = 0.6). It was noted that the measured enhancement would be only half as great.

I have made a calculation of the effects of reduced emissivity on nighttime temperature measurements. An empirical relation between $\gamma = (\kappa\rho c)^{-1/2}$ and the antisolar temperature, T_M, has been determined from numerical solutions of the one-dimensional homogeneous lunar thermal

model (Mendell, unpublished data). Based on the model presented in equation (2.13), the fitted relation is

$$T_M \varepsilon^{1/4} = 265.9 - 56.01 \log_{10} (\gamma\varepsilon^{1/4}) \qquad (3.1)$$

over the range $400 < \gamma\varepsilon^{1/4} < 1300$. The results of the enhancement calculation are shown in Table I.

The actual enhancement of the midnight temperature ranges from +3.2 K (ε = 0.9) to +16.9 K (ε = 0.6). An infrared sensor sensitive to a wavelength of 22 μm would measure only half the true enhancement. At an effective wavelength of 11 μm the measured enhancement is 75% of the actual one. The relationship between the actual and measured enhancements can change if the emissivity is wavelength dependent. For example, if the emissivity is depressed only in the band around 11 μm, a measurement at that wavelength might show a negative anomaly whereas the 22 μm measurement would show a positive one.

Thermal emission from particulate mineral surfaces has little spectral contrast, approaching gray-body behavior as the particle size approaches the wavelength of the emission (Van Tessel and Simon, 1964). An early attempt to measure lunar surface emissivity from Earth (Murcray, 1965) established a value less than unity in the 8 μm to 10 μm band. No significant spectral structure was observed. Subsequent work in the field has led to disagreement on the occurrence of spectral contrast between lunar features (Salisbury et al., 1970).

Measurements have now been made on the spectral emissivity of Apollo soils (Birkebak, 1972; Birkebak and Dawson, 1973; Logan et al., 1972; Salisbury et al., 1973). Unfortunately no data has been taken at

TABLE I

Effect of Reduced Surface Emissivity on

Nighttime Lunar Temperatures

(γ = 1000 $cal^{-1} sec^{1/2}$ K cm^2)

Emissivity	$\gamma\epsilon^{1/4}$	Actual T_M (K)	Measured T_M (K)	
			λ_{eff} = 22 μm	λ_{eff} = 11 μm
1.0	1000	97.9	97.9	97.9
0.9	974	101.1	99.5	100.3
0.8	946	104.9	101.3	103.1
0.7	915	109.3	103.2	106.1
0.6	880	114.8	105.4	109.9

wavelengths longer than 14.5 μm. Between 8 μm and 15 μm the emissivity is fairly constant, $0.92 < \varepsilon < 1.0$. Below 8 μm the emissivity has a broad minimum at 3.5 - 4.0 μm. The depth and location of the minimum varies from soil to soil and depends on the packing density. The values at the minimum fall in the range 0.6 to 0.8. A calculation of the total emittance as a function of temperature (Birkebak, 1972; Birkebak and Abdulkadir, 1972) shows that this short wavelength minimum affects only high temperature emission. Its effect on the nighttime thermal emission is probably not large.

In summary, emissivity differences between lunar features do exist, but they may not be common. The emissivity is generally less than unity, but values for wavelengths greater than 15 μm have yet to be determined.

C. Geometrical effects

The influence of surface geometry on radiometric measurements has been studied theoretically. The phenomenon has been broken down into two categories: surface roughness and view factor effects in the interiors of craters and rilles. The categories differ only in scale. A review of work on this form of enhancement can be found in Bastin and Gough (1969).

Gear and Bastin (1962) proposed a centimeter-scale surface "corrugation" to explain observed directionality in daytime thermal emission (Pettit and Nicholson, 1930) and the apparent disagreement between values of γ deduced from eclipse and from nighttine observations. Bastin (1965) later invoked the same model as a possible explanation for eclipse anomalies. Bastin and Gough (1969) presented an analysis of a

model of intermediate scale roughness and compared its predictions to 19 known observational discrepancies relative to a plane model.

Although centimeter scale roughness appears to explain satisfactorily the global directionality of lunar thermal emission, it is less successful as a model for dark side thermal anomalies. Nighttime enhancements $\lesssim$ 10 K were obtained from a surface of parallel rectangular troughs. Such a model is not a reasonable representation of the mutual view factors of lunar surface elements. Yet the enhancements from this extreme model still fall short of the measured anomalies associated with large lunar features.

Buhl et al. (1968) invoked a more reasonable lunar morphology to analyze the effects of roughness. A surface having craters larger than a fraction of a meter exhibits an effective thermal inertia which is greater than the actual thermal inertia by a factor

$$1 + (^{2d}/_{D})^2,$$

where $^{d}/_{D}$ is the crater depth to diameter ratio. Numerical models showed nighttime thermal enhancements on the order of 15 K - 20 K.

There are some problems with the model. Reflected sunlight is improperly accounted for in the energy balance. As a result, the enhancement of the thermal inertia is overstated by approximately 8% with a resulting overestimate in the dark side anomaly of 2 K - 3 K. The model is based on hemispherical craters, implying that d:D = 1:2. A more realistic ratio falls in the range 1:5 to 1:20, yielding a total nighttime anomaly <4 K. Finally, and most importantly, the lunar surface is saturated everywhere with craters smaller than a kilometer. It would be more reasonable to turn the model around and speculate that cold anomalies

are unusually flat areas. However, the model is useful in understanding at least part of the enhancements associated with large craters. In this respect, the results agree with those of Staley (1968).

D. Rock populations

Most workers in the field have believed that some combination of exposed rock mixed with the lunar soil would nicely explain thermal anomalies. A dissenting voice was that of Sinton (1962). He presented evidence to the point that a two layer soil model fit the eclipse cooling of Tycho better than a soil-rock mixture. The large scatter in the experimental points weakens the argument. In addition the argument may not be valid because the temperature curves for the two components were apparently added linearly to get the curve for the mixture. No allowance was made for the detector response function.

Hopfield (1967) pointed out the dramatic and nonlinear effect of a small percentage of rock on the measured temperature of a lunar region. Disagreements in the magnitude of the lunar midnight temperature can be explained by assuming ~1% of the surface covered by rock and taking into account the spectral response of the various detectors. He proposed that microwave measurements would weight the radiance of the surface rock component linearly with temperature and abundance and that anomalies due to rocks should disappear.

Hopfield also emphasized the significance of the thermal wavelength in the rock relative to the size of the rock. When the size exceeds the thermal wavelength, thermal contrast is maintained relative to the soil. His argument suggested that rocks on the order of a meter or larger would cool independently of the soil during a lunation.

The thermal response of an isolated rock on the lunar surface was calculated by Roelof (1968). From that analysis, Winter (1970) concluded that surface rocks would have a small effect on the surface brightness temperature provided that the majority of the rock population was submeter and that the percentage of the surface covered by rocks was less than 10%. Hopfield's idea of an anomaly with a 1% rock surface would apply only if the rocks were boulders larger than 10 meters.

The infrared signature of large boulders as predicted by Hopfield and Roelof was observed experimentally by Allen and Ney (1969). They measured the color temperature as well as the brightness temperature of three major ray craters during the lunar night. Although the brightness temperatures decreased, the color temperatures remained constant at ∿200 K throughout the night. The data is consistent with 2% to 10% of the crater area covered with rock outcrops or large boulders. Later, Allen (1971) observed similar behavior for many other thermal anomalies.

Most thermal anomalies are bright ray craters. These features are classified as geologically young with arguments based on morphology and superposition. A large hypervelocity impact into the lunar surface is expected to produce boulders by excavation of bedrock and by shock lithification. The boulders are eroded by lunar surface processes such as micrometeorite bombardment. The intensity of a thermal anomaly should correlate with its geologic age. In addition, the visual and thermal characteristics should change in a regular way with time.

Fudali (1966) proposed a model of the evolution of the thermal signature. The new impact feature is bright with a ray pattern and

exhibits thermal enhancement over the crater floor and rim. Erosional processes cause these features to disappear in the following sequence:

(a) the ray pattern;

(b) thermal enhancement of the outer rim

(c) thermal enhancement of the crater floor

(d) visual brightness of the floor and outer rim

(e) thermal enhancement of the inner rim

(f) visual brightness of the inner rim

Photogeology is limited to the classifications as fresh impacts, (a), (d), and (f). Thermal maps from the ISR will immediately distinguish categories (b) and (e). Once corrections for view factor effects have been applied to crater floor temperatures, category (c) can also be distinguished. Thus the ISR should provide new details on lunar evolution using kilometer-sized craters as benchmarks.

IV. Conceptual Design of the ISR

The Apollo 17 Infrared Scanning Radiometer is a cross-track scanner, designed to map the Moon's thermal radiation from lunar orbit. Figure 4-1 is an optical schematic. The optical system is basically Cassegrainian. The 45° scan mirror accepts radiation which is initially incident perpendicular to the optical axis and folds it onto the primary mirror. The Cassegrain optics converge this radiation onto the detector assembly. The scan mirror and secondary mirror rotate as a unit about the optical axis.

The instantaneous field of view has a 20 milliradian acceptance angle. Its axis emerges from the ISR housing in a direction determined by the position of the scan mirror. Thus a complete rotation of the mirror causes the instantaneous field of view to sweep out a solid angle of revolution centered about a plane perpendicular to the rotation axis. The portion of the solid angle which lies within an aperture in the housing is called the external field of view of the instrument.

The ISR housing is approximately 21.5 cm x 22.8 cm x 58.4 cm (Figure 4-2). The optical axis runs parallel to the longest dimension. The extent of the external field of view is 189 degrees as determined by the size of the aperture.

The intact face of the housing which lies opposite to the aperture defines the mounting plane. A Cartesian coordinate system for the ISR can be established using the Cassegrain optical axis and the perpendicular to the mounting plane which intersects the optical axis at the plane of the scan mirror. The optical axis (and the rotation axis) will be designated as the y-axis. The perpendicular to the mounting plane becomes the x-axis.

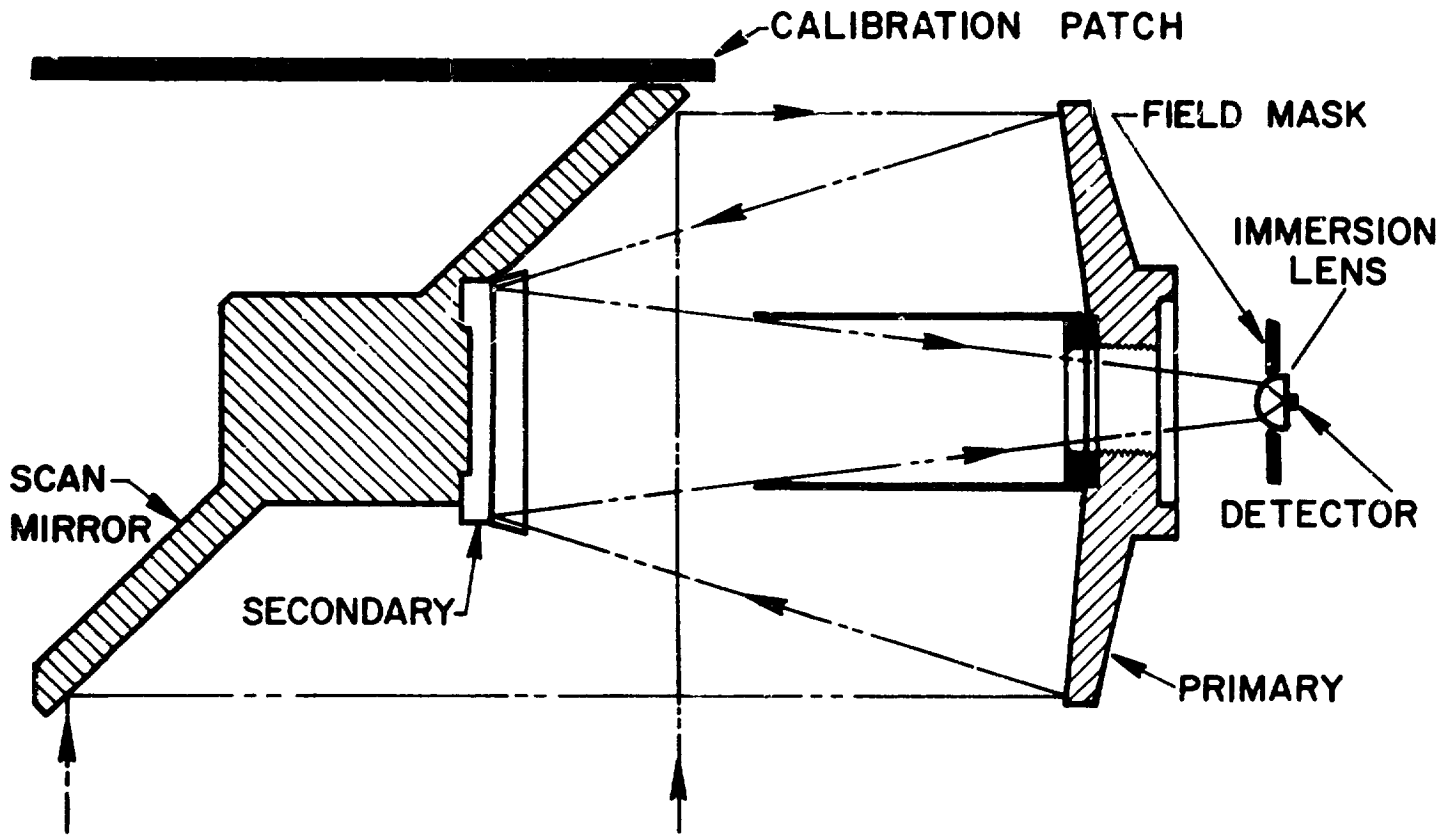

ISR OPTICAL SYSTEM

Figure 4-1 ISR OPTICAL SYSTEM. Incoming radiation is folded by the scan mirror onto the primary mirror. The Cassegrain optics direct the beam to the detector assembly where the immersion lens focuses energy on the detector.

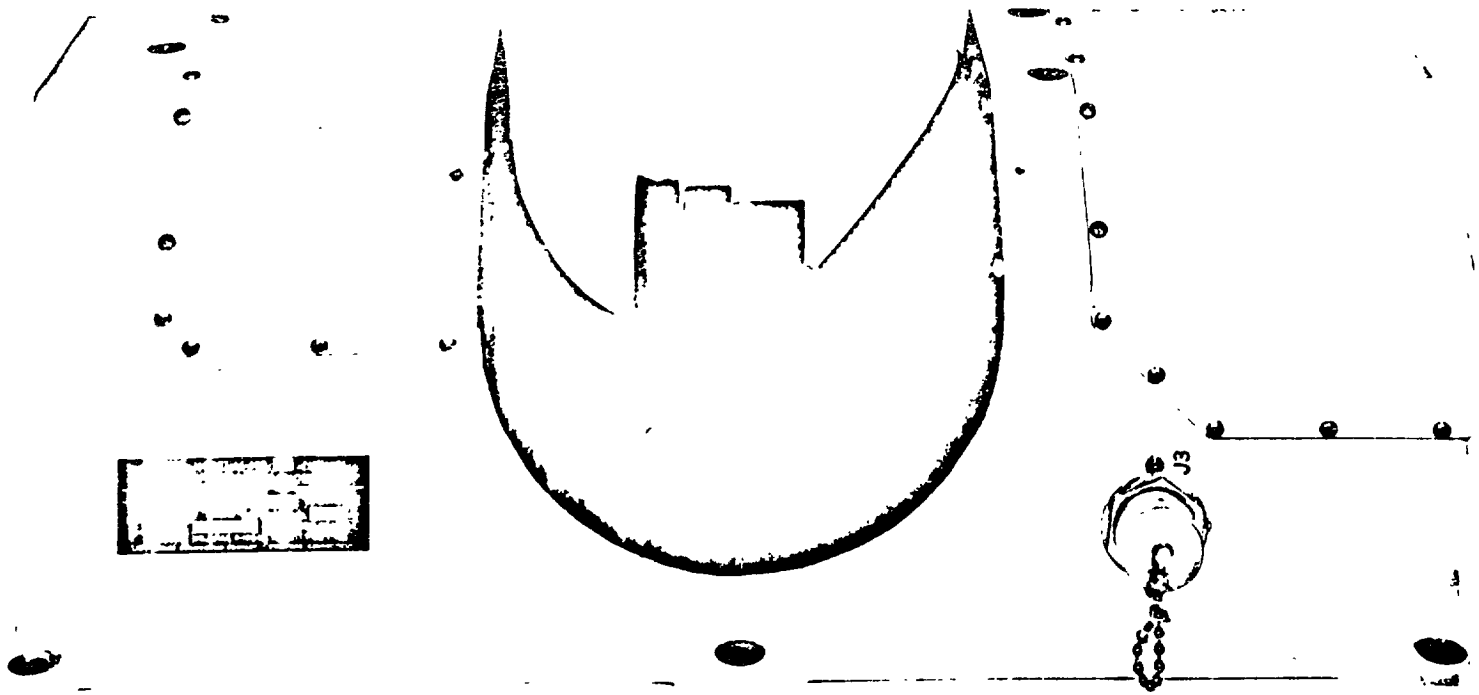

Figure 4-2 INFRARED SCANNING RADIOMETER. (Photo)

The -x direction passes through the aperture near the center. The +y axis goes through the detector. As viewed from the detector, the sense of rotation is clockwise.

The ISR was mounted in the Scientific Instrument Module Bay of the Apollo 17 spacecraft (cf. Chapter V). During data collection the -x axis was oriented toward the lunar surface. The external field of view crossed from horizon to horizon, perpendicular to the orbital ground track. The orbital motion of the spacecraft spaced successive scans along the ground track, thereby allowing the ISR to sample the entire surface visible from the orbital altitude.

If the ISR is H kilometers above the lunar surface and if the instantaneous field of view (α = 20 mrad.) is directed toward nadir, the circular surface resolution element has a selenocentric angular diameter

$$\delta \tilde{=} \frac{H}{R_{\mathbb{D}}} \alpha \qquad (4.1)$$

where $R_{\mathbb{D}}$ (= 1738.1 km) is the radius of the Moon. From a design altitude of 111 km, δ = 1.27 mrad. The surface spatial resolution is

$$d = R_{\mathbb{D}} \delta = 2.22 \text{ km.} \qquad (4.2)$$

For a circular orbit, the selenocentric angular velocity is constant. The scan mirror rotation period can be chosen such that the scans intersect the ground track at a spacing of one resolution element.

$$P_I = \delta (R_{\mathbb{D}} + H)^{3/2} (GM_{\mathbb{D}})^{-1/2} = 1.44 \text{ sec,} \qquad (4.3)$$

where the lunar gravitational coefficient $GM_{\mathbb{D}}$ = 4902.6 $km^3 sec^{-2}$. The actual ISR scan rate was set slightly higher than suggested by this criterion to allow for tolerances in construction.

ISR scan rate = 41.7 rpm

ISR scan period = 1439 msec. (4.4)

The Cassegrain primary and secondary are spherical mirrors. The primary mirror clear aperture has an outer diameter of 177.8 mm and an inner diameter of 63.5 mm (BEC Drawing 20590-2003-1). The effective collecting area is 217 cm^2. The objective has an effective focal length of 590.55 mm (Heilman and Nawyn, 1972).

The detector assembly consists of a silicon-immersed thermistor bolometer. The hyperhemispheric lens is 9.6 mm thick at the detector and is the only transmitting element in the optical train. The short wavelength cuton at 1.2 μm is determined by absorption in the lens. The long wavelength cutoff falls approximately at 65 μm as the detector becomes transparent to the infrared radiation.

The bolometer is composed of a resistor pair in a bridge arrangement with an applied bias voltage. One thermistor, the active flake, is bonded to the back of the lens at the focal point. The passive flake is bonded nearby, out of the beam of radiation. Absorbed radiation on the active flake thermally induces changes in its resistance. The result is a bridge imbalance and, therefore, a detector signal.

The noise power from this arrangement is particularly large at low frequencies. Noise sources include any intrinsic bridge imbalance, component drifts in the electronics, and current (1/f) noise. Since the ISR output contains information down to 0.1 Hz, it becomes important to periodically "zero" the signal and cancel the accumulated drifts.

The hardware contractor (cf. Chapter V), Barnes Engineering Company, proposed a space clamp circuit as a solution to the problem. During each

revolution of the scan mirror, the instantaneous field of view briefly sweeps across a sector of empty space on either side of the Moon. The detector receives no radiation during these space looks; and the output contains only noise, consisting mostly of the accumulated drifts in the system.

The space clamp circuit samples this noise signal once per scan during the space look which precedes encounter of the lunar limb. The offset voltage is preserved on a capacitor and is subtracted from the remainder of the scan as a dc shift.

A sample and hold circuit which preserves an instantaneous value of a signal is called a hard clamp. BEC demonstrated in their proposal (Plakun et al., 1969) that a hard clamp statistically samples high frequency noise spikes superimposed on the drift offset. In this way the high frequency noise is aliased into the low frequency regime, i.e., into the applied dc shift.

To minimize aliasing, BEC designed a more complex circuit called an integrating clamp. The integrating clamp samples the detector output for 24 milliseconds and averages out the high frequency noise. Although the noise suppression characteristics of the integrating clamp are good, its extended sampling time posed potential operational problems in early mission planning. A discussion of these problems will be postponed until the next chapter.

Figure 4-3 is a diagram of the electronic signal processing for the ISR. The detector signal is amplified by the preamplifier and shaped in frequency by the post-amplifier. Following the clamp circuit, a low pass filter guards against aliasing at the sampling frequency of the spacecraft data system (400 Hz). The processed signal is fed to each of three buffer

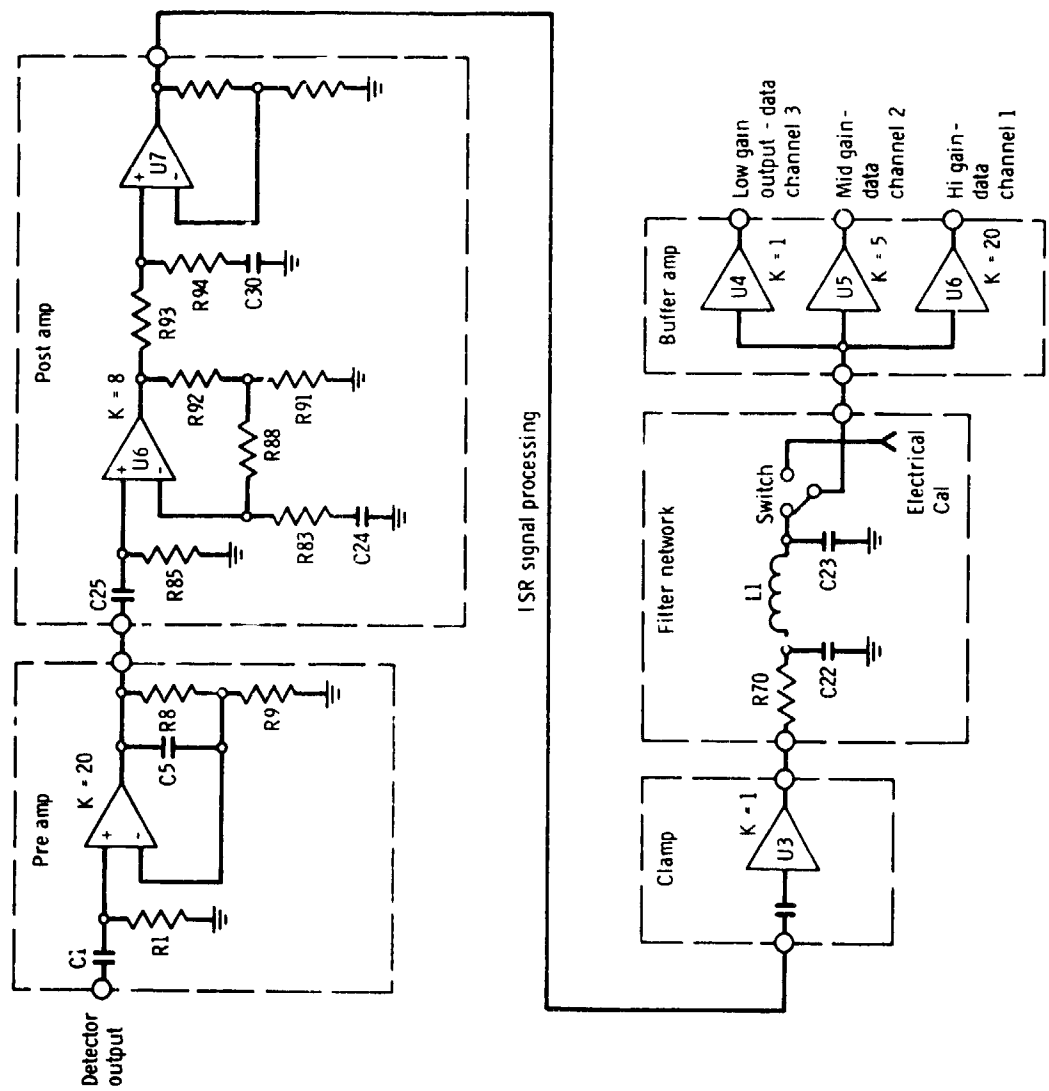

Figure 4-3 ISR SIGNAL PROCESSING. The detector output is amplified by the preamp, and the frequency response is shaped in the post-amplifier. After processing by the clamp circuit, the signal passes through a low pass filter to the output amplifiers.

amplifiers having approximate gains of 20 (Channel 1), 5 (Channel 2), and 1 (Channel 3). Three outputs of differing gains are necessary to fit the large dynamic range of the thermal data within the capabilities of the spacecraft telemetry system.

Once per scan four electrical voltage steps are inserted into the data stream. The duration of each step is ten milliseconds. The steps serve to verify the gain of the final output amplifiers and can be used as synchronization pulses for the location of individual scans in the continuous data stream.

V. Design Constraints Imposed by the Apollo Mission

The general design philosophy of the ISR as well as certain instrument details cannot be justified unless the constraints of the Apollo program are understood. Formulation of the experiment was shaped by the engineering envelope of the spacecraft, the operational plan of the mission, and the managerial philosophy inherent in the Apollo program.

A. General Design Philosophy

In early planning of the experiment NASA emphasized achieving a high probability of success and maintaining tight schedules for the delivery of flight hardware to Cape Kennedy. A corollary to these goals was the elimination from the program of unnecessary development of new hardware and new techniques. If an "off-the-shelf" system could be shown to satisfy the stated scientific requirements, then it would be chosen over any unproven system which might be superior in concept.

A major early decision made the ISR an ambient temperature radiometer. Performance calculations based on radiometers in weather satellites had shown that the sensitivity was adequate for the lunar measurement if the entire available spectral bandwidth was utilized. The experimenters felt justified in accepting some risk in the development of a new system having the much higher sensitivity available with a cryogenic detector. NASA vetoed the proposal. The performance of a pyroelectric detector was projected to be an order of magnitude better than the proposed thermistor bolometer, but consideration of it was dropped because of difficulties with qualification of a similar detector assembly on a weather satellite program.

Other early design decisions were also rooted in a conservative management approach. Mounting the ISR on a shelf in the SIM Bay restricted somewhat the external field of view of the instrument. An extendable and retractable boom was rejected on the basis of reliability. The experimenters were also unenthusiastic about its pointing stability. Image motion compensation was considered too complex to implement. A single-sided scan mirror was selected over less conventional scan systems which improved the duty cycle but complicated the hardware or data reduction.

B. Program Management

Within the Apollo program three options were available for the design and construction of the instrument itself.

a. The entire activity could be carried out by the Principal Investigator (PI) as part of his contract with NASA;

b. the experimental hardware could be built commercially under a subcontract from the PI's institution; or

c. the hardware contract could be separate from the PI contract and administered by NASA with the PI in the role of a technical advisor. Since Rice University lacked the experienced manpower and resources to conduct the program under either of the first two modes, the hardware contract was awarded competitively by the Manned Spacecraft Center (MSC). The winner of the competition was Barnes Engineering Company (BEC) of Stamford, Connecticut.

In some respects mode c. has the elements of a three-ring circus. NASA, the PI, and the hardware contractor have slightly different perspectives, interests, and motives. The administrative machinery for instituting changes and uncovering mistakes can be ponderous. The scientist is

not in direct control of the experimental apparatus. To avoid possible compromise of the scientific objectives, the PI team must plan activities and documentation requirements well in advance, must keep up with reports, and must maintain a good informal working relationship with both the NASA Technical Monitor and the program management at the hardware contractor. Although the ISR program received praise for proceeding smoothly, some problems with the experiment, particularly in the area of testing, can be traced to the indirect contact of the Principal Investigator and the experiment hardware. These problems will be covered in later chapters.

C. Data Coverage

Previous discussion has made clear that the ideal radiometric experiment would monitor the temperature of a surface element throughout a lunation (29.53 days). The length of time in orbit for the Apollo Command-Service Module (CSM) was limited to 6 days (20% of a lunation).

Under the constraint of limited time in orbit, the prime experimental objective became the measurement of surface nighttime temperatures. An operational constraint of the Apollo missions required lighting from a morning Sun during the landing. Therefore arrival at the Moon was timed to coincide approximately with sunrise at the landing site. The sunrise terminator moved from approximately 28°E to approximately 46°W during ISR data collection in the lunar orbit. Nighttime measurements were limited in general to the lunar western hemisphere.

Just as the longitude of the landing site dictated the position of the sunrise terminator, the latitude determined the orbital inclination. Initially the inclination was approximately 160° (i.e., a retrograde orbit) and was changed at REV 47 to approximately 157°, enabling

the ISR scans to cover slightly higher latitudes. The moderate inclinations precluded measurements in the polar regions and allowed considerable orbit to orbit overlap.

On the near side of the Moon nighttime coverage included southern portions of Mare Serenitatis and Mare Imbrium, Oceanus Procellarum, and equatorial regions on the western limb. On the far side, ground tracks passed south of the craters Hertzsprung and Korolev over to the craters Aitken and Van de Graaff.

D. Spacecraft Geometry

The Apollo 17 CSM consisted of the conical Command Module joined at the base to the cylindrical Service Module. One sector of the Service Module, called the Scientific Instrument Module (SIM) Bay, housed the orbital science experiments including the ISR (Figure 5-1). The SIM Bay wall was jettisoned with pyrotechnic bolts prior to lunar orbit insertion, providing the orbital science complement a view outside the spacecraft.

A convenient coordinate system within the CSM can be defined by the cylindrical axis (X axis) and the SIM Bay centerline. The +X direction lay toward the nose of the Command Module.

The ISR was mounted on the outer edge of a shelf in the SIM Bay. The axis of rotation of the ISR scan mirror (instrument y-axis) was parallel to the CSM X-axis. The external field of view was limited to 162 degrees by the walls of the SIM Bay. This number represents a reduction of 15% in the external field defined by the ISR aperture alone.

During ISR data collection the CSM maintained a lunar orientation called SIM Bay attitude. The spacecraft reaction control system was programed to maintain the SIM Bay centerline pointed at nadir on the lunar

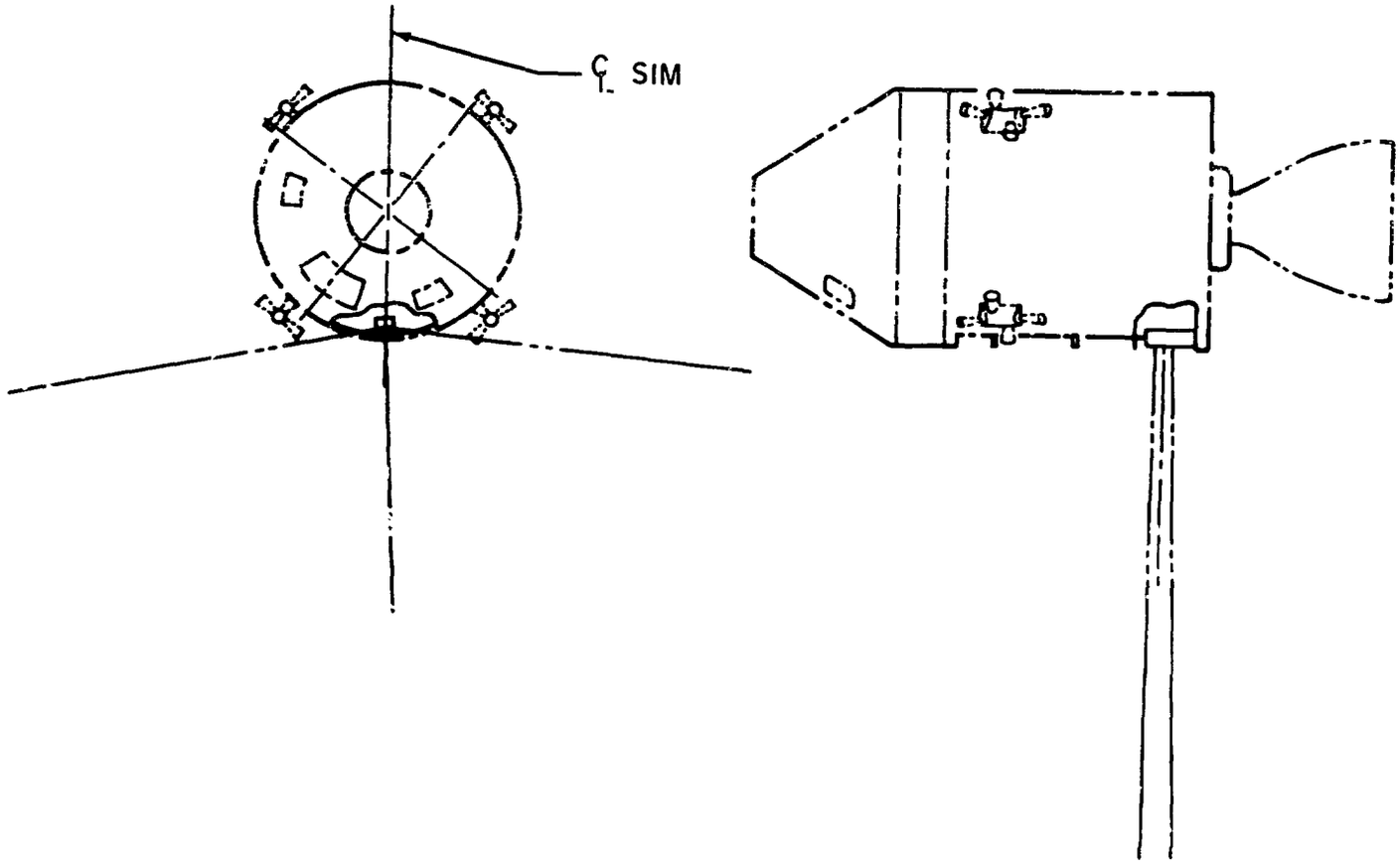

Figure 5-1 SIM BAY GEOMETRY. A configuration of the Command-Service Module (CSM) shows the mounting geometry of the ISR in the Scientific Instrument Module Bay.

surface and to keep the X axis in the orbit plane. While in SIM Bay attitude the CSM could be orbiting with either th +X axis or the -X axis pointing along the velocity vector.

Limitations on available fuel prevented the attitude thrusters from firing continuously to maintain any orientation. Firings occurred only after the accumulated drift in pitch, roll, or yaw had reached a preset tolerance limit. On the Apollo 17 mission two tolerance settings were available to the astronaut, a wide deadband of 3 degrees and a narrow deadband of 0.5 degrees. For Apollos 15 and 16 the wide deadband has been 5 degrees, and that number was assumed in the design of the SIM Bay experiments for Apollo 17.

The ISR collected data during a large fraction of the total time that the CSM was in lunar orbit. It was important to demonstrate to engineers planning the mission that the ISR was capable of nominal operation while the spacecraft held the more economical (in terms of fuel) wide deadband. Implementation of the integrating clamp circuit caused concern among the mission planners.

The central question was whether the lunar limb would fall into the ISR field of view during the space clamp. A false offset would seriously degrade the entire scan. Some calculations indicated that the ISR would not operate nominally at the extremes of the wide deadband if pointing errors, installation errors, and the overall geometry were taken into account.

To minimize the problem, the ISR was installed with its -x axis canted 2.67 degrees off of the SIM Bay centerline. This position placed the field of view at the start of the clamp as close to the SIM Bay wall as tolerances would allow. I performed a detailed analysis of the geom-

etry and pointing errors to predict the probability of degraded data while operating in a wide deadband. The analysis is presented in Appendix A. It showed that data degradation would be minimal, thereby allowing planning of extended data periods for the ISR. The error analysis of postflight pointing knowledge was useful in planning data reduction and formed the justification for actually measuring the direction of the ISR -x axis on the launch pad after installation in the SIM Bay.

E. Spacecraft Data System

The SIM Bay data system digitized each of the ISR outputs into 8-bit words at a rate of 800 samples per second. Telemetry words consisting of all zero-bits or all one-bits were disallowed, giving a total of 254 possible levels. Each level corresponded to a signal change of 20 millivolts for a total range 0 - 5.06 volts.

The dynamic range of the ISR data was known to be considerably greater than the capacity of the SIM Bay data system. The bolometer output is proportional to lunar radiance rather than lunar temperature. If the ISR Noise Equivalent Delta Temperature (NEΔT) is approximately 1K at 90K, the Stefan-Boltzmann Law can be used to approximate the signal to noise ratio.

$$S/N\ (90K) \sim (91^4/90^4-1)^{-1} = 22 \qquad (5.1)$$

Assume the spectral sensitivity of the ISR is constant between 1 μm and 60 μm. At the subsolar point (400 K) all of the radiance will be transmitted to the detector. For a scene temperature of 90 K only 68% is transmitted. The approximate signal to noise ratio at 400 K is

$$S/N\ (400\ K) = \left(\frac{400}{90}\right)^4 \times \frac{22}{.68} = 1.3 \times 10^4 \qquad (5.2$$

Clearly the dynamic range of the measurement swamps the capacity of a telemetry channel.

Three approaches were considered to resolve the mismatch:

a. Optical filtering

A filter which rejected wavelengths shorter than approximately 20 μm or 30 μm would remove the reflected solar radiance from dayside measurements and would remove a significant portion of the high temperature flux. No short wavelength rejection filter could be found which would not degrade the long wavelength sensitivity of the radiometer. A brief study of scatter filters yielded promising results, but their experimental nature removed them from consideration. It was also realized that any absorption filter would be a thermally varying noise source in the optical path.

b. Nonlinear amplification

A logarithmic buffer amplifier preserves measurement sensitivity at low signal levels yet compresses the total dynamic range. This option was rejected because the nonlinear electronic components lack stability as a function of time and temperature.

c. Multiple channels

Fortunately extra scientific channels were available in the Apollo 17 data system. The entire range of measurement from 80K to 403K was covered by a low gain channel. A high gain channel, which preserved sensitivity in the measurement, saturated at 173K. Therefore an intermediate channel was also implemented.

F. Spacecraft Environment

SIM Bay temperature extremes were a major concern in the ISR design. The calibration of the radiometer is good only as long as a

constant detector temperature is maintained. A detailed thermal model of the ISR was developed to predict detector temperature as a function of hypothetical SIM Bay temperature histories provided by NASA.

To simplify detector temperature control it was decided to heat the detector to a fixed temperature above the predicted extreme. For a "hot-biased" mission profile the maximum detector temperature was predicted to be 306K (91°F) (Heilman and Nawyn, 1972). The detector temperature set point was chosen to be 311K (101°F). The detector heater was controlled by an active feedback loop from a thermistor mounted on the detector assembly. Although detector performance is somewhat degraded at this high temperature, the design maintains constant temperature simply and reliably.

Another design problem was the potential degradation of the ISR optics by condensation of rocket exhaust products. Reaction control clusters are mounted on the exterior of the CSM, and some of the jet plumes extended into the open SIM Bay. The actual magnitude of the problem was never evaluated satisfactorily prior to the mission.

Two types of precaution were implemented to deal with the problem. During orbital science operations, those reaction control jets actually pointing into the SIM Bay were inhibited. Since all jets were necessary for major maneuvers, each instrument was provided with a cover which could be opened or closed by the astronaut in the Command Module. Figure 5-2 shows the ISR cover in open and closed configurations.

G. Experiment control

An astronaut in the Command Module could switch the ISR on or off and could raise or lower the cover. No other direct control of the instrument was possible.

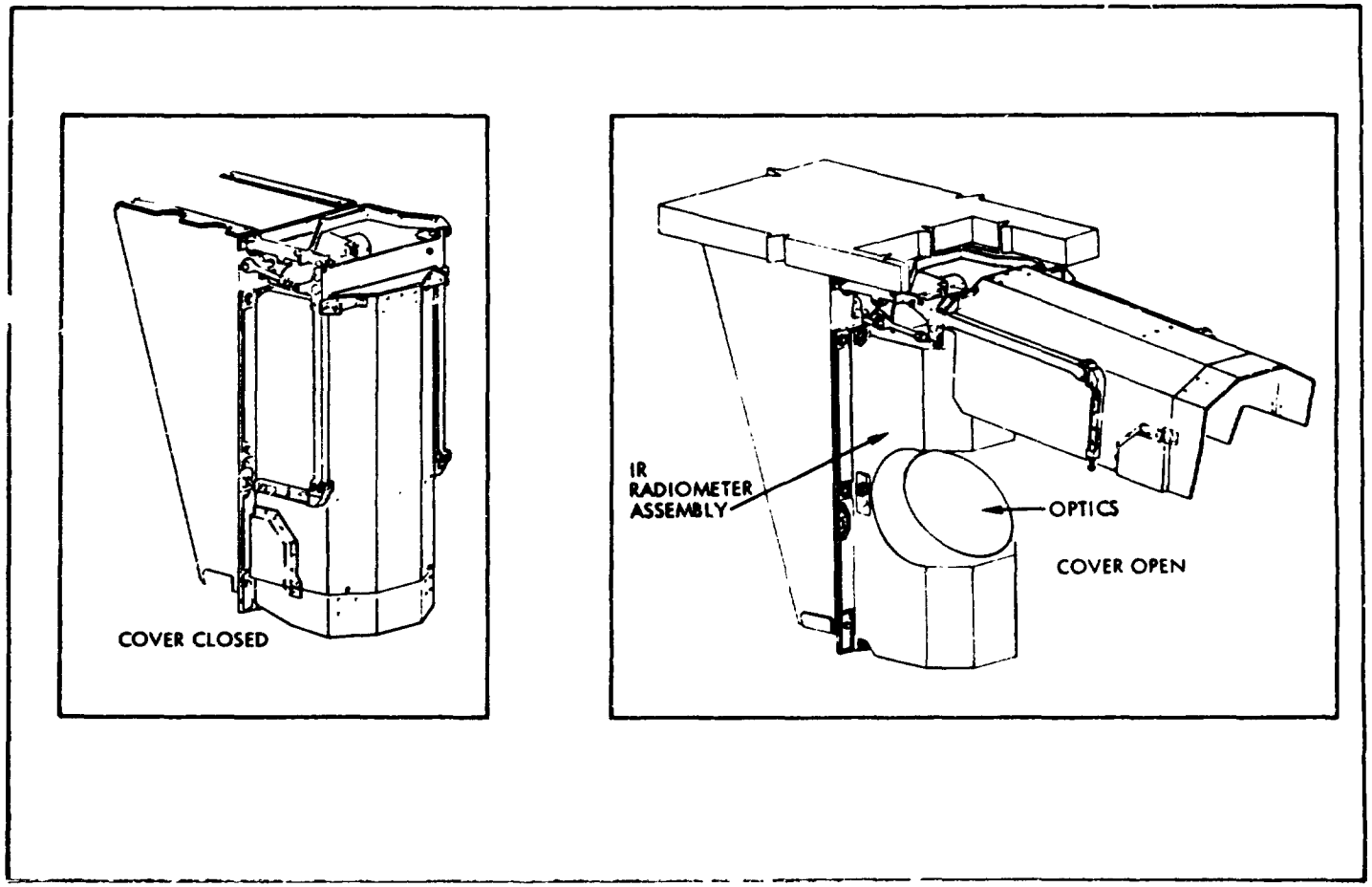

Figure 5-2 ISR PROTECTIVE COVER DETAIL. The contamination cover protected the ISR optics from degradation by rocket exhaust products. It was opened and closed from a switch inside the Command Module.

NASA required from the PI team a real-time evaluation of experiment performance during the mission. For the ISR, this requirement implied sampling the actual scientific output. Housekeeping data, consisting of some temperatures and voltages, was insufficient to judge the quality of the data. However, 800 samples per second was too high a rate for the available real time data lines into the Mission Control Center.

A scheme was devised whereby 3 seconds of ISR data was stripped from the SIM Bay telemetry stream and buffered at a ground receiving station. The buffered data was transmitted to the Mission Control Center at a rate of 20 samples per second over a period of two minutes. In effect, two scans were available every two minutes. In terms of the lunar surface, the data stream was sampled every 6 degrees of longitude. The real time data enabled us to evaluate instrument performance and to optimize operating strategy during the mission.

VI. Predicted Performance

An infrared radiometer consists of three functional parts: the optics, the detector, and the signal processing electronics. The optics serve to collect and focus infrared radiation onto the detector. Absorbed radiation heats the detector, which transduces the resultant temperature change into an electrical signal. The signal processing electronics amplify the detector output and shape the time constants and bandwidth of the system to enhance the signal to noise ratio.

A. The Optics

A schematic of the ISR optical system has been presented in Figure 4-1. The scan mirror folds incident infrared radiation into the Cassegrain optical system. The spherical Cassegrain mirrors are simpler to manufacture and are less sensitive to defocusing than the more common parabolic-hyperbolic Cassegrain pair. Since the ISR is not intended as true imaging system, spherical aberrations are acceptable. Ray traces of the optical design by BEC showed only a small edge blur.

The detector assembly at the Cassegrain focus incorporates the hyperhemispherical silicon lens shown in Figure 6-1. The lens reduces the effective f-number of the system and allows a smaller active flake. As the detector size decreases, the noise figure improves and the required bias voltage is less. A smaller bias voltage is easier to regulate. On the negative side, reflection and absorption losses at the lens reduce the throughput of the system. The net result, however, is a gain in performance.

The total power collected by a radiometer is equal to the product of the irradiance at the aperture, the area of the clear aperture,

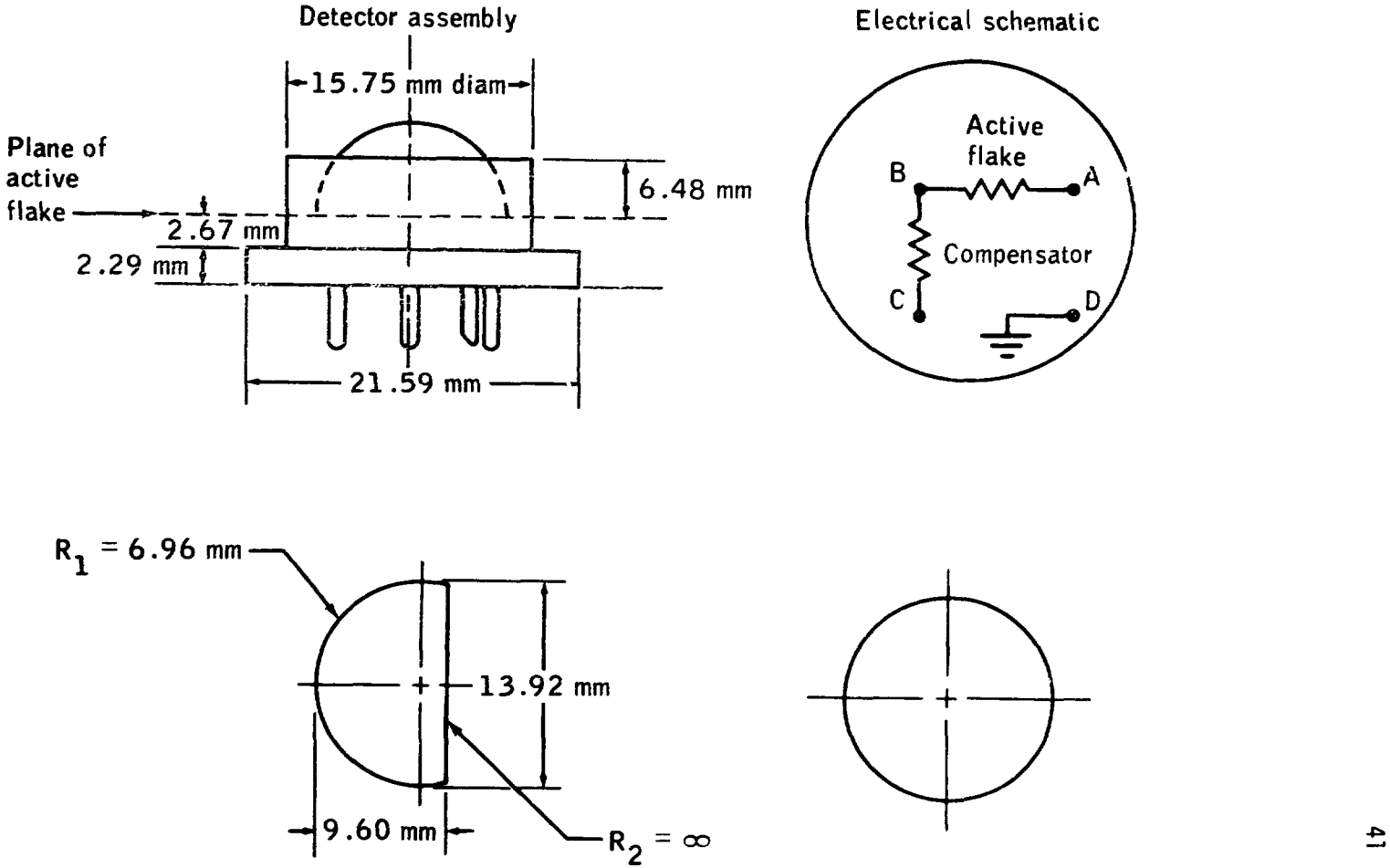

Figure 6-1 ISR DETECTOR ASSEMBLY. The active flake is bonded to the hyperhemispherical silicon lens with arsenic modified selenium. The compensator flake is bonded with mylar.

the solid angle of acceptance, and the efficiency of the system. The spectral power absorbed by the ISR detector at a particular wavelength, λ, is given by

$$dP = K_0 A\Omega\rho^3\alpha(\lambda)\tau(\lambda)N(\lambda,T)d\lambda \qquad (6.1)$$

where $K_0 (= \frac{\pi}{4})$ - a geometrical degradation factor due to the fact that a circular aperture is imaged onto a square flake;

$A (= 217\ cm^2)$ - the unobstructed collecting area;

$\Omega (= 3.14 \times 10^{-4}\ ster)$ - the solid angle corresponding to the 20 mrad. field of view,

$\rho (= 0.96)$ - the reflectivity of each of the mirrors;

$\alpha(\lambda)$ - the absorptivity of the detector flake

$\tau(\lambda)$ - the transmittance of the lens

$N(\lambda,T)$ - the Planck radiance function for temperature T.

In equation (6.1) the quantities $\tau(\lambda)$ and $\alpha(\lambda)$ are difficult to estimate.

Reflection losses at the surface of the lens are on the order of 50%. As a result, antireflection coatings are often applied on immersed detectors. The ISR is unusual, however, in that its design objectives require a broadband, long wavelength response. All coatings considered would degrade the low temperature measurement capability of the radiometer. Consequently, the lens is uncoated. Optical losses in the detector assembly are predicted from the properties of silicon, the bonding material for the flake (arsenic-modified selenium), and the flake itself.

The transmission curve for the lens is difficult to construct from data in the scientific literature. Measurements on modern optical quality silicon are rare. Samples are thin (≤2 mm) for measuring the extinction coefficient in absorption bands. Vendor data sheets give nice transmission curves, but no details of the measurement are discussed.

Figure 6-2 displays four sets of transmission data for silicon. Curves (a) and (b) represent samples of comparable thickness from the same vendor. Curve (a) comes from the vendor's data sheet whereas curve (b) was found in the literature (Randall and Rawcliffe, 1967). In the critical 25 μm to 50 μm region, there is a disagreement of approximately 10% in transmission. From the figure and other available data several points can be made about silicon transmission. For wavelengths between 1.2 μm and 6 μm the transmission is approximately 50% and only weakly dependent on sample thickness. In the reststrahlen region from 6 μm to 20 μm the absorption coefficient can be high with little transmission through a thick sample. Beyond 20 μm the reflectivity is approximately constant at 30% (Yoshinaga, 1955), and no absorption band has been observed between 20 μm and 60 μm (Aronson et al., 1964). The absorption coefficient at the long wavelengths can be assumed approximately constant.

McIntosh (unpubl. memo) cited a transmission measurement on a 5 mm sample from the boule of silicon from which the ISR immersion lenses were fabricated. From a 40% transmission at 30 μm, he calculated an absorption coefficient of approximately 0.05 cm^{-1}. The transmission to the detector flake through the 9.6 mm lens was calculated at 42% because the reflection losses at the silicon-selenium interface are much smaller than at a silicon-air interface.

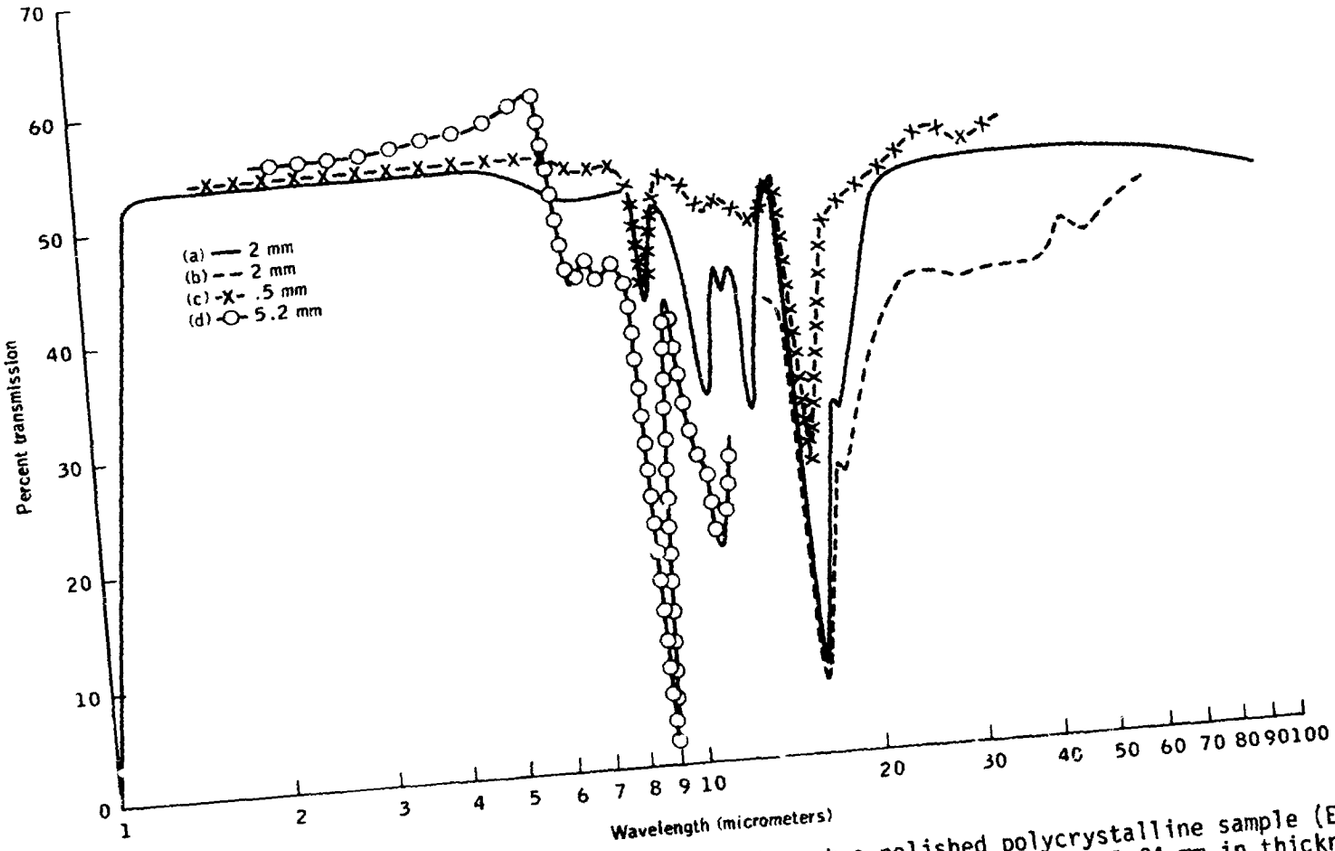

Figure 6-2 SILICON TRANSMISSION DATA. (a) Transmission through a polished polycrystalline sample (Exotic Materials, Inc., Technical Data Sheet, Sept., 1974), (b) Silicon sample 1.94 mm in thickness (Randall and Rawcliffe, 1967), (c) Sample 0.535 mm thick (F. J. Low, priv. comm.), (d) DuPont silicon sample 5.18 mm thick (Briggs, 1950).

Any prediction based on plane parallel geometry must be considered an upper limit to the actual transmission of a converging beam incident on a hyperhemispherical surface. As supplementary information, BEC supplied a spectral response curve for another silicon immersed bolometer. The lens thickness was comparable to that of the ISR detector assembly, but an antireflection coating had been applied to the lens. The curve is presented in Figure 6-3. The response of the detector is depressed relative to the maximum at 2 μm when compared to the silicon data in Figure 6-2.

BEC also supplied an engineering version of the ISR detector to Rice University for testing. A Beckman IR-9 spectrophotometer at MSC was used to measure the spectral response between 2.5 μm and 25 μm. The comparison detector was a Mullard pyroelectric. A Beckman IR-11 in the Rice Chemistry Department was used to measure the response beyond 12.5 μm. Its internal Golay cell was the comparison detector. Both comparison detectors are thought to be reasonably flat spectrally, but were chosen largely as a matter of convenience. The measurements were done on a "quick look" basis, and proper attention was not given to optical alignments or the condition of the spectrometers. It should also be noted that the ISR detector behaved erratically throughout.

On each spectrometer the output of the ISR detector was digitized by hand and divided by the digitized output from the comparison detector. Each set of data was then scaled to match reasonably well in the overlap region, 12.5 μm to 20 μm. The large scatter at long wavelengths arises partly from the difficulty in avoiding water vapor absorption bands in digitization and partly from scaling and matching the different spectral ranges of the spectrometer. Data from 2.5 μm to 5 μm

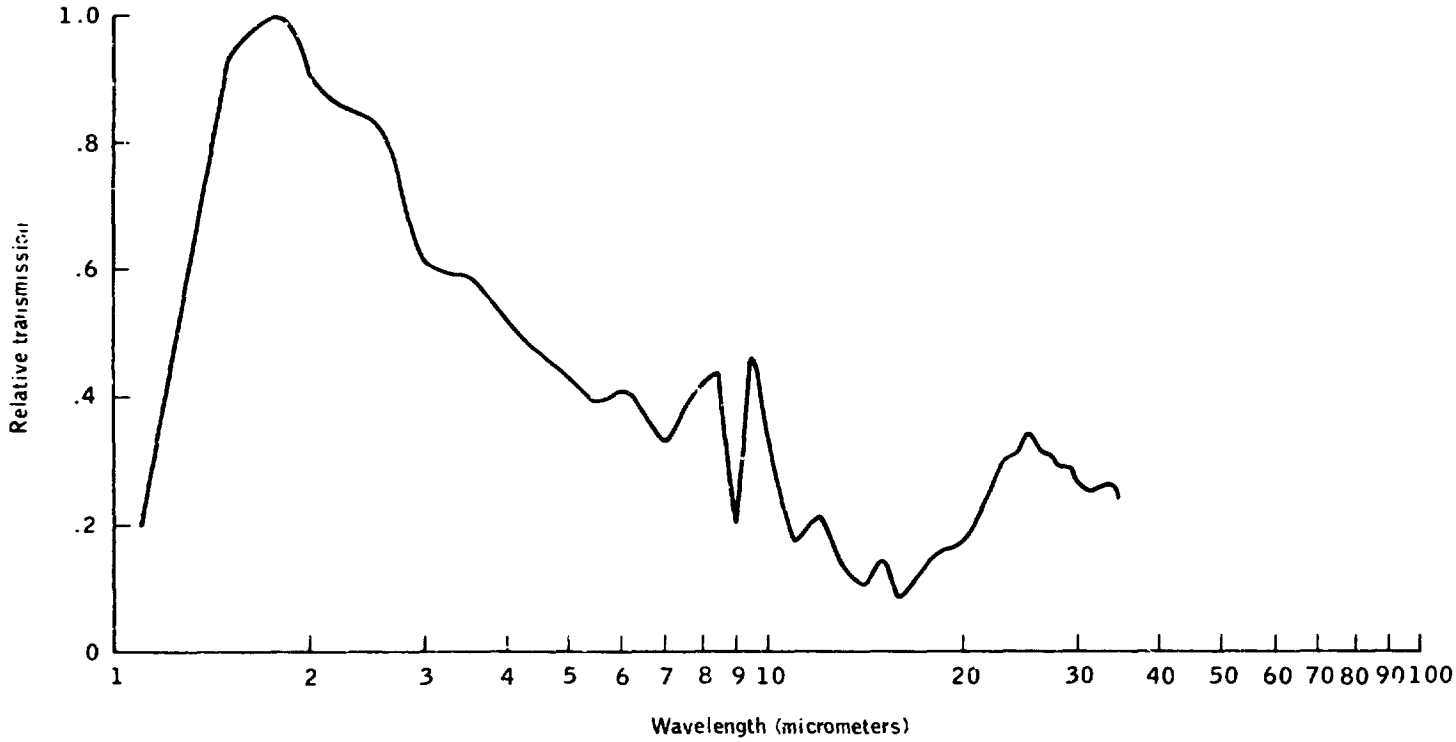

Figure 6-3 SPECTRAL RESPONSE CURVE FOR BOLOMETER BE6328. This data was supplied by BEC for a silicon immersed bolometer similar to the ISR detector but having an anti-reflection coating applied to the lens.

was discarded when a problem was discovered in the registration of the ISR spectrometer trace with that of the comparison detector.

Although the results are largely qualitative, a few important conclusions can be drawn from the data. First, the ISR response extends past 60 μm. Previous models had assumed a 40 μm cutoff. A comparison of Figure 6-4 with Figure 6-3 shows that the spectral structure in the reststrahlen region agrees very well. The major difference is an enhanced response at 15 μm in the ISR detector. The relative response between long wavelengths and the regions of transparency in the reststrahlen bands are similar for both immersed bolometers. The deep absorption below 8 μm is present in both bolometers although it is not evident in the silicon curves of Figure 6-2. The response of the ISR detector below 5 μm probably increases in a manner similar to Figure 6-3. However, the 3 to 1 enhancement at 2 μm over the long wavelength peak is probably exaggerated by the antireflection coating. Taking into account the silicon data and the partial transparency of the detector material we can place short wavelength enhancement factor at approximately 1.5.

We can conclude that Figure 6-4 is a reasonable representation of the ISR spectral response. In particular, we can estimate

$$\tau(\lambda)\alpha(\lambda) \approx 0.3 \quad (\lambda = 40\ \mu m) \qquad (6.2)$$

The above estimate and the spectral response curve will be used later in the chapter to compute the sensitivity of the ISR.

B. The Detector

A bolometer is a type of infrared detector in which some measurable physical property varies with temperature. In a thermistor bolometer the detector is a flake of semiconductor material whose intrinsic

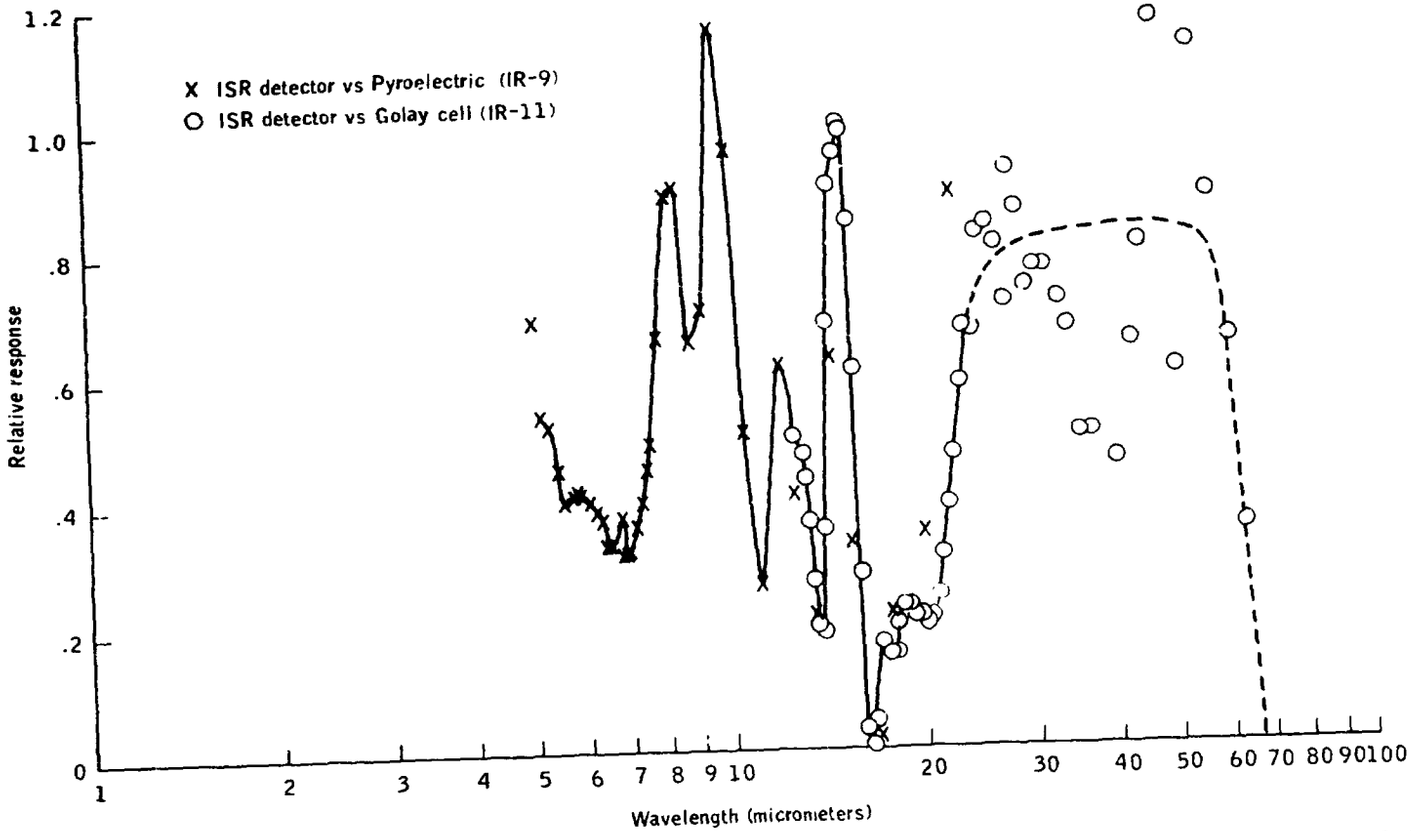

Figure 6-4 ESTIMATED SPECTRAL RESPONSE FOR THE ISR DETECTOR. The symbols represent measurements of the ISR detector response relative to comparison detectors in two infrared spectrometers. The line (solid and dashed) is the estimate of the response based on the measurements together with silicon transmission data.

resistance is a function of temperature. An electrical schematic of the ISR detector is shown in the upper right-hand corner of Figure 6-1.

The active flake is exposed to the beam of radiation while the compensator flake is positioned nearby, outside the beam. A carefully regulated bias voltage is maintained across the resistor pair. When the temperatures of the two flakes are equal, no voltage appears at the detector output, B. If the active flake is illuminated, the absorbed radiation raises its temperature, thereby changing its resistance and causing a voltage to appear at the output.

A simple model of a bolometer (Smith et al., 1968) illustrates the role of certain physical parameters. Absorbed radiation is converted to heat, part of which raises the temperature of the flake and part of which is conducted to the surroundings. The temperature contrast, ΔT, between the flake and its environment is given by the heat conduction equation

$$P(t) = C \frac{d(\Delta T)}{dt} + G(\Delta T) \tag{6.3}$$

where P is the absorbed power, t is time, C is the heat capacity of the flake, and G is its conductance.

Consider an ISR scan across a point source. If the source is within the instantaneous field of view for t_o seconds, the power incident on the detector can be represented by the function

$$P(t) = \begin{cases} P_o, & 0 \leq t \leq t_o \\ 0, & \text{otherwise} \end{cases} \tag{6.4}$$

The solution for equation (6.3) becomes

$$\Delta T(t) = \begin{cases} \frac{P_o}{G}\left[1-\exp\left(\frac{-t}{\tau_d}\right)\right] & , 0 \le t \le t_o \\ \frac{P_o}{G}\exp\left(\frac{t_o-t}{\tau_d}\right)\left[1-\exp\left(\frac{-t_o}{\tau_d}\right)\right] & , t_o \le t \end{cases} \tag{6.5}$$

where $$\tau_d = \frac{C}{G} \tag{6.6}$$

is the thermal time constant. The magnitude of τ_d determines how closely the temperature change approaches the maximum. The detector response time can be lowered by minimizing C and maximizing G. Optical constraints on the physical dimensions of the element set a lower limit on C. The flake must be large enough to fill the image and thick enough to be opaque to the radiation. The chosen value of G must represent a tradeoff between detector speed and the size of ΔT_{max}.

The responsivity of the detector (R), as measured in volts per watt, should be high to ensure a maximum signal from a given irradiance. High values are achieved by maximizing the temperature rise in the flake, the rate of change of resistance with temperature, and the bias voltage.

BEC utilized an empirical formula (McIntosh, unpubl. memo) to predict the responsivity of a thermistor.

$$R = 100 \quad \frac{\mathcal{R}\tau_d}{A} \text{ volts/watt,} \tag{6.7}$$

where τ_d = (3.5) is the thermal time constant in milliseconds, $\mathcal{R}$ (= 0.25) is the detector resistance in megohms, and A (= 0.74 mm^2) is the detector area. Using the values in parentheses, the predicted responsivity for the ISR detector is

$$R_{ISR} = 109 \text{ volts/watt.} \tag{6.8}$$

C. Signal Processing

Although the principal noise mechanisms originate in the detector, the final signal to noise ratio is strongly affected by the transfer function of the electronics. Important parameters of the frequency response are the high and low frequency corners and cutoffs.

The spacecraft data rate of 800 samples per second sets the high frequency cutoff. The sampling theorem (e.g., Bracewell, 1965) states that all information beyond the sampling frequency is aliased back into the system bandpass as noise. Therefore, the sampling frequency, 400 Hz, is the upper limit for the high frequency cutoff.

The location of the high frequency corner determines the responsiveness of the radiometer to radiance changes. As the corner is moved to higher frequencies the contrast in the image becomes greater and detail becomes more distinct. The thermal time constant of the detector provides a natural high frequency rolloff, but its corner is generally lower than desired. A treble boost to raise the corner incurs a noise penalty, and the amount of high frequency enhancement becomes a system tradeoff.

In principle, the frequency content in the data can be manipulated either in the electronic signal processing or in digital processing on the ground. In reality, the two approaches are not perfectly equivalent. Digital enhancement of high frequencies will amplify not only intrinsic instrument noise but also noise induced by telemetry or by data handling. It can never recover frequencies whose signal amplitude at the instrument output fell below the quantization increment of the spacecraft data system. Treble boost in the electronic design increases the aliased power, a non-random noise source.

A debate over the placement of the high frequency corner was won by the BEC design engineers. They applied a standard response criterion which requires a point source to remain in the field of view for three system time constants. For the ISR

$$3\tau_u = \alpha\left(\frac{2\pi}{\omega}\right) 60 \tag{6.9}$$

where α (.02 radians) is the instantaneous field of view and ω (41.7 rpm) is the rotation rate of the mirror. The high frequency corner becomes

$$s_{max} = \frac{1}{2\pi\tau_u} = 104 \text{ Hz} \tag{6.10}$$

The final specification read $s_{max} = 105\ ^{+55}_{-0}$ Hz.

A low frequency corner can be established by defining the allowable droop in the system. Consider a full scale (5 volt) step function input to the system. A valid droop criterion might be maintenance of the true value to within one telemetry bit (20 millivolts) over the period of a lunar scan (0.56 seconds). The design engineers felt this corner might be difficult to achieve in practice, and the criterion was set at a 1% (50 millivolts) droop. The associated time constant is

$$\tau_1 = -.56/\ln(1-.01) = 56 \text{ seconds}, \tag{6.11}$$

and the low frequency corner becomes

$$s_{min} = \frac{1}{2\pi\tau_1} = 2.86 \text{ mHz}. \tag{6.12}$$

An analysis of the system shows that the low frequency rolloff characteristics are set by the space clamp circuit. The complete action

of the integrating clamp is difficult to describe in the frequency domain, so we must resort to a simpler analytical model.

The ISR detector output is strongly periodic with almost all of the spectral power concentrated in the vicinity of the mirror rotation frequency P_I^{-1} and its harmonics. The clamp circuit samples the output once every P_I seconds at a signal minimum (the space look). A dc offset is applied to the signal such that the minimum point becomes zero volts at the output of the instrument.

Consider a detector output waveform V(t). The clamp output $V_c(t)$ is basically a histogram approximation to V(t). The height of each step in the histogram is the value of the detector output at times $t = nP_I$, $n = 0, \pm1, \pm2, \ldots$ Using Bracewell's (1965) notation for rectangle functions, the clamp output becomes

$$V_c(t) = \frac{1}{P_I} \sum_n V(nP_I) \prod\left\{\frac{t-(n + 1/2)P_I}{P_I}\right\} \qquad (6.13)$$

where the function $\prod$ in each term is a rectangle of unit height and width P_I, centered at $(n + 1/2)P_I$.

The Fourier transform of $V_c(t)$ can be written as

$$\mathcal{F}_c(s) = \sum_n \mathcal{F}_{cn}(s) \qquad (6.14)$$

where $\mathcal{F}_{cn}$ is the transform of the n^{th} term in the summation (6.13). Using the derivative rule for Fourier transforms and knowing the transform of the impulse function, we can write

$$\mathcal{F}_{cn}(s) = P_I\, V(nP_I)\, \frac{\sin\pi P_I s}{\pi P_I s} \exp\left[-\pi i(2n + 1)\, P_I s\right] \qquad (6.15)$$

The transform of the clamp function becomes

$$\mathcal{F}_c(s) = \frac{\sin\pi P_I s}{\pi P_I s} \exp(-i\pi P_I s) \sum_n V(nP_I)\exp(-i2\pi nP_I s) \qquad (6.16)$$

It can be readily shown that the summation in (6.16) is the (partial) Fourier series expansion of $\mathcal{F}(s)$, the transform of V(t).

$$\mathcal{F}(s) \sim \sum_n V(nP_I)\exp(-i2\pi nP_I s) \qquad (6.17)$$

For the sake of discussion, we shall treat (6.17) as an equality. In this approximation the ISR output frequency response becomes

$$\mathcal{F}(s) - \mathcal{F}_c(s) = \mathcal{F}(s)\left\{1 - \frac{\sin\pi P_I s}{\pi P_I s} \exp(-i\pi P_I s)\right\} \qquad (6.18)$$

The modulus and phase of the expression in brackets from (6.18) are plotted on Figure 6-5. The effect of the clamp not only tends to cancel low frequencies but also introduces a phase lag. The frequency P_I^{-1} and its harmonics are relatively unaffected, and the data in the ISR output is relatively well preserved. However, it can be seen that in certain frequency regimes (e.g., $.37<P_I s<1$) the clamping is counterproductive.

To achieve a flat frequency response between the low and high frequency corners, the ISR electronics must incorporate a treble boost to compensate for the high frequency rolloff of the detector itself. If the input power for (6.3) has the form $P(t) = P_o\exp(2\pi ist)$, then it can be shown that the frequency response of the bolometer is proportional to

$$D(s) = (1 + 4\pi^2 s^2 \tau_d{}^2)^{-1/2} \qquad (6.19)$$

For a thermal time constant of 3.5 msec the 3 db corner frequency is 45 Hz. The transfer function of the post amplifier was designed to provide

$$E(s) = (1 + 4\pi^2 s^2 \tau_d{}^2)^{1/2}\left(1 + \frac{s^2}{s_c{}^2}\right)^{-1}, \qquad (6.20)$$

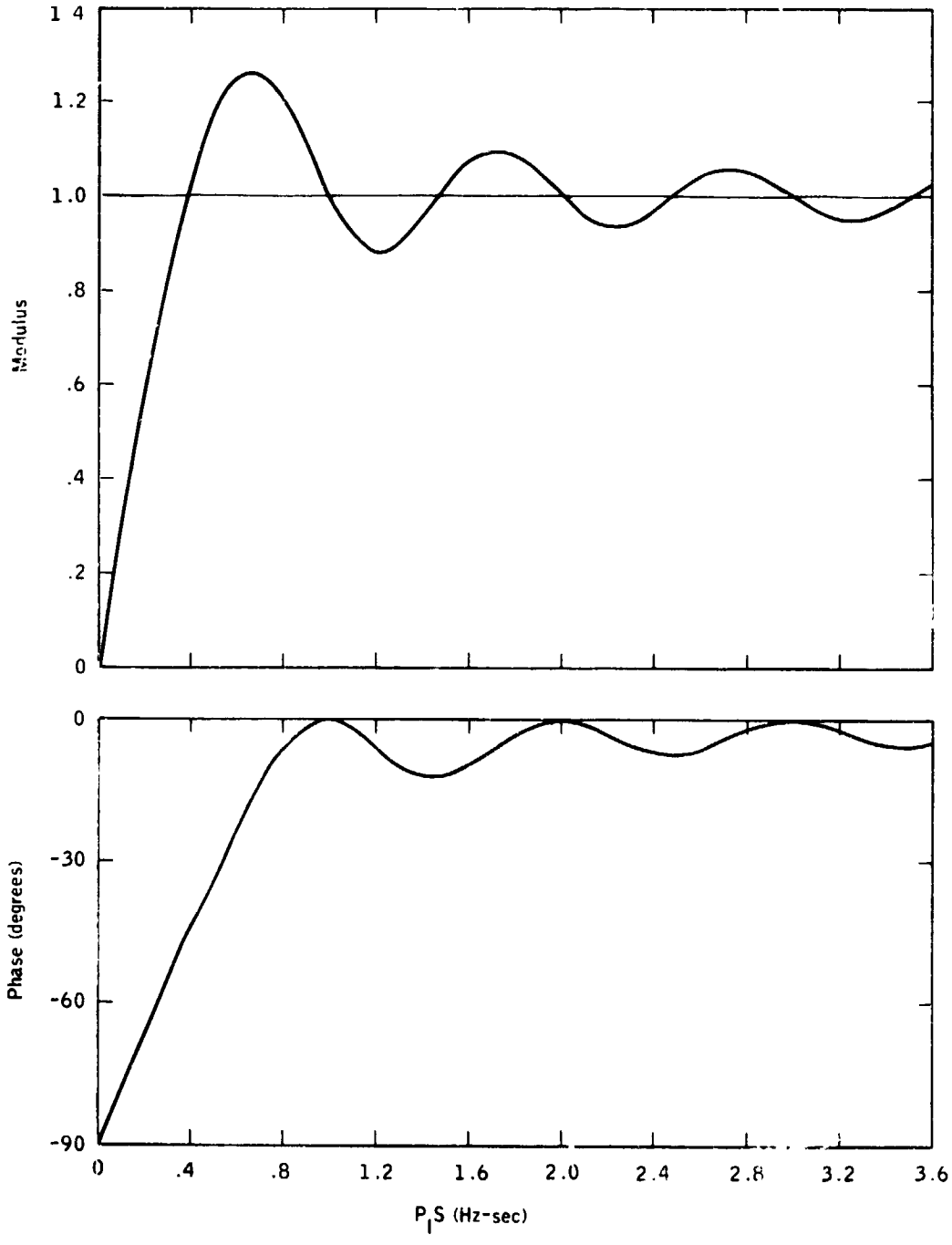

Figure 6-5 TRANSFER FUNCTION OF THE SPACE _AMP CIRCUIT. The modulus and phase of the clamp circu[illegible] requency response was calculated using a model des[illegible]ed in the text.

thereby creating the desired total transfer function

$$G(s) = D(s)\,E(s) = \left(1 + \frac{s^2}{s_c^2}\right)^{-1}, \tag{6.21}$$

The corner frequency s_c is chosen to satisfy the constraint $G(105) = 2^{-1/2}$.

D. Noise Bandwidth

The noise bandwidth of the system can now be calculated. The noise voltage V_n can be found by

$$V_n^2 = V_J^2 \int_0^\infty (|G(s)|^2 |N(s)|^2) ds, \tag{6.22}$$

where V_J is the detector Johnson noise and N(s) the thermistor noise spectrum given as (Plakun et al., 1969)

$$|N(s)|^2 = \begin{cases} 250\ s^{-2} & s \le 5Hz \\ 50\ s^{-1} & 5Hz \le s \le 50Hz \\ 1 & 50Hz \le s \end{cases} \tag{6.23}$$

At low frequencies the ISR transfer function is dominated by the clamp, and the shaping in the post amplifier is negligible. At high frequencies the converse is true. The crossover point occurs at 18 Hz, where each circuit modifies the transfer function by approximately 1%. We shall choose the boundary at $26\ P_I^{-1} = 18.1$ Hz in order to integrate over an integral number of cycles of (6.18). Below 5 Hz the treble boost in (6.20) can also be neglected. With these approximations, the total noise transfer function is

$$|G(s)N(s)|^2 = \begin{cases} 250\ s^{-2}\left|1 - \dfrac{\sin\pi P_I s}{\pi P_I s}\exp(-i\pi P_I s)\right|^2 & 0Hz \leq s \leq 5Hz \\ 50\ s^{-1}(1 + 4\pi^2 s^2 \tau_d{}^2)\left|1 - \dfrac{\sin\pi P_I s}{\pi P_I s}\exp(-i\pi P_I s)\right|^2 & 5Hz \leq s \leq 26P_I{}^{-1} \\ 50\ s^{-1}(1 + 4\pi^2 s^2 \tau_d{}^2)(1 + \dfrac{s^2}{s_c{}^2})^{-2} & 26P_I{}^{-1} \leq s \leq 50Hz \\ (1 + 4\pi^2 s^2 \tau_d{}^2)(1 + \dfrac{s^2}{s_c{}^2})^{-2} & 50Hz \leq s \end{cases} \quad (6.24)$$

The integral (6.22) is evaluated in Appendix B using τ_d = 3.5 msec and s_c = (105) (1.554) Hz. The result is

$$\frac{V_N{}^2}{V_J{}^2} = 2313 + 69 + 71 + 1125 = 3578 \quad (6.25)$$

The major noise contributions come from current noise at low frequencies and the effects of the treble boost at high frequencies.

E. Predicted ISR Signal to Noise Ratio

The Johnson noise V_J in the detector is readily calculable from the effective resistance of the bridge $\mathcal{R}_e$ (125 kΩ), and the detector ambient temperature T_a (311K).

$$V_J = \sqrt{4kT\mathcal{R}_e} = 46.3\ nV\ Hz^{-1} \quad (6.26)$$

where k is Boltzmann's constant. The total noise figure for the detector is then

$$V_N = \sqrt{3725}\ V_J = 2.83\ \mu V \quad (6.27)$$

The specification for the ISR required an NEΔT of 2K at a background temperature of 90K. The power incident on the detector for those

conditions is given by the integration of (6.1). The function $\tau(\lambda)\,\alpha(\lambda)$ can be obtained from Figure 6-4.

$$NE\Delta P = K_o A\Omega\rho^3 \int_0^\infty \tau(\lambda)\alpha(\lambda)[N(\lambda, 92K) - N(\lambda, 90K)]d\lambda \tag{6.28}$$

$$= \frac{\pi}{4}(.0217)(3.14 \times 10^{-4})(.96)^3(.024) = .114\ \mu\text{watts}$$

The calculated power translates into a detector voltage

$$V_s = (\Delta P)(R) = 12.4\ \mu V, \tag{6.29}$$

which is a signal to noise ratio of

$$S/N = \frac{12.4}{2.83} = 4.4, \tag{6.30}$$

satisfying the specification. The uncertainty in (6.30) could be as large as 40%.

VII, Acceptance Testing

NASA required that each ISR unit satisfy a program of testing as a precondition to acceptance of delivery. The program was designed by the hardware contractor's quality control organization, subject to the review and approval of NASA and the Principal Investigator. Two general objectives of the test program were (1) verification that the ISR satisfied scientific requirements as stated in the contract and (2) qualification of the unit for the rigors of space flight. Only those tests supporting the scientific objectives of the experiment will be discussed in this paper.

Four ISR units, identical in design, were constructed. Expensive, high reliability parts were not used in the Prototype (Ser. No. 101). Calibration test experience with the Prototype led to significant upgrading of test procedures and facilities. The Qualification Unit was subjected to special space qualification tests including severe shock, vibration, and thermal cycling. Other units were space qualified by similarity to the Qualification Unit. A Flight Unit and a Flight Spare were also built. Although Ser. No. 103 was originally installed in the spacecraft, it was switched out with Ser. No. 104 after the latter proved to have a better calibration and better performance. In this paper, the term "Flight Unit" will refer to Ser. No. 104.

ISR testing which was performed in support of scientific objectives can be broken down into three categories. Optical tests included measurement of the instantaneous field of view, the external field of view, the alignment of the optical axis, and the position of the space clamp within the scan sequence. Frequency response measurements on the two early units consisted only of the magnitude of signal droop and the

location of the high frequency corner. For the two flight units the amplitude and phase of the frequency response was measured between 20 Hz and 400 Hz. In calibration tests each ISR unit scanned black bodies of known temperature. The magnitude of the signal as a function of source temperature was plotted to produce a calibration curve. The calibration sequence evolved from unit to unit and will be treated separately in the next chapter.

In the ISR design the Cassegrain optical axis lies parallel to the mounting plane. The 45° scan mirror folds the axis of the instantaneous field into the scan plane, which is perpendicular to the optical axis. The optical tests determined the alignment of the optics in a coordinate system defined by the mounting plane and its perpendicular through the center of the scan mirror.

In Figure 4-2 two mounting holes can be seen on the upper face of the ISR, just to the right of the aperture. An alignment check tool can be mounted there for the purpose of field checking the ISR alignment. During acceptance testing the mirror on the check tool was aligned parallel to the mounting plane (the opposite face) to within 5 arc seconds.

For optical testing a pair of rotary turntables were configured to provide two axes of rotation for an ISR unit. These turntable axes coincided with the ISR "y" and "z" axes (cf. Chapter IV and Figure 7-1). The line of sight from a collimated infrared source was established through the center of a mounting fixutre on the turntables. The ISR was mounted in the fixture and rotated until the mounting plane was perpendicular to the axis of irradiation. The geometry was determined by an auto collimator and an alignment mirror shown in Figure 7-1. This configuration determined the zero position for both turntable axes.

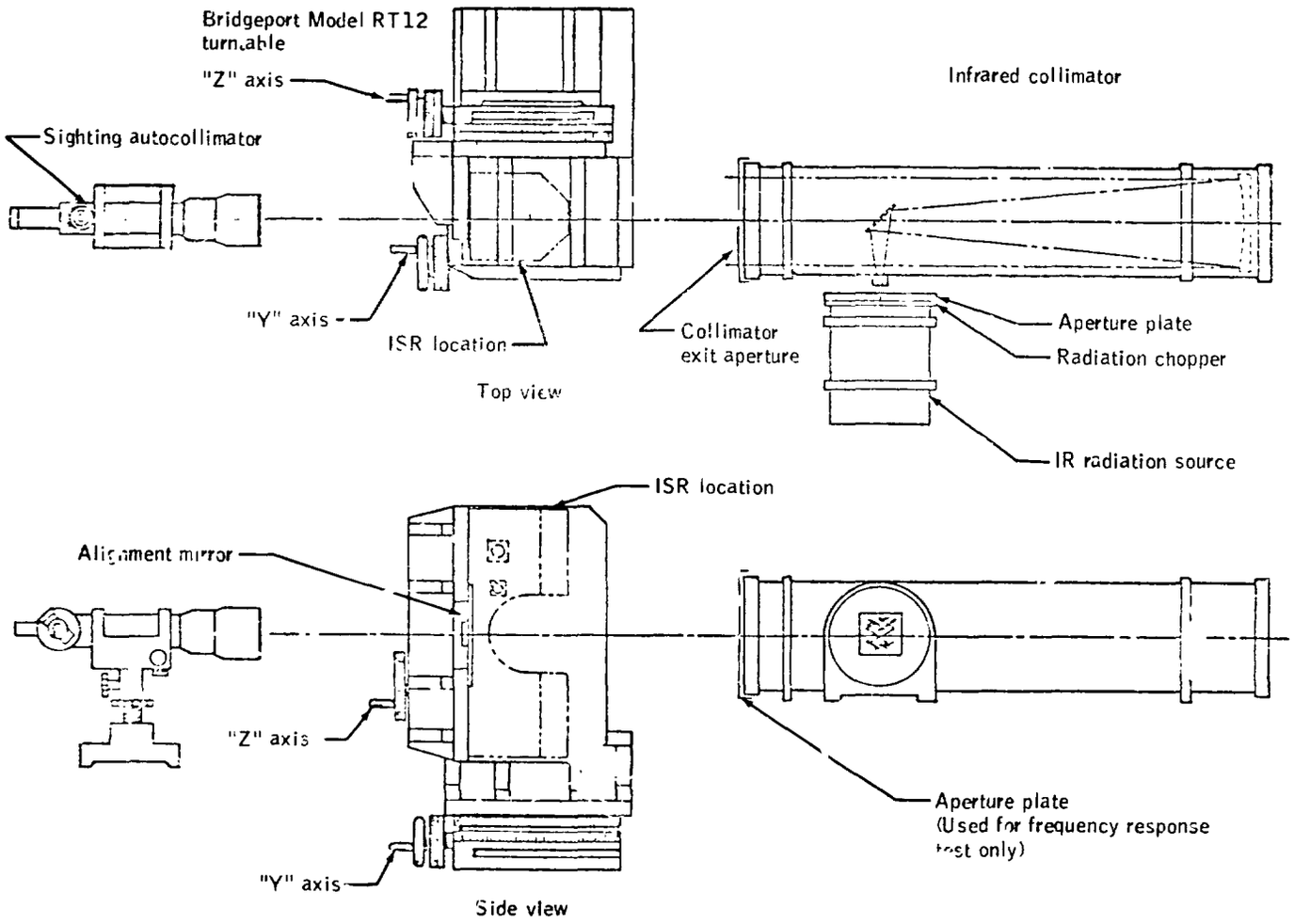

Figure 7-1 ISR OPTICAL TEST SETUP. For the optical testing the ISR was mounted on precision turntables and aligned relative to the beam from an infrared collimator. (After Plakun, et al., 1972)

The unit was rotated 180° about the y-axis and 45° about the z-axis to align the scan mirror for the instantaneous field of view tests. The scan mirror was rotated by hand and clamped into place when it was aligned with the autocollimator. The turntables were returned to the zero position, and the repeatability of the zero was found to be less than 15 arc seconds.

During the measurements the infrared radiation source was chopped at 100 Hz. The ISR was rotated about the y-axis until the approximate center of the field of view was found from the signal output. The "y" turntable was locked, and the ISR response was mapped about the z-axis. The "z" turntable was then locked at the center of field, and the resolution element was mapped about the y-axis. Field of view measurements were done both before and after a random vibration test sequence on all units. Both sets of data are plotted in Figure 7-2 for the Flight Unit.

The enhanced response at the edge of the field of view is common to all units and is attributable to spherical aberration. The asymmetry of response about the center of field is also seen in the other units. No response was detected, at the signal levels shown, for angles greater than approximately 40 arc minutes from the axis.

The position of the space clamp in the scan sequence was measured with the optical setup described above. The scan mirror was unclamped, and power was applied to the motor. The gate waveform which activates the clamp circuit was monitored on a dual channel oscilloscope. The ISR output was monitored on the same oscilloscope. The "y" turntable was rotated until the signal pulse due to the collimator was superimposed on the leading or trailing edge of the clamp gate. The angle was read from the turntable.

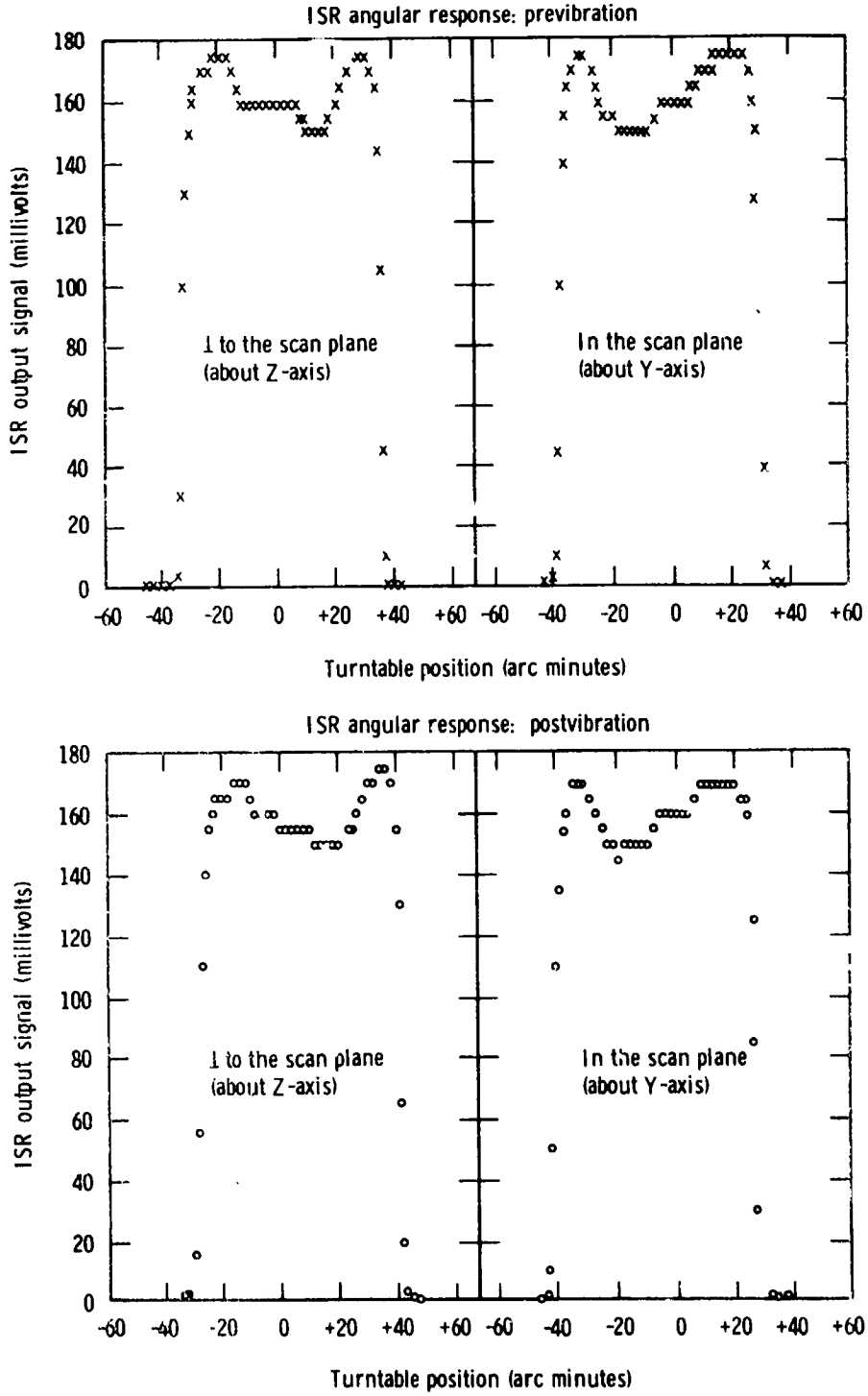

Figure 7-2 ISR INSTANTANEOUS FIELD OF VIEW. The optical test setup in Fig. 7-1 was used to map the ISR response as a function of angular distance from the optical axis. Measurements were made in the scan plane and perpendicular to it, both before and after vibration testing.

The extent of the external field of view as defined by the aperture in the housing was similarly measured. The turntable was rotated until vignetting by the edge of the aperture caused the collimator signal to fall to 90% of its clear field value.

The optical parameters listed in Table II are post-vibration values. The uncertainty in the optical alignment is approximately 0.7 milliradians. Shifts in the alignment between measurements are no greater than the uncertainty.

For frequency response measurements the exit aperture of the collimator was stepped down and a variable speed chopper was placed in front of the radiation source (Figure 7-1). The chopped radiation was sensed at the entrance aperture of the collimator, and the signal was input to a Beckman Eput meter for monitoring the chopping frequency. The peak to peak amplitude of the ISR signal was read from an oscilloscope over the range 20 Hz to 400 Hz. The results for the Flight Unit are plotted in Figure 7-3. The high frequency corner was measured to be 142 Hz. At the spacecraft sampling frequency, 400 Hz., the response is less than -27 db.

A phase angle voltmeter was used to determine the phase of the frequency response. The results are also plotted on Figure 7-3.

Signal droop was measured using an irradiation input chopped at 0.5 Hz. The ISR output was a square wave of amplitude 2 volts. The "sag" on both the top and the bottom of the waveform was 8 millivolts over a period of 0.56 seconds. The droop is calculated to be 0.4%, implying a time constant of 140 seconds.

It should be noted that the measurements described in this chapter were made while monitoring the ISR output from the post amplifier. The

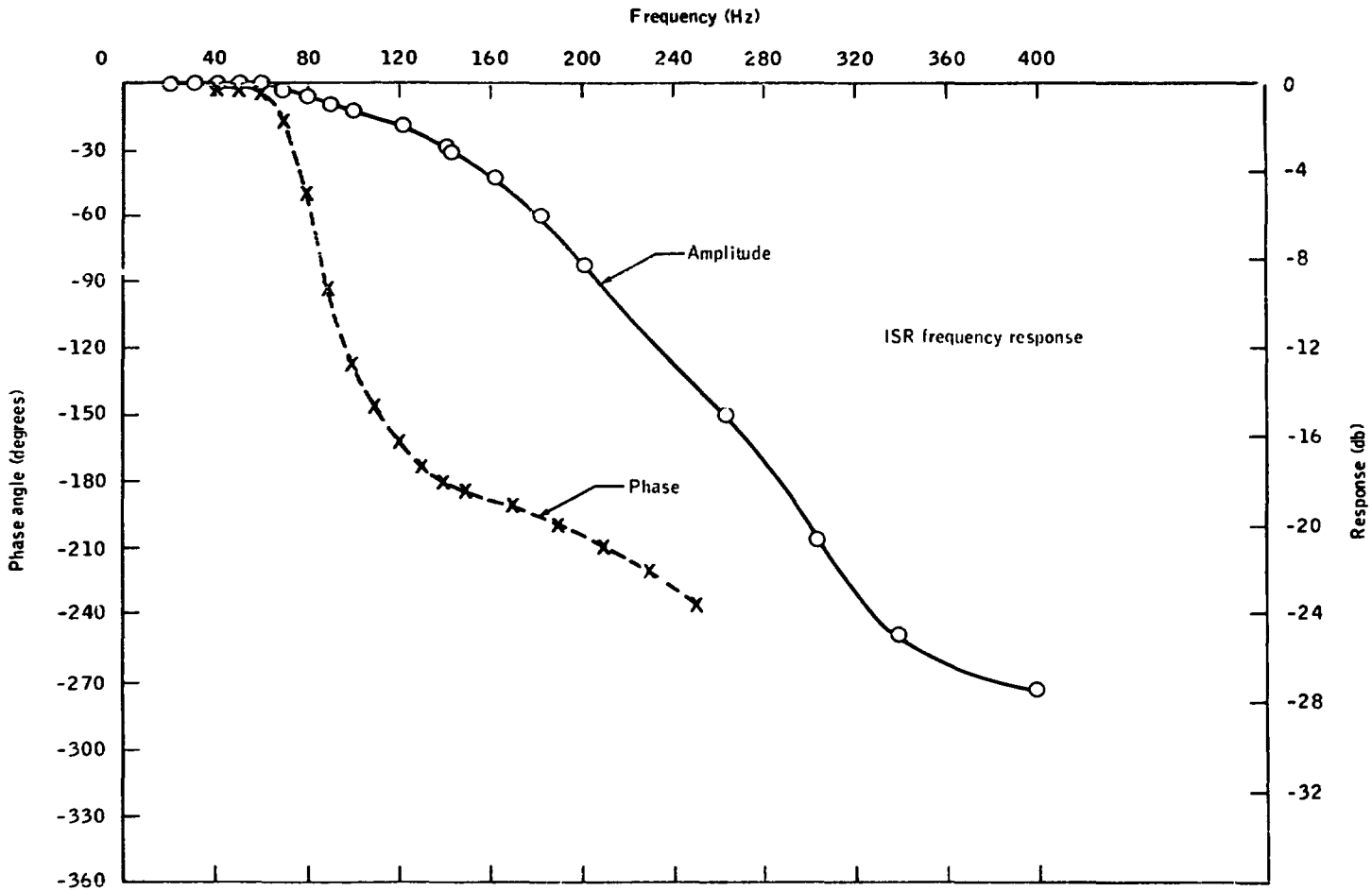

Figure 7-3 ISR FREQUENCY RESPONSE. Plotted are the amplitude and phase angle of the ISR transfer function as measured at the output of the post-amplifier.

TABLE II

OPTICAL PARAMETERS OF ISR FLIGHT UNIT

(Ser. No. 104)

Optical alignment	+0.470 mrad.	-0.931 mrad.
Field of View (50% points)	19.85 mrad.	20.00 mrad.
Edge Sharpness (90% - 10%)	0.82 mrad.	0.82 mrad.
External Field of View* (90% points)		189° 15'
Leading edge		+95° 05'
Trailing edge		-94° 10'
Space Clamp Position		6° 04'
Leading edge		+80° 45'
Trailing edge		+74° 41'

*Measured prior to vibration testing only

clamp circuit cannot operate while the scan mirror is stationary, as was required by many of the measurements. Therefore the frequency response and the droop measurements exclude any shaping from the clamp circuit or the buffer amplifiers. The latter are designed to be broad band and should not affect signal properties. However, as has been shown in Chapter VI, the frequency response of the clamp circuit can be significant at low frequencies.

VIII. Calibration

A. Introduction

The most complex test sequence in the ISR program was the calibration of the instrument. Experience gained with the Prototype and Qualification Units led to modification of procedures and equipment. Malfunctions in test equipment and unanticipated instrument characteristics played a major role in the results; and, as we shall see, post facto corrections must be applied.

B. Calibration Test Fixture

A calibration test fixture was constructed by BEC (Figure 8-1). It was a cylinder, approximately 80 cm in diameter and approximately 80 cm tall. The ISR was mounted in the base on a heater plate which was capable of maintaining the radiometer at temperatures characteristic of the SIM Bay. The upper end and wall were cooled by liquid nitrogen. The interior of the fixture was painted with high emissivity black paint.

Two blackbody sources (BB1 and BB2), approximately 32.5 cm x 21.6 cm, were mounted at the upper end of the chamber. A third black body, the space patch, was mounted on the fixture wall at the position of the space clamp in the scan sequence. The two blackbody calibration sources were built by Eppley Associates. They were designed to be identical and to operate over a temperature range from 77K to 400K, with an intrinsic gradient less than 0.1K. The base of each source consisted of a 1.9 cm copper plate. A winding channel, 1.3 cm deep, was milled into one side of the plate. Copper tubing was soldered in the channel to carry cryogenic liquids or gas. A heater blanket covered with conducting silicone grease was sandwiched between the flat surface of the base and a

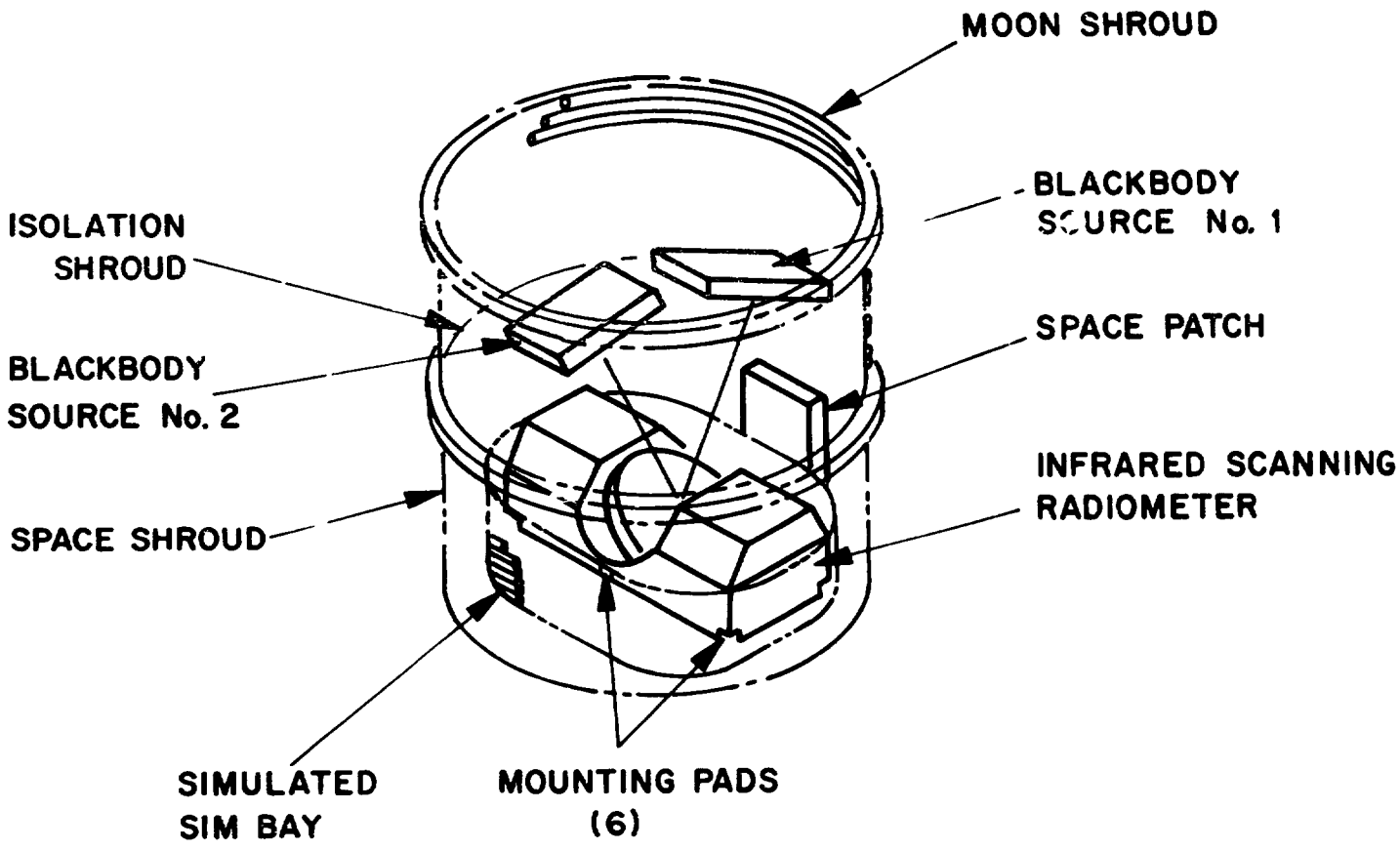

THERMAL VACUUM TEST FIXTURE

Figure 8-1 THERMAL VACUUM TEST FIXTURE. The thermal vacuum test fixture pictured was placed in a vacuum chamber for the ISR calibration. The fixture contained black body calibration sources and was capable of simulating the spacecraft thermal environment.

second copper plate, 0.6 cm thick. The two plates were mated with four screws and conducting epoxy. A thin copper honeycomb, 2.5 cm high, was soldered to the face of the second plate. All radiating surfaces were painted with a 3M velvet Black paint. Four copper-constantan thermocouples were installed in the copper plate beneath the honeycomb.

The test fixture and the ISR itself were also instrumented with thermocouples so that the thermal regime in the fixture could be monitored. All thermocouples were operated with an ice point reference.

C. Calibration Technique

A variation of the near extended-source technique (Nicodemus and Zissis, 1962) was chosen by BEC. The dimensions of available vacuum chambers dictated the choice of a near-field source. Since the Moon is an extended source from lunar orbit, an extended calibration target most closely parallels the measurement.

Consider now the manner in which a test fixture such as the one described might be utilized to calibrate the ISR. If the space patch were maintained at a brightness temperature below the noise equivalent temperature (NET) of the ISR, the clamp circuit would sample a noise signal on each scan. The operation of the instrument in space would be accurately simulated. The temperature of a single blackbody calibration source could be varied throughout the anticipated range of measurement, and the respective ISR output voltages would be those encountered for similar irradiance levels from the lunar surface. I refer to this concept as a zero-point calibration in the sense that all ISR signals are referenced to a true zero established by the clamp circuit.

BEC originally intended to perform a zero-point calibration but ran into design problems with the fixture. The space patch was cooled by conduction to the chamber wall and never became as cold as the calibration sources under liquid nitrogen cooling. The lowest temperature reached by the sources, 82K, was well above the NET of the radiometer.

Consequently BEC switched to a relative calibration technique. The two blackbody sources are maintained at known temperatures, and the significant quantity is the difference between the output signals from the two sources. The actual temperature of the space patch is not very critical so long as it is reasonably constant during measurements from the two sources. In fact, it can actually be slightly warmer than one or both sources because the ISR can produce small negative voltages before saturating at -0.6 volts.

Care must be exercised in planning test procedures for a relative calibration. As an example let us assume that one source is maintained at a constant temperature (e.g., liquid nitrogen); and the second one is varied throughout a range of temperature. Unless the variable source is cooled below the NET for the radiometer, the relative calibration curve can never be converted to the zero point curve except by extrapolation. Since the curve is quite nonlinear at low temperatures, extrapolation is highly uncertain.

Increased error is the other drawback of the relative technique. Since two signal measurements must be made for each calibration point, the total error is the rms sum of the individual errors. If the reference source drifts in temperature, then all the points must be bootstrapped to a common reference, additional errors being accumulated in the process.

It was anticipated that the calibration of the ISR would be independent of the temperature of the instrument within the range of ambient temperatures expected in the SIM Bay. To verify this hypothesis two complete calibration runs were planned for each unit. The ISR temperature was maintained at 272K (30°F) for the first run and 300K (80°F) for the second. The two runs also served as a check on the repeatability of the calibration.

D. Prototype Calibration

After review of Acceptance Test data, the PI team judged the calibration of the Prototype Unit to be unacceptable. The two calibration curves disagreed significantly. Neither curve approached a zero slope at the low temperature end, indicating that the NEI had not been reached. Black Body Source No. 1 (BB1) reached a minimum temperature of 80K in the first run but could not be cooled below 87K in the second run. Black Body Source No. 2 (BB2) had a minimum temperature of 82K. The inability of the sources to attain liquid nitrogen temperature (77K) and the inconsistencies between the two runs indicated possible problems with the fixture and/or the temperature measurements.

A silicone oil spill had occurred in the chamber during testing, and the radiating surfaces of the sources had been cleaned. No effort to determine the radiometric equivalency of the two sources had been made before or after the spill. In addition, voltmeters used to read out the thermocouples were found out of calibration subsequent to the tests.

The PI team proposed several substantive changes to the test fixture and the test procedures. Implemented modifications included the following:

a. The blackbody sources were returned to the manufacturer for refurbishment, including repainting. Upon their return, a simple radiometric equivalency test was performed. The two sources were replaced in the test fixture and stabilized to the same temperature, within 0.5K. The Prototype output signal for the two sources was compared. The test was repeated for temperatures ranging from 82K to 398K. The results are presented in Figure 8-2. Corrections for the residual temperature differentials place the sources within 20 millivolts (1 telemetry bit) of each other. Although uncertainties were large, the sources seemed equivalent. Subsequently, a source equivalency check at one temperature (82K) was performed prior to each calibration run.

b. A platinum resistance thermometer (PRT) was installed in each source to provide the primary temperature measurement. The thermocouples were retained and read out as supplementary data.

c. The test fixture was modified to permit liquid helium cooling for BB2. The space patch was redesigned for helium cooling to avoid negative voltage saturation in the ISR output. The space patch was plumbed in series with BB2, thereby forcing that source to be the colder of the two sources at any point in the test sequence.

In the modified procedure, each calibration run consists of two portions. At first, BB2 and the space patch are cooled with helium to approximately 40K. BB2 is subsequently warmed stepwise to 90K while BB1 is maintained at 82K as a reference.

In the second part of the calibration run, BB2 is maintained at 82K as a reference while BB1 is heated stepwise from 90K to 400K. The 90K and 100K calibration points are taken in both portions of the run in order to tie the two curves together.

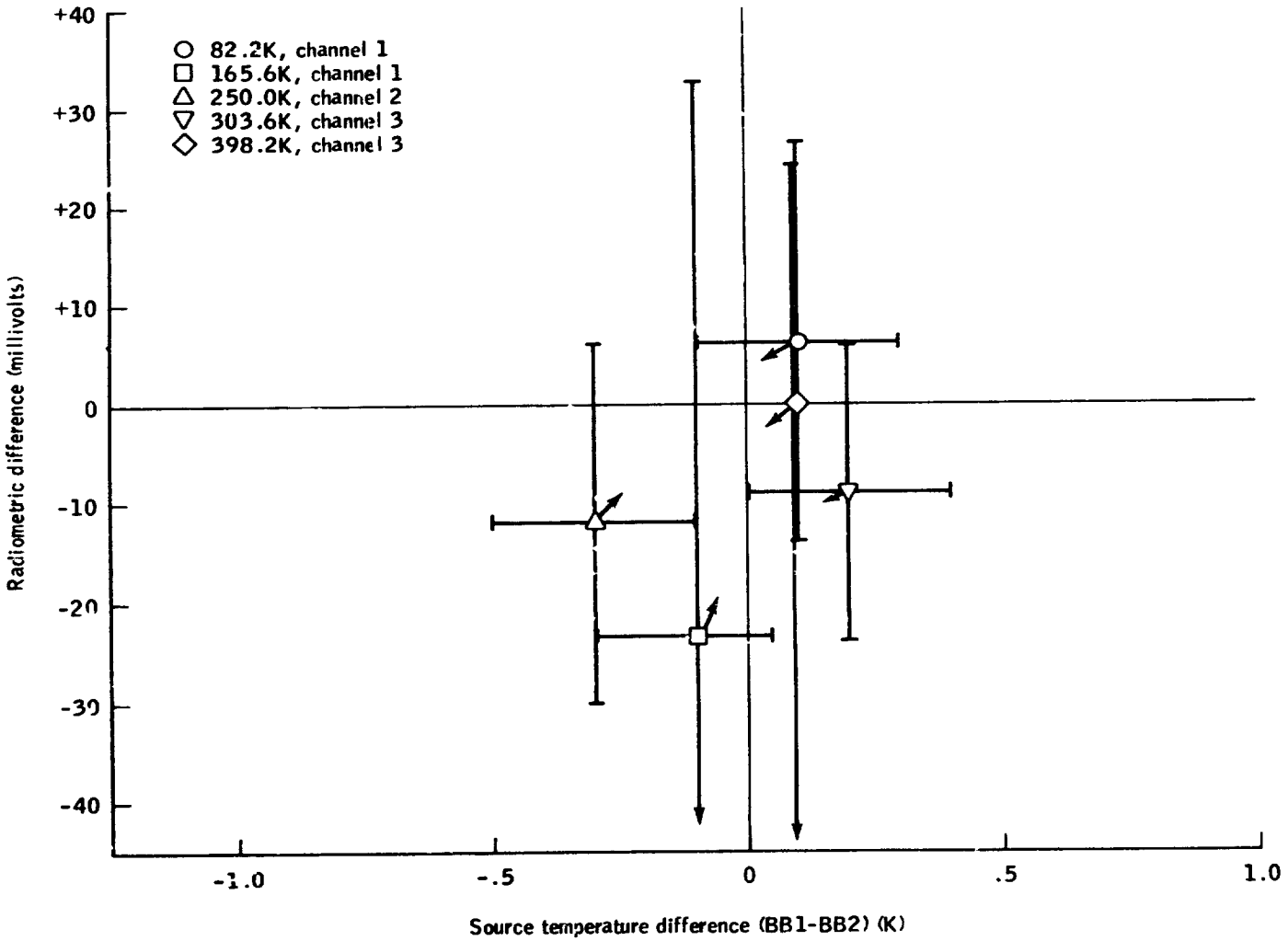

Figure 8-2 RESULTS OF SOURCE EQUIVALENCY TEST. The radiometric offset of the two black body calibration sources is plotted as a function of their actual temperature difference. The arrows give the direction of the correction to adjust each data point to zero temperature difference.

At each calibration point the two sources were allowed to stabilize. The ISR output waveform was monitored on an oscilloscope until the traces from the sources showed no slope due to thermal gradients across their radiating surfaces. The PRT's were monitored until the thermal drift was less than 0.1K per minute. When these two stabilization criteria had been met, the ISR output was sampled with a digital voltmeter at the position of each of the black bodies. Readings from the PRT's and the thermocouples were recorded both before and after the sampling of the ISR output signal. A polaroid photo was taken of the waveform on the oscilloscope. Thus the state of the test fixture and the ISR could be reconstructed in subsequent analysis of the data.

E. Qualification Unit Calibration

The two calibration curves for Ser. No. 102 agreed well. The agreement was taken as evidence that the calibration testing had been "fixed".

The PRT in BB1 failed between the two calibration runs. The second run was made using corrected thermocouple readouts for BB1. The corrections were derived from data taken in the previous run. Once again, the agreement between the curves seemed to validate the procedure.

The source equivalency checks prior to the calibration runs gave a radiometric offset of 40 millivolts between the two sources. This value was much larger than any offset indicated in the original equivalency test. On the other hand, it did not exceed the official tolerance (50 mv); and it was on the order of the peak to peak noise (35-50 mv) in the Qualification Unit.

BEC commented on the offset as part of an analysis of the PRT failure (Bartlett, unpubl. memo.). Thermocouple readouts from the source equivalency checks for the Prototype and the Qualification Units were compared. It was concluded that the PRT in BB1 had shifted its calibration relative to the thermocouples between test sequences for the two units. If corrections were applied to the thermocouple readings, the sources could be shown radiometrically equivalent. Reexamination of the problem shows that the data does not unambiguously support this conclusion, but all parties accepted the analysis at the time.

F. Calibration and Recalibration of the Flight Spare

The calibration of Ser. No. 103 was relatively trouble free. In the second part of the low temperature run, the ISR temperature controller malfunctioned, allowing the unit to go from 30°F to 49°F. A second set of points from 90K to 400K were generated at an ISR temperature of 30°F.

The source equivalency checks confirmed the radiometric offset between the calibration sources. The accepted explanation attributed the difference to a reflection from BB2 It was unknown whether the surface of BB2 was faulty or whether some special geometry favored reflection from that source alone. The ISR was the warmest object in the fixture and was thought to be the source for the reflected radiation. No one could explain the disagreement between the original equivalency test and the subsequent checks.

The two calibration curves for Ser. No. 103 did not agree. The phenomenon was particularly disconcerting because this unit was intended for the lunar missions. Searching for an explanation, BEC evaluated all

temperature readouts, tested the criteria for thermal stability of the sources at each calibration point, checked the stability of the detector temperature, and calculated worst case temperature shifts in electronic gain. None of the effects could explain the displacement of the curves.

My original analysis of temperature readouts and oscilloscope photos of ISR signal traces indicated a small shift in the calibration of the PRT in BB2. A recent re-evaluation of the data leads to a different conclusion. Apparently the thermocouple printouts are mislabeled, and one of them was never supplied to me. The recorded temperatures for points below 60K may be in error for the 30°F run, but all other points seem to be in order. The erroneous points could be due to instrument malfunction or operator error.

Approximately four months later, after Ser. No. 103 was removed from the spacecraft, it was recalibrated. In the intervening period both platinum resistance thermometers had been replaced in the blackbody sources. I have used all the calibration data for Ser. No. 103 in a study of the large discrepancies encountered in the curves for that unit. The study bears directly on the final error analysis for the calibration of the Flight Unit.

All the data for channel 1 on Ser. No. 103 is plotted in Figure 8-3. No corrections have been applied to the very low temperature points for the 30°F run.

The data points from the recalibration fall between the two curves from the primary calibration. The spread in the data is difficult to reconcile in terms of the known experimental errors. If a temperature dependence exists in the radiometer, then the magnitude of the effect

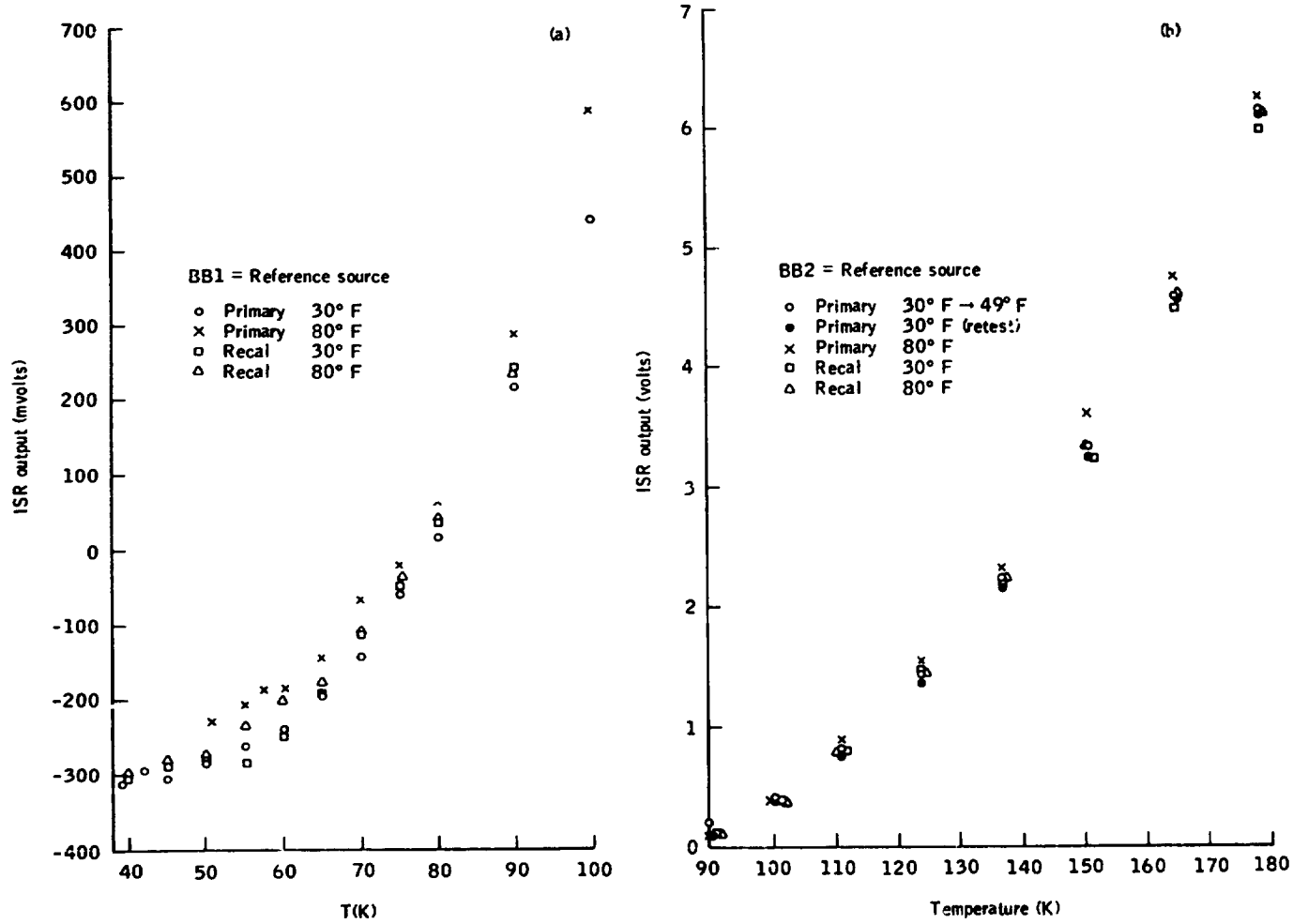

Figure 8-3 SN 103 CALIBRATION DATA. Data points from several calibration runs for SN 103 are compared to estimate errors. (a) Plotted are the first portions of each run in which BB1 was the reference (const. temp.) source. (b) Plotted are the second portions in which BB2 was the reference.

needs to be estimated. However, here I wish to present evidence for sloppy procedures in the original calibration of Ser. No. 103.

G. Analysis of Overlap Points

As has been described previously, each calibration run consists of two parts, in which the reference source is changed. Certain points at the transition temperature were measured in both parts of a run. The overlapping data can be used to estimate the radiometric offset of the sources, but here the data will be examined for self-consistency.

Figure 8-4 shows all the measurements of the 90K point and the 100K point for Ser. No. 103. The raw calibration point is plotted as a function of reference source temperature. The arrow with each point gives the correction to a constant 82K reference temperature. A small correction to the exact calibration temperature is also included. The small symbol "p" in the figure represents a measurement of the signal traces from oscilloscope photos. The photo points are plotted at the same reference temperature as the corresponding point from the test data sheets. Where the photo point would fall directly on the official value, the former is plotted slightly to one side. The error bars signify the peak to peak noise in the signal.

For each calibration temperature the points fall into two clusters, corresponding to values from the two parts of a run. The displacement of the clusters should be twice the radiometric offset between the sources. For each temperature the scatter in the first part of a run (upper cluster) is greater than that for the second part (lower cluster).

In approximately half the measurements the disparity between the photo and the data sheet is somewhat larger than one might expect

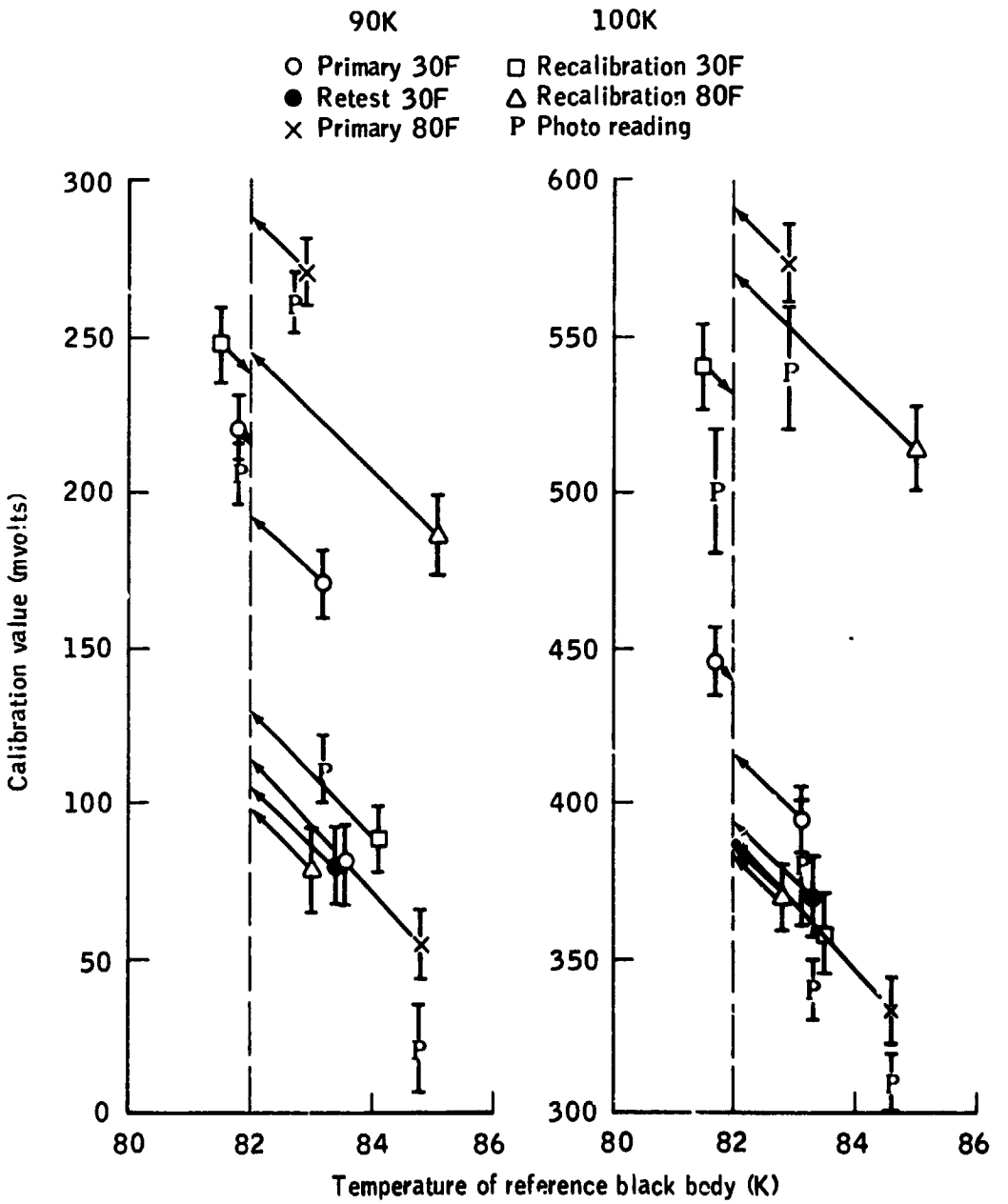

Figure 3-4 REPEATABILITY OF SN 103 CALIBRATION. The symbols represent calibration points from data sheets for the various tests of SN 103. Each "P" is a reading from polaroid photos of the ISR waveform on an oscilloscope at the time of the calibration tests. Arrows indicate the correction to a constant reference black body temperature.

from instrument noise alone. The photo values are systematically low, possibly indicating a difference in the gain calibration of the two measuring instruments. In two instances the disagreement is so large that one measurement must simply be incorrect. Both cases occur in the 30°F primary calibration, and the photo point appears to be better each time.

This photo data, in conjunction with the thermocouple histories, supports the hypothesis that much of the disagreement in the primary calibration of Ser. No. 103 can be attributed to sloppy technique. The self-consistency of the recalibration is indicative of more careful work.

H. Temperature Transition Test

After the original calibration of Ser. No. 103, the possibility of a large temperature effect in the ISR was real. An additional test was inserted into the Acceptance Test Procedure for Ser. No. 104 at the suggestion of Dr. Low. In the standard procedure the ISR is cooled from ambient to 30°F prior to the low temperature calibration run. For Ser. No. 104, the two sources were temperature stabilized at 151K and 82K, respectively, during the ISR cooling. The ISR output was measured and temperature readouts were made periodically during the operation.

My original analysis of the Temperature Transition Test is presented as Appendix C. It was concluded that the ISR exhibits an increase in gain of approximately 2% with temperature in the range 30°F to 80°F.

For test purposes the temperature of the ISR was defined by Thermocouple No. 2, located on the casting near the detector. In the spacecraft telemetry stream the only instrument temperature comes from a thermistor in the primary mirror. In Figure 8-5 data from the Temperature Transition Test is plotted. The temperature from Thermocouple No. 2

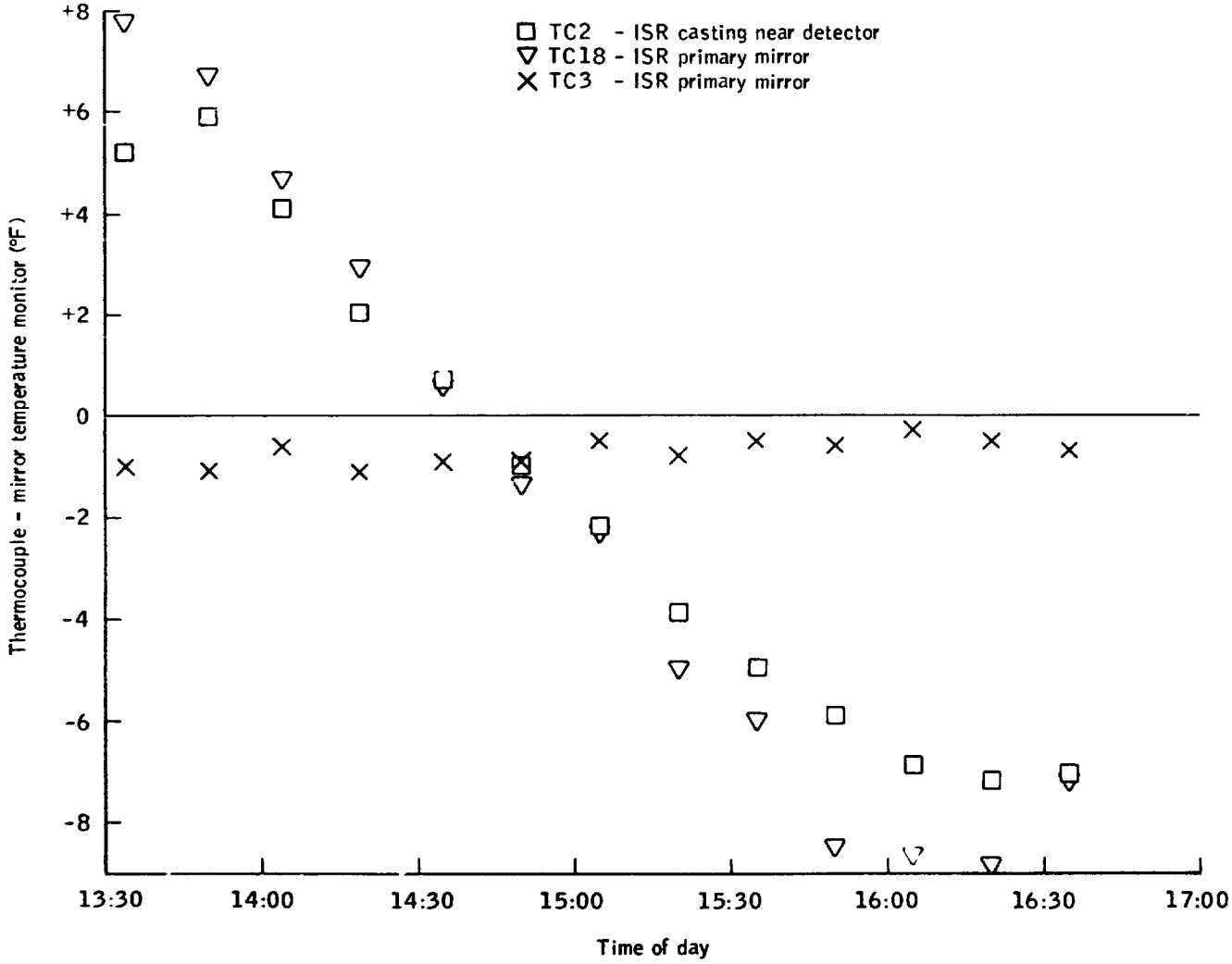

Figure 8-5 ISR THERMAL HISTORY IN THE TEMPERATURE TRANSITION TEST. Readings from three thermocouples attached to the ISR are compared to the "official" instrument temperature as given by the primary mirror temperature monitor. The different temperature histories indicate that the ISR was not well equilibrated during the test.

and temperatures from two thermocouples installed on the primary mirror are plotted as deviations from the simultaneous reading of the Primary Mirror Temperature Monitor.

Clearly the ISR was not well equilibrated thermally during the tests. The two distinct temperature patterns imply that the thermal gradients are real and not simply artifacts of the sensor calibration or sensor installation. When the ISR temperature dependence is referenced to the Primary Temperature Monitor, the gain increase is 2.5% to 3%, depending on what points are considered bad data. The calibration data for Ser. No. 104 is consistent with a gain factor of 3% or more. A value of 3($\pm$1)% has been chosen for calibration correction.

The Temperature Transition Test is not consistent with the hypothesis attributing the radiometric offset to thermal emission from the ISR. Such a reflection should vary with the temperature of the unit. If the emissivity of the ISR radiating surface is 0.03%, then the reflectivity of BB2 must be enhanced by at least 4%. That value is unlikely but not impossible. As the temperature of the unit falls from 300K to 272K, the enhancement of BB2 should drop at least 10 millivolts. The signal from BB2 in Figure 2 of Appendix C shows no such variation.

I. Determination of the Radiometric Offset

Sometime after completion of the ISR test program, I learned of an accident in the test fixture which had occurred after Prototype testing but before acceptance testing of the Qualification Unit. The heater in BB2 had been left on overnight and had melted the solder in the source. Although the source had been repaired, the famous offset was noted in the next equivalency check.

This new information raised the possibility that BB2 had acquired a thermal resistance between the copper base and the radiating surface. At low source temperatures thermal loading by the relatively high temperature ratiometer could cause a temperature dependent enhancement. BEC was contracted by Rice University to perform a full Source Equivalency Test. The Qualification Unit was the only one available for testing at the time.

The results of the test were transmitted in the form of Polaroid oscilloscope photos. The measured radiometric offset in Channel 1 as a function of blackbody temperature is presented in Figure 8-6. The error bars indicate the effect of peak to peak noise and therefore represent a rather conservative error estimate. Corrections have been applied to the raw data to compensate for small residual temperature differences between the sources. At the high temperature points the corrections can be large, amounting to 18 millivolts for a temperature residual of 0.2K. The data in the figure is best interpreted as a temperature independent offset of 55 millivolts.

That value is somewhat higher than the one derived from all of the Source Equivalency Checks. Most of the latter fall at 40 millivolts although values as high as 50 millivolts have been recorded. A close look at the Acceptance Test Data shows that a residual temperature difference of 0.2K almost always exists between the two sources during the checks. That residual is the maximum permitted by the test procedure. The direction of the residual always lowers the offset. Thus the data from the Source Equivalency Checks appears to be systematically biased downward by at least 4, and perhaps as much as 10, millivolts.

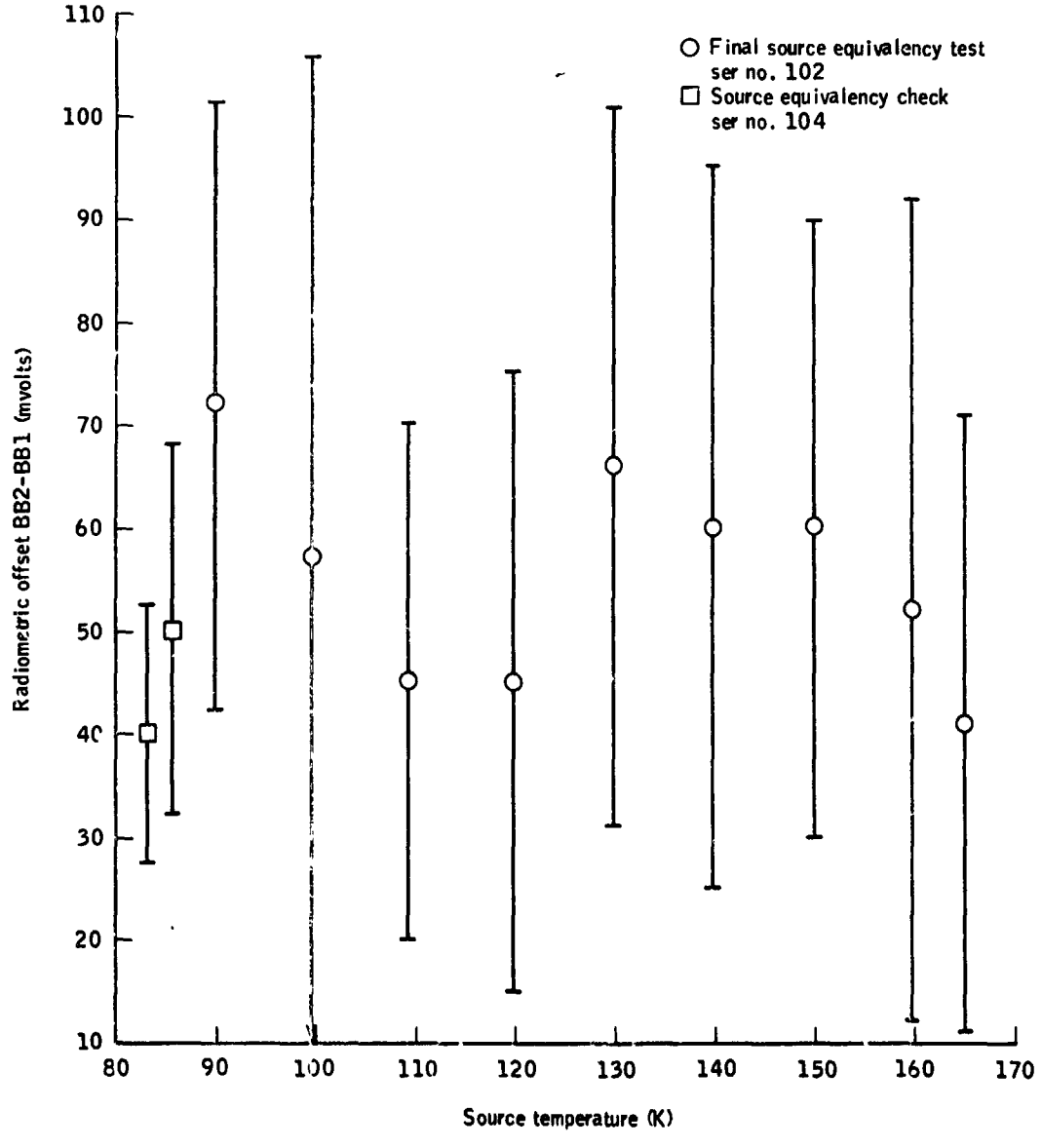

Figure 8-6 RADIOMETRIC OFFSET OF THE CALIBRATION SOURCES. The circles represent data from the post-calibration source equivalency test. The squares are values for the offset at the routine Source Equivalency Checks during the calibration of SN 104.

The magnitude of the radiometric offset can be evaluated in other ways. The corrected calibration curves are referenced to 8.K and thus shoud be zero at that temperature. For the Flight Unit residuals of 68 and 54 millivolts occur for the 30°F and the 80°F calibration runs, respectively. In the recalibration of Ser. No. 103 the residuals are 73 and 81 millivolts, respectively.

As part of both calibrations just mentioned overlap points were taken at 90K, 100K, and 111K. These twelve measures of the offset give 72 (±10) millivolts. If the two worst points are removed, the offset is 72 (±6) millivolts. The value from the calibration data is distinctively higher than that from the final Source Equivalency Test.

It is possible that the discrepancy arises from comparing oscilloscope photos with digital voltmeter readings. It has been pointed out in the discussion of Figure 8-4 that the photo measurements are systematically lower than the digital readouts. However a check of photos for the calibration of the Flight Unit gives very good agreement between the oscilloscope trace and the voltmeter readings. The results of the Equivalency Test establish that the offset is independent of source temperature, but I prefer to adopt a value of 70 millivolts in accord with the calibration data for the Flight Unit.

The constancy of the enhancement in BB2 suggests that the anomaly is indeed a reflection. The black body could have been installed in such a manner that the detector "sees" itself in the bottom of the honeycomb. This phenomenon occurs much more dramatically in ISR output from the spacecraft when its contamination cover is closed. The detector radiates at 311K, independent of the temperature of the ISR itself. A simple calculation from the calibration data shows that the required reflectivity

is approximately 0.1%. A reflectivity of this magnitude is not only possible but probable.

J. Flight Unit Calibration

The calibration of the Flight Unit proceeded without significant problems. The voltmeter readings from the data sheets agree well with the oscilloscope photos. PRT readings and thermocouple printouts are mutually consistent. During the first portion of the 30°F run the test fixture was exceptionally stable. The slope of the corrected calibration curve at 82K agrees well with other units. The offset at 82K agrees with the adopted value.

During the first portion of the 80°F run the space patch warmed from helium temperatures (45K) to nitrogen temperatures (85K) between the 65K and the 90K calibration points. Theoretically the temperature of the space patch is not critical in the relative source calibration method. However, a warming rate of 41K per hour can have a significant effect if the readings from the two sources are separated in time by as much as a minute or two. It should be noted that the slope and offset at 82K for the 80°F run are lower than those for the 30°F run by approximately one standard deviation.

The construction of the final calibration curve consists of the following steps:

a. A raw calibration is established for the 75K, 90K, and 100K points for each run. That is, the signal from BB1 is subtracted from th signal from BB2 as given on the Acceptance Test data sheets.

b. A polynomial fit to these points establishes the correction factor to 82K for each BB1 reading.

c. The corrected calibration values for the reference points are fit with another polynomial, and the correction factors are checked. When a final fit is confirmed, all reference source temperatures are corrected to 82K. A corrected calibration curve is generated by the appropriate subtractions.

d. The curve from c. is corrected further for gain variations with temperature of the ISR as derived from Thermocouple No. 3. The reference ISR temperature is taken to be 298K (77°F). The correction factor is 0.03 per 50°F, relative to the reference temperature.

e. The radiometric offset of 70 millivolts is subtracted from the first part of each run and added to the second part. The values for the offset in Channels 2 and 3 are 18 and 4 millivolts respectively.

f. The entire curve is shifted so that the lowest values become zero voltage. The shifts are +345, +80, and +60 millivolts, respectively, for the three channels.

A complete calibration curve is given in Figure 8-7.

K. Error Analysis

The knowledge of the temperature of a given calibration point is directly related to the accuracy of the platinum resistance thermometer in the black body target. The PRT readouts were recorded to the nearest 0.1K. The manufacturer's claimed accuracy is a factor of two or three times better than the readout increment. Other factors such as thermal resistance between the PRT and the radiating surface or calibration shifts due to thermal cycling can degrade the accuracy, but I shall adapt $\pm$0.1K as the error value.

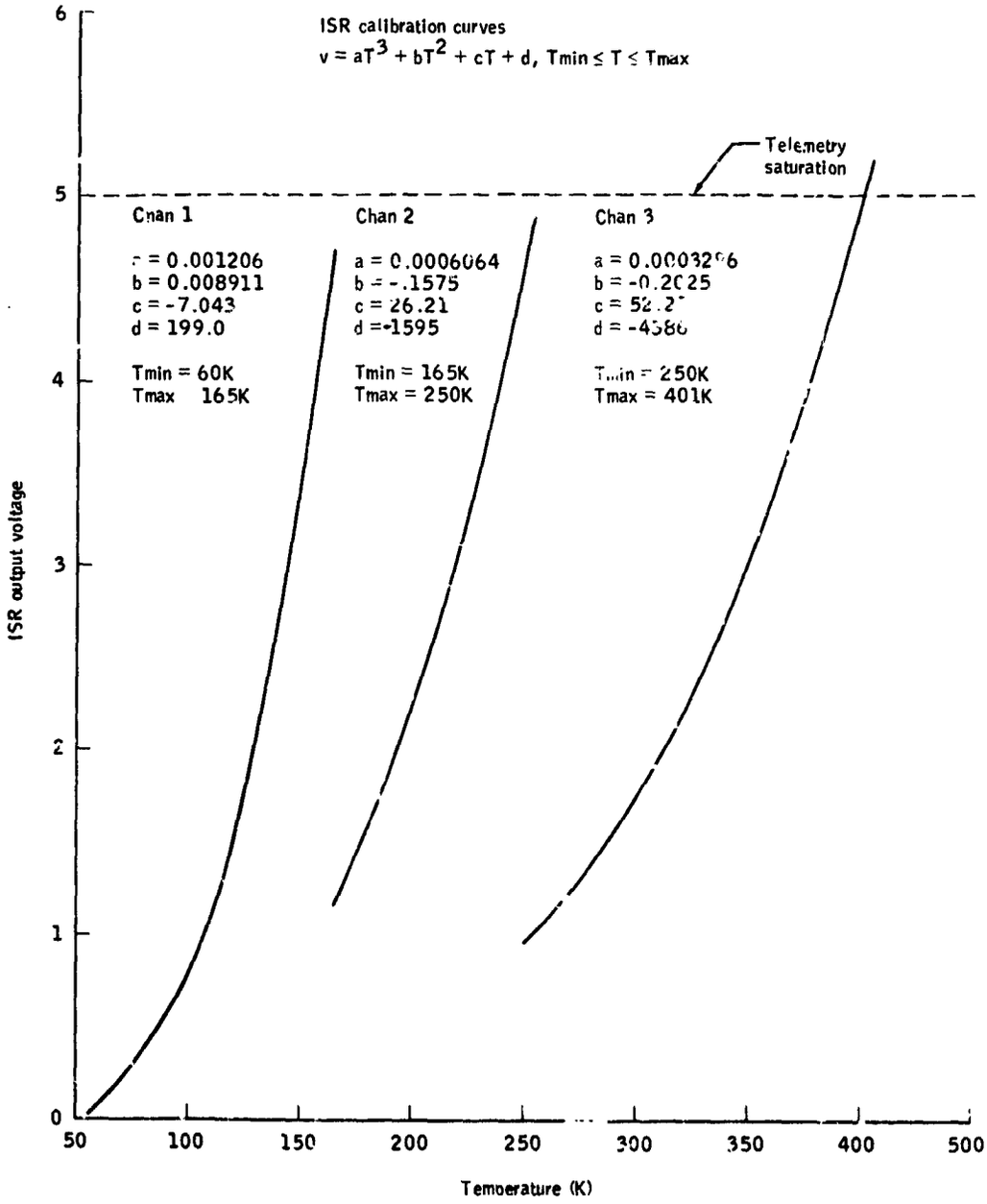

Figure 8-7 ISR CALIBRATION CURVES. Calibration data for SN 104 can be represented to within the accuracy of the measurement by a least squares cubic polynomial. Coefficients for the fits to the three channels are given.

Assignment of errors to the radiometric values is more complicated and can vary from point to point. Estimated contributions from various error sources are presented in Table III. Most of the items relate directly to the construction of the calibration curve. Temporary instabilities in the test fixture refers to such things as the transient warming of the space patch during the 80°F run.

The calibration targets very likely have an emissivity less than unity, but this is not listed in the table. The effect on the calibration curve is a small, negative, systematic bias. In other words, the temperature of a true black body would be overestimated using the curve. Since the emissivity of the lunar surface is not well known, interpretation of ISR data will not be significantly affected by this error source.

Reflection from the sources is a more serious problem. However, this error is canceled in the subtraction process and in the source equivalence corrections.

Table IV gives some typical estimated errors in radiometric response in millivolts and their temperature equivalent. At low temperatures the error is less than one telemetry bit (20 mv). In practice, the ISR noise causes a 1 bit jitter in the telemetry, thereby effectively doubling the instrument noise contribution. Thus the actual errors are somewhat larger than those shown in the table. In Channels 2 and 3 the telemetry quantization error (10 mv) dominates noise. For all channels, the uncertainty in temperature effects on gain is the major error source at high signal levels.

TABLE III

RADIOMETRIC ERROR SOURCES

(CHANNEL 1)

Source	Error Value	Comment
ISR noise	6 mv	
Voltmeter readout accuracy	5 mv	above 100K only
Reference source correction to 82K	0-5 mv	
Temperature dependent gain correction	0.5 %	
Radiometric offset correction	10 mv	
Curve adjustment to true zero voltage	10 mv	
Temporary instabilities in the test fixture	0-5 mv	

TABLE IV

TYPICAL ERROR VALUES

Calibration Point (K)	Calibration Value (mv)	Error (mv)	(K)
80	304	15	0.9
111	1178	16	0.4
151.3	3524	27	0.4

IX. ISR Flight Performance

As the Apollo 17 spacecraft approached the Moon, the ISR was activated inside the SIM Bay. This precaution guarded against damage to bearings by the shock from pyrotechnic bolts as the SIM Bay door was jettisoned. The first telemetry from this operation was received at the Mission Control Center at 0855 GMT, December 10, 1972. All engineering parameters were nominal, and they remained so throughout the 6 day mission. The signal showed a series of peaks as the hot detector viewed itself in successive facets of the closed contamination cover.

The first lunar scans at 2130 GMT looked good. The predawn limb deflection showed a signal to noise ratio of approximately 10 to 1. Instrument noise manifested itself in the telemetry as a tendency for the signal to shift back and forth between two adjacent levels. Signal quality remained good through the last lunar scans taken as the spacecraft sped away from the Moon on December 17, shortly after midnight GMT. During Trans-Earth Coast (TEC) operation remained nominal until the ISR was finally shut down at 1701 GMT, December 19, prior to re-entry into the Earth's atmosphere.

In lunar orbit the ISR operated according to a complex timeline dictated by the requirements of spacecraft operations and other instruments. Since no astronaut participation was required in the experiment, the longest continuous operational segments came during the 8-hour crew sleep periods. Overall, approximately 97 hours of lunar data (10^8 data points) were returned during the mission.

Two unanticipated signal characteristics will be analyzed in this chapter. First, the lunar radiance in the vicinity of the subsolar point saturated the ISR low gain channel, implying that the surface temperature

was higher than that reached by a black body in equilibrium with the solar constant. The second anomalous signal characteristic was excessive drift in the scan baseline during a sweep across the lunar surface.

A. Subsolar Point Saturation

On each orbital pass, as the spacecraft approached the subsolar meridian, the signal in channel 3 began to saturate. In the vicinity of the subsolar point, most of each scan was in saturation. It follows from the calibration curve that the subsolar point temperature exceeds 401K. Since this value exceeds a reasonable estimate of the temperature of a black body in radiative equilibrium with the solar constant, the possibility of some kind of systematic calibration error must be explored.

A Wang 720C Programmable Calculator was programmed to compute total radiance as a function of black body temperature for a given spectral transmission function expressed a piecewise continuous polynomial. Several calibration points were selected for each ISR channel, and the computer radiance for the respective temperatures was fit in a linear least squares sense to the ISR calibration values. The spectral model was adjusted until the residuals were minimized and the zero radiance value for the fit was reasonable. From the final spectral model the ISR saturation temperature was calculated to be 401.5K $\pm$ 0.5K. A least squares cubic fit to the entire set of calibration curves gives a saturation temperature of 401.1K.

The same spectral model was used to calculate the contribution of reflected solar radiation to the subsolar point signal. The Sun was assumed to have the spectral distribution of a 6000K black body (Johnson, 1965). The energy content was corrected to the solar constant (Laue and Drummond, 1968). If 10% of the solar radiation were reflected to the ISR by the Moon, the additional signal would give a 400K black body an

apparent temperature of 401.7K. The enhancement is approximately linear with the percentage of reflected radiation.

Measurements of the total reflectance of an Apollo 11 soil in white light (Birkebak et al., 1970) give a value of 10%. The actual integrated solar reflectance would be somewhat greater after the near infrared component was included. In addition, highland material would be brighter than a mare soil. On the other hand, the reflected radiation is distributed over a hemisphere and not concentrated in the direction of the radiometer. Considering these arguments plus the retroreflective character at the lunar surface, I estimate that the ISR saturated when the lunar surface temperature was approximately 400K.

The saturation in the scans begins approximately 20° in longitude from the subsolar meridian. A subsolar point temperature of approximately 406K can be inferred from this observation and simple geometric arguments.

The anticipated subsolar point temperature can be estimated from equation (2.12). The solar constant at 0.984 Astronomical Units is 0.1383 watts cm^{-2}, and the corresponding black body equilibrium temperature is 395K. A solar absorbance on the order of 0.85 for the lunar surface lowers the calculated subsolar point temperature to 379K. A surface emissivity of approximately 0.9 tends to restore the temperature thermometrically but has little effect on a radiometric measurement. The final temperature discrepancy is approximately 25K to 30K.

One possible explanation of the discrepancy lies with a misleading characterization of the ISR field of view during acceptance testing. As detailed in Chapter VII, the field of view was mapped with a collimated source. The results of the mapping were shown in Figure 7-2.

If the figure were a true representation of the field of view, then a mapping by an extended source (e.g., the Moon) would look something like the solid curve in Figure 9-1. If the normalized maximum corresponds to a full scale signal in a given channel, the level corresponding to 1/2 of a telemetry bit (10 mv) is approximately 0.002. It follows from the curve that the lunar limb should be undetectable 10 mrad from the optical axis.

An actual hot limb deflection is plotted as the open circles in Figure 9-1. The actual limb profile is less sharp than the calculated one, and the limb is detectable at a separation of 25 mrad. An estimate of the actual ISR field of view from the limb profile shows that the half power point is approximately 10 mrad from the optical axis, in agreement with the test results. However, the 10% power point is located at 15 mrad rather than 11 mrad, indicating the presence of weak wings in the field of view which would be undetectable with the test procedures used.

This property of the optical response has significance for the calibration curve, which was measured with extended sources. The design of the Calibration Test Facility assumed the maximum beam divergence to be 11 mrad, whereas the proper number is seen to be 25 mrad. If the calibration sources are too small to intercept the entire beam, the calibration curve will be systematically depressed at high temperatures.

Engineering drawings of the Calibration Test Facility place the ISR rotation axis 480 mm from the surface of each calibration source. The distance over which the beam diverges, measured from the aperture stop (the secondary mirror), is 860 mm. The width of the source, perpendicular to the scan plane, is 216 mm; and the beam itself is 178 mm across. Thus the source is wide enough to permit a divergence of 22 mrad for a perfectly

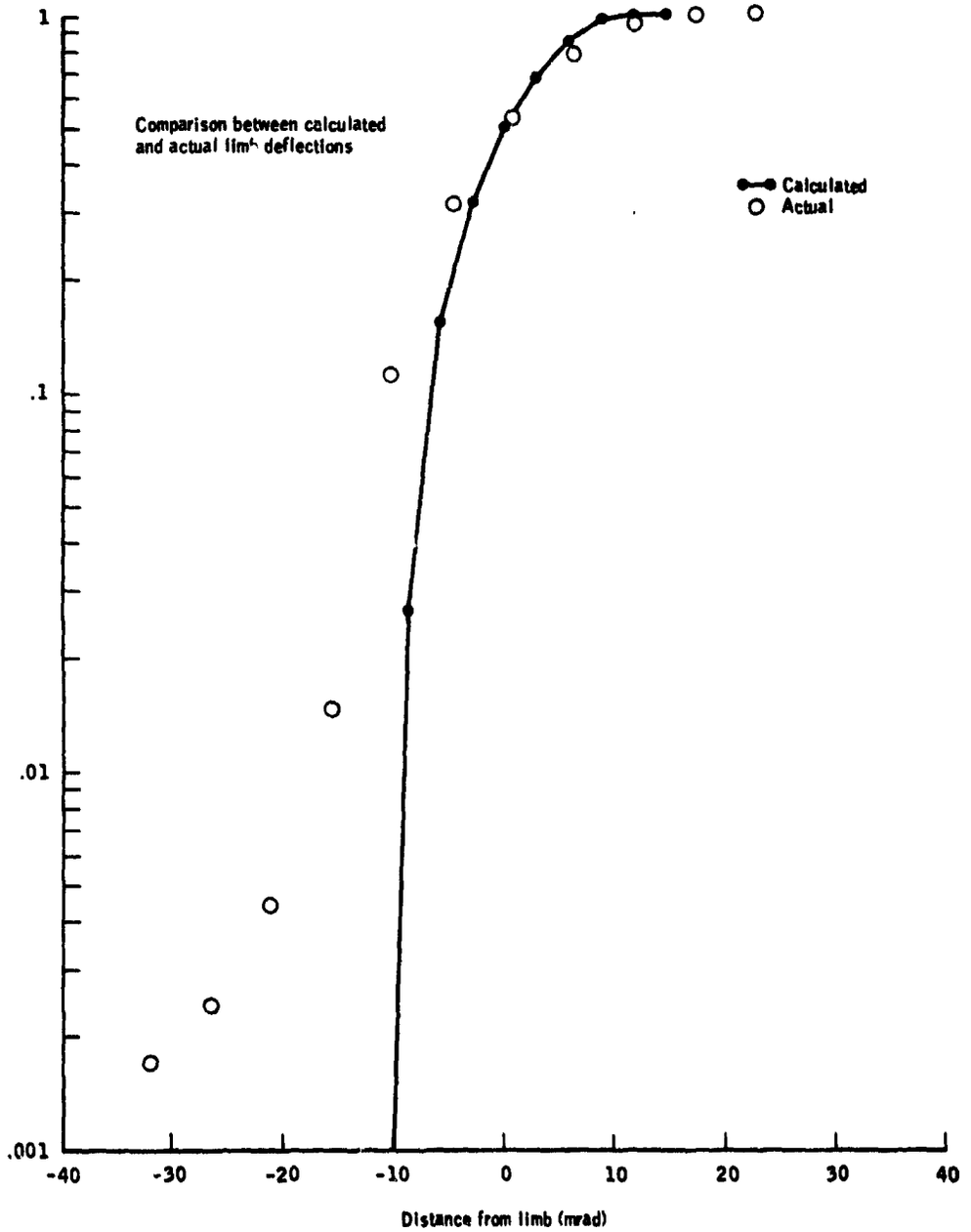

Figure 9-1 CALCULATED AND MEASURED LUNAR LIMB DEFLECTIONS. The dots connected by line segments represent the calculated ISR signal for a scan across the lunar limb. The calculation assumes the off-axis response shown in Fig. 7-2. Open circles are data from an actual bright limb crossing.

centered beam. Referring to Figure 9-1, I infer an error of approximately 1% in the high temperature calibration. At full scale this amounts to 50 mv or approximately 1K in temperature.

The width of the source in the scan plane was scaled to permit 7.5 deg of scan with a 22 mrad beamwidth. For a 50 mrad beamwidth the scan angle is reduced to 6 deg or 5 resolution elements. Thus the residence time of the beam on the source is adequate in terms of the system time constants.

It is clear that excess energy received in the wings of ISR field of view is insufficient to explain the temperature enhancement seen at the subsolar point.

The problem of enhanced subsolar emission normal to the surface is not new. Pettit and Nicholson (1930) measured a subsolar point temperature of 407K at full Moon. Sinton (1961) obtained a value of approximately 402K. The former value is probably too high because the observers were unaware of atmospheric transmission beyond 16 μm (Saari, 1964). The enhancement has been attributed to non-Lambertian surface emission.

The apparent directional emissivity of the lunar surface has been explained by several workers in terms of lunar surface roughness. Buhl et al. (1968) have shown that the bottoms of hemispherical craters (diameter to depth ratio of 2) reach temperatures of 420K. Shallower craters show less enhancement. Although hemispheres are not realistic models of large scale lunar features, their geometrical view factors may be representative of surface roughness on the centimeter scale. Bastin and Gough (1969) calculated subsolar point temperatures of 420K in the bottoms of troughs in a corrugated surface model. Both models are capable of predicting the type of directional emissivity presented by Six et al. (1968) from Earth-based thermal maps.

The enhancement observed by the ISR requires that the deep, small scale depressions must cover approximately 50% of the surface. The same percentage is estimated by Buhl et al. (1968a) from the lunar emissivity dependence on view angle. The model would predict limb darkening of ISR scans as the view angle causes the cool rims of the depressions to occult the hot interiors. Such limb darkening is observed on day side scans and, to a lesser extent, on nighttime scans.

The ISR data establishes the existence of ubiquitous small scale roughness where the distance between highs and lows is of the same order as the relief. This observation is important for models of surface correlated processes such particle track exposure and gas adsorption. Models which assume a plane surface geometry will seriously underestimate the probability of surface exposure of a soil grain.

B. Zero Point Drift

Soon after real time data began arriving in the Mission Control Center, we noted that the ISR signal consistently failed to return to zero as the field of view scanned across the Moon and looked at space. The effect of droop in the frequency response of the ISR would be expected to cause a gradual rise in the scan amounting to approximately 60 millivolts by the time the field of view begins to re-enter the housing. However, the observed effect was on the order of 200 to 400 millivolts.

The nature of the effect became somewhat more clear on REV 37 when the spacecraft performed a "pitch up" maneuver as part of the Ultraviolet Spectrometer Experiment. Figure 9-2 reproduces every scan during the final portion of that maneuver. The final scan is completely off of the Moon, yet a quasi-linear feature remains. Although the telemetry output is zero until the middle of the scan, the actual output voltage could be negative during that time. Nevertheless, the scan sequence gives the

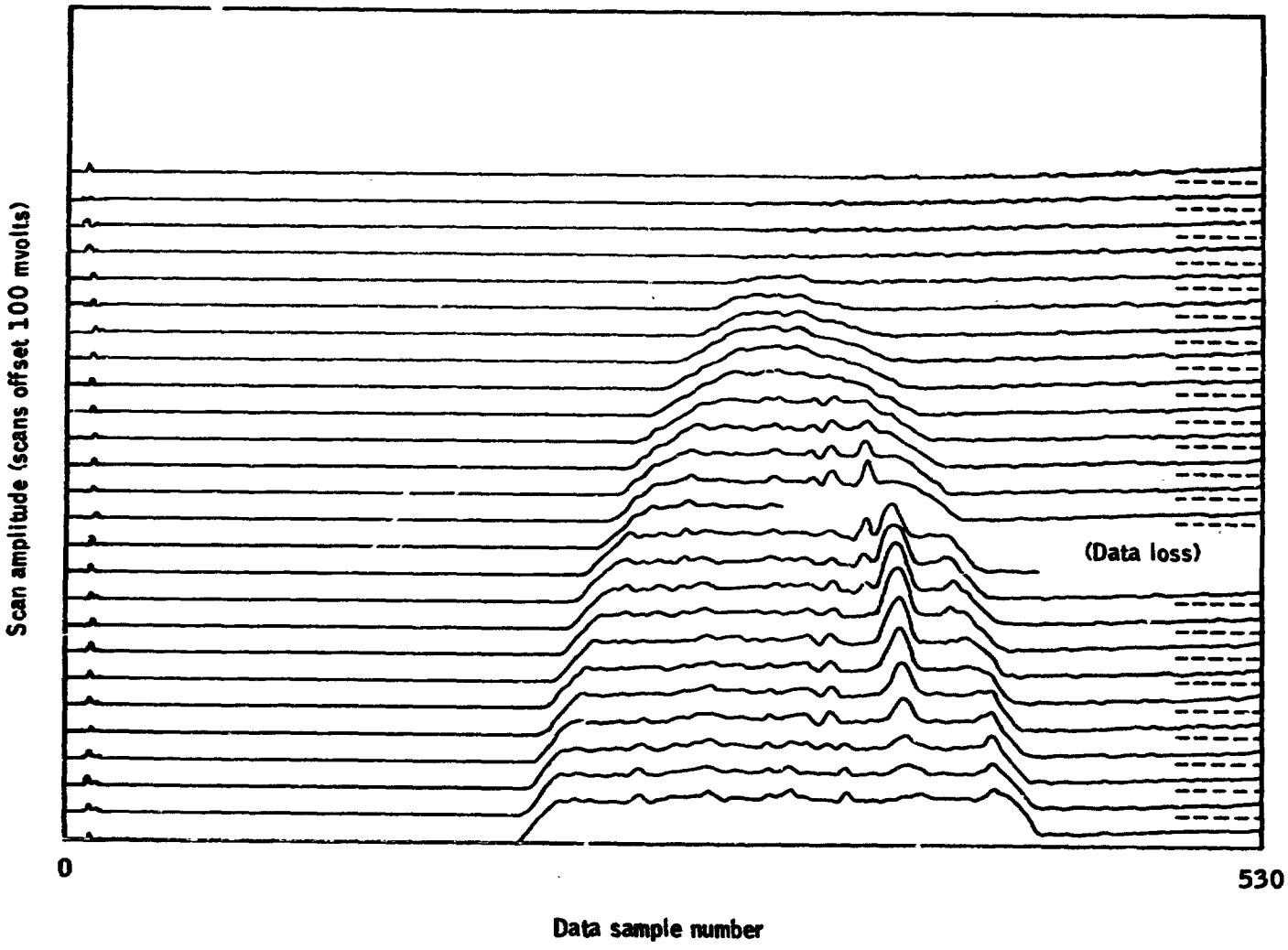

Figure 9-2 SCAN SEQUENCE DURING SPACECRAFT PITCH MANEUVER. As the pitch angle increases, the lunar sphere intercepts less and less of the scan swath. Eventually the entire scan crosses only deep space. The dashed segments at the right represent the scan baseline. Enhancement of the signal above the baseline is seen at the end of each scan.

impression that the ramp feature is always present and is superimposed upon the lunar signal when the Moon is in the field of view of the radiometer.

During the mission we hypothesized that the ramp signal either was some form of low frequency drift in the signal processing or was an object in the wings of the ISR field of view. The flight plan was altered to keep the ISR operating during Trans-Earth Coast (TEC), taking sky scans. We hoped that the sky scans would form a suitable data base for study of the drift.

In the post-mission data reduction, individual nighttime scans showed a distinct tilt throughout the entire scan. The simplest correction algorithm was tried first. A straight line defined by the clamp point and the observable offset in the trailing space look was subtracted from each scan. Contour maps of lunar data showed that the drift was insufficiently compensated.

Linear regression analyses were performed on several thousand sky scans. In general the correlation coefficient of the fit ranged from 0.94 to 0.98, the standard deviation typically ranged from 6 to 8 millivolts, and the residuals show no lack of fit. In most cases the inclusion of a second order Chebyshev polynomial improved the fit only marginally.

Such statistics strongly suggest a linear waveform, but quantization of the signal in the spacecraft can distort the real nature of the signal. Computer simulations of the digitization process show that exponentials of the form

$$V = K + A\,(\exp(t/\tau) - 1),$$

where K, A, τ are constants, can reproduce the regression statistics. The curvature from the exponential is almost undetectable in the limited portion of the feature available in the sky scans.

Digitization alters a purely linear input also. A regression analysis of the digitized signal reproduces the original slope rather well, but the y-intercept is systematically lowered by an amount ranging from 5 to 15 mv. Any correlations involving the y-intercept automatically acquire a 10 mv peak-to-peak uncertainty due to the digitizing process.

Scan-to-scan noise introduced by the telemetry or the clamp can be reduced by coherently adding sky scans and taking the average. One such scan constructed from 100 scans (2.4 minutes of data) is shown in Figure 9-3. A linear regression fit over the interval from data point 400 through data point 515* gives the regression line

$$V = -262.9\ (\pm\ 1.4) + 0.7585\ (\pm\ .0030)\ P, \quad 400 \leq P \leq 515 \qquad (19.1)$$

$$\rho = 0.9991, \quad \sigma = 1.088 \text{ mv},$$

when V is the signal amplitude in millivolts, P is the data point number, ρ is the correlation coefficient and σ is the standard deviation of the fit. The bending of the curve below 20 mv (1 telemetry bit) is an artifact caused by the lack of negative voltage values in the telemetry. For comparison, the anticipated droop characteristic is included in the figure.

Sky scans were analyzed for a correlation between the slope of the scan and the scan value at data point 530 in order to develop a correction for drift. At sample #530 the ISR housing contributes approximately 20 millivolts of signal, but the contribution is relatively constant. The choice of a data point at the far end of the scan maximizes the roll angle at which the offset cannot be calculated.

*The numbering system for scan points begins with the first point following the third calibration pulse. This point is easily found with a programmed search routine. The first point following the clamp is number 28. A scan is sampled until point 540 where vignetting by the ISR housing becomes severe.

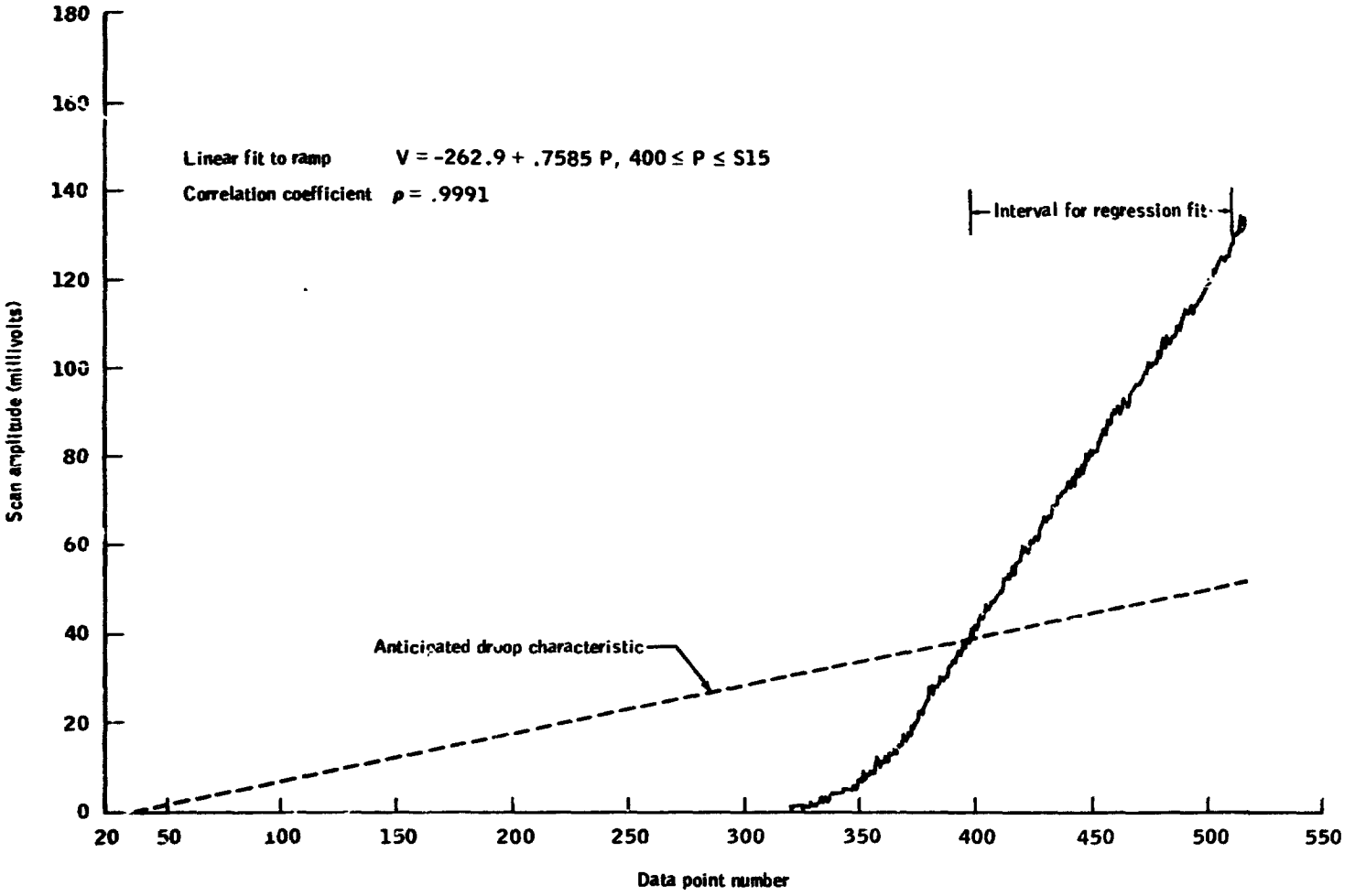

Figure 9-3 ZERO POINT DRIFT FROM AVERAGED SKY SCANS. The solid line represents the average signal from 100 sky scans, added coherently. The dashed line gives the baseline drift calculated from the ISR low frequency response.

Any correlation analysis involving the value of a particular data point is degraded by noise contributions to the signal. The major noise sources are intrinsic instrument noise, scan-to-scan offsets due to variation in the clamp level, and telemetry quantization. At certain times in the mission the telemetry stream itself becomes noisy, and binary zeros randomly become binary ones causing spikes in the scans.

Various numerical filters and algorithms have been developed to reduce the noise contribution from all these sources. In particular, the ramp amplitude at sample #530 is derived by first checking for anomalous bit patterns caused by telemetry noise and then averaging the values from samples 528 through 532 to reduce instrument and quantization noise. Finally, the resultant value is averaged with similar values from the 4 previous scans to reduce scan-to-scan noise from the clamp.

The slope of an averaged scan such as the one in Figure 9-3 is equal to the mean of the regression slopes of the individual component scans. Figure 9-4 is a plot of mean slope versus ramp amplitude for three mission periods when the correlation coefficients for the sky scans were consistently greater than 0.94. Each point on the plot represents the time average over 2.4 minutes of data.

Data set A (Figure 9-4a) occurs during the pitch maneuver for the UV Spectrometer Experiment on REV 37. The data in Figure 9-4b were taken after Trans-Earth Injection as the spacecraft left the Moon. Although good regression lines were obtained for data set B, the field of view caught just enough of the receding Moon to depress the slope of the ramp. After a data gap, the effect continues at the beginning of data set C. The discontinuity between C and D can be traced to noise in the

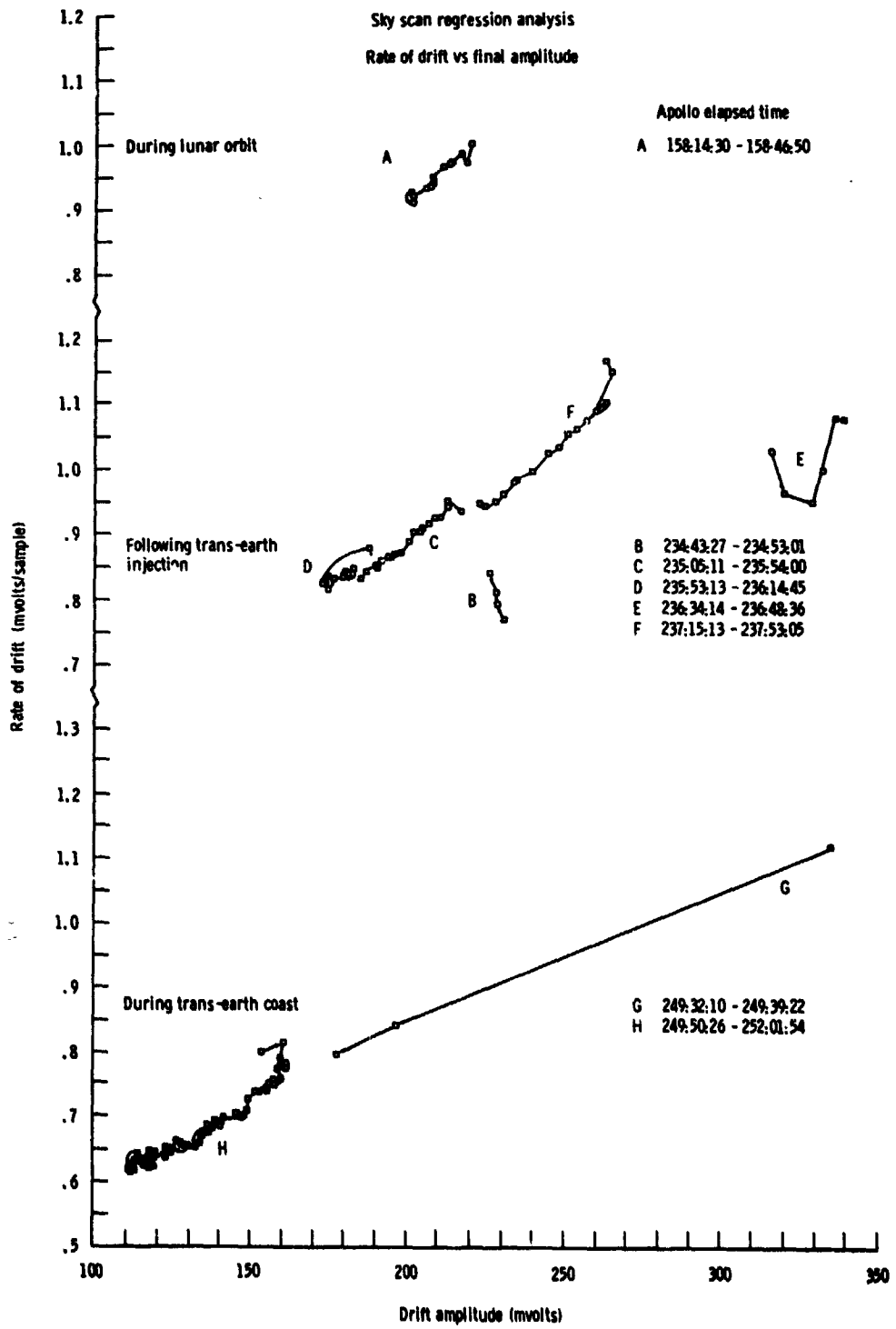

Figure 9-4 ZERO POINT DRIFT: REGRESSION SLOPE VS. AMPLITUDE. Linear regression analyses were performed on the zero point drift during 8 distinct sets of sky scans from the mission. Each data point represents the average value from approximately 144 seconds of data.

latter set, possibly associated with a changeover in the range station receiving the Apollo telemetry. The erratic behavior exhibited from the end of D through the beginning of F occurred while the UV Spectrometer was directed toward the Earth. Figure 9-4c includes scans taken later in the Trans-Earth Coast phase. Data set G is associated with a transient response occurring after the ISR was switched on.

Regression analyses were performed on data sets A and G and those portions of C, F, and H which represent steady state behavior. The results are presented in Table V. Clearly the same dependence of the ramp slope on the ramp amplitude is exhibited in A, C, and H. The correlation coefficient in all three regressions is low, probably due to considerable noise in the dependent variable. The agreement is significant nevertheless because the three data sets represent quite different operational histories. Note that when the three analyses are combined, the correlation is greatly improved.

Data set F was taken while the UV Spectrometer was pointed at the Moon. At that time, only a few hours after Trans-Earth Injection, the Moon was still a large object in the sky and could well have biased the ISR response. I will assume that F is a contaminated data set.

A regression analysis relating y-intercept to ramp amplitude is presented in Table VI. The two regressions permit a linear correction to be derived once the ramp amplitude has been computed.

When the linear correction derived from the regression analyses is applied, it is found that the scans are overcompensated. The necessity of a second order correction term is indicated by the regression analyses as well as observable curvature in high amplitude drifts such as occur during switching transients (e.g., data set G).

TABLE V

REGRESSION ANALYSIS CORRELATING RAMP SLOPE TO RAMP AMPLITUDE FOR SKY SCAN DATA

Data Set	No. of Scans	Regression Slope (sample^{-1}) x 10^5	Regression Intercept (mv/sample) x 10^3	Std. Dev. (mv/sample)	Corr. Coeff.
A	1160	349 ± 22	221 ± 46	0.0518	0.4216
C	1797	355 ± 15	176 ± 30	0.0598	0.4759
F	1234	395 ± 13	55 ± 32	0.0598	0.6513
G	285	197 ± 4	450 ± 10	0.0572	0.9523
H	2474	342 ± 10	214 ± 16	0.0549	0.5286
Combined A, C, H	5431	350 ± 3	200 ± 5	0.0572	0.8732

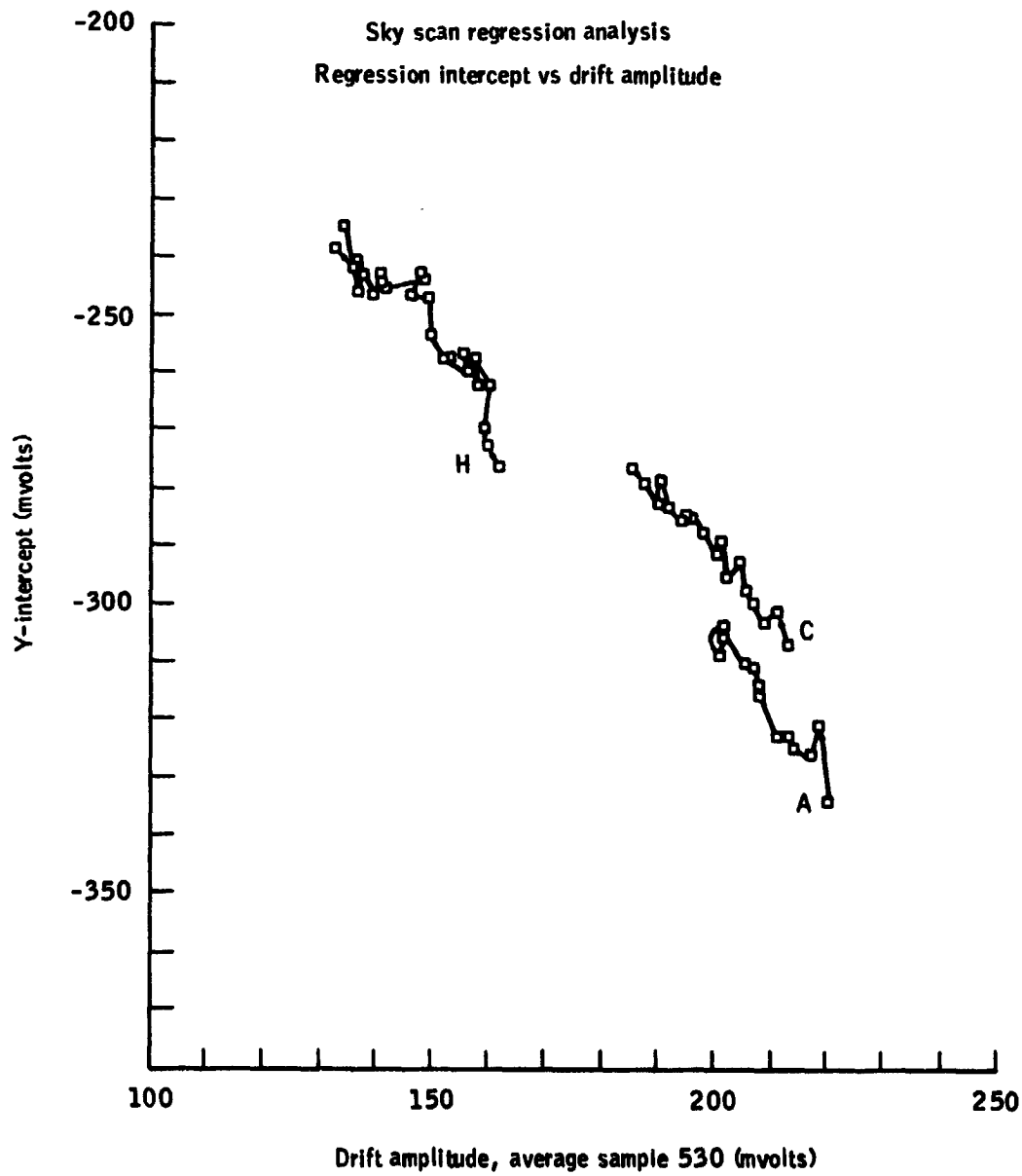

Figure 9-5 ZERO POINT DRIFT: REGRESSION INTERCEPT VS. AMPLITUDE. See caption for Fig. 9-4. Points are shown here only for those data sets considered free of off-axis energy from the bright lunar limb.

TABLE VI

REGRESSION ANALYSIS CORRELATING RAMP INTERCEPT TO RAMP AMPLITUDE FOR SKY SCAN DATA

Data Set	No. of Scans	Regression Slope (mv/mv) x 10^2	Regression Intercept (mv)	Std. Dev. (mv)	Corr. Coeff.
A	1160	-103 ± 10	-101 ± 22	24.56	-0.2821
C	1797	- 95 ± 8	-102 ± 14	27.43	-0.3000
H	2474	- 92 ± 5	-116 ± 8	25.96	-0.3350
Combined	5431	- 91 ± 1	-116 ± 2	26.82	-0.7065

The scan correction polynomial is assumed to have the form

$$\Delta V = c(P-P_0)^2 + bP + a, \tag{19.2}$$

where b and a are the slope and intercept computed from the ramp amplitude, P_0 is the abscissa of a standard point assumed to lie on the regression line, and c is given by

$$c = \frac{b - s}{2(P_0-P')} \tag{19.3}$$

where s is an assumed constant slope at point P'. The value for s was taken to be zero at $P' = 28$, the first data point after the clamp is set. The point P_0 was taken equal to 457.5, the midpoint of the regression analysis. The final correction algorithm appears quite successful in removing the instrument bias from contour maps.

The cause of the baseline drift remains unclear. No line of evidence presently available points unambiguously to an electronic cause or an object (e.g., the contamination cover) in the wings of the ISR field of view.

X. Preliminary Results

A. Lunar Surface Coverage

Table VII lists the operating periods during which the ISR took lunar data. The beginning and the end of each data period are given in terms of Greenwich Mean Time (GMT) and Apollo Elapsed Time (AET). The latter time frame is referenced to the Apollo 17 launch at 17:33:00 GMT on December 6, 1972. The table also includes information on the spacecraft orbit and the location of the sunrise terminator on the lunar surface.

Data gaps do exist within most of the operating periods. Gaps of several minutes often are associated with the transition from onboard recording of farside data to real time data acquisition by ground stations. Degraded and missing signals also occur during roll maneuvers for oblique photography and during off-nominal attitudes for the UV Spectrometer Experiment.

During the second data set listed in the table, the spacecraft was in a Lunar Module descent orbit having a perilune of approximately 19 km. When the spacecraft altitude falls below 95 km, the angle subtended by the Moon becomes so large that the lunar limb encroaches into the space look required by the ISR space clamp circuit. In that case, the scan baseline is offset to negative voltages by the clamp. If the limb encroachment is too great (e.g., at low altitudes), the entire scan is offset below the zero level of the telemetry. When the offset is not too severe, the scan can be corrected in principle. Since perilune occurred over the landing site in the descent orbit, the most degraded data lies in the vicinity of the sunrise terminator.

TABLE VII: ISR LUNAR SURFACE COVERAGE

Data Set	Transition Operation*		Transition Times GMT	Transition Times AET	Lunar Coord. Long.	Lunar Coord. Lat.
1	co	12/10	21:30:06	87:57:06	250	18S
	cc		22:09:49	88:36:49	127	2N
2	co	12/11	01:53:16	92:20:16	180	16S
	cc		03:42:01	104:09:01	109	5N
3	on		20:31:00	110:58:00	268	11S
	off		21:59:30	112:26:30	357	17N
4	on		22:57:36	113:24:36	180	17S
	off	12/12	00:18:59	114:45:59	295	1S
5	on		06:02:29	120:29:29	331	12N
	off		17:45:06	132:12:06	358	19N
6	on		22:16:25	136:43:25	255	11S
	cc	12/13	15:32:18	153:59:18	348	19N
7	on		15:57:49	154:24:49	271	3S
	off		17:36:57	156:03:57	328	16N
8	on		17:56:31	156:23:31	270	3S
	cc		18:03:20	156:30:20	250	10S
9	co		19:35:15	158:02:15	329	16N
	off		22:00:19	160:27:19	250	9S
10	on	12/14	02:45:05	165:12:05	104	4S
	cc		15:39:51	178:06:51	269	1N
11	on	12:15	08:45:05	195:12:05	44	16N
	off		21:55:26	208:22:26	169	23S
12	on	12/16	02:24:05	212:51:05	76	0
	off		17:14:45	227:41:45	264	4N
13	on		18:51:22	229:18:22	326	23N
	off		22:50:58	233:17:58	320	23N

*co = cover open, cc - cover closed

TABLE VII (Continued)

Data Set	Operating Time (hrs)	Total Orbits	Perilune, Apolune	Sunrise Term. Long.
1	0.66	0.3	95 x 309 km	27.6 27.3
2	11.80	6.2	19 x 111 km	25.4 19.4
3	1.46	0.7	97 x 127 km	16.0 15.2
4	1.36	0.7	97 x 127 km	14.7 14.0
5	11.71	5.9	96 x 128 km	11.1 5.2
6	17.26	8.7	95 x 127 km	2.9 354.1
7	1.65	0.9	96 x 126 km	353.9 353.1
8	0.11	0.1	96 x 126 km	352.9 352.9
9	2.42	1.2	96 x 126 km	352.1 350.9
10	12.91	6.6	97 x 125 km	348.5 341.9
11	13.17	6.6	112 x 118 km	333.3 326.6
12	14.84	7.5	111 x 119 km	324.3 316.8
13	3.99	2.0	109 x 121 km	316.0 314.0
	93.34			

Another type of degradation occurs at the beginning of each data set. When the ISR is switched on, the detector requires 15 to 30 minutes to stabilize. The starting times labeled "ON" in column 2 of Table VII were chosen to coincide with the first scan of the set in which the radiometric signal from the internal calibration patch reached its steady state value. However, at that time baseline drift (cf. Chapter IX) is in a transient phase, as exemplified by data set "G" in Figure 9-4c and Table V. A similar transient in the baseline drift occurs when the contamination cover is opened. In the second case the transient is induced by the clamp circuit adjusting its reference voltage level from the interior cover signal to the empty space signal. Consequently, at the beginning of any data set the baseline correction algorithm derived in the previous chapter may not be strictly valid.

Each ISR scan extended from horizon to horizon as seen from the spacecraft. At altitudes of 95 km and 125 km, the lunar horizon lies 560 km and 640 km, respectively, from the orbit ground track. The spacial resolution of the measurement is so poor at the horizon that ISR mapping is described more realistically as being limited to approximately 300 km to either side of the ground track.

Since the mapping of nighttime thermal patterns was a major objective, the position of the sunrise terminator is a parameter of interest in the description of surface coverage. The first usable predawn data was taken in data set #3 (Table VII). The terminator crossing occurred at 112:21 AET (selenographic longitude 15 deg), just west of the crater Bessel E in western Mare Serenitatis. A good map was obtained of the Sulpicius Gallus formation and the dark mantling material inside the

southwestern rim of Mare Serenitatis. The last ISR predawn map includes Aristarchus and its environs.

Nighttime coverage during the mission followed the Apollo 17 ground track from the Haemus Mountains across southern Mare Imbrium through central Oceanus Procellarum past the northeast corner of the Orientale Basin. Major craters included in the mapping are Copernicus, Kepler, Marius, Olbers A, and Aitken.

B. Data Reduction

If the spacecraft orbit and attitude are known as a function of time, the selenographic coordinates of any data point can be computed. The Johnson Space Center (JSC) has provided trajectory and attitude histories for most of the ISR data set, but this supporting information has not been fully integrated into the data tapes. Data presentations in this work use approximate orbits generated from Keplerian state vectors supplied by JSC. The only correction for spacecraft attitude is a simple search routine which locates the limbs on each scan, thereby compensating for the roll angle. Neglecting pitch and yaw corrections can cause a selenographic positional error as great as 9 km at distances 300 km from the ground track. Note that topographic relief, which determines the real altitude, can induce positional errors of the same magnitude.

Corrections for noise and instrument effects are made on an individual scan basis. After correction for baseline drift, a 9-point numerical filter suppresses high frequency noise. Temperatures are derived from the telemetry voltage by solution of a cubic polynomial using a Newton-Raphson scheme.

C. Surface Temperature History

The general goal for all lunar infrared measurements is the construction of the temperature history for one surface element throughout a lunation. This objective has not been attained in Earth-based efforts, and it was not accomplished in this work because the mission was too short. A rather unsatisfactory compromise is to plot temperature versus selenographic longitude from points lying along some latitude circle, usually the equator. Such data contains measurements from a variety of lunar terrain types and is useful only for qualitative analysis.

Figure 10-1 shows temperature plotted against brightness longitude (phase angle) at a selenographic latitude of 10 deg. The points from approximately 0 deg phase (noon) to 180 deg (midnight) comes from regions south of the equator. In terms of selenographic longitude, that set of data runs from 278 deg westward to 73 deg. The complementary set of points lies along latitude +10 deg, running from 107 deg westward to 265 deg of selenographic longitude.

The lunar afternoon cooling data show significant scatter. The points come from the farside highlands, which exhibit a great deal of topographic relief. The scatter can be traced to slope variations, which are equivalent to changes in local sun angle. The lunar morning points fall across the smoother surfaces of Mare Tranquillitatis, Mare Vaporum, and Sinus Aestuum; and the curve appears well behaved as a consequence. The scatter prior to noon occurs in a rough highland region outside the southern rim of Mare Crisium.

Temperatures near the subsolar meridian south of the equator appear to be significantly cooler than those north of the equator. Most of the difference seems to be real, equivalent to the surface in the north

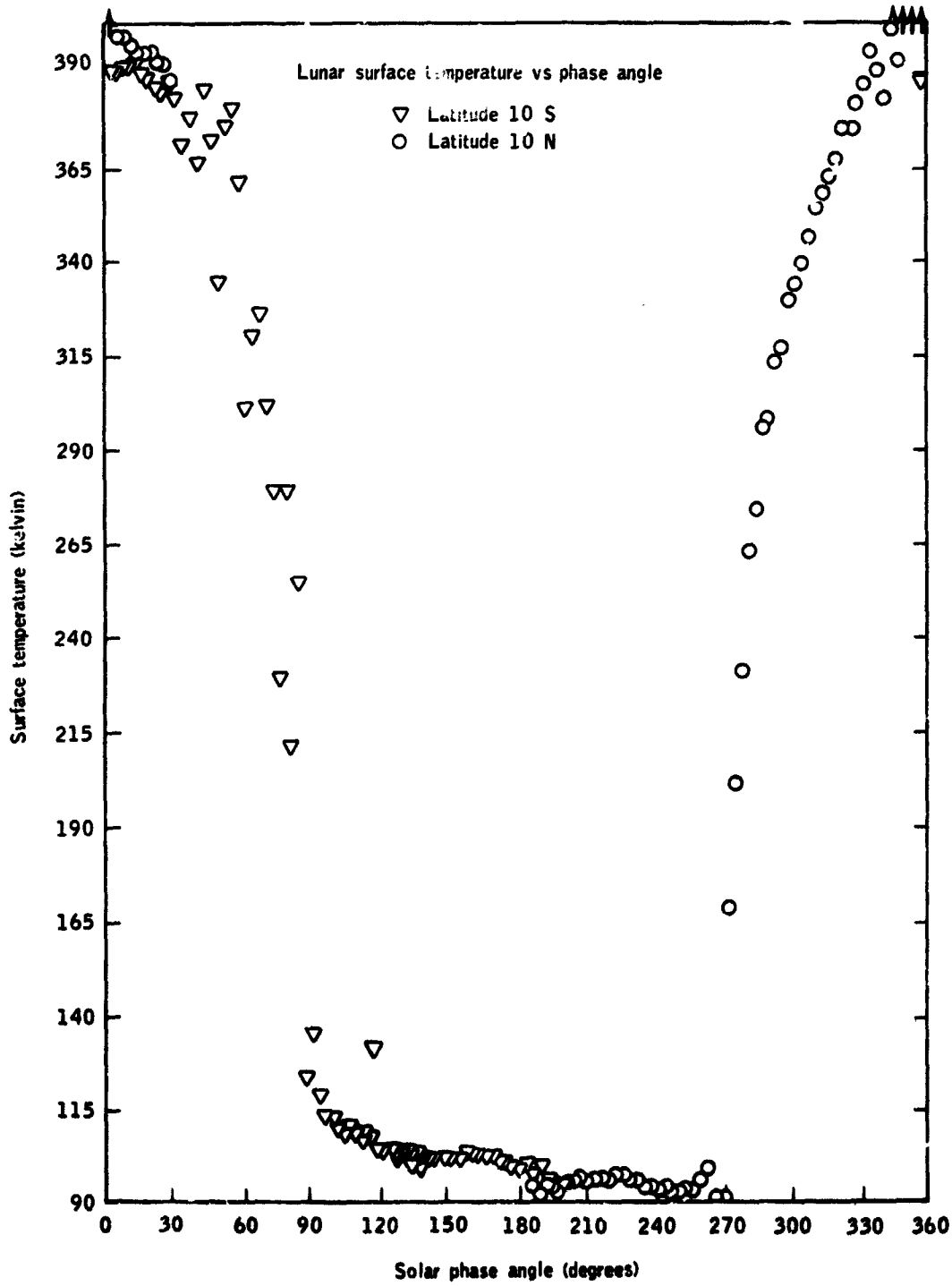

Figure 10-1 LUNAR SURFACE TEMPERATURE VS. PHASE ANGLE. The lunar surface temperature at the 10° latitude circle was picked from every fortieth scan on REV 42. The particular orbit was chosen because data coverage was complete over the entire revolution.

having an albedo 8% lower than the material in the south. These subsolar regions lie approximately between 80 deg and 105 deg longitude.

The predawn temperature of 90K was recorded inside the ghost crater Stadius. The apparent discontinuity at phase angle 265 deg is the thermal anomaly from Copernicus. Another prominent anomaly at 118 deg of phase is associated with the crater Crookes. The slight hump in the post-midnight points between phases 215 deg and 235 deg results from a dense population of small scale thermal anomalies.

The nighttime data prior to midnight are difficult to interpret. The regions measured do not have good photographic coverage, and the various dips and rises are not readily correlated with terrain types. It is clear, however, that the farside highlands (premidnight points) generally exhibit higher nighttime temperatures than the frontside western maria (postmidnight points). Approximately extrapolating the two halves of the curve, I get midnight temperatures of 102K and 97K for the two types of material. With an allowance for the higher albedo of highland material, relation (3.1) suggests an effective γ of 800 for the farside highlands and 1040 for the western maria.

A value of $\gamma = 1040$ is typical for lunar soils returned to Earth (Cremers, 1974). However, the lower value for the highlands implies that the soil density is on the order of 2 g cm^{-3}, quite high by lunar standards. The data may imply that the farside highland soils are highly consolidated. Alternatively, the highland soils may physically differ from those at the Apollo landing sites.

D. Regional Terrain Types

Figure 10-2 shows two collections of nighttime scans from a single orbit. Each data set is 2 minutes long, representing approximately

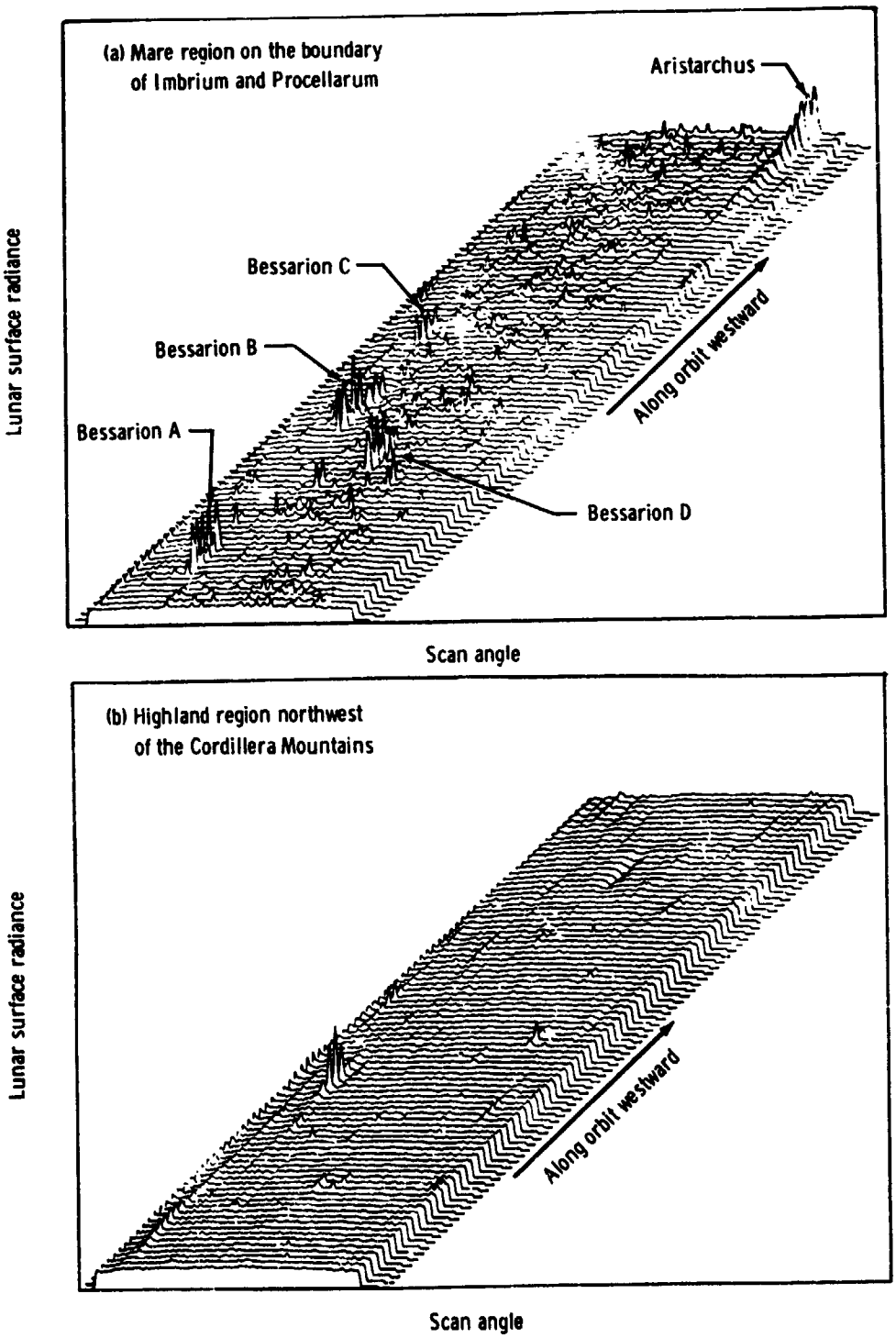

Figure 10-2 CONTRASTING THERMAL STRUCTURE IN MARE AND HIGHLANDS. Sequences of ISR scans show (a) the wealth of thermal structure in a mare region having a shallow basalt fill and (b) the featureless signals over part of the Orientale Basin ejecta blanket.

180 km of travel along the orbital ground track. Each individual trace contains the voltage output from the ISR during a lunar scan after correction for baseline drift and low pass filtering.

The scans in Figure 10-2a were taken in northeastern Oceanus Procellarum near the craters Bessarion A and Bessarion B. Figure 10-2b shows data from the farside highlands, northwest of Mare Orientale. The dense population of anomalies on the mare consists of craters with diameters on the order of 0.1 to 1 km, surrounded by blocky ejecta. The striking contrast in the thermal structure over the two types of terrain can be understood in terms of a simple model of lunar surface processes.

The underlying principle behind the model is simply that older surfaces on the Moon have been bombarded by more meteorites. In fact, photogeologists obtain relative ages among lunar regions by comparing surface crater density. Therefore older surfaces have been more heavily reworked, have experienced more large scale impacts, and have a deeper regolith. In this simple picture, the crater with blocky ejecta (the thermal anomaly) has penetrated the regolith and has excavated pieces of the relatively competent underlying rocks. The smallest blocky crater establishes the approximate depth of the regolith, which in turn helps to date the surface. Thermal maps from the ISR show that the smallest anomalies in the farside highlands have a size on the order of 10 km, implying that the regolith there has a depth approaching 1 km.

The use of anomaly populations in the mare to indicate regolith thickness is not so straightforward. The maria are composed of basaltic lava flows overlying presumably anorthositic basement rocks. Photogeologic arguments and radioactive dating of lunar samples associate the various maria with ages in the general range of 3.0 to 3.8 billion years.

It is unknown whether any given mare filled quickly or slowly, continuously or episodically. The lavas erupted during a time when the flux of meteorites impacting the lunar surface was rapidly declining. Any particular flow unit in the sequence could be relatively pristine or heavily reworked, depending on its age and the time of surface exposure before it was covered.

Young et al. (1974) have compared craters 0.5 to 2.0 km in diameter in Mare Imbrium with craters of similar size and "freshness" in Mare Serenitatis. The Serenitatis craters are blocky whereas the Imbrium craters are not, even though the Serenitatis surface is older and should have the deeper regolith. Young et al. try to associate the observations with the existence of competent, unreworked, subsurface flow units in southern Serenitatis.

The observations can also be explained by a relatively shallow basalt fill in southern Serenitatis. The blocks would be pieces of more competent basement rocks. Young et al. reject this explanation because Imbrium craters near sinuous rilles or collapsed lava tubes, "where lava flows can be reasonably inferred to be close to the surface", show no blocks. However, lava tubes are simply surface manifestations and do not directly relate to depth of fill.

Green (1969) contoured the spatial distribution of thermal anomalies across the lunar disk as determined from Earth-based eclipse observations. The regions of highest number density were northwestern Mare Tranquillitatis, central Oceanus Procellarum, the Fra Mauro Formation, and central Imbrium, in decreasing order of importance. An examination of the eclipse thermal map (Saari et al., 1966) shows that the most intense anomalies in Tranquillitatis lie along the western edge and

the boundary with Mare Serenitatis to the north. The placement of anomalies mirrors the shallowest parts of the Tranquillitatis Basin as determined by De Hon (1974, 1975). The blocky craters studied by Young et al., also fall in a region of shallow basalts. Similarly, the dense anomaly population in Oceanus Procellarum, as seen in Figure 10-2a and Green's map, correlates with a very shallow fill as estimated by Eggleton et al. (1974).

The population of intense eclipse anomalies extends from northeastern Procellarum into Mare Imbrium. However, a region west of Diophantus to Aristarchus is notably free from thermal structure. It is this region which contains the fresh craters without blocky material, described earlier. No estimates for the depth of basalts have been published, but the Aristarchus Plateau is thought to represent flooding distinct from the maria to the south and east (Head, 1974).

In summary, I propose that the size of minimum thermal anomaly is a reliable indicator of regolith thickness only in the highlands and the deeper maria. Most mare anomalies apparently reflect the depth of basalt fill.

Figure 10-3 is a thermal contour map of data from REV 57, contoured at a temperature interval of 3K. The map projection is oblique Mercator, centered on the orbital ground track. In other words, the map "equator" (abscissa) is the intersection of the orbit plane with the lunar surface. The ordinate is "latitude" relative to the orbit plane. A grid of selenographic longitude and latitude is drawn on the map with 2 deg. increments.

At the time of this orbit the sunrise terminator was located at selenographic longitude 330 deg. The local lunar time at the right end

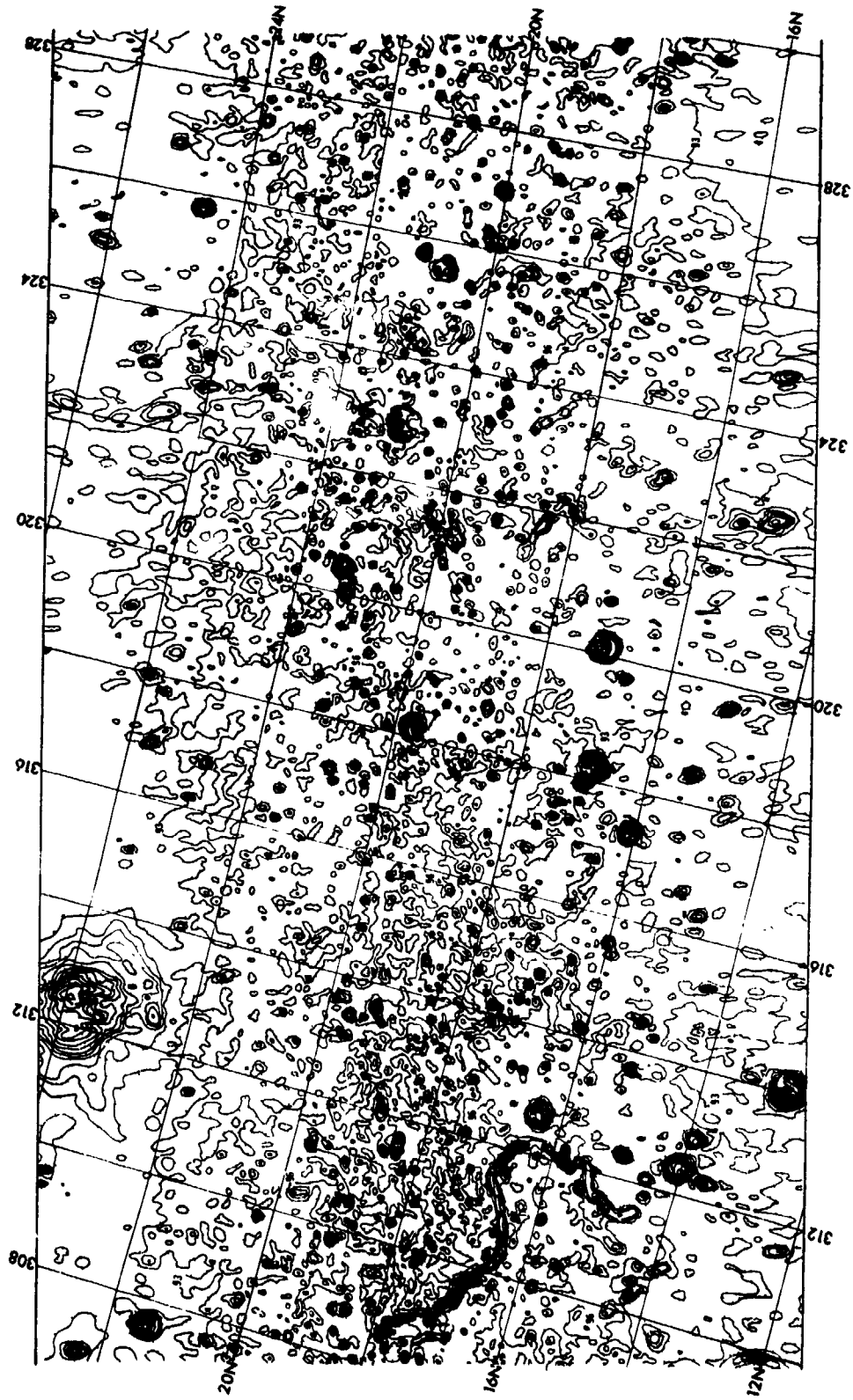

Figure 10-3 LUNAR SURFACE ISOTHERMAL MAP. ISR data from REV 59 has been contoured at an interval of 3 K. The sunrise terminator lay at longitude 330 deg, at the right side of the map.

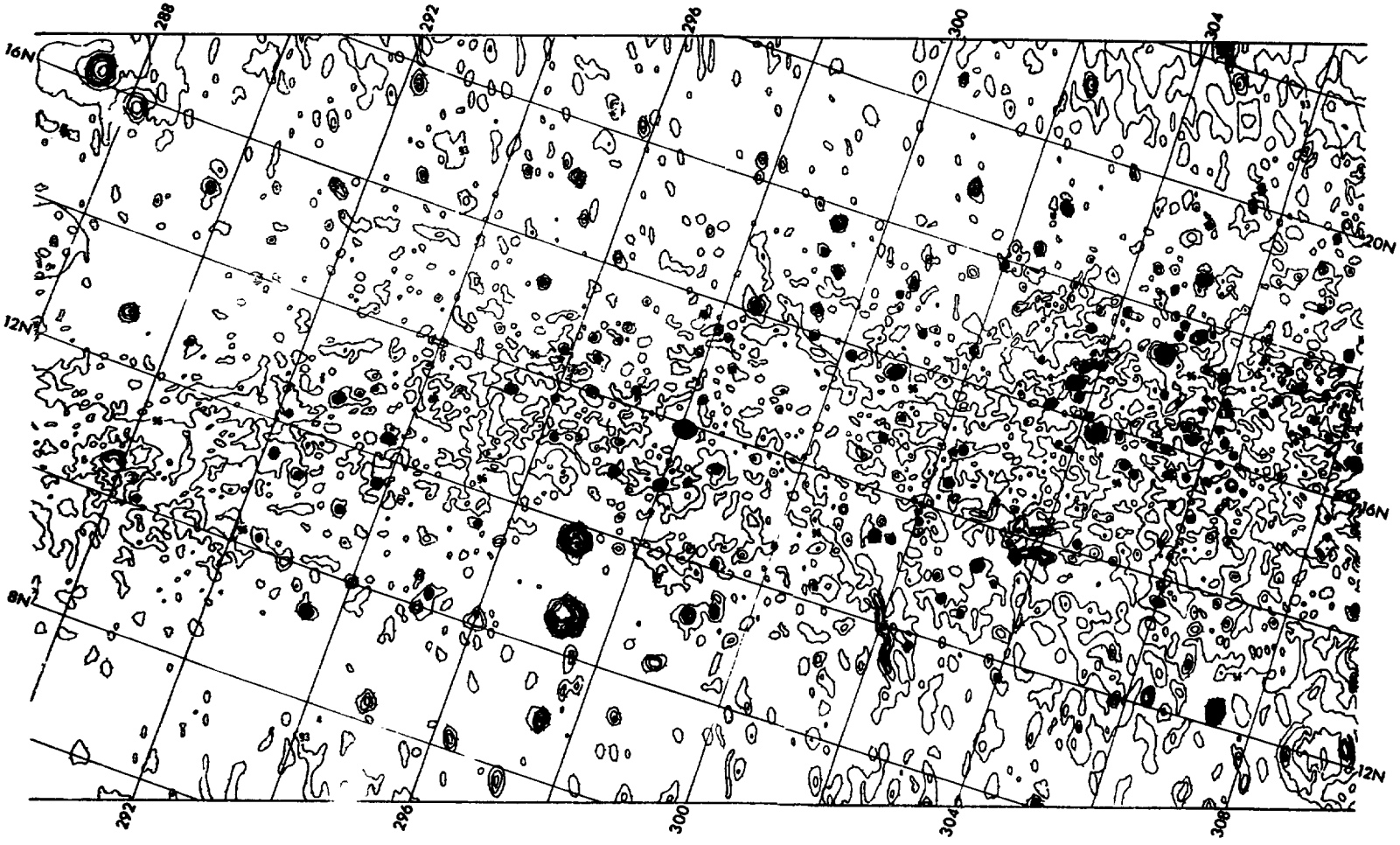

Figure 10-3 (Continued)

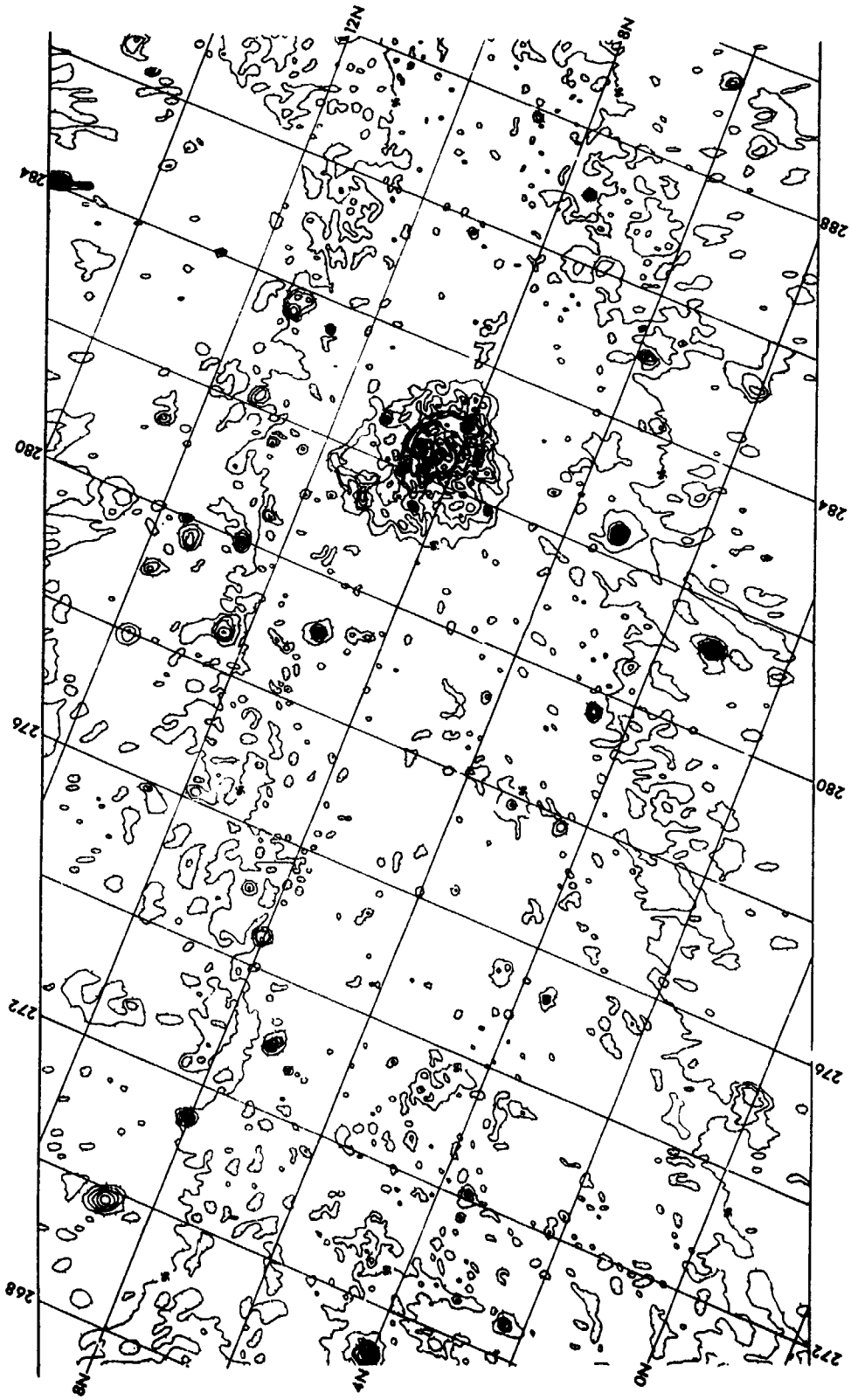

Figure 10-3 (Continued)

of the map is predawn, at the left end it is just after midnight. The coverage included on the map represents approximately 20% of the data from one orbit.

The nighttime cooling behavior manifests itself as a fall in temperature from approximately 100K at the left side of the map to approximately 94K at the right end of the map. Since the Sun's path during a lunar day lies approximately in the plane of the lunar equator, the contour lines associated with the nighttime gradient should lie more or less parallel to the lines of selenographic longitude. Instead, the contours have a "V" shape, the point of the "V" lying in the center of the map. If a line were drawn vertically across the map, the temperature at either end would be somewhat lower than the temperature at the middle. In other words, the thermal map shows the limb darkening discussed in the previous chapter. The effect supports the hypothesis of ubiquity of small scale roughness.

The jumble of contours on the right hand section of the map results from the myriad of small scale anomalies in Oceanus Procellarum. The comparative paucity and large scale of anomalies in the farside highlands is readily seen on the left-hand section.

E. Crater Degradation Model

Pohn and Offield (1970) proposed a morphological classification scheme whereby lunar craters can be placed into one of seven classes. The principal criterion is rim crest sharpness; but the textural detail of ejected materials, the morphology of wall terraces, and the number of superposed craters are also considered. By means of this scheme, any lunar crater larger than a few kilometers can be assigned a number ranging from 0.0 (most degraded) to 7.0 (freshest). The morphologic sequence

is equivalent to a relative age sequence under the assumptions that crater morphology is crisp and sharp immediately after formation, that the initial morphologies of most lunar craters are similar, and that continuous degradation processes act on all lunar features (Head, 1975).

Head (1975) has attempted to assign absolute ages to some morphologic classes based on lunar sample dating. A grade of 4.8 implies that the crater is contemporaneous with the formation of the last major lunar basin, Mare Orientale, roughly 3.9 billion years ago. Thus the bulk of lunar history is spanned by 2 of the 7 classes. The heavy erosion in the first 15% of the Moon's lifetime was caused by the massive bombardment occurring during that time. In particular, the projectiles in the large size range added proximity weathering and seismically induced landslides to the direct mechanism of surface reworking from primary and secondary impacts.

Head also has re-examined the process of crater erosion. He observes that relatively small volumes of fill material can blanket floor roughness and can have a significant effect on parameters which measure the shallowness of a crater. Sources of infill include erosion of the crater wall by landslides and ejecta from impacts just outside the crater rim. The latter source is probably less important during "Period II", the time span from the end of basin formation to the present.

As discussed in Chapter III, Fudali (1966) proposed a crater degradation sequence in which the thermal signature would evolve with time as does the visual appearance. In order of disappearance, Fudali listed thermal enhancement of the outer rim, floor, and inner rim. The following ISR maps will illustrate just such a sequence. They will also demonstrate that a crater disappears thermally at morphologic class 5.5, i.e., long before it disappears visually.

In Figure 10-4, Olbers A is the prominent thermal anomaly near the center of the map (longitude 282, latitude +8). A bright, fresh, rayed crater, it is not well known because it lies at the West limb and is not readily visible from Earth. Figure 10-4a shows the anomaly as it appeared on REV 57, contoured at a temperature interval of 5K. The solar phase angle at the crater was approximately 220 deg. Figure 10-4b comes from REV 71, 28 hours later. The orbit ground track has moved somewhat north of the crater; and the effects of foreshortening can be seen, particularly in the case of the small satellite crater to the south. The temperature on the crater floor appears to have fallen 5K, although part of the decrease might arise from lower spatial resolution which tends to average out temperature contrast. Figure 10-c is a Lunar Orbiter photo of the same area.

Olbers A exemplifies the freshest crater type in the thermal signature degradation sequence. The most intense enhancement lies on the floor of the crater. The anomaly extends to the ejecta blanket before grading into the soil background. The ejecta enhancement pattern is elongated to the northwest, possibly indicating that the impacting projectile came from the southeast.

In Figure 10-4b the 95K contour interval extends southward to merge with the smaller anomaly. The 97.5K contour (dotted line) in Figure 10-4a traces out the same pattern. The striking similarity in cooling rate, and therefore physical properties, of the ejecta from the large crater and the small crater suggests that the two are contemporaneous. The photograph gives no hint of a relationship. In this example the thermal map contains geological relationships which are absent in conventional photography.

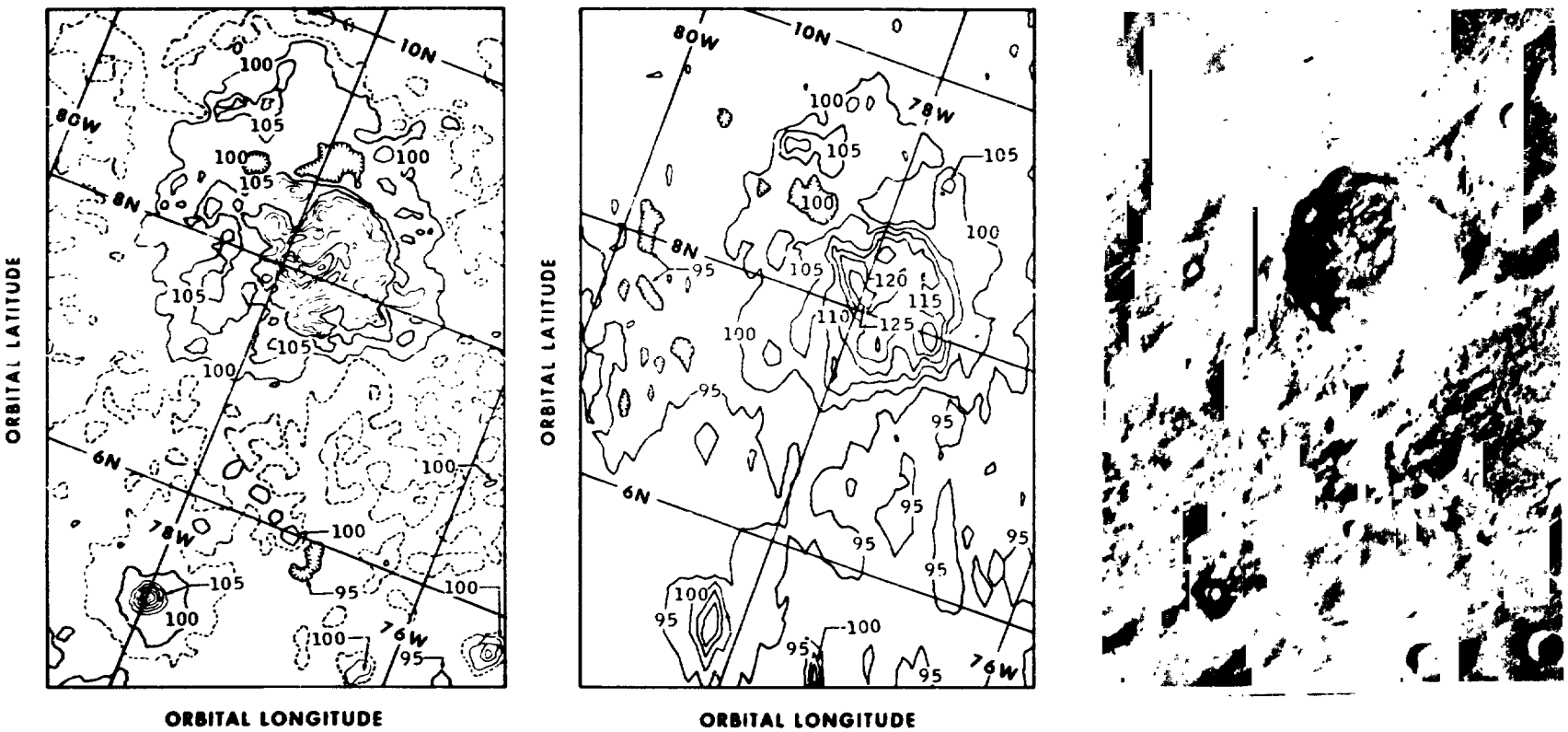

Figure 10-4 OLBERS A AND ENVIRONS. Two thermal maps of the crater Olbers A, taken 28 hours apart, are compared with a lunar orbiter photo of the same region. The thermal contour interval is 5 K. The dashed contour on the left represents an intermediate level, 92.5 K.

Figure 10-5 is a thermal map of the crater Aristarchus (313, + 24) at a phase angle of 263 deg. Aristarchus is another example of a fresh ray crater and is one of the brightest features on the near side of the Moon. Floor temperatures are the highest, as is the case with Olbers A. The hottest points appear to be associated with the central peak and with a rock slide inside the north rim.

Olbers A and Aristarchus invite comparison because they have the same diameter (40 km) and appear to be of similar age. Figures 10-4b and 10-5 both come from REV 71 when the two craters lay at comparable distances from the ground track. The displacement of 31 deg. in selenographic longitude implies that Aristarchus is 61 hrs further along the nighttime cooling curve. The difference in latitude (8 deg. vs. 24 deg.) lowers the effective thermal parameter γ at Aristarchus by approximately 3K cooler than at Olbers A. Ejecta blanket contours bear this out; but floor temperatures in Aristarchus are 1K to 2K hotter, indicating more exposed rock there. Either Aristarchus has less fill material on the floor (i.e., is younger), or the impact in the mare had better access to competent rock at the basalt-basement interface.

Ejecta blanket enhancements for the two craters are similar in spatial extent. The thermal pattern at Aristarchus is more nearly symmetrical. It is circumscribed by a thermally featureless region which may be slightly cooler than Oceanus Procellarum to the south. The featureless halo appears to be a characteristic of the large mare craters but not the anomalies in the farside highlands. Green (1969) comments on the low number density of thermal anomalies surrounding both Copernicus and Tycho.

Kepler (Fig. 10-6) is a ray crater rated at 6.5 on the morphologic scale (Pohn and Offield, 1970). The diameter is 31 km, and the phase angle

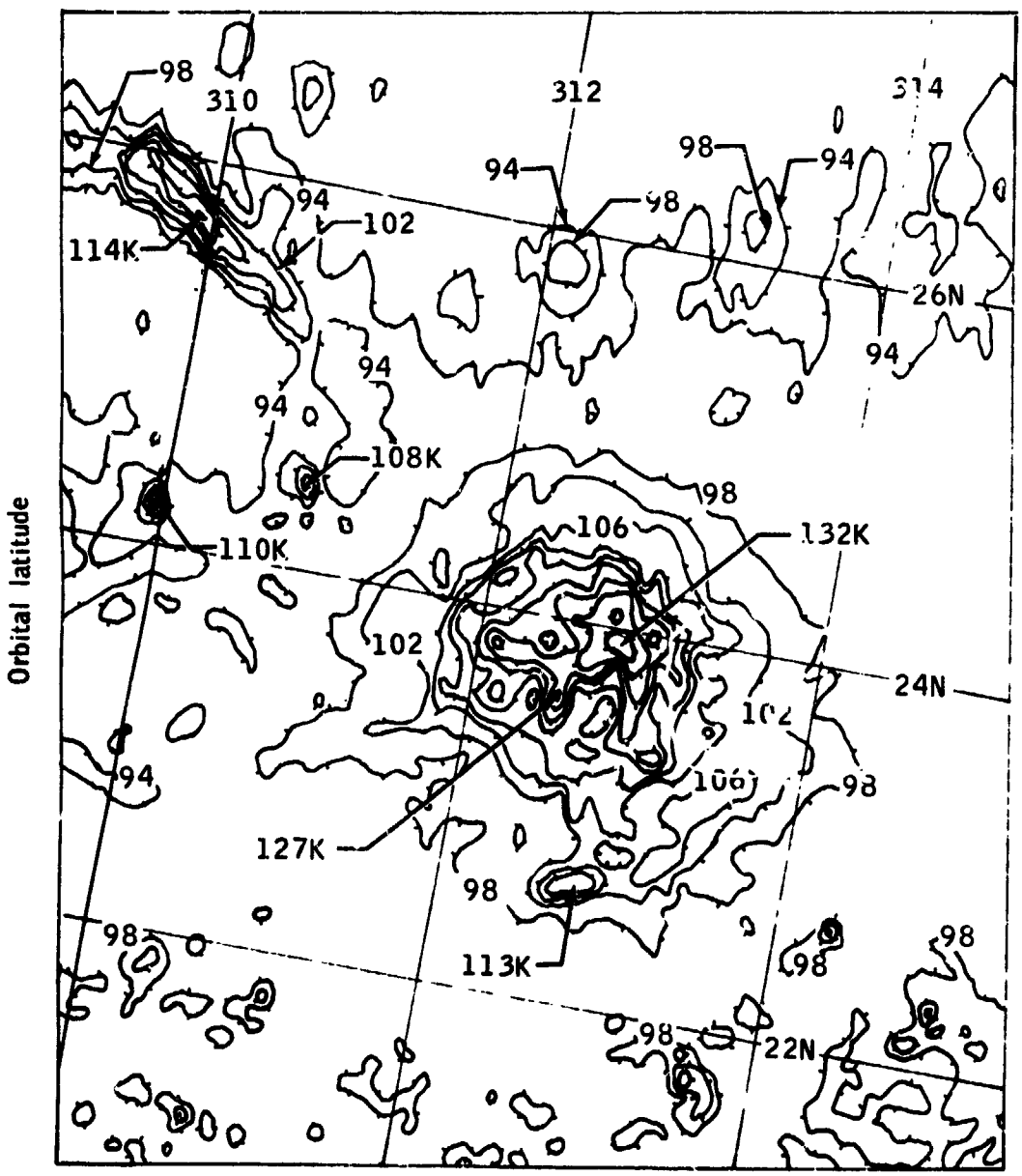

Figure 10-5 THERMAL MAP OF ARISTARCHUS. Thermal emission from Aristarchus was mapped 7 hours before sunrise at the crater. The contour interval is 4 K. The major enhancement lies on the floor of the crater.

at the crater is 222 deg. Olbers A in Fig. 10-4a can be directly compared with Kepler because the phase angles and latitudes are similar. Kepler has prominent hot spots on the north and south rims and on the central peak. All parts of the floor are warmer than the ejecta pattern, which is preferentially displaced to the North and the West. However, floor temperatures are at least 5K cooler than those in Olbers A. Part of the southwest rim has almost vanished thermally.

The thermal patterns in Kepler can be understood in terms of a simple crater degradation model. Eroded wall material has partly blanketed surface roughness on the floor, exposing blocks on the rim. The uneven patterns on the rim itself are less well understood although most degraded craters show nonuniform wall enhancement. Blockiness possibly indicates parts of the wall where shock lithification preferentially occurred due to directionality of the impact. Conversely, the cooler portions of the rim may be places where landslides have not yet occurred.

Figure 10-7 is a thermal map of the crater Copernicus (340, + 10) at a phase angle of 240 deg. The 95 km crater was located approximately 5 deg. south of the ground track, and the map suffers somewhat from foreshortening. Thermal enhancement is concentrated on the central peaks and the rim. Large areas on the crater floor exhibit temperatures in the range 95K to 98K, which are characteristic of the material in the ejecta blanket beyond the rim. Rim enhancement is quite asymmetric, and part of the eastern rim has disappeared thermally. The extent of the ejecta blanket enhancement in units of crater radii is not significantly different from that of Aristarchus or Olbers A. A featureless, cool halo circumscribes the ejecta pattern. The morphologic class for Copernicus is 6.2 (Head, 1975).

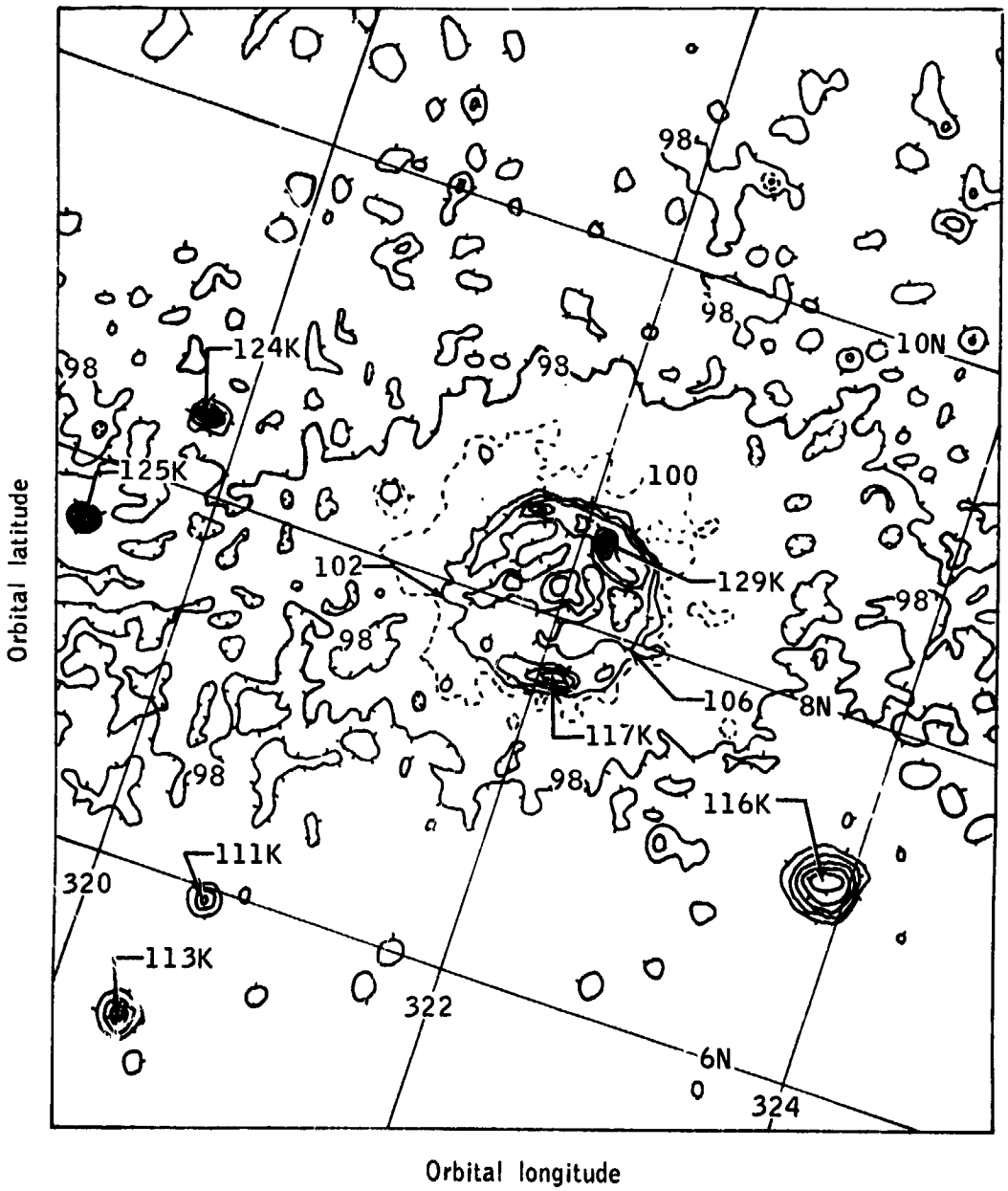

Figure 10-6 THERMAL MAP OF KEPLER. The crater Kepler was mapped 103 hours prior to sunrise at the crater. The contour interval is 4 K. The dashed contour is an intermediate level of 100 K showing asymmetrical enhancement of the outer rim deposits.

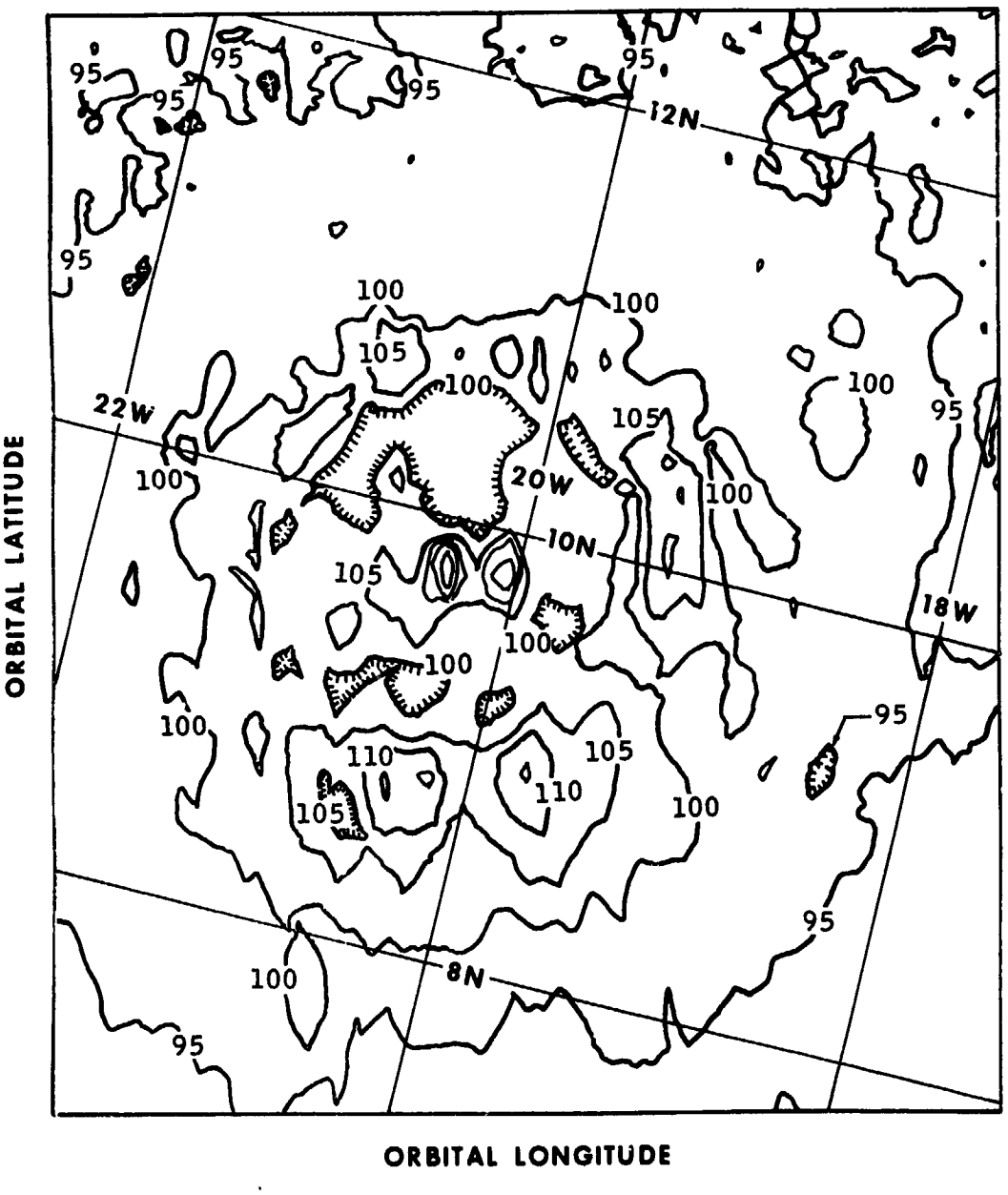

Figure 10-7 THERMAL MAP OF COPERNICUS. This data was taken 59 hours prior to local sunrise. The contour interval is 5 K. The floor of Copernicus exhibits large cool regions, and the east rim contour is broken.

Howard's Geologic Map of the Crater Copernicus (1975) provides a reference point for analysis of the thermal map. The pair of intense anomalies (120K - 125K) on the crater floor are both associated with the northern most of the two central uplifts. The southernmost peaks are much less enhanced (~109K) although their morphology, altitude, and extent are similar to the first set of peaks. A third major floor anomaly to the northwest of the peaks corresponds to a pair of blocky craters, each having a diameter of a kilometer or less.

Howard maps two major units over most of the crater floor. The predominant unit is hummocky floor material, which occupies all of the floor except for the northwest quadrant. Textured floor material, the second unit, fills the remaining quadrant, hugs the base of the rim in the northeast, and exists as small enclaves along the base of the southern rim. The textured floor material gives the appearance of having been molten and is interpreted by Howard as pooled impact melt. A minor unit called fill material is mapped on the northcentral floor within the textured floor material. The fill material is younger than the other units and can be interpreted as mass-wasted detritus or as volcanics.

Thermal contours on the floor of the crater correlate well with the geologic map units. The hummocky floor material exhibits temperatures in the range from 100K to 106K; the textured floor material, from 96K to 100K; and the fill material, below 96K. If this thermal definition is adopted, the extent of the textured floor material is somewhat greater than mapped by Howard. If the thermal boundary is moved from 100K to 99K, the unit becomes less prominent than on the geologic map. The thermal sensitivity of the boundary indicates the difference between the two units is highly gradational. The correspondence between the two types of maps

is remarkable despite the poor resolution (4 km) and large slant angle (∿50 deg) of the infrared data.

On the east rim the temperature drops below 100K at one point. Photometric data, attributed to Pohn and Wildey (1970) and displayed as an inset on Howard's map, shows a tongue of low albedo material extending from the crater floor up to the rim at the approximate location of the cool area. The combination of the thermal and photometric data strongly suggest some sort of blanketing effect associated with the textured floor material. The crater Copernicus A (3.5 km in diameter) lies on the east rim at the location of the cool material. That crater and its environs represent the lowest point on Copernicus' inner wall, lower than most of the textured floor material on the north-central floor of Copernicus. On high resolution orbital photography the rim crater lies in shadow, and the region is difficult to characterize.

In the simple degradation model for thermal signatures, Copernicus represents an intermediate case. Thermal enhancement has disappeared or been strongly degraded on the floor. The rim has several strong anomalies, yet one section appears to be highly degraded. Many smaller craters in Oceanus Procellarum have similar thermal patterns.

A final example of thermal signatures is the crater Eratosthenes (Figure 10-8), which has a diameter of 60 km and a morphologic grade of 5.7 (Offield and Pohm, 1970). The phase angle at the crater (349, + 14.5) is 259 deg in the figure. In the nomenclature used the U. S. Geological Survey for lunar mapping, the term "Eratosthenian" refers to materials postdating the basin fills but preceding the young ray craters designated as "Copernican" (Shoemaker and Hackman, 1962). On the thermal

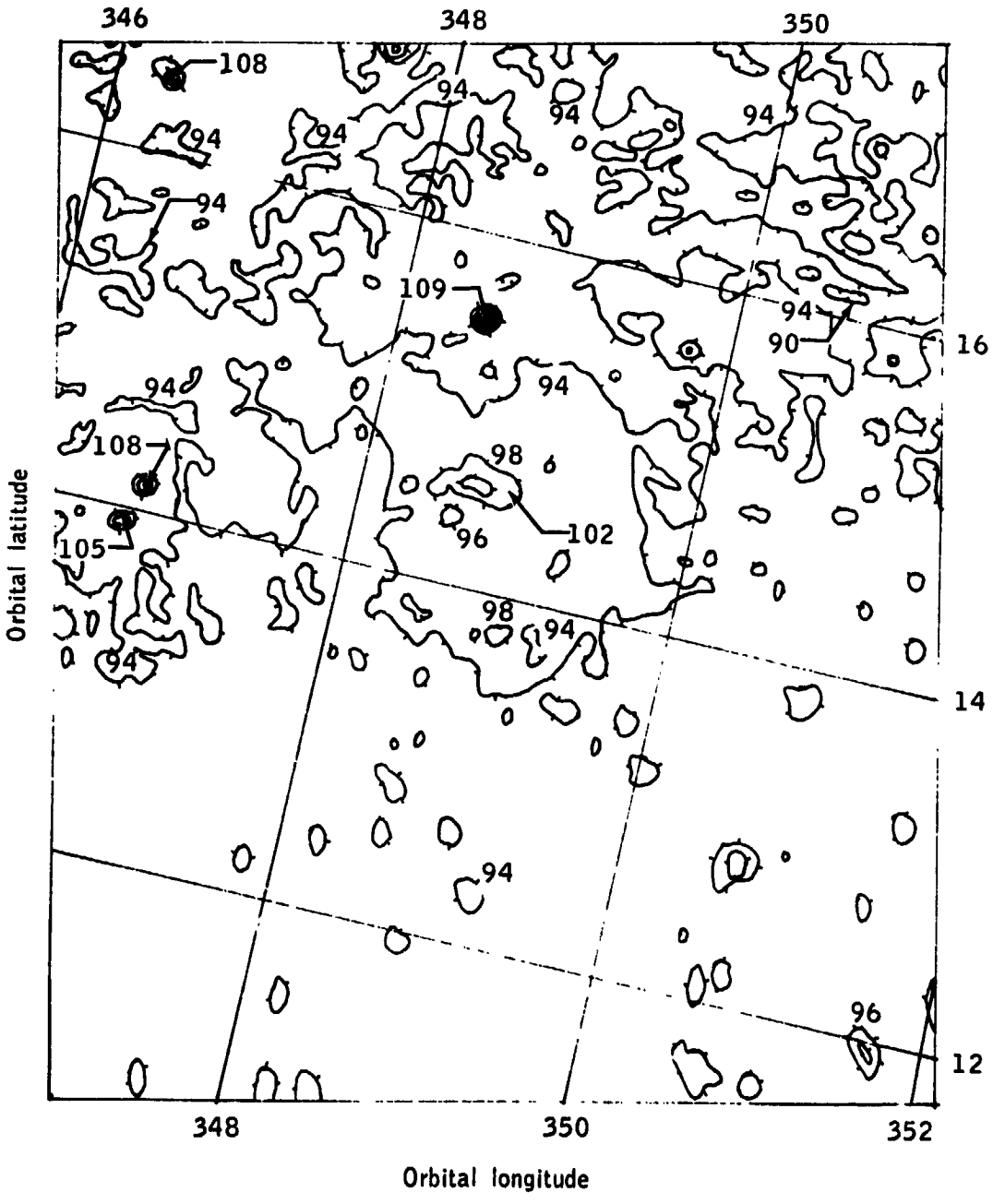

Figure 10-8 THERMAL MAP OF ERATOSTHENES. The thermal contour interval is 4 K. Thermal enhancement is minimal at Eratosthenes 50 hours prior to sunrise.

map a 94K contour traces out most of the outer rim of the crater. The west wall and a large part of the north wall are cooler than 94K. The small, intense anomaly just north of the crater corresponds to a prominence on the north rim. The major enhancement on the floor of the crater is associated with the complex of central peaks.

The thermal maps in Figures 10-4 through 10-8 demonstrate that the thermal signature of lunar craters evolve as a function of age of the crater. The freshest craters exhibit the highest temperatures on their floors. Temperatures decrease monotonically from the floor radially out across the wall, rim, and ejecta blanket. In the next stage hot spots develop on the wall and rim. Although floor temperatures remain elevated with respect to the ejecta blanket, they are less enhanced than in the freshest craters. In a third step the floor temperatures become comparable to the ejecta blanket enhancement. The principal hot spots are on the crater wall and the central peaks. Subsequently ejecta blanket enhancement disappears, and floor temperatures are similar to the environs. The final thermal signature is a low level enhancement associated with the rim and with the central peaks, if they exist. Craters older than Eratosthenian appear to be too degraded to be detectable thermally.

The general evolution of the thermal signature appears to be consistent with Head's (1975) ideas on the degradation of Period II craters. The crater wall is the principal source of fill material which gradually covers the crater floor, thereby eliminating the thermal enhancement. The removal of fine material from the walls exposes blocks, causing hot spots on the rim. Eventually the blocks on the walls are ruptured and comminuted, and the crater disappears from nighttime thermal maps.

The geologic mapping of Copernicus by Howard (1975) presents certain problems to this simple model of crater filling. Howard interprets the cool material on the floor of Copernicus as impact melt. If that interpretation is true, then the amount of melt in any given crater could significantly influence the rate of change in the thermal signature. Any interpretation of thermal maps would have to consider an additional parameter - the extent of melting in the impact - and adjust the "age" of the thermal signature accordingly.

Since Copernicus fits very neatly into a crater degradation scheme based on infill from the walls, the impact melt hypothesis warrants reexamination. In the first place, any flowing associated with molten material ceased very soon after the formation of the craters. Simonds (1975) argues that the melt is quenched in seconds by the inclusion of relatively cold material at the time of deposition. If a more conventional cooling history is assumed, the melt crystallizes in times ranging from a few days to a few years, depending on thickness (Provost and Bottinga, 1972). In any case, the distribution of melt represents an initial condition in the billion-year lifetime (Silver, 1971) of the crater.

Once its initial configuration had been established, Copernicus must have experienced erosion similar to that seen in other craters. In this context, the most reasonable interpretation of flow features on the walls is the movement of soil downslope rather than the drainage of impact melt. The material on the floor is then interpreted as crater fill rather than pooled melt.

The mechanism for the fill is the avalanche. Lunar avalanches can travel for kilometers, blanketing the preexisting relief more or less

evenly and thereby preserving it to a surprising extent (Howard, 1973). A series of such avalanches could produce flow-like morphology. Since the fill material would have a finer grain size than the preexisting floor soil, it would be much more susceptible to agglutination and, therefore, darkening (Adams and McCord, 1973). The cool appearance on nighttime thermal maps would be the natural consequence of the grain size distribution. Supporting evidence for this view can be found in the thermal map of Copernicus (Fig. 10-7) where there exists a good azimuthal correlation between hot spots on the rim and fill material in the lower elevations.

F. Cool Halo Craters

As mentioned earlier, eastern Oceanus Procellarum and southwestern Imbrium possess a superabundance of blocky craters on the scale of 0.1 to 10 km. The thermal map of that region (Fig. 10-3) presents a complex of interlaced contours. Amidst the jumble of contours, two relatively cool, relatively featureless regions stand out. One circumscribes the craters Bessarion A (320, + 17) and Bessarion B (322, + 17); the second is centered on the crater Marius A (314, + 13). Other examples exist but are less well defined (e.g., Herodotus A (308, + 21)). The phenomenon is not universal as evidenced by Brayley, Brayley B, Brayley C, and Bessarion D, where no cool halos exist.

The configuration appears to be an ejecta blanket associated with the central crater. However, impact ejecta is known to contain rubble and to have a significantly coarser grain size distribution than lunar soil. Consequently, ejecta blankets should be thermally enhanced rather than thermally depressed.

The cool halo phenomenon in Oceanus Procellarum can be understood in terms of the catastrophic rupture model for the erosion of lunar rocks (Hörz et al., 1975). The sandblasting effect of prolonged micrometeorite bombardment erodes lunar rocks less efficiently than fragmentation of the rock by the occasional impact having higher kinetic energy. In a Monte Carlo simulation of rock erosion, meter-sized rocks had a lunar surface lifetime 100 times longer than centimeter-sized rocks. The model predicts that a surface which initially has equal proportions of large and small rocks will evolve to a state in which a diminished population of large rocks remains but where small rocks essentially have disappeared.

This model suggests the following scenario for Oceanus Procellarum. In the late stages of the "Period I" bombardment numerous small craters (~0.1 km) containing blocky ejecta were formed in the relatively thin basalt flows. Relatively infrequent large impacts (e.g., Brayley - 15 km) either covered or destroyed the blocks with a rubble blanket of centimeter-scale material. Subsequently, the smaller impacts reestablished the population of blocky craters in the rubble blanket. As the bombardment rapidly subsided, the rubble blankets of late stage large craters (e.g., Marius A - 16 km) remained relatively undisturbed. In the relatively quiescent "Period II" environment the rubble blankets were comminuted into soil much more rapidly than the blocks in the small craters. Consequently, the late stage large craters now appear to be surrounded by a thermally featureless soil blanket - the cool halo.

If the above scenario is correct, then thermal maps contain another clue to relative ages among craters.

G. Cold Anomalies

Low (1965) detected lunar regions having nighttime temperatures $\lesssim$ 70K, implying an unusually high value for the thermal parameter, γ. The regions must have dimensions larger than 10 km to be detectable by Earth-based techniques. No such areas were measured by the ISR, but isolated "cold anomalies" were found. They are generally a few kilometers across and exhibit a temperature contrast $\gtrsim$ 5K relative to their environs.

Figure 10-9 depicts the cool halo region surrounding Bessarion A (to the right) and Bessarion B (to the left). Northwest of Bessarion B lies a positive thermal anomaly with a central temperature of 111K. Flanking the hot spot are two cool regions where the temperature falls to 89K. The hot anomaly is associated with a bright patch and/or the crater within it. The cool areas lie outside the bright patch. Nothing visually distinguishes the cool material from other dark mare nearby.

A second, isolated cool area (88K) lies north of a point midway between the two large craters at approximately (319, + 18). The associated photographic feature appears to be a small, indistinct, bright patch. In principle a high albedo soil should exhibit slightly lower nighttime temperatures compared to an otherwise identical dark soil. However, bright patches usually are found to be strong positive anomalies associated with boulder fields. The entire region in the figure is laced with high albedo rays from Aristarchus, Copernicus, and Kepler; but no thermal correlation with the albedo patterns can be seen.

This one figure illustrates the observation that cold anomalies occur in a variety of geological contexts and show no clear correlation with optical properties. Any explanation involving variations in albedo,

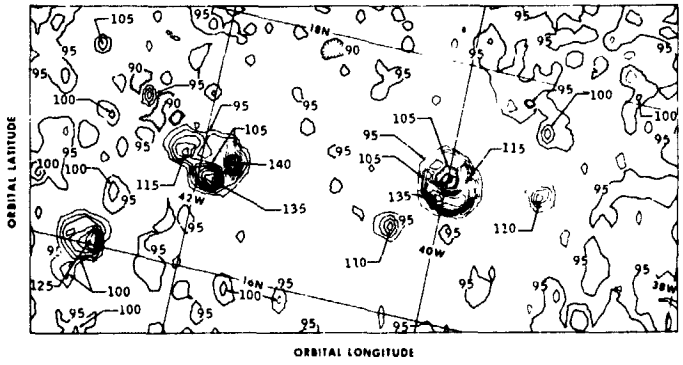

Figure 10-9 BESSARION A AND B AND ENVIRONS. Bessarion B is the coublet crater on the left, and Bessarion A is the companion crater on the right. The thermal data, contoured at 5 K intervals, was taken 26 hours before sunrise. Note cold regions flanking a small anomaly northwest of Bessarion B. Another isolated cold region lies north of the two craters.

infrared emissivity, or surface roughness cannot be general. Indeed, reasonable combinations of these properties can account for no more than half of the observed thermal contrast.

The cold anomaly must arise from real differences in the physical properties of the soil, most likely density and grain size. The particular anomalies in Figure 10-9 can be assigned a $\gamma \sim 1100$ within a soil having $\gamma \sim 850$ cal^{-1} cm^2 $sec^{1/2}K$. Clearly they do not represent extreme soil conditions. They are interesting because they are rare and isolated. Lunar soil evolution is understood in terms of ubiquitous processes. Any small, isolated irregularity must be associated with a local event. Additionally, the event must be geologically recent to have retained its signature in spite of the homogenizing lateral transport processes on the lunar surface.

Usually the adjectives "young" or "fresh" in the regolith context refer to impact structures. A kilometer-scale impact in a demonstrably thin regolith will leave a positive anomaly. The cold anomalies must represent other processes. One possibility is an underdense deposit of mass-wasted material in a topographic low. Alternatively, some type of eruptive event might spread fine-grained material over a large area.

If the features are eruptive, they establish the presence of endogenic activity after the filling of the mare basins. Their ages would set an upper limit of the efficiency of horizontal transport processes in the lunar regolith.

XI. Conclusions

The successful operation of the ISR on the Apollo 17 mission establishes the viability of spaceborne radiometry of low temperatures using an uncooled detector. The sensitivity exhibited by the ISR is sufficient to map the thermal emission of bodies in the solar system out to the orbit of Saturn. The thermal sensitivity can be increased by lowering the operating temperature of the detector and by modifications to the optical system. A new generation of pyroelectric detectors also promises substantial gains in performance of an uncooled system.

Geological applications of thermal maps, pioneered on the Moon, have immediate application to a mission to Mercury. The technique is applicable generally to airless bodies (asteroids or satellites) large enough to exhibit surface heterogeneity from surface processes. Scanning radiometry also can be useful for Mars, but the spectral response of the instrument must be tailored to atmospheric windows. Incorporation of a simple filter wheel adapts the ISR to atmospheric sounding of the Jovian planets.

Design and testing of the ISR could have been improved in several ways. For example, the imaging criterion of butted scan lines, common to infrared imaging systems, was chosen because it minimized the instantaneous field of view and minimized the spot size on the ground. However, in such a system the resolution perpendicular to the scan direction (one line pair) is only half that along the scan. A true mapping requires a 50% overlap between scans to insure uniform sampling in two dimensions. Imposition of a uniform sampling criterion upon the ISR would have required increasing the field of view and the scan rate due to performance limitations of the system.

The field of view should have been mapped during acceptance testing with an extended source as well as with a collimated source. The additional mapping would have detected the low level sensitivity to sources far from the optical axis. If the problem could not have been solved by modification of the optical design, then at least it could have been considered in the calibration procedure.

The ISR signal should have been recorded (preferably digitally) during key phases of the calibration. The recordings would have provided valuable information on signal drifts, scan to scan noise, calibration source stability, thermal gradients across the sources, and the field of view. The accuracy and the precision of calibration would have been enhanced significantly.

The zero-point calibration method discussed in Chapter VIII is much preferable to the relative calibration actually performed. It requires liquid helium cooling of at least one black body source, but that presents no particular technical problems.

In this document I have attempted to present in an orderly fashion the entire scope of a spaceflight experiment from conception to culmination. The sequence of development contains elements not ordinarily encountered in the laboratory environment. Certainly the concept of the experiment arises from a theoretical base and from the state of knowledge, but the design approach is heavily influenced by the management philosophy as well as the hardware constraints of the mission. Calibration and testing becomes an exercise in negotiation and compromise as well a an application of technology. Today's researcher in such fields as oceanography, high energy physics, and planetary science can find himself in a

complex venture confronted with problems of bureaucracy and group interaction as well as those of science. I hope this exposition conveys some flavor of the total experience and for that reason will be useful beyond its technical content.

Bibliography

Adams, John B. and McCord, Thomas B. (1973) Vitrification Darkening in the Lunar Highlands and Identification of Descartes Material at the Apollo 16 Site. Proc. Lunar Sci. Conf. 4th, 1, 163-177.

Adler, I.; Trombka, J. I.; Lowman, P.; Schmadebeck, R.; Blodget, H.; Eller, E.; Yin, L.; Lamothe, R.; Osswald, G.; Gerard, J.; Gorenstein, P.; Bjorkholm, P.; Gursky, H.; Harris, B.; Arnold, J.; Metzger, A.; and Reedy, R. (1973) Apollo 15 and 16 Results of the Integrated Geochemical Experiment. The Moon, 7, 487-504.

Allen, D. A. and Ney, E. P. (1969) Lunar Thermal Anomalies: Infrared Observations. Science, 164, 419-421.

Allen, David A. (1971) Infrared Studies of the Lunar Terrain, II: Thermal Anomalies. The Moon, 2, 435-462.

Aronson, James R.; McLinden, Hugh G.; and Gielisse, Peter J. (1964) Low-Temperature Far-Infrared Spectra of Germanium and Silicon. Phys. Rev., 135, A785-A788.

Bastin, J. A. (1965) Lunar Hot Spots. Nature, 207, 1381-1382.

Bastin, J. A. and Gough, D. O. (1969) Intermediate Scale Lunar Roughness. Icarus, 11, 289-319.

Birkebak, R. C.; Cremers, C. J.; and Dawson, J. P. (1970) Directional, Spectral, and Total Reflectance of Lunar Material. Proc. Apollo 11 Lunar Sci. Conf., 3, 1993-2000.

Birkebak, Richard C. (1972) Apollo 12 Thermal Radiation Properties. The Moon, 4, 128-133.

Birkebak, Richard C. and Abdulkadir, Ariono (1972) Total Emittance of Lunar Fines. JGR, 77, 1340-1341.

Birkebak, Richard C. and Dawson, James P. (1973) Thermal Radiation Properties of Apollo 14 Fines. The Moon, 6, 93-99.

Bracewell, Ron (1965) The Fourier Transform and its Applications. McGraw-Hill Book Co., New York.

Briggs, H. B. (1950) Infra-Red Absorption in Silicon. Phys. Rev., 77, 727-728.

Buettner, K. J. K. (1962) The Moon's First Decimeter. Memorandum RM-3263-JPL, The Rand Corp., Sept. 1962 (X63-12151).

Buhl, David; Welch, William J.; and Rea, Donald, G. (1968a) Reradiation and Thermal Emission from Illuminated Craters on the Lunar Surface. JGR, 73, 5281-5295.

Buhl, David; Welch, William J.; and Rea, Donald, G. (1968b) Anomalous Cooling of a Cratered Lunar Surface. JGR, 73, 7593-7608.

Carslaw, H. S. and Jaeger, J. C. (1959) Conduction of Heat in Solids, Oxford at the Clarendon Press, 510pp.

Cremers, Clifford J. (1974) Heat Transfer within the Lunar Surface Layer in Advances in Heat Transfer, Vol. 10, ed. James P. Hartnett and Thomas F. Irvine, Jr., Academic Press, New York.

De Hon, R. A. (1974) Thickness of Mare Material in the Tranquillitatis and Nectaris Basins. Proc. Lunar Sci. Conf. 5th, 1, 53-59.

De Hon, R. A. (1975) An Isopach Map of the Eastern Mare Basalts, Origins of Mare Basalts, p. 29-31, Lunar Science Institute, Houston, Texas

Eggleton, R. E.; Schaber, G. G.; and Pike, R. J. (1974) Photogeologic Detection of Surfaces Buried by Mare Basalts. Lunar Science V, p. 200-202, Lunar Science Institute, Houston, Texas.

Fudali, R. F. (1966) Implications of the Nonuniform Cooling Behavior of the Eclipsed Moon. Icarus, 5, 536-544.

Gear, A. E. and Bastin, J. A. (1962) A Corrugated Model for the Lunar Surface. Nature, 196, 1305.

Green, Richard R. (1969) An Analysis of the Distribution of the Major Surface Characteristics and the Thermal Anomalies Observed on the Eclipsed Moon. Boeing Sci. Res. Lab. Dcmt. D1-82-0775, January, 1969.

Head, James W. (1975) Processes of Lunar Crater Degradation: Changes in Style with Geologic Time. The Moon, 12, 299-329.

Heilman, M. and Nawyn, B. (1972) Final Report for the Infrared Scanning Radiometer (ISR). NASA Contract NAS9-10845, Barnes Engineering Co., Stamford, Connecticut.

Hopfield, J. J. (1967) Optical Properties and Infrared Emission of the Moon in Physics of the Moon, ed. S. Fred Singer, AAS Science and Technology Series, Vol. 13.

Hörz, F.; Schneider, E.; Gault, D. E.; Hartung, J. B. and Brownlee, D. E. (1975) Catastrophic Rupture of Lunar Rocks: A Monte Carlo Simulation. The Moon, 13, 235-258.

Howard, Keith A. (1973) Avalanche Mode of Motion: Implications from Lunar Examples. Science, 180, 1052-1055.

Howard, K. A. (1975) Geologic Map of the Crater Copernicus. Geol. Atlas of the Moon, Map I-840, U.S. Geol. Surv., Reston, Virginia.

Johnson, Francis S. (1965) Solar Radiation in Satellite Environment Handbook, ed. Francis S. Johnson, 2nd Edition, Stanford Univ. Press. Stanford, California.

Laue, E. G. and Drummond, A. J. (1968) Solar Constant: First Direct Measurements. Science, 161, 888-891.

Linsky, Jeffrey L. (1973) The Moon as a Proposed Radiometric Standard for Microwave and Infrared Observations of Extended Sources. Astrophys. J. Suppl. Ser., 25, 163-204.

Logan, Lloyd M.; Hunt, Graham R.; Balsamo, Salvatore, R.; and Salisbury, John W. (1972) Midinfrared Emission Spectra of Apollo 14 and 15 Soils and Remote Compositional Mapping of the Moon. Proc. Lunar Sci. Conf. 3rd, 3, 3069-3076.

Low, Frank J. (1965) Lunar Nighttime Temperatures Measured at 20 Microns. Astrophys. J., 142, 806-808.

Mendell, W. W. and Low, F. J. (1970) Low-Resolution Differential Drift Scans of the Moon at 22 Microns. JGR, 75, 3319-3324.

Mendell, Wendell W. (1971) Lunar Differential Flux Scans at 22 Microns. Master's Thesis, Rice University, Houston, Texas.

Mendell, W. W. and Low, F. J. (1972) Post-Sunset Cooling Behavior of the Lunar Surface. The Moon, 4, 18-27.

Murcray, Frank H. (1965) The Spectral Dependence of Lunar Emissivity. JGR, 70, 4959-4962.

Murray, Bruce C.and Wildey, Robert L. (1964) Surface Temperature Variations During the Lunar Nighttime. Astrophys. J., 139, 734-750.

Nicodemus, Fred E. and Zissis, George J. (1962) Methods of Radiometric Calibration, Report of BAMIRAC, Infrared Lab., Inst. of Sci. and Tech., Univ. of Michigan.

Offield, T. W. and Pohn, H. A. (1970) Lunar Crater Morphology and Relative-Age Determination of Lunar Geologic Units - Part 2. Applications. U.S. Geol. Survey Prof. Paper 700-C, p. C163-C169.

Pettit, Edison and Nicholson, Seth B. (1930) Lunar Radiation and Temperatures. Astrophys. J., 71, 102-135.

Plakun, B. D.; Falbel, G.; Schwarz, F.; and Spangenburg, P. (1969) Technical Proposal for Scanning IR Radiometer, BEC P-1414, Barnes Eng. Co., Defense and Space Contracts Div., Stamford, Connecticut.

Pohn, H. A. and Offield, T. W. (1970) Lunar Crater Morphology and Relative-Age Determination of Lunar Geologic Units - Part 1. Classification. U.S. Geol. Survey Prof. Paper 700C, p. C153-C162.

Pohn, H. A. and Wildey, R. L. (1970) A Photoelectric-Photographic Study of the Normal Albedo of the Moon. U.S. Geol. Survey Prof. Paper 599E, 20pp.

Provost, A. and Bottinga, Y. (1972) Rates of Solidification of Apollo 11 Basalt and Hawaiian Tholeiite. Earth and Plan. Sci. Lett. 15, 325-337.

Randall, C. M. and Rawcliffe, R. D. (1967) Refractive Indices of Germanium, Silicon, and Fused Quartz in the Far Infrared. Appl. Optics, 6, 1889-1895.

Roelof, Edmond C. (1968) Thermal Behavior of Rocks on the Lunar Surface. Icarus, 8, 138-159.

Saari, J. M. and Shorthill, R. W. (1963) Isotherms of Crater Regions on the Illuminated and Eclipsed Moon. Icarus, 2, 115-136.

Saari, J. M. (1964) The Surface Temperature of the Antisolar Point of the Moon. Icarus, 3, 161-163.

Saari, J. M. and Shorthill, R. W. (1967) Isothermal and Isophotic Atlas of the Moon, NASA CR-855, 186pp.

Salisbury, John W.; Vincent, Robert K.; Logan, Lloyd M.; and Hunt, Graham R. (1970) Infrared Emissivity of Lunar Surface Features, 2. Interpretation. JGR, 75, 2671-2682.

Salisbury, John W.; Hunt, Graham R.; and Logan, Lloyd M. (1973) Infrared Spectra of Apollo 16 Fines. Proc. Lunar Sci. Conf. 4th, 3, 3191-3196.

Shoemaker, E. M. and Hackman, R. J. (1962) Stratigraphic Basis for a Lunar Time Scale in The Moon, ed. Z. Kopal and Z. K. Mikhailov, Academic Press, New York and London.

Shorthill, R. W.; Borough, H. C.; and Conley, J. M. (1960) Enhanced Lunar Thermal Radiation During a Lunar Eclipse. Publ. Astron. Soc. Pacific, 72, 481-485.

Shorthill, Richard W. and Saari, John M. (1965) Radiometric and Photometric Mapping of the Moon through a Lunation. Ann. N.Y. Acad. Sci., 132, 722-739.

Shorthill, R. W. and Saari, J. M. (1969) Infrared Observations on the Eclipsed Moon. Boeing Sci. Res. Lab. Dcmt. D1-82-0778.

Silver, Leon T. (1971) U-Th-Pb Isotope Systems in Apollo 11 and 12 Regolithic Materials and a Possible Age for the Copernicus Impact Event. Trans. AGU, 52, 534.

Simonds, Charles H. (1975) Thermal Regimes in Impact Melts and the Petrology of the Apollo 17 Station 6 Boulder. Proc. Lunar Sci. Conf. 6th, 1, 641-672.

Sinton, William M. (1962a) Eclipse Temperatures of the Lunar Crater Tycho in The Moon, ed. Z. Kopal and Z. K. Mikhailov, Academic Press, New York and London, p. 469.

Sinton, William M. (1962b) Temperatures on the Lunar Surface in Physics and Astronomy of the Moon, ed. Zdenek Kopal, 1st Edition, Academic Press, New York and London.

Six, N. F.; Montgomery, C. G.; Saari, J. M.; and Shorthill, R. W. (1967) Directional Characteristics of Lunar Thermal Emission in Thermophysics of Spacecraft and Planetary Bodies, ed. Gerhard B. Heller, Academic Press, New York.

Smith, R. A.; Jones, F. E.; and Chasmar, R. P. (1968) The Detection and Measurement of Infra-red Radiation. Oxford at the Clarendon Press, 2nd edition.

Staley, D. O. (1968) Radiative Enhancement of Lunar Hot Spots during Eclipse. JGR, 73, 2049-2055.

Toksoz, M. N. and Solomon, S. C. (1973) Thermal History and Evolution of the Moon. The Moon, 7, 251-278.

Van Tassel, Roger A. and Simon, Ivan (1964) Thermal Emission Characteristics of Mineral Dusts in The Lunar Surface Layer, ed. John W. Salisbury and Peter E. Glaser, Academic Press, New York and London, p. 445.

Wesselink, A. F. (1948) Heat Conductivity and Nature of the Lunar Surface Material. Bull. Astron. Inst. of the Netherlands, X, 351-363.

Wildey, Robert L.; Murray, Bruce, C.; and Westphal, James A. (1967) Reconnaissance of Infrared Emission from the Lunar Nighttime Surface, JGR, 72, 3743-3749.

Wilson, James H. (1971) Two Over Mars. NASA EP-90.

Winter, D. F. and Saari, J. M. (1968) A Particulate Thermophysical Model of the Lunar Soil. Boeing Sci. Res. Lab. Dcmt. D1-82-0725, 50pp.

Winter, Donald F. (1970) The Infrared Moon: Data, Interpretations, and Implications. Radio Science, 5, 229-240.

Yoshinaga, Hiroshi (1955) Reflectivity of Several Crystals in the Far Infrared Region between 20 and 200 Microns. Phys. Rev., 100, 753-754.

Young, Richard A.; Brennan, William J.; and Nichols, Douglas J. (1974) Problems in the Interpretation of Lunar Mare Stratigraphy and Relative Ages Indicated by Ejecta from Small Impact Craters. Proc. Lunar Sci. Conf. 5th, 1, 159-170.

APPENDIX A:*

A MISSION STRATEGY FOR THE ISR BASED ON POTENTIAL ERRORS IN THE SPACE LOOK

Abstract

An error analysis is performed to arrive at an estimate for the probability of a lunar limb encounter during operation of the integrating clamp on the Infrared Scanning Radiometer. The calculated probability is 1.1×10^{-5} at 110 km and 6.6×10^{-4} at 102 km. The probability of degraded data is low and therfore no change in the scientific deadband requirements is anticipated at this time.

Introduction

The Infrared Scanning Radiometer (ISR) is an Apollo 17 orbital experiment (S-171) designed to map the thermal emission of the Moon. The radiometer is mounted in the Scientific Instrument Module (SIM) such that lunar thermal radiation can enter an aperture in the instrument housing while the spacecraft orbits the Moon. A rotating scanning mirror in the housing reflects thermal radiation into the collecting optics, which in turn direct the radiation onto a detector at the Cassegrain focus. A schematic of the optical system has been shown in Figure 4-1.

During a complete rotation of the scanning mirror, the detector will view successively (1) a portion of deep space between the wall of the SIM

*This appendix originally was a working paper written during the ISR program. It has been edited for compatibility with the main body of text.

and the leading lunar horizon, (2) the Moon, (3) a second portion of deep space between the trailing lunar horizon and the wall of the SIM, and (4) the interior of the instrument housing. For the next rotation this sequence is repeated. The spacecraft is not a stationary platform relative to the Moon, and in particular it will exhibit oscillations about the roll axis. The roll motion causes the two portions of space on either side of the Moon to subtend varying angles at the center of mirror rotation. This effect is illustrated in Figure A-1.

The duration of the leading space look is critical to the operation of the radiometer. During this space look the electronics perform a sample and hold operation which establish an absolute reference level for the succeeding scan across the Moon. The validity of the technique is predicated on the assumption that the signal from deep space during the space look is a true zero. The sample and hold sequence has a fixed duration; thus the space look must be at least as long as this period of time. If the space look is too short, some energy from the leading lunar limb will fall on the detector during the clamp period. This condition will lead to a false zero and incorrect temperatures for the scan in the reduced data.

Since a lunar limb encounter during the space look is important to the experiment, the probability of such an occurrence has been analyzed in some detail. It has been found that while the probability is low, the validity of the analysis is entirely at the mercy of estimates of errors in the various parameters. In spite of possible unknowns in the error estimates, the scientific requirements regarding the required deadband have not been restated.

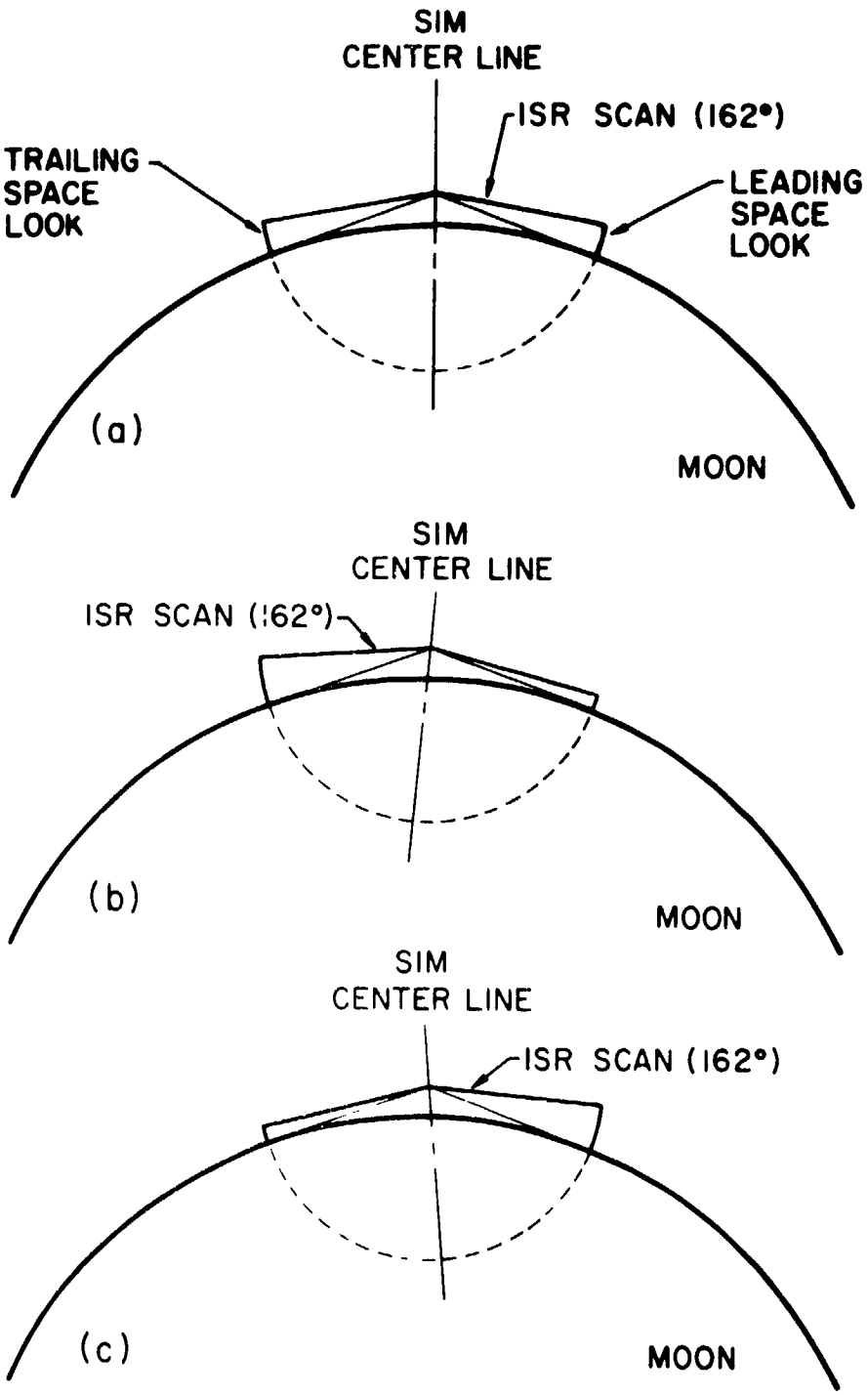

Figure A-1 EFFECT OF SPACECRAFT ROLL ON SPACE LOOK. (a) Nominal SIM Bay attitude, having the SIM Bay centerline directed along local vertical, (b) and (c) opposite extremes of ±5° about vertical.

Geometry

Figure A-2 shows the mounting of the ISR in the SIM Bay. The radiometer has been placed at the outer edge of the shelf at the center of the bay to take advantage of a maximum field of view outside the spacecraft. The centerline of the ISR has been canted 2°.67 from the centerline of the bay to maximize the duration of the space look prior to encounter of the leading lunar limb. If the instrument were canted any further, there would be a danger of receiving radiant energy from the SIM wall at the beginning of the space look.

Whereas the arrangement of the radiometer in the SIM constrains the beginning of the space look, the Moon itself constrains the end of the clamp period. Figure A-3 illustrates this. The angle λ is the minimum angle allowed between the local nadir and the lunar horizon. This angle is a function of the altitude of the spacecraft. The relationship between the two is

$$\sin \lambda = \frac{R}{R+H} , \qquad (A.1)$$

where R is the radius of the Moon (1738 km) and H is the altitude of the spacecraft. At the nominal altitude of 111 km (60 naut. miles), $\lambda = 70°.0$. It should be pointed out here that small changes in λ correspond to quite significant changes in H, approximately 11 km per degree. Since the anticipated deviation of the orbit from circularity during a mission is on the order of 9 km, a change of 1° in the angle subtended by the Moon can mean a great deal in terms of the allowable deadband during operation of the ISR.

The problem to be analyzed arises from the combination of the constraints depicted in Figures A-2 and A-3. The pertine relationships

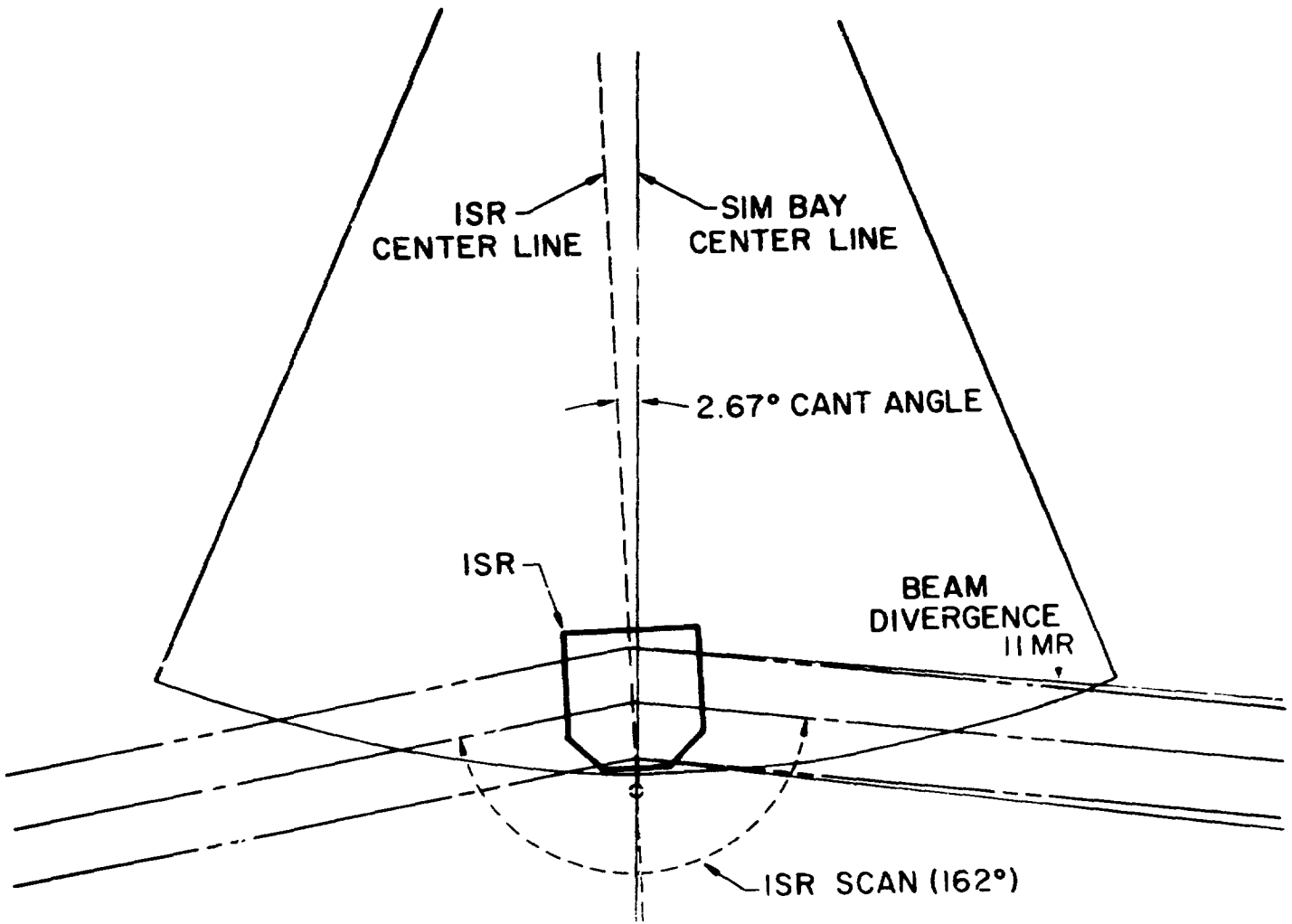

Figure A-2 SIM BAY MOUNTING GEOMETRY FOR THE ISR.

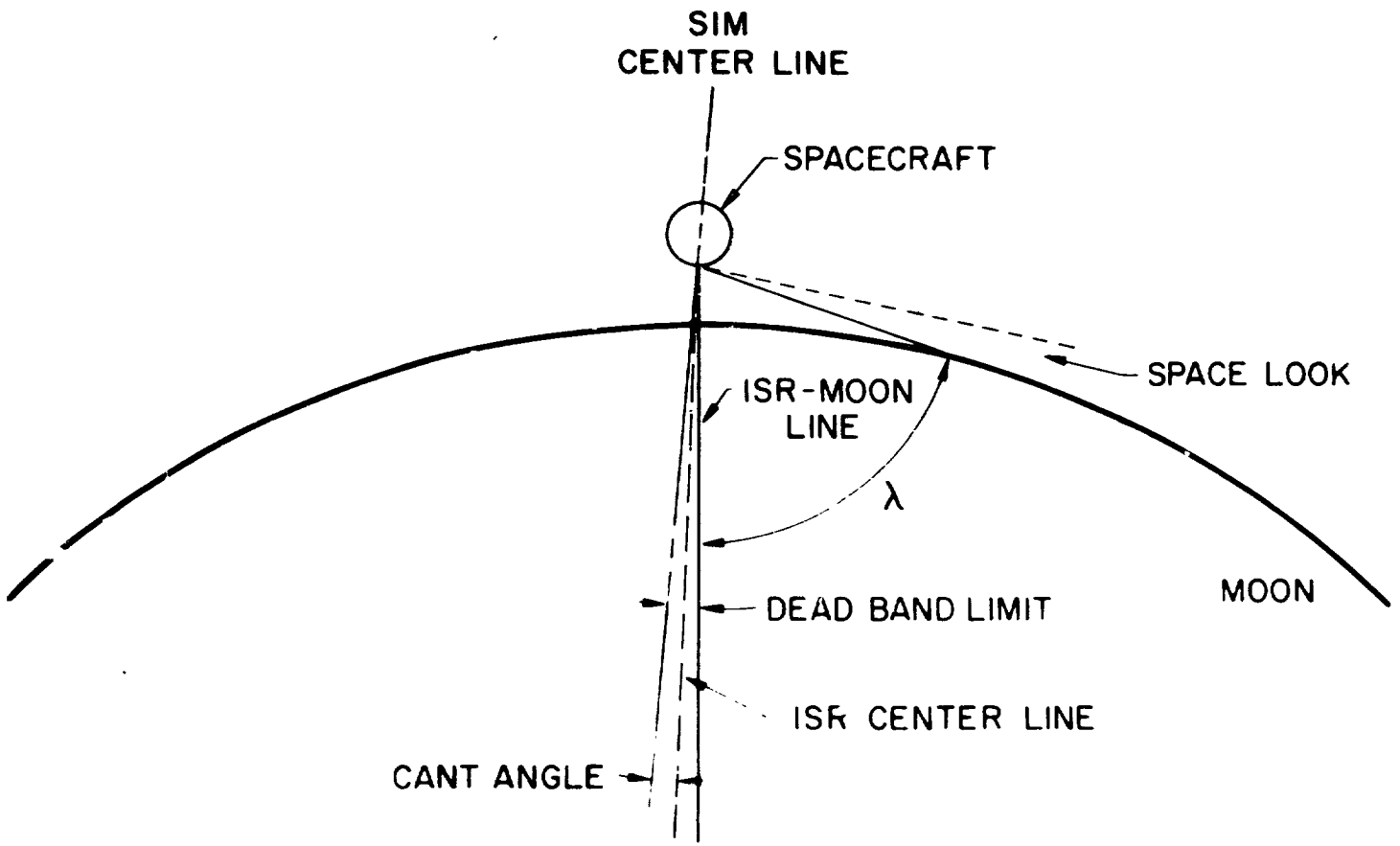

Figure A-3 GEOMETRY FOR SPACE LOOK EVALUATION. The calculation of the angular extent of the space look depends on the altitude of the spacecraft (through the angle λ) and variations in spacecraft attitude from the nominal.

have been drawn and labeled. The formula for calculating λ is given by

$$\lambda = s + t - d - c, \qquad (A.2)$$

where s is the angle between the start and the midpoint of the ISR scan, t is the angle of tilt between the SIM centerline and the ISR centerline, d is the maximum deadband of the spacecraft, and c is the angle corresponding to the clamp period. All of the error analysis is based on the simple additive relationship expressed in equation (A.2).

Before proceeding into this analysis, however, there is one more geometrical point which should be made clear. In all the figures, the beam of energy between the radiometer and a target is drawn as a single line, the implication being that this beam can be treated as an infinitesimally thin light ray. Actually the beam is 17.8 cm wide at the radiometer aperture and has a divergence of 20 milliradians at the 50% power points (22 milliradians between the 10% power point Thus a line drawn on the figure represents the center of the field of view, and energy can enter the radiometer from portions of the target on either side of this line.

The beam divergence enters the analysis only at the start and end of the space look. It has already been taken into account with respect to the beginning of the clamp period through the mounting geometry in the SIM (see Figure A-2). The radiometer has been carefully placed so that the diverging beam does not intersect the SIM wall while the space clamp is activated. If the clamp is activated for 24 milliseconds, the beam moves 6 degrees due to the rotation of the scan mirror. At the end of the period the leading half of the diverging beam can receive some energy from a target lying beyond the nominal 6 degree sector of space. This

energy would become part of the "zero" established by the space look. It is clear that the value assigned to c in equation (A.2) should include the 11 milliradians (0.63 degrees) of beam divergence out to the 10% power point. Although it is true that some energy can be collected beyond the 10% power point, it shall be neglected in this analysis.

Error Analysis

First, we will consider nominal values for the components of equation (A.2) and calculate λ.

$$\lambda = 80.75 + 2.67 - 5.00 - 6.63 = 71.79 \text{ degrees} \qquad \text{(A.3)}$$

or

$$H = R(\csc \lambda - 1) = 91.7 \text{ km}$$

For nominal values of the relevant parameters, there is no problem because the 111 km circular orbit should not decay beyond approximately 102 km perilune.

Unfortunately each one of the angles in equation (A.2) has errors associated with it. For a conservative analysis we must consider the worst case value for each component of the overall error. All errors are assumed to be 3σ values unless otherwise discussed. Error due to relief on the lunar limb is negligible.

A. Error in the angle "s"

Since the installation of the radiometer is referenced to its mounting plane, the important error in s arises from the establishment of the beginning of the scan relative to the ISR centerline, which is perpendicular to the mounting plane. The beginning of the scan (which coincides with the beginning of the space look) is determined by a light-

emitting diode placed in the ISR housing. This diode is installed in the ISR at the Barnes Engineering Company (BEC), and it can be installed to within ±0.25 degrees from a given location. There is a requirement from North American Rockwell (NR) that s be no larger than 81.00 degrees. Therefore the diode will be installed so that s = 80.75 ±0.25 degrees. Presumably BEC has the capability to measure s to an accuracy much greater than the error in the installation. Therefore it is probable that the actual value of s will be well-known prior to SIM installation, but for this analysis the error of 0.25 degrees is appropriate.

B. Error in the angle "c"

Uncertainties in the duration of the space look arise from drifts in the analog timing circuits which control the switching of the clamp. BEC gives 0.5 milliseconds as an rms value for this drift. The 3σ value would correspond to ±0.38 degrees.

C. Error in the angle "i"

The error in the cant angle of the radiometer should be entirely contained in mounting inaccuracies. Since the instrument is mounted directly astride the bisecting plane of the SIM Bay, there should be no degradation in pointing about the roll plane due to structural deformation of the SIM in flight. The mounting accuracies take two forms - those due to SIM structural tolerances, and those due to instrument mounting tolerances.

There exists a prime reference in the SIM which represents a typical pointing line of SIM-mounted instruments. According to the spacecraft contractor, all drawing and manufacturing tolerances will maintain instrument mounting holes to ±0.50 degrees of the prime reference.

For the instrument mounting tolerance NR assumes a worst case condition of 0.78 mm clearance between bolt and hole and a hole spacing of 254 mm. The ISR mounting holes are spaced 193.7 mm. The mounting holes are 9.53 mm in diameter with a tolerance of 0.05 mm. It is probably more realistic to assume a worst-case clearance between the bolt and the hole which is five times this tolerance, or 0.25 mm. Using these revised numbers, the mounting inaccuracy is ± 0.08 degrees.

D. Error in the angle "d"

This angle is the most complex to analyze because it involves the interaction between the Guidance and Navigation Control System (GNCS) and the SIM structure. Many factors must be considered. To simplify the analysis, we can ask two questions and discuss them separately:

1. How well known is the position of the SIM prime reference relative to the GNCS?

Both prelaunch and postlaunch considerations are involved here. In flight the GNCS guides the spacecraft assuming the SIM prime reference is located at a position obtained by analysis. The errors involved in the analysis (see below) are structural in nature and quite significant. Oddly enough, a measurement of the position of the SIM prime reference relative to the GNCS is made on the pad; but this information is not utilized by the guidance system during the mission. The measurement removes the errors in the positional analysis but can be used in postflight reconstruction only.

The analysis of the location of the SIM optical reference to the navigation base can be divided into four sections:

(1) the location of the SIM reference point relative to the SIM-Service Module (SM) interface;

(2) misalignment across that interface;

(3) misalignment across the SM-Command Module (CM) interface; and

(4) location of the CM body axes relative to the navigation base.

Location of mounting holes in the SIM relative to the reference point has already been established at ±0.50 degrees, and this value will be assigned to (1). The relationship between the navigation base and the CM body axes is established during manufacture; the error in (4) is negligible.

An error of ±0.23 degrees has been estimated to occur during installation of the SIM into the SM. This number is based on racking the SIM 6.4 mm across its 1.5 m width to obtain hole alignment. This misalignment error will tend to compensate for the manufacturing error (1), but the two sources will be treated as independent to be conservative.

The mating error between the CM a he SM is unknown but can be estimated in a manner similar to previous mounting error estimates. Assuming hole misalignments and bolt-hole mismatches amounting to ±6.4 mm across a 3.66 m diameter, we can estimate an error of ±0.20 degrees.

During and after launch certain structural deformations can occur in the spacecraft due to the boost environment, the change in gravitational field, and firings of the Service Propulsion System (SPS). The accumulated error from these sources is estimated to be ±1.00 degrees. In addition, thermally induced variations caused by changes in the spacecraft's orientation to the Sun can amount to ±0.33 degrees.

2. How accurately can the GNCS locate the center of the Moon (local nadir)?

Conversations with MSC personnel from the Guidance and Control Division have led to identification of the errors inherent in the GNCS. The Inertial Measurement Unit (IMU) can be aligned very accurately, but experience has shown that the unit drifts ±0.015 degrees per hour. The total error associated with IMU drift is ±0.10 degrees, based on six hours between realignments. The onboard computer simplifies the calculation of the local vertical from IMU information, and the worst case error amounts to ±0.7 degrees. The 5 degree deadband relative to the computed local vertical is reproduced with negligible error.

Discussion

An error analysis has been performed on the real time pointing accuracy of the ISR in the scan plane. For the purpose of the analysis, the scan plane has been assumed perpendicular to the roll axis of the spacecraft. An attempt has been made to assign a 3σ value to each of the components of the total error. Figure A-4 summarizes the analysis diagrammatically.

The root sum square of the component errors gives a total error of

$$3\sigma_{tot} = 1.554 \text{ degrees.} \qquad (A.4)$$

If the GNCS were programmed to orient the spacecraft according to the location of the SIM optical reference as measured on the launch pad, the various assembly errors between the GNCS and the SIM would be eliminated. The 3σ total error would fall to 1.440 degrees.

Equation (A.2) and Figure A-3 describe the marginal situation in which the end of the space look butts up against the leading lunar limb at extreme deadband. For this condition to occur under nominal values

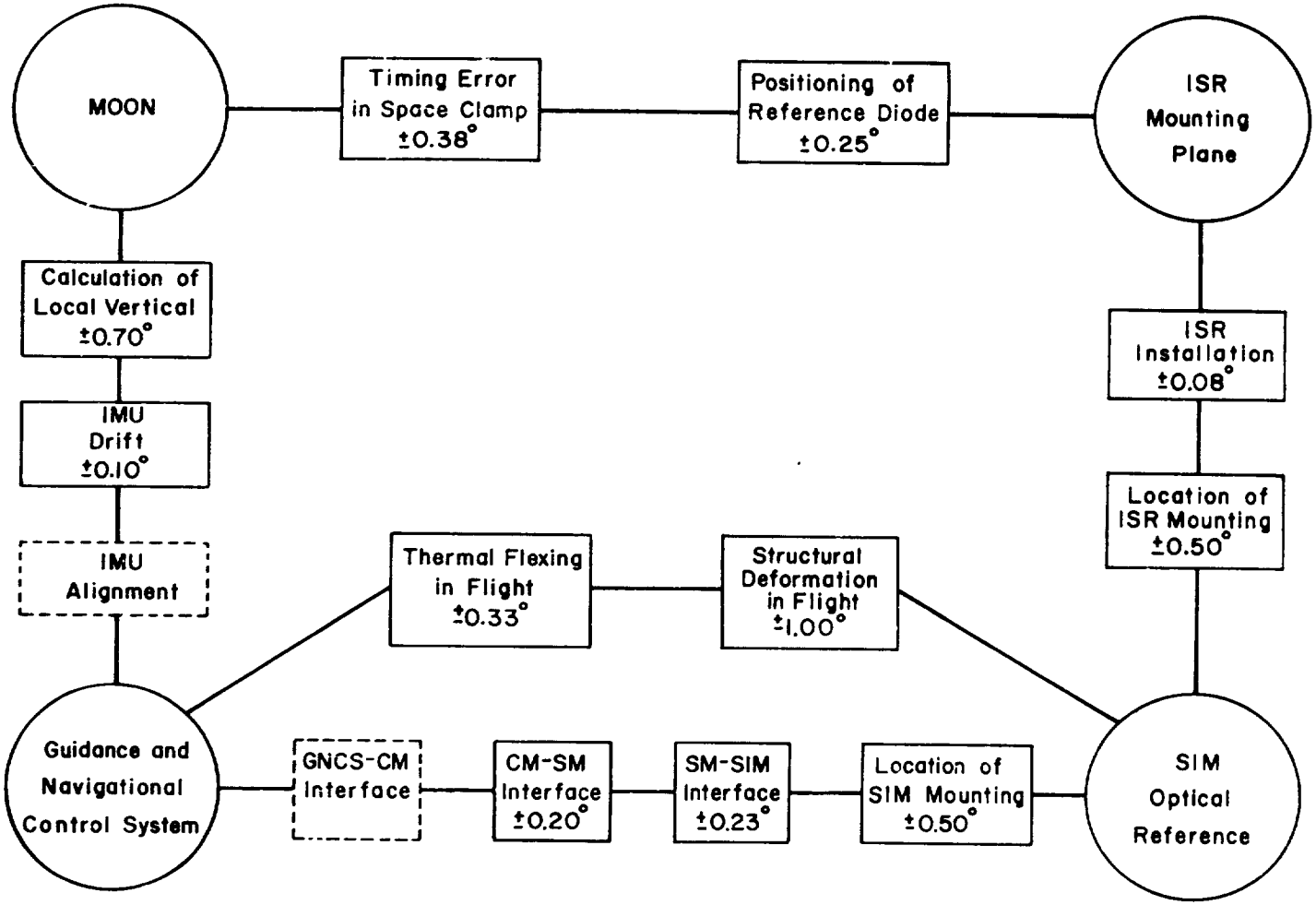

Figure A-4 ERROR FLOW DIAGRAM. The diagram shows the relationship of the various components of the ISR pointing error. Dashed boxes are error sources which could be eliminated by modification of procedures.

for all parameters, the angle d must equal +5.00 degrees and the spacecraft altitude must be 91.7 km. In general the altitude and angular orientation of the spacecraft will have different values. For example, the deadband angle oscillates between -5 and +5 degrees about the vertical. To describe the more general situation, we rewrite equation (A.3) for nominal conditions,

$$\lambda = 76.79 - d - \alpha', \tag{A.5}$$

where d can assume any value from -5 to +5 and α' is the spacing between the end of the space look and the leading lunar limb. The angle λ is a function of the altitude of the spacecraft given by equation (A.1).

The presence of errors cause the actual value of the spacing to be larger or smaller than the nominal value. We can write

$$\alpha' = \alpha - \varepsilon, \tag{A.6}$$

where α is the actual value of the spacing and ε is the actual value of the accumulated errors. The critical parameter is α; if α is negative, the lunar limb is encountered during a scan. Since the scan rates are much greater than the angular drift rates of the spacecraft, we can also say that the limb is encountered during the space look. A rearrangement of equations (A.5) and (A.6) gives

$$\alpha = 76.79 - \lambda - d + \varepsilon \tag{A.7}$$

The purpose of this paper can now be stated as finding the probability that $\alpha<0$. It is clear from (A.7) that this probability is a function of altitude through λ. Assuming that the accumulated pointing error is independent of the angular orientation of the spacecraft, we can conclude from (A.7) that

$$\text{Prob}(\alpha<0) = \text{Prob}\ (\varepsilon-d<\lambda-76.79)$$

$$= \int_{-5}^{5} \text{Prob}(d=x) \cdot \text{Prob}(\varepsilon<\lambda+x-76.69)dx \qquad (A.8)$$

We assume at any time that the spacecraft will be at any position in the 10 degrees of deadband with equal probability. We can write

$$\text{Prob}(d=x)dx = \frac{1}{10}\,dx \qquad (A.9)$$

Throughout the analysis we have implicitly assumed that the error ε is normally distributed. Thus

$$\text{Prob}(\varepsilon<y) = \frac{1}{\sigma\sqrt{2\pi}} \int_{-\infty}^{y} \exp\left[\frac{-w^2}{2\sigma_{tot}^2}\right] dw \qquad (A.10)$$

Substituting (A.9) and (A.10) into (A.8), we get the curve shown in Figure A-5. The numbers become more meaningful when translated into the expected time of operation between degraded scans. We souls anticipate a single degraded scan during 37 minutes of operation at 102 km, during 2.8 days of operation at 111 km, and during 6.8 years of operation at 120 km. If the prelaunch structural measurements are used by the GNCS, the times become 1.1 hours, 13.5 days, and 66.5 years, respectively.

It is apparent from these results that only a few degraded scans can be expected during a mission. The experiment should perform successfully in a 5° deadband. During periods when the orbit is unusually elliptical, the 0.5° deadband would be preferred. However, at this time we feel that it is not necessary to alter the scientific requirements of the experiment.

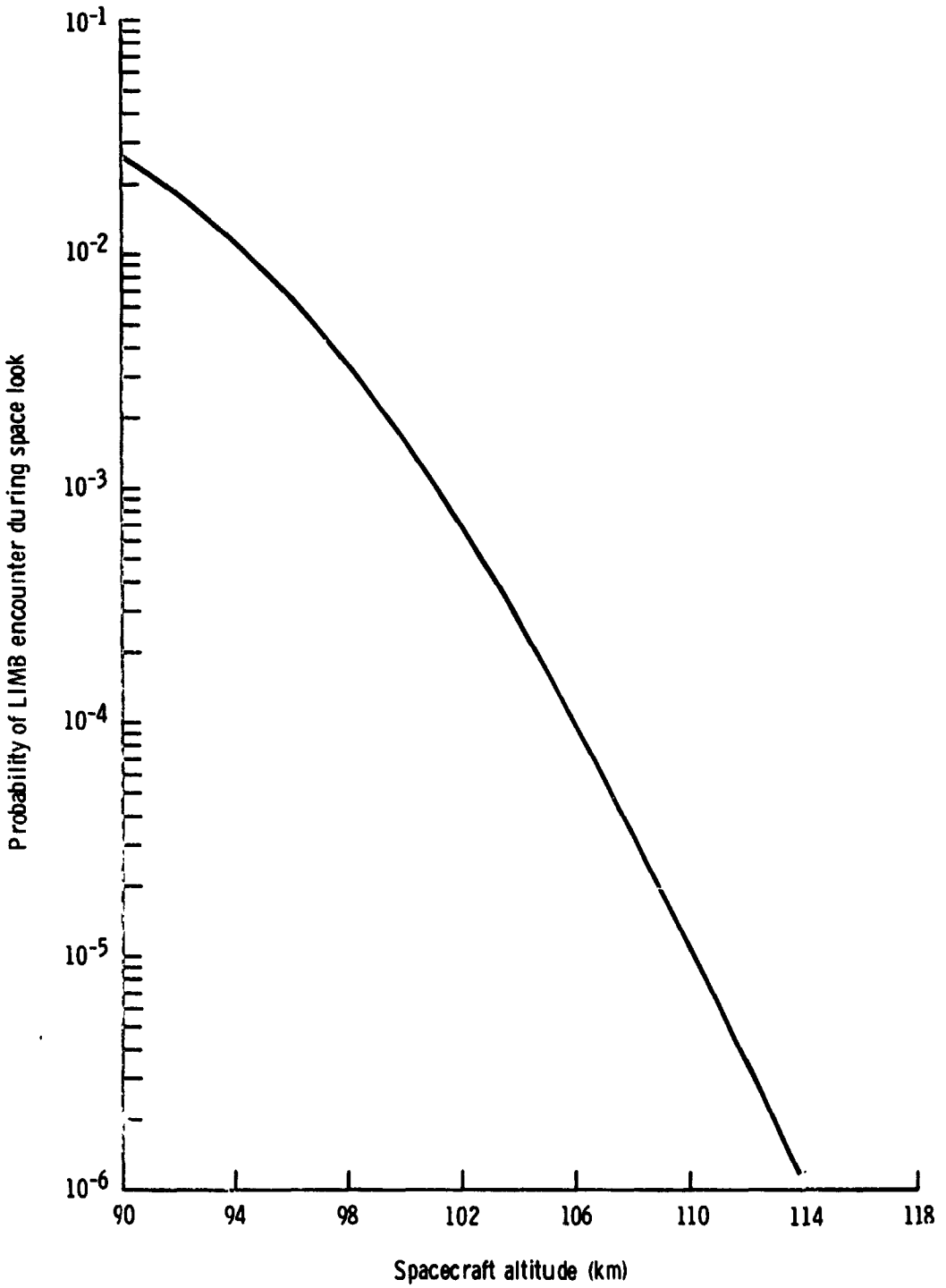

Figure A-5 PROBABILITY OF A DEGRADED SCAN VS. SPACECRAFT ALTITUDE. The curve assumes the total 3σ error is 1.554°.

APPENDIX B:

EVALUATION OF THE NOISE BANDWIDTH INTEGRAL

The integral (6.22) for the noise bandwidth of the ISR electronics can be written as the sum of four integrals (cf. 6.24).

$$\int_0^\infty |G(s)N(s)|^2 \, ds = I_1 + I_2 + I_3 + I_4$$

$$I_1 = \int_0^5 \frac{250}{s^2} \left|1 - \frac{\sin(\pi Ps)}{\pi Ps} \exp(-i\pi Ps)\right|^2 ds$$

$$I_2 = \int_5^{26/P} \frac{50}{s}(1 + 4\pi^2\tau^2 s^2) \left|1 - \frac{\sin(\pi Ps)}{\pi Ps} \exp(-i\pi Ps)\right|^2 ds$$

$$I_3 = \int_{26/P}^{50} \frac{50}{s} \frac{1 + 4\pi^2\tau^2 s^2}{(1 + s^2/s_c^2)^2} \, ds$$

$$I_4 = \int_{50}^{\infty} \frac{1 + 4\pi^2\tau^2 s^2}{(1+ s^2/s_c^2)^2} \, ds$$

With a change of variable $\theta=\pi Ps$ we can write

$$\left|1 - \frac{\sin(\theta)}{\theta} \exp(-i\theta)\right|^2 = 1 + \frac{\sin^2(\theta)}{\theta^2} - \frac{\sin(2\theta)}{\theta}$$

The first two integrals then become

$$I_1 = 250\pi P \int_0^{5\pi P} \left(\frac{1}{\theta^2} - \frac{\sin(2\theta)}{\theta^3} + \frac{\sin^2(\theta)}{\theta^4}\right) d\theta$$

$$I_2 = 50 \int_{5\pi P}^{26\pi} (1 + A^2\theta^2) \left(\frac{1}{\theta} + \frac{\sin^2(\theta)}{\theta^3} - \frac{\sin(2\theta)}{\theta}\right) d\theta$$

where $A=2\tau/P$.

The two preceding equations contain terms of the form

$$\frac{\sin^2(\theta)}{\theta^n} d\theta = \frac{1-\cos(2\theta)}{2\theta^n} d\theta \, .$$

Using the above transformation we are faced with a group of integrals of the form

$$\frac{\sin(u)}{u^n}\,du \quad \text{and} \quad \frac{\cos(u)}{u^n}\,du\ ,$$

which can be reduced by successive integration by parts.

$$\frac{\sin(u)}{u^n}\,du = -\frac{\sin(u)}{(n-1)u^{n-1}} + \frac{1}{n-1}\,\frac{\cos(u)}{u^{n-1}}\,du$$

$$\frac{\cos(u)}{u^n}\,du = -\frac{\cos(u)}{(n-1)u^{n-1}} - \frac{1}{n-1}\,\frac{\sin(u)}{u^{n-1}}\,du$$

After reduction we make use of the definition of the sine integral (Abramowitz and Stegun, Handbook of Mathematical Functions, NBS Appl. Math. Series 55. p.231).

$$Si(z) = \int_0^z \frac{\sin(u)}{u}\,du \quad \text{and} \quad Ci(z) = \text{const.} + \ln(z) + \int_0^z \frac{\cos(u)-1}{u}\,du.$$

The integrals I_3 and I_4 are also readily soluble using integration by parts and partial fractions. For example,

$$I_3 = 50\int_{26/Ps_c}^{50/s_c} \left(\frac{1}{t} - \frac{t^2}{1+t^2} + \frac{(4\theta^2\tau^2 s_c^2 - 1)t}{(1+t^2)^2}\right) dt.$$

After application of these techniques and some algebra we find

$$I_1 = \frac{1000\pi P}{3}\left[Si(u) - \frac{1-\cos(u)}{u^3} + \frac{\sin(u)}{u^2} - \frac{3-2\cos(u)}{2u}\right]_{u=0}^{u=10\pi P}$$

$$= 2313$$

$$I_2 = 50\left[\frac{A^2}{2}\left(\frac{u^2}{4} + \cos(u)\right) - \frac{1-\cos(u)}{u^2} + \frac{\sin(u)}{u} + \left(1+\frac{A^2}{2}\right)(1.\ldots)-Ci(u)\right]$$

$$= 69$$

$$I_3 = 25\ln\left(\frac{2500}{s_c^2+2500} \Big/ \frac{676/P^2}{s_c^2+676/P^2}\right) + 25s_c^2(4\pi^2\tau^2 s_c^2-1)\left(\frac{1}{s_c^2+676/P^2} - \frac{1}{s_c^2+2500}\right)$$

$$= 71$$

$$I_4 = (1 + 4\pi^2\tau^2 s_c^2)\left(\frac{s_c}{2}\left\{\frac{\pi}{2} - \arctan(50/s_c)\right\} - \frac{25s_c^2}{s_c^2 + 2500}\right)$$

$$= 1125$$

In the above evaluations the parameter values were s_c=1.63 Hz, ℓ=1.439 sec, and τ=0.035 sec. The total integral is

$$I = 2313 + 69 + 71 + 1125 = 3578.$$

APPENDIX C:*

ANALYSIS OF ISR SENSITIVITY VARIATIONS WITH AMBIENT TEMPERATURE

Introduction

After the calibration of ISR SN 103, it was noted that the calibration curve for an instrument temperature of 30F disagrees significantly with the curve for an instrument temperature of 80F. At the Customer Acceptance Readiness Review (CARR) for SN 103 no good explanation for this behavior was found. No temperature effect had been seen ... the calibration of the Qualification Unit (SN 102). There had been discrepancies in the Prototype (SN 101) runs, but these had been attributed to problems in the test equipment and procedure rather than in the instrument. The Principal Investigator gathered all available data, printouts, and photographs of the calibration of SN 103 and studied them in great detail. It was discovered that the Platinum Resistance Thermometer (PRT) in Black Body No. 2 (BB2) had undergone a small shift in its calibration at the beginning of the procedure. However, this shift could not account for the discrepancies between the two calibration curves.

At the CARR for SN 103, the PI requested an extra test during the calibration of SN 104 to determine whether sensitivity variations with instrument temperature were real. The test was performed in the thermal vacuum chamber at the time of the calibration runs. The two black bodies were held at fixed temperatures and were scanned continuously while the

*This appendix originally was a working paper written during the ISR program. It has been edited for compatibility with the main body of text.

instrument temperature was varied from 80°F 30°F. The data sheets from the test are reproduced as Tables C-I and C-II.

Analysis

A study of the conversions from resistance to temperature for the PRT in Black Body No. 1 (BB1) as given in Table C-I reveals that the post-measurement values for Measurements 1 and 4 are probably in error. Accordingly these have been corrected from 151.3K to 151.2K and from 151.0K to 151.1K, respectively. Conversion of the resistance values for BB2 are listed in Table C-III.

It can be seen from Table C-III that the temperature of BB2 varied considerably from the nominal value of 82.0K. For each measurement, a correction to the Channel 1 output was computed from a model of the ISR low temperature response. The model is based on the calibration data and is discussed elsewhere. The corrections, in millivolts, are listed in Table C-III.

The nominal value for the temperature of BB1 was taken to be 151.3K This is the value recorded on both calibration runs and on the majority of the measurements in the temperature test. Althougn the BB1 temperature varies much less than the BB2 temperature, a correction must still be computed because the sensitivity of the ISR is so high at the higher temperature. The slope of the calibration curve at 151.4K was calculated to be 77.6 mv/deg ±0.7 mv/deg. The corrections for the pre-measurement and post-measurement BB1 temperatures are given in Table C-III. Where the two temperatures differ, the final correction was chosen as the mean of the two calculated corrections.

TABLE C-I

AMBIENT TEMPERATURE SENSITIVITY TEST

Blackbody Calibration Source Data

Meas. No.	PRT* (Before) BB2 (ohms)	(K)	ISR Data Channel Outputs (Volts) BB1 Chan.1	Chan.2	Chan.3	BB2 Chan 1	Chan.2	Chan.3	PRT* (After) BB2 (ohms)	BB1 (ohms)	(K)
1	706.86	151.1	3.13	0.79	0.20	0.095	0.03	0.05	302.6	707.1	151.3
2	707.0	151.2	3.07	0.77	0.20	0.050	0.02	0.05	301.6	706.0	150.9
3	707.5	151.3	2.71	0.68	0.18	-0.354	-0.08	+0.03	307.2	707.4	151.3
4	707.5	151.3	3.12	0.79	0.20	0.110	0.03	0.05	307.9	706.5	151.0
5	707.4	151.3	3.14	0.79	0.20	0.105	0.03	0.05	302.6	707.5	151.3
6	707.2	151.2	3.14	0.79	0.20	0.095	0.03	0.05	299.8	707.3	151.2
7	707.7	151.3	3.14	0.79	0.20	0.080	0.03	0.05	298.1	707.7	151.3
8	707.6	151.3	3.11	0.78	0.20	0.085	0.03	0.05	296.4	707.0	151.2
9	707.5	151.3	3.13	0.78	0.20	0.080	0.03	0.05	295.1	707.6	151.3
10	707.6	151.3	3.12	0.79	0.20	0.080	0.03	0.05	294.0	707.6	151.3
11	707.6	151.3	3.10	0.78	0.20	0.080	0.03	0.05	293.0	706.8	151.3
12	708.4	151.4	3.11	0.78	0.20	0.075	0.03	0.05	292.8	708.4	151.4
13	707.5	151.3	3.09	0.78	0.20	0.070	0.02	0.05	291.4	707.6	151.3

*PRT = Platinum Resistance Thermometer. Nominal PRT values: 82K - 294.94 ohms; 151K - 706.93 ohms.

TABLE C-II

AMBIENT TEMPERATURE SENSITIVITY TEST

ISR Temperature Data

Meas. No.	ISR Temp. (mvolts)	(°F)	Mirror* (volts)	Detector* (volts)	Cal. Patch* (volts)
1	0.993	77	1,96	0.426	2.51
2	1.033	79	1.91	0.425	2.45
3	1.001	77.4	1.89	0.424	2.50
4	0.944	75.0	1.91	0.425	2.58
5	0.891	72.6	1.96	0.426	2.70
6	0.814	69.2	2.04	0.428	2.85
7	0.728	65.4	2.16	0.429	3.03
8	0.625	60.7	2.30	0.431	3.24
9	0.500	55	2.51	0.434	3.50
10	0.369	49.9	2.75	0.435	3.78
11	0.210	41.8	3.03	0.437	4.07
12	0.083	35.9	3.30	0.437	4.33
13	-0.043	30.0	3.57	0.437	4.57

*Housekeeping measurements included in engineering telemetry during mission.

The corrections were applied to the Channel 1 outputs for the two black bodies. The corrected output for BB2 was subtracted from the corrected output of BB1 to obtain a calibration point for each measurement.

Associated with each calibration point is an error estimate. The noise on Channel 1 for SN 104 is 15 mv peak-to-peak. This value translates to an rms error of $\pm$ 3 mv for each of the two BB values. However, the BB1 output is only recorded to the nearest 10 mv. For this value the error is raised to $\pm$ 5 mv. Thus the total error in the calibration point from the readings is $\pm$ 8 mv.

The black body temperatures were recorded to the nearest 0.1K. This fact leads to a total error in the correction factors of $\pm$ 5 mv, with 4 mv coming from BB1 and 1 mv coming from BB2.

When the before and after BB1 temperatures disagreed, an error equal to half of the difference in the correction factors was assigned to the point. Errors in the corrections due to the models used in the calculation was neglected.

The total error assigned to a calibration point is the sum of the error from the above sources. The points and their errors are plotted in Figure C-1 as a function of ISR ambient temperature. The two points from the calibration curves are also plotted. The data clearly shows a systematic decrease in the response of the ISR as the temperature falls below 65°F. The response possibly restabilizes at approximately 45°F, but the data is insufficient to confirm this. The total drop amounts to approximately 2%.

Corrected points at 151.3K for the calibration of SN 102, SN 103, SN 104, and the re-calibration of SN 103 are presented in Table C-IV. The calibration of SN 101 was omitted because of the uncertainties in

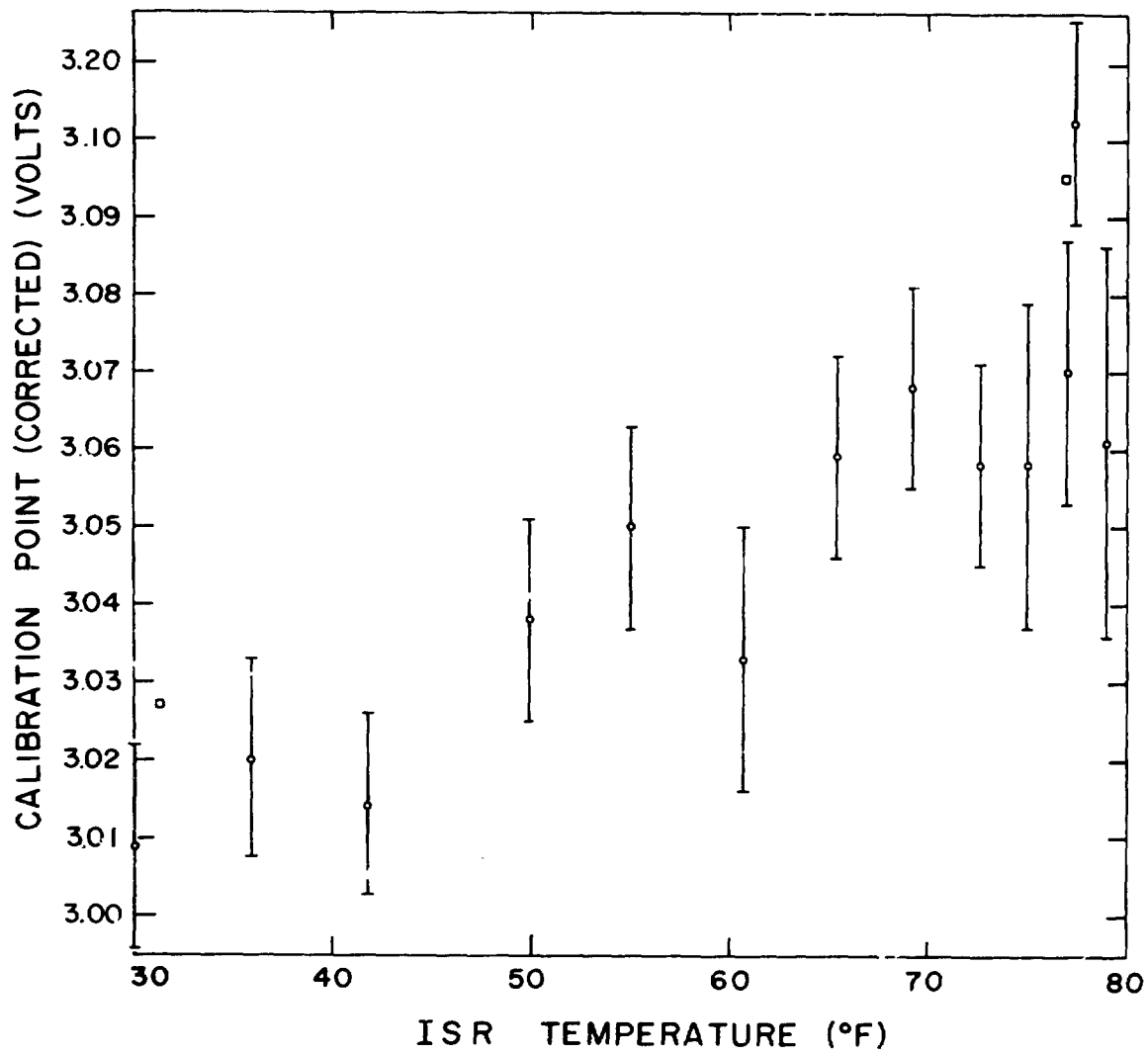

Figure C-1 EFFECT OF AMBIENT TEMPERATURE ON ISR RESPONSE. The circles show the 151 K calibration value as the ISR was heated from 30°F to 80°F. The squares represent the same calibration point in the regular calibration runs.

the procedure. In all the cases presented, the point at an ambient temperature of 80°F is higher than that at 30°F. The assembled evidence points to the fact that there is a small, but real, difference in the calibration of the ISR with ambient temperature.

In Figure C-2 are plotted the various components of the measurement as a function of time during the period of the test. The topmost plot is the ISR temperature in degrees Farenheit. It can be used to key this figure to the results of Figure C-1. At each measurement, two readings of the system were taken. The readings were about a minute apart, and the difference in ISR temperature was never more than a degree.

The second plot tracks the temperature of the space patch. It stayed at liquid nitrogen temperature except during the third measurement. There were two thermocouples on the space patch. The error bars on the points reflect a spread between the two temperature measurements as well as differences between the two printouts. It can be seen that the third point was unstable as well as anomalously high.

The bottom two plots represent the ISR output for each of the black bodies. The difference between the two values is the quantity plotted on the abscissa of Figure C-1. Note that the scales of the two plots in Figure C-2 differ by a factor of 10. The plotted values have been corrected for off-nominal temperatures of the black bodies.

Conclusions

It is clear from Figure C-2 that the space patch was not stable for the first few measurements. The anomalously high point in Figure C-1 corresponds to the third measurement when the space patch was warmer than BB2. The system apparently was stable from 14:35 onwards. The

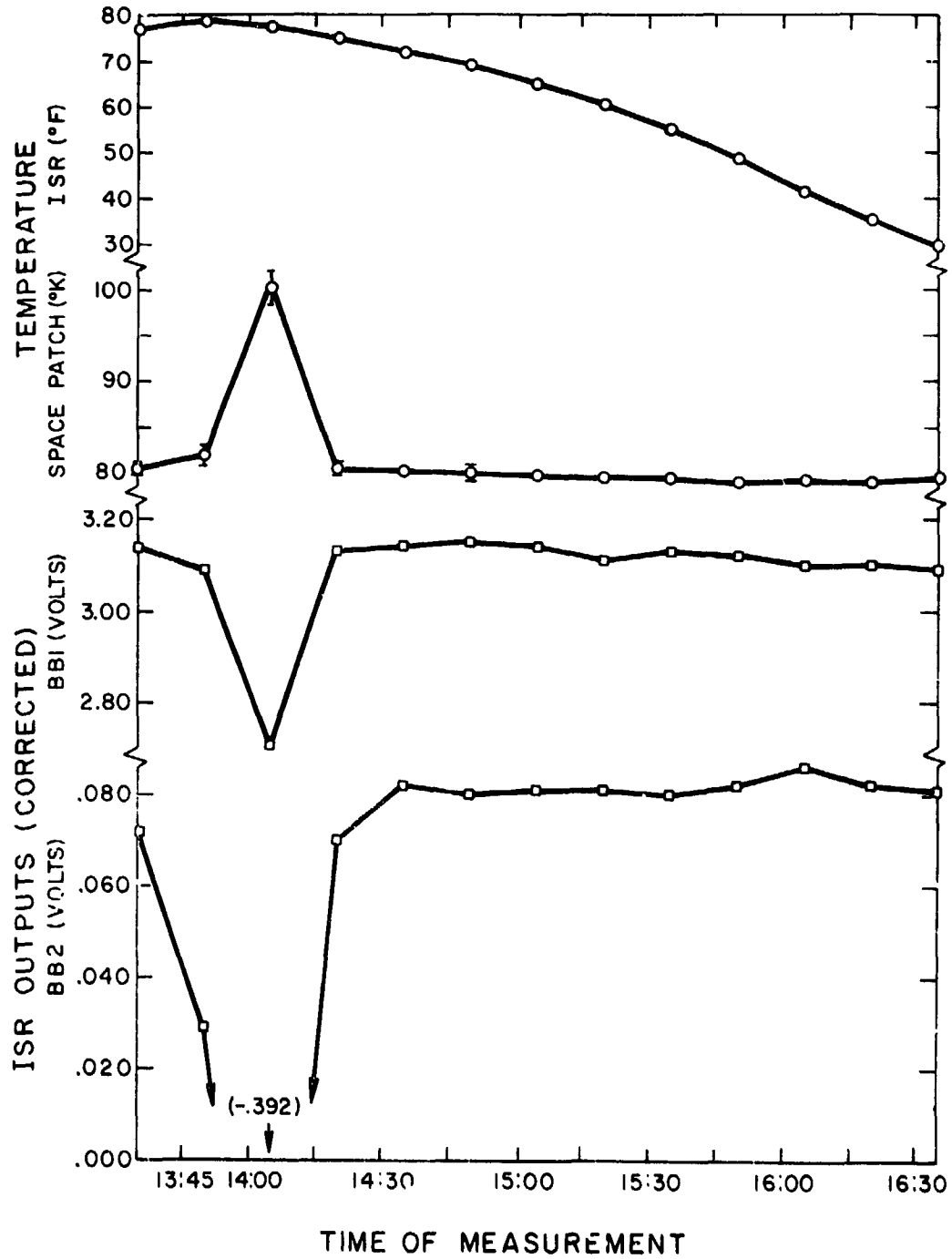

Figure C 2 VARIATIONS IN SIGNIFICANT TEST PARAMETERS. The data show that the Space Patch temperature was unstable early in the test sequence.

first four measurements should be suspect despite their good agreement in Figure C-1.

The roll-off with decreasing temperature in Figure C-1 is entirely due to a fall in the radiometric value for BB1. The magnitude of the decrease is approximately 2%. A gain variation with temperature could account for the phenomenon. If the radiometric value of BB2 also suffered a 2% decrease, the decrease would be undetectable in the presence of the instrument noise.

It is important to evaluate explanations of the data which involve the calibration facility rather than the instrument itself. It is known that the Channel 1 outputs for the two black bodies differ by approximately 50 millivolts when the two are at the same temperature at approximately 82K. One potential explanation of this radiometric discrepancy is reflection of a hot object from the black body into the ISR. I. Heilman of BEC has suggested that if the phenomenon is self reflection, then the decreased response with temperature might be the decreased reflected energy from the ISR. This explanation can be rejected because the "hotter" black body in the source equivalency test is BB2, which remained stable during the ambient temperature test. In addition, the magnitude of the decrease in signal for BB1 amounts to approximately 50 millivolts. It would be difficult to explain a decrease this large in terms of a total difference in reflected energy amounting also to 50 millivolts.

Therefore we conclude that the shift in response is within the instrument. The data in Figure C-1 will serve to correct the calibration curves.

TABLE C-III

BLACKBODY TEMPERATURES AND ISR OUTPUT CORRECTIONS

Meas. No.	Black Body #2			Black Body #1				
				Before		After		
	PRT (ohms)	Temp. (^{o}K)	Output Correction (m volts)	PRT (ohms)	Temp. (^{o}K)	PRT (ohms)	Temp. (^{o}K)	Output Correction (m volts)
1	302.6	83.2	-23	706.9	151.1	707.1	151.2	+12
2	301.6	83.1	-21	707.0	151.2	706.0	150.9	+20
3	307.2	84.0	-38	707.5	151.3	707.4	151.3	0
4	307.9	84.1	-40	707.5	151.3	706.5	151.1	+ 8
5	302.6	83.2	-23	707.4	151.3	707.5	151.3	0
6	299.8	82.8	-15	707.2	151.2	707.3	151.2	+ 8
7	298.1	82.5	- 9	707.7	151.3	707.7	151.3	0
8	296.4	82.2	- 4	707.6	151.3	707.0	151.2	+ 4
9	295.1	82.0	0	707.5	151.3	707.6	151.3	0
10	294.0	81.9	+ 2	707.6	151.3	707.6	151.3	0
11	293.0	81.7	+ 6	707.6	151.3	706.8	151.3	0
12	292.8	81.6	+ 7	708.4	151.4	708.4	151.4	- 8
13	291.4	81.4	+11	707.5	151.3	707.6	151.3	0

TABLE C-IV

CORRECTED CALIBRATION FOR ISR UNITS AT 151.3 K

	ISR Temp. (°F)	Calibration Point (Volts)
SN 102	28.5	3.17
	~80	3.21
SN 103	31.3	3.262
	39.2	3.348
	78.5	3.627
SN 104	31.3	3.027
	77.1	3.099
SN 103 (recalibration)	~30	3.237
	~80	3.361

LIST OF FIGURES

LIST OF FIGURES (Continued)

LIST OF TABLES

Acknowledgements

There is insufficient space for a complete list of contributors to a program as complex as the ISR experiment. However, I do wish to acknowledge a few who carried the program over rough spots to a successful and trouble-free conclusion.

Dr. Frank Low lobbied convincingly for an orbital infrared experiment and accepted the great responsibility of Principal Investigator when his arguments carried the day. His key decisions in design and testing of the ISR made it a viable scientific instrument. I particularly thank him for his trust in me to act for him in much of the planning, execution, and interpretation of the experiment.

When Eugene Zetka and I sat down in 1969 to lay out the program for instrument development, neither of us knew much about the process. However, Gene planned "by the book", paying great attention to details. Although a transfer within NASA caused him to leave the program in the early stages, his program plan operated smoothly for several years.

In the planning phases Vern Dauphin was our interface with mission operations at JSC. His skill at negotiation and political savvy saved our scientific objectives from the onslaught of engineering management.

At Barnes Engineering Company Mort Heilman was an invaluable aid to me. His cooperation and information enabled us to keep the ISR test program on course. Also, Gerry Falbel has been an instant reference for anything I wanted to know about infrared radiometers.

I thank Elinor Stockton for typing this document and others in time for last-minute deadlines. Her considerable secretarial skill has saved me much time and effort in the course of my work.

Finally, I thank my wife Bev for hanging in there with me during this rather lengthy ordeal.

NASA-JSC

PRELIMINARY RESULTS OF THE APOLLO 17 INFRARED SCANNING RADIOMETER*

W. W. MENDELL
Manned Spacecraft Center, Houston, Tex., U.S.A.

and

F. J. LOW
University of Arizona, Tucson, Ariz., U.S.A.

(Received 27 March, 1973)

Abstract. The thermal emission of the lunar surface has been mapped by an infrared scanner from lunar orbit. Samples from approximately $2.5 \cdot 10^5$ scans reveal the full range of lunar temperatures from 60 K to 400 K. The temperature resolution was 1 K with about ± 2 K absolute precision. Spatial resolution was approximately 2 km over most of the horizon-to-horizon scan. The total mapped area amounted to approximately 30% of the lunar surface.

The data currently available confirms the large population of nighttime thermal anomalies in western Oceanus Procellarum predicted by Earthbased observations. Most of these 'hot spots' are associated with fresh impact features or boulder fields. Also seen in the data are 'cold spots' where the local nighttime temperature is depressed relative to the general soil background. Such regions exhibiting low surface conductivity are inferred to be relatively young, non-impact features.

1. Introduction

The Infrared Scanning Radiometer (ISR) was among the complement of lunar orbital science experiments aboard the Apollo 17 Command-Service Module (CSM). The principal experimental objective of the ISR was the mapping of infrared thermal radiation emitted from the nighttime lunar surface within view of the spacecraft. The nighttime temperatures and cooling rates can be analyzed to provide values of the thermophysical parameters of the lunar surface layer.

Earth-based telescopic measurements have shown that the lunar soil layer is an excellent thermal insulator (Pettit and Nicholson, 1930). During the lunar day the surface temperature is strongly controlled by absorbed solar radiation. Very little heat is conducted into the subsurface layer. During the lunar night this small amount of stored heat is reradiated into space. Nighttime temperature measurement is a sensitive indicator of the surface thermal properties.

A simple, one-dimensional conductive model of the soil layer (Krotikov and Shchuko, 1963) demonstrates very well the general behavior of surface temperature. In such a model, families of temperature curves can be generated in terms of a single thermal parameter, $\gamma = (k\varrho c)^{-1/2}$, where k is the thermal conductivity, ϱ is the bulk density, and c is the specific heat. The model is simplified in that it disregards radiative transfer in the surface layer, but it is still useful to characterize the thermal response in terms

* Paper presented at the Lunar Science Institute Conference on Geophysical and Geochemical Exploration of the Moon and Planets, January 10–12, 1973

The Moon 9 (1974) 97–103.

of γ. The best Earth-based measurements of the lunar midnight temperature (Mendell and Low, 1970) place $\gamma \sim 850$ cal^{-1} cm^2 K s$^{1/2}$.

Thermal mapping of the nighttime lunar surface from Earth is a difficult observational task (Mendell, 1971). An orbital experiment, on the other hand, eliminates the problem of the terrestrial atmosphere and simultaneously allows an increase in spatial resolution.

2. Instrument Description

The ISR is a thermal imaging line scanner, built by Barnes Engineering Company (McIntosh and Mendell, 1972). A schematic of the optical system is shown in Figure 1. The spherical-spherical Cassegrain optical system has a 7-in. aperture. The instantaneous field of view is 20 mrad. The latter translates to a circular lunar surface resolution element ranging from 2.0 to 2.6 km in diam during accumulation of prime data. This spatial resolution is an order of magnitude improvement over Earth based observation.

The secondary mirror is mounted concentrically with the 45° plane scan mirror, and the entire assembly rotates continuously at 41.7 rpm during ISR operation. An aperture in the casting allows the beam to sweep from horizon to horizon perpendicular to the spacecraft ground track. The orbital motion of the CSM spaces the scans along the ground track. The angular velocity of mirror rotation was chosen such that consecutive scans would be contiguous on the lunar surface when the spacecraft altitude was 60 nautical miles (111 km).

At the Cassegrain focus of the detector system is mounted the detector assembly, consisting of a thermistor bolometer bonded to a hyperhemispheric silicon immersion lens. The spectral response of the radiometer is determined primarily by the lens as the only transmitting element in the optical path. The effective spectral pass band detectable by the ISR ranges from 1.2 μm to approximately 70 μm. The long wavelength cutoff is apparently caused by transparency of the detector flake. No filter was found which would both filter out reflected solar radiation at short wavelengths and also not compromise the long wavelength (low temperature) sensitivity.

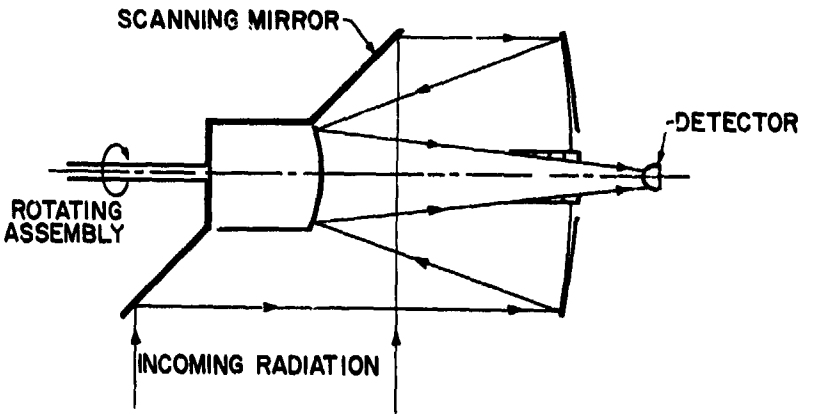

Fig. 1. Optical system schematic for Apollo 17 infrared scanning radiometer.

The ISR measured the full range of lunar temperatures from 80 K to 400 K. The instrument output was simultaneously transmitted on three different channels at three different gains. In this manner the low temperature sensitivity was maintained while the large dynamic range of signal was covered.

A special feature of the ISR radiometric calibration is the space clamp circuit. Once each scan, as the radiometer views deep space prior to crossing the lunar limb, the detector output is sampled and saved. This stored voltage is electronically subtracted from the detector output for the remainder of the scan. Therefore, each lunar scan is referenced to the radiometric 'zero' of deep space. The clamp circuit enhances the absolute accuracy of the measurement while suppressing low frequency detector noise.

3. Lunar Surface Coverage

The sunrise terminator was located at longitude 82° E, in the eastern part of Mare Serenitatis, at the time of the first ISR scans of the Moon. By the time of Trans-Earth Injection, it had moved to 46° W, just east of Aristarchus. On the front side of the Moon, the orbit constrained nighttime coverage to the southern portions of Mare Serenitatis and Mare Imbrium, Oceanus Procellarum, and the equatorial region at the western limb. On the far side, the night-time ground tracks passed south of Hertzsprung and Korolev over to Aitken and Van de Graaff.

A horizon-to-horizon scan from an altitude of 111 km includes an arc of 40° on the lunar sphere. Foreshortening seriously degrades surface resolution at the horizon. Good spatial resolution is achieved over a lunar spherical arc of 20° centered on the ground track. It follows from this fact that approximately 20–25% of the lunar surface was mapped at a spatial resolution better than 10 km.

4. Data Quality

The ISR transmitted approximately 97 hr of lunar data during the mission. Approximately 10^8 independent measurements of the lunar temperature were made. Data was received via telemetry at range stations around the world and recorded on magnetic tape. Samples of the data were available in real time at the Mission Control Center so that instrument performance could be assessed continuously. The available sampling was equivalent to a scan of the lunar surface once every six degrees of longitude. The tentative conclusions presented here are based on a quick look at this real-time sample, which comprises less than 2% of the entire data set.

The scans shown have not been processed, and the amplitudes are proportional to radiance (instrument output voltage) rather than temperature. The figure captions indicate the approximate temperature of various features.

Examination of the scans will show that the radiance of space just past the trailing (right-hand) limb of the Moon is not zero. Although the offset is not entirely understood, there is strong evidence that some object aboard the spacecraft falls into the skirts of the ISR field of view on that side of the aperture where the beam enters the

housing. Scans of space during Trans-Earth Coast show that the feature is approximately linear and can be removed with only a modest increase in the noise on the affected portion of the scan.

Figure 2 shows three lunar night-time scans. Scan 2(A) comes from Oceanus Procellarum. The center of the scan is dominated by the crater Kepler A. The altitude

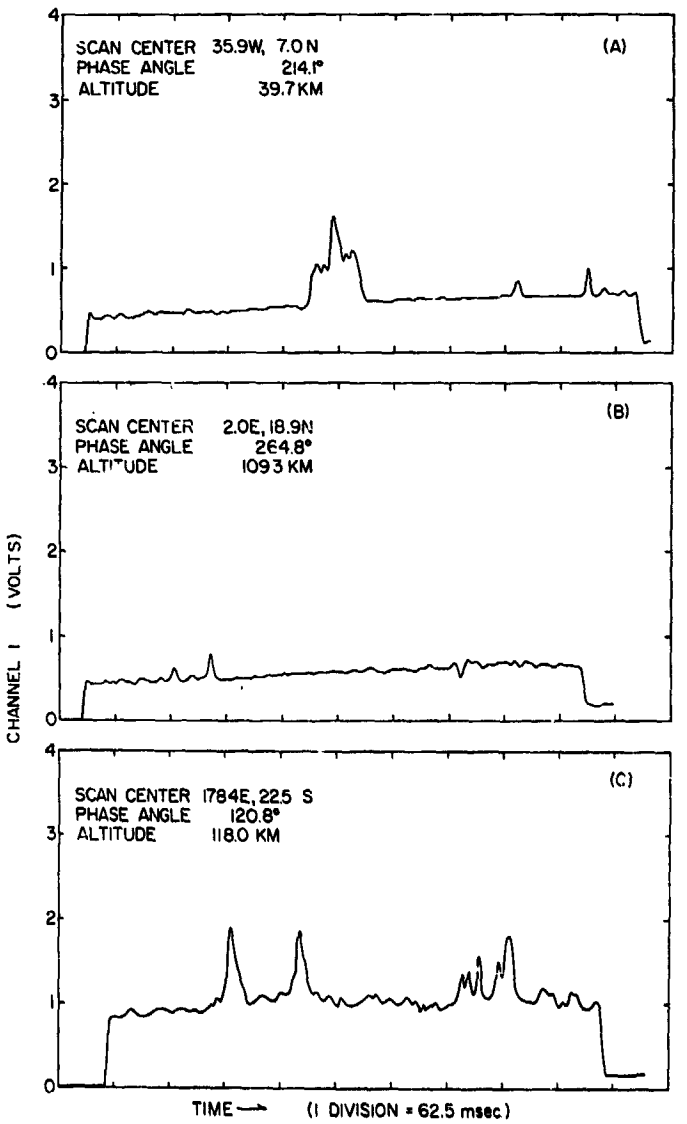

Fig. 2. Nighttime scans of the lunar surface. (A) Kepler A is thermally enhanced relative to the 92 K background in Oceanus Procellarum. The temperature in the crater ranges from 112 K on the walls to a maximum of 126 K in the center. (B) A pre-dawn cold spot shows an 8 K contrast to the 90 K background in the Apennine Mountains. (C) These large farside anomalies are enhanced approximately 22 K relative to an 108 K background two and one-half days after sunset.

of the spacecraft was 39.7 km at the time of the scan, making the ISR resolution element 0.8 km across on the surface. The width of the broad base of the enhancement is 10 km, coinciding with the crater diameter. The thermal pinnacle in the center is approximately 2 km across. The measured radiance in the central region increases linearly from both sides to the center, implying that the actual temperature at the center has not been fully resolved. The dramatic change of material properties within the crater probably reflects exposure of bedrock. The radial gradient may be caused by a corresponding radial distribution of slump material from the crater walls. Unfortunately, no lunar photographs have been found which contain a good view of the crater bottom.

Scan 2(B) contains pre-dawn temperatures, the coldest for any given surface region. The scan center is located just north of Mare Vaporum and south of the Apollo 15 landing site. On the right-hand portion of the scan can be seen a negative anomaly, i.e., a region whose temperature is depressed relative to its environs. In this case, the temperature difference is $\gtrsim 8$ K. A lower limit is given because the deflection is only one resolution element across, implying that the anomaly may not be fully resolved. The anomalous region lies south of the crater Conon in the Apennine Mountains. The magnitude of the temperature contrast implies that the thermal conductivity of the soil there is approximately one-half that of the surrounding material. These underdense regions cannot be impact features. The preservation of the density contrast also implies that they are relatively young on a geologic scale. Low (1965) has previously detected cold anomalies from Earth, but their thermal behavior has not been studied.

Scan 2(C) depicts far-side anomalies. Our abbreviated data survey shows that such features are not common in the nighttime data on the back side. A low frequency of occurrence was anticipated because front side anomalies occur preferentially in the maria, regions which are generally absent in the other hemisphere. The two prominent anomalies on the left side of the scan are located between the large craters Aitken and Van de Graaff. The large peak at the right limb corresponds to the crater Birkeland; the smaller structure to its left is in Van de Graaff.

Figure 3 contrasts two daytime scans. The scan centers are separated by only 6° of longitude, but the contrasting effects of topography in the maria and the highlands are quite clear. The thermal spike to the right of the mare and the dip to the left correspond to the northern and southern rims. The difference in the thermal signatures from the two scarps demonstrates the dominance of local slope (i.e., local sun angle) in the daytime thermal regime.

In Figure 4 lunar temperatures as measured by the ISR are plotted as a function of brightness longitude. The values were taken from scans on the twentieth lunar orbit by the Apollo spacecraft. An attempt was made to choose a point from each scan on the lunar equator. The spacecraft orbital motion causes the actual sequence of the points to go from right to left on the figure. The first point at $t/P = 0.43$ was measured at 08:26 GMT on December 12, 1972. The final point (at approximately the same lunation coordinate) was measured at 10:25 GMT. A data gap exists near the subsolar point for this orbit.

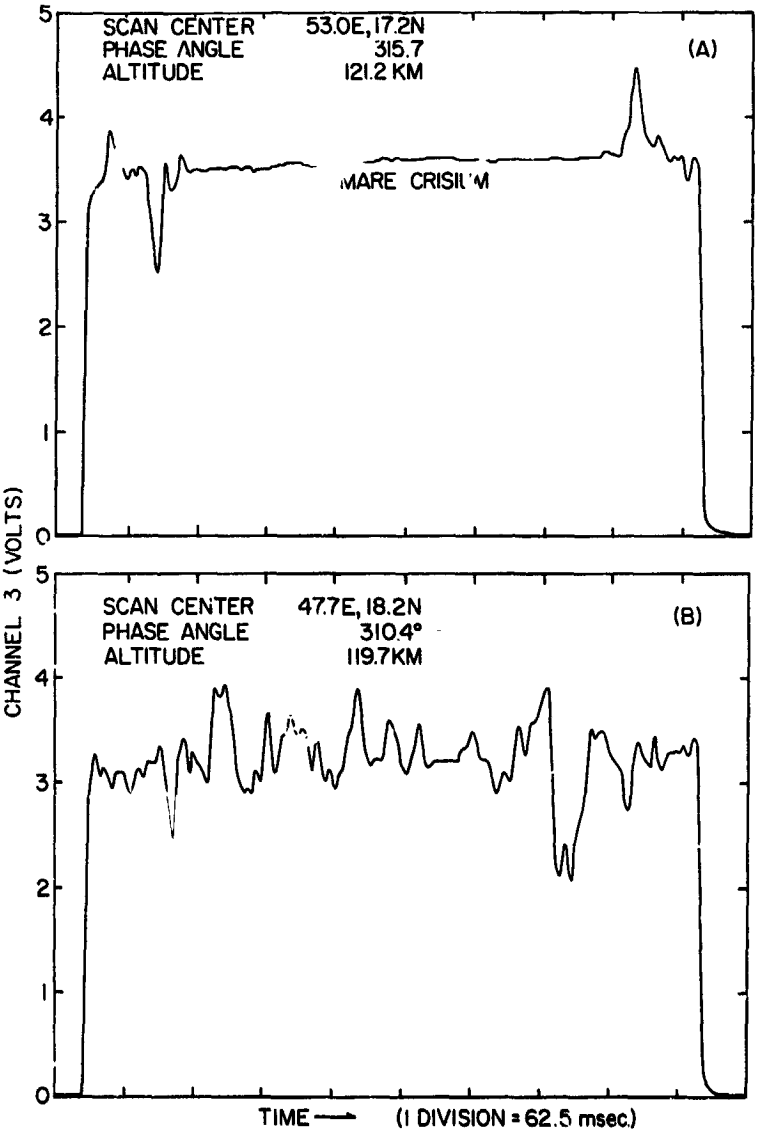

Fig. 3. Two daytime scans demonstrate the extreme contrast in amount of thermal structure in nearby mare and highland terrain. The temperature in Mare Crisium is approximately 368 K.

The plotted temperatures will change as the ISR values are refined. The error estimate is 3 K for the nighttime measurements; the values probably are systematically low. No correction for albedo or topography have been made.

On the same figure are plotted theoretical curves for various values of γ. The theoretical calculations represent the cooling behavior at a single point whereas the data is taken over many different types of material. The cooling curve apparently falls

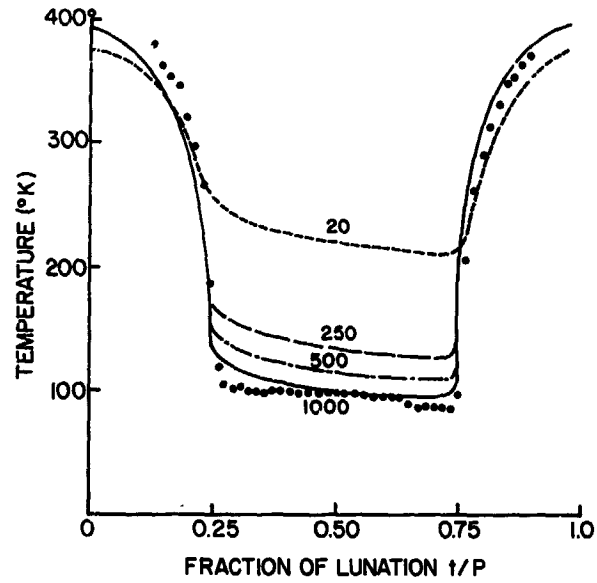

Fig. 4. Equatorial temperatures are plotted as a function of the lunation coordinate. Theoretical curves come from Krotikov and Shchuko (1963).

below $\gamma \sim 850$, even if the error estimate is taken into account. The elevated temperatures near lunar midnight fall in Oceanus Procellarum where general thermal enhancement has been noted in eclipse measurements (Saari and Shorthill, 1965).

The data for lunar afternoon temperatures comes from the highlands on the far side, and the morning points fall in Mare Fecunditatis and Mare Tranquillitatis. The combined effects of albedo and directionality of emissivity account for the apparent systematic deviations to either side of the theoretical curve.

This brief survey of the ISR data has confirmed that a variety of thermal behavior exists on the lunar surface. Further work on the measurements will establish the cooling behavior of the major types of lunar regions and the most interesting exceptions within each category.

References

Krotikov, V. D. and Shchuko, O. B.: 1963, *Soviet. Astron. AJ* **7**, 228.
Low, F. J.: 1965, *Astrophys. J.* **142**, 806.
McIntosh, R. B., Jr. and Mendell, W. W.: 1972, *Proceedings of the Technical Program of the Fourth Annual Electro-Optical Systems Design Conference*, Industrial and Scientific Conference Management, Inc., Chicago, pp. 356–361.
Mendell, W. W. and Low, F. J.: 1970, *J. Geophys. Res.* **75**, 3319.
Mendell, W. W.: 1971, 'Lunar Differential Flux Scans at 22 Microns', Master's Thesis, Rice University.
Pettit, Edison and Nicholson, Seth B.: 1930, *Astrophys. J.* **71**, 102.
Saari, J. M. and Shorthill, R. W.: 1965, *Nature* **205**, 964.

Proc. Lunar Sci. Conf. 6th (1975), p. 2711–2719.
Printed in the United States of America

Infrared orbital mapping of lunar features

W. W. MENDELL
NASA Johnson Space Center, Houston, Texas 77058

F. J. LOW
Lunar and Planetary Laboratory, University of Arizona, Tucson, Arizona 87515

Abstract—A computer program has been developed which constructs second generation isothermal contour maps of the lunar surface from Apollo 17 Infrared Scanning Radiometer (ISR) data. The maps clearly show large-scale trends such as the lunar cooling curve and directionality of lunar emission. Direct evidence has been found for the downslope transport of lunar soil. Studies of features have led to a crater degradation sequence based on thermal contours. Unusual cold regions have been found which are not well understood.

INTRODUCTION

THE INFRARED SCANNING RADIOMETER (ISR) on Apollo 17 was a line scanner designed to map the thermal emission of the lunar surface from orbit (Mendell and Low, 1974; McIntosh and Mendell, 1972). A continuously rotating scan mirror swept the field of view of the detector across the lunar surface, perpendicular to the ground track. The rotation rate of the scan mirror (4.37 rad/sec) was chosen to make consecutive scans contiguous on the ground when the Command-Service Module (CSM) had an orbital altitude of 110 km. At this nominal altitude the instantaneous field of view of the radiometer (20 mrad) projected a circular resolution element, 2.2 km in diameter, onto the surface at the spacecraft nadir point. Simple geometry causes the surface resolution element to become progressively more elliptical as the scan points toward the lunar horizon, away from nadir.

During six days in lunar orbit, the ISR returned approximately 10^8 measurements of the surface temperature distribution. The sensitivity of the ISR was better than 1 K over the entire range of lunar temperatures (85–400 K). The accuracy of the measurement was approximately ±2 K in brightness temperature, as determined from instrument noise and evaluation of calibration data.

Mapping the lunar surface nighttime temperature distribution was the primary objective of the experiment. The nighttime temperature is determined primarily by the thermophysical properties of the surface layer rather than local slope or albedo. Consequently, thermal maps potentially can elucidate geophysical and geological relationships among surface features.

Earth-based infrared maps of the moon during an eclipse (Shorthill and Saari, 1969) have demonstrated the existence of hundreds of local thermal enhance-

ments ("thermal anomalies") during the cooling of the surface associated with the passage of the earth's shadow. Attempts to map the nighttime thermal emission from the earth (Wildey *et al.*, 1967) have been less successful due to instrumental limitations.

Several effects can cause local thermal enhancement, but most thermal anomalies are associated with the presence of surface rocks (Winter, 1970). The intensity and the duration of an anomaly in the lunar night are functions of the size distribution and the number density of the rock populations. Generally, the rocks must be larger than a decimeter to have a noticeable thermal effect.

Fudali (1966) hypothesized that the thermal signature of an impact crater would change with time as the floor, rim, and ejecta blanket progressively eroded. Maps of nighttime thermal emission can be used to establish a degradation sequence which will complement the standard photographic criteria of "freshness."

ISR data lends itself well to the preparation of thermal maps, from which such selenological problems as crater degradation can be studied. The improved spatial and thermal resolution of the orbital data has brought to light new lunar problems. Measurements on the lunar farside are also available for the first time.

CONSTRUCTION OF THERMAL MAPS

We have recently generated from a computer a set of second-generation orbital maps of lunar nighttime emission. These maps represent an improvement over a previously published version (Mendell, 1974) in that major instrumental effects have been corrected to first order and the data is expressed in temperature rather than radiance. Unfortunately, the press of the deadline for this volume precludes publication here of the complete maps. However, certain features of the maps will be discussed.

The map projection is basically an oblique Mercator, with the orbit ground track serving as the "equator." Therefore the abscissa represents longitude in the orbit plane while the ordinate is "orbital latitude." Spacecraft pitch and yaw have been neglected by assuming each scan lies perpendicular to the ground track. Compensation for spacecraft roll has been achieved by a simple search routine for both limb deflections on each scan.

The location of each data point on the map and the position of a superimposed selenographic grid are calculated from a simple elliptical orbit. The trajectory is generated by the program from an appropriate Keplerian state vector supplied to us by the Johnson Space Center. This approximate procedure has sufficient accuracy to correlate thermal patterns with mapped lunar features.

The ordinate of the maps encompasses $\pm 6°$ of orbit plane latitude. The horizon-to-horizon scan sweeps out approximately $\pm 20°$. If this entire arc is included in the maps, features toward the horizon become poorly resolved and greatly distorted. Although the maps span only 30% of the area covered by each pass, they contain approximately 60% of the data.

Discussion of the Data

Nighttime cooling gradients are clearly seen on the maps. The temperature falls from approximately 100 K at the antisolar meridian to 90 K at the sunrise terminator. These values are in excellent agreement with earth-based measurements at a wavelength of 22 μm (Low, 1965; Mendell and Low, 1970).

The temperature at the top or the bottom of the map tends to be 2–3 K lower than that the center of the map. This directionality in the lunar emissivity is seen here for the first time in dark-side emission although it has been discussed for daytime data (Montgomery *et al.*, 1967). The cause is surface roughness on millimeter and centimeter scales.

We observe that local topographic highs tend to be warmer than surrounding low areas. The peaks of Montes Apenninus are 7–10 K warmer than the foothills prior to sunrise. The hottest points on the floor of Copernicus are the central peaks. A crater rim is the last remnant enhancement of a degraded crater. Apparently mass wasting and downslope movement of soil exposes rocks at the tops of local elevations. This phenomenon may have implications for correlations with topography found in other remote sensing measurements.

Figure 1 is a thermal map of the prominent anomaly Olbers A. On REV 57 (Fig. 1a) the spacecraft passed directly over the crater, and a day later on REV 71 it passed 4° to the north. Some geometrical distortion from foreshortening can be seen at the bottom of Fig. 1b. Although Olbers A lies in heavily cratered highlands northeast of Mare Orientale, the surrounding relief is essentially invisible thermally. The only comparable feature on our maps is the bright-ray crater Aristarchus.

The thermal anomaly in Olbers A is clearly associated with the floor of the crater. Thermal enhancement from the continuous ejecta blanket can be seen extending beyond the rim. The highest temperature in the crater on REV 57 is 133 K, and it has fallen to 129 K 28 hr later.

The small anomaly in Fig. 1 is a crater with a bright ejecta blanket laying in the southeast quadrant of Hedin A. Its temperatures in REV's 57 and 71 are 138 K and 114 K, respectively. The latter value is probably too low due to poor resolution of the feature on REV 71 and illustrates the problems of foreshortening.

No obvious relationship exists between Olbers A and the smaller feature on orbital photography. However, the 95 K contour in Fig. 1b connects the ejecta blankets of the two craters. The 97.5 K contour in Fig. 1a (dashed lines) shows the same pattern of connection. The maintenance of this small (1 K) but distinct enhancement through the lunar night implies some sort of genetic relationship between the two features. It also illustrates the wealth of detail in the ISR data.

The enhancement of Copernicus (Fig. 2) is largely associated with the rim, and the central peaks are the principal hot areas on the crater floor. The relatively cool region inside the northern rim correlates well with a mapped geologic unit (Schmitt *et al.*, 1967). The rim enhancement is asymmetric with the most prominent anomalies lying on the south rim. The ejecta blanket enhancement does not extend far beyond the rim. Surrounding the crater, particularly to the

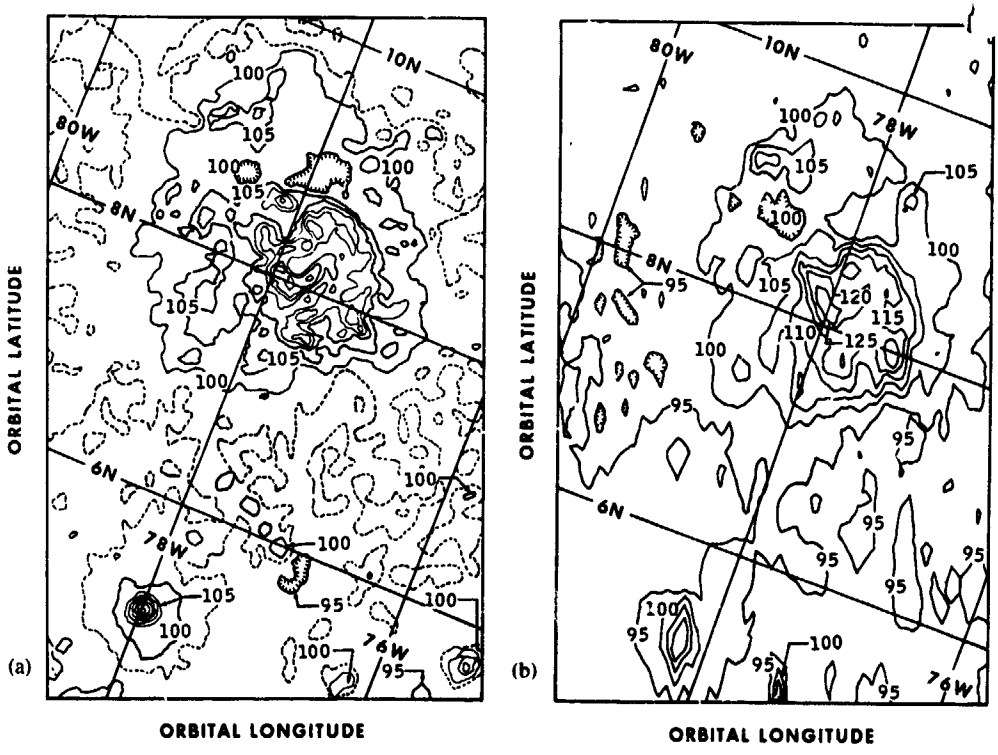
(a)
ORBITAL LATITUDE
ORBITAL LONGITUDE
10N
8N
6N
80W
78W
76W
100
105
95
(b)
ORBITAL LATITUDE
ORBITAL LONGITUDE
10N
8N
6N
80W
78W
76W
0
100
105
95
110
115
120
125


(c)

north, is a blanket of material lacking small-scale thermal structure and slightly cooler than soil farther away.

Aristarchus (Fig. 3) may be an intermed' :e case between the previous two features. The thermal anomaly lies with the floor of the crater and the ejecta blanket is prominent. Slightly cool, thermally quiescent material surrounds the ejecta, particularly to the north. This predawn map of the crater may be compared with the map of Olbers A in Fig. 1b.

In the upper left-hand corner of Fig. 3, the crater at the head of Schroeter's Valley can be seen as a thermal anomaly. The portion of the rille immediately to the north of the crater is missing from this map and is only a weak anomaly. The thermal enhancement in the remainder of Schroeter's Valley is quite strong. The southern tip of the enhancement can be seen at the upper edge of the figure, above the head crater.

The slightly cooler halo can also be seen around Marius A and the craters Bessarion A and B (Fig. 4). Marius A has a floor anomaly, and the latter two craters have rim anomalies. The floor of Bessarion A is only slightly enhanced relative to the soil environs. The rim anomalies are highly asymmetric, possibly indicating the original direction of the impact.

Approximately 20-km northwest of Bessarion B is a small anomaly flanked by two extensive cold regions where the temperature falls below 90 K. The small anomaly can be correlated with a bright patch on a good Lunar Orbiter photo. There is no crater obviously associated with the bright patch. Directly north of the two craters (approximately 41 W, 18 N) is an isolated cold region where the temperature falls to 88 K. We have not been successful in correlating the cold regions with photographic features.

Earth-based eclipse maps of the moon have shown that Oceanus Procellarum is slightly enhanced relative to other maria. We associate this enhancement with a myriad of subresolution (10^2–10^3 m) anomalies on our orbit maps. The unexpected cooler halos surrounding some craters appear to exist because the subresolution structure is absent. Since an impact crater always lies at the center of the thermally quiescent region, we presume that some sort of blanketing action has occurred. However, ejecta blankets contain rocky material which causes thermal enhancement rather than the opposite.

To resolve this apparent paradox we propose the following scenario. Oceanus Procellarum is a young mare with a thin regolith. Craters with diameters on the order of 100 m or larger can excavate blocks of a meter scale. However, these blocks are largely confined to the crater itself. Craters larger than a few kilometers can blanket the smaller features effectively with rubble of a smaller grains size (i.e.

Fig. 1. Thermal contour maps of the Olbers A region at a contour interval of 5 K. A grid of selenographic longitude and latitude is superimposed on the map. (a) Local time is 10.7 days past sunset. The r...imum temperature inside Olbers A is 133 K while inside the small crater to the south the maximum is 138 K. (b) Twenty-eight hr later (11.8 days after sunset) the maximum ter..rature inside Olbers A has fallen to 12[illegible] K while inside the smaller crater it is 114 K. The latter temperature is probably too low since foreshortening causes poor resolution of the feature. (c) Lunar Orbiter photo of the region.

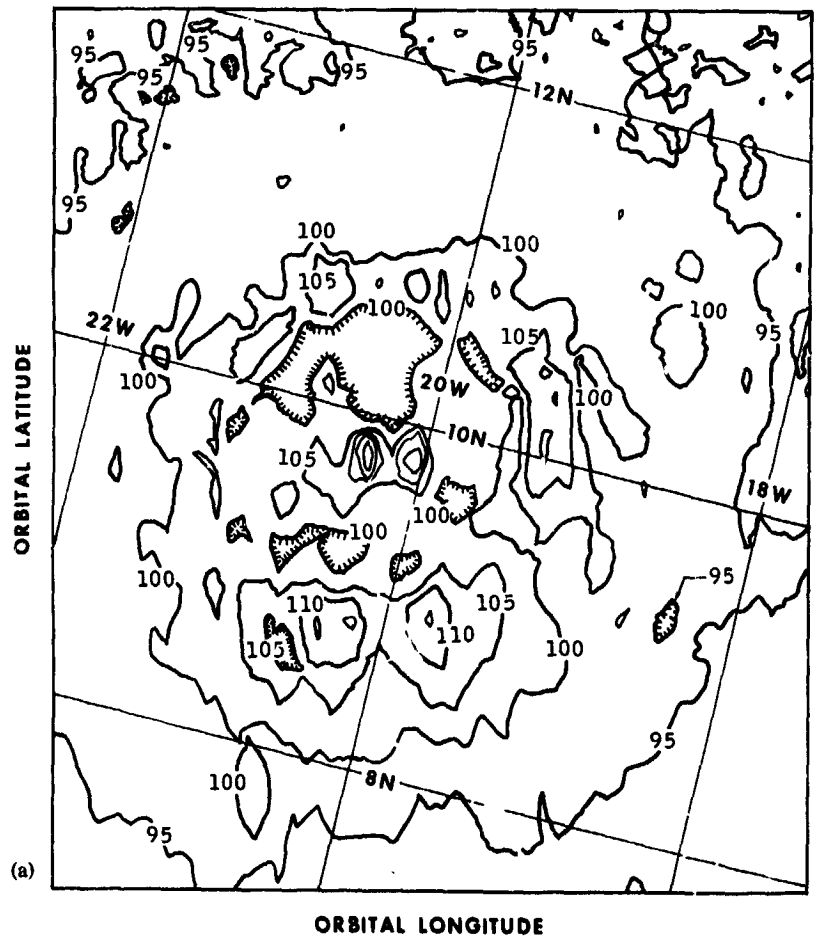

(b)

Fig. 2. (a) Thermal contour map of Copernicus, 12.3 days after sunset. Two hot spots on the southern rim are 115 K. The central peaks exhibit temperatures of 120 K (east) and 125 K (west). (b) Lunar Orbiter photo.

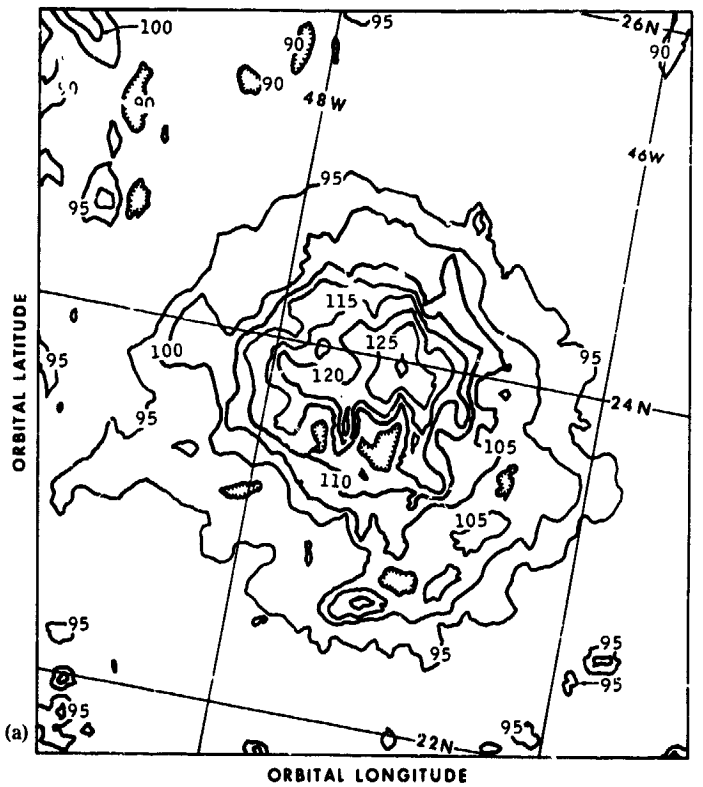

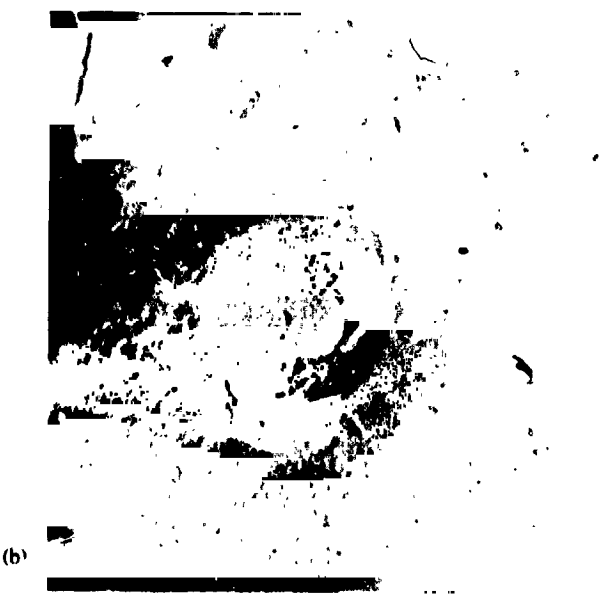

Fig. 3. (a) Thermal contour map of Aristarchus, 14.4 days after sunset. The maximum temperature on the floor of the crater is 130 K. (b) Lunar Orbiter photo.

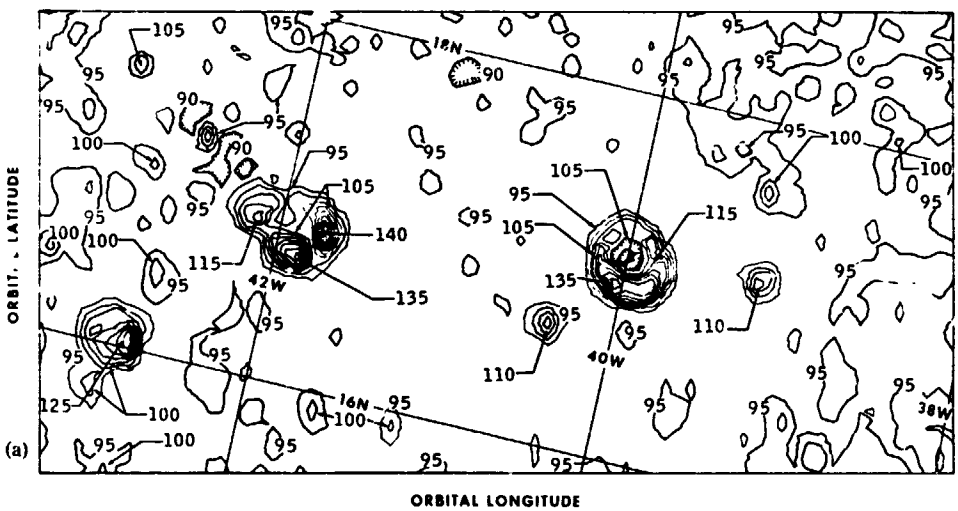

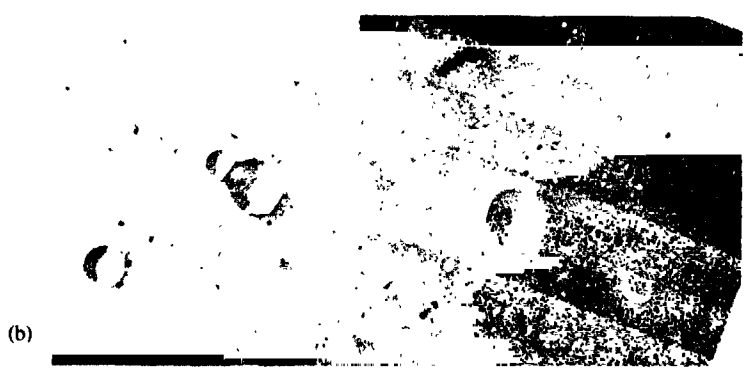

Fig. 4. (a) Thermal contour map of Bessarion A and B, 13.7 days after sunset. The temperature on the rim of Bessarion A (east crater) reaches 137 K, while on the rim of Bessarion B the temperature reaches 141 K. The unusual cold regions northwest of Bessarion B and lying at (319, 18 N) have minimum temperatures of 88 K. (b) Lunar Orbiter photo.

centimeters). The blankets need not be thicker than 2 or 3 m. Generally the ejecta blankets are disrupted again by the smaller scale events. However, if a large crater forms during the end of the period of bombardment, the ejecta blanket remains relatively intact. Under the usual lunar erosional processes, the centimeter scale ejecta is much more efficiently comminuted than the meter scale blocks elsewhere on the mare. Therefore the craters with the thermally quiescent environs are actually the younger features.

In summary, the infrared orbital maps can be used to supplement photogeologic studies in establishing relative ages and chronology for various surfaces. Geological relationships which are suggested by the thermal maps are

often missing in photographs. Direct evidence for lunar surface processes such as mass wasting and microscale roughening can be found in the data. A crater degradation sequence can be derived from thermal contour data.

We intend to publish complete versions of our second-generation orbital maps as quickly as possible. In future versions the entire spacecraft ephemeris will be integrated into the map program, and large-scale trends such as the lunar cooling curve and limb darkening will be extracted. Finally, the unusual cold regions will be studied to determine what effects are responsible for them.

Acknowledgments—Part of this research was performed under NASA contract NAS-9-10428. We wish to thank Dr. Fred Hörz for helpful discussions during preparation of the manuscript.

References

Fudali R. F. (1966) Implications of the nonuniform cooling behavior of the eclipsed moon. *Icarus* **5**, 536–544.

Low F. J. (1965) Lunar nighttime temperatures measured at 20 microns. *Ap. J.* **142**, 806–808.

McIntosh R. B., Jr. and Mendell W. W. (1972) Infrared scanning radiometer for temperature mapping of the lunar surface on the Apollo 17 flight. Proc. of the Tech. Prog. of the Fourth Ann. Electro-Optical Sys. Designs Conf., p. 356–381. Industrial and Scientific Conference Management, Chicago.

Mendell W. W. (1974) Apollo 17 infrared scanning radiometer lunar farside radiance map. *Proc. Lunar Sci. Conf. 5th*, Frontispiece, Plate 10.

Mendell W. W. and Low F. J. (1970) Low-resolution differential drift scans of the moon at 22 microns. *J. Geophys. Res.* **75**, 3319–3324.

Mendell W. W. and Low F. J. (1974) Preliminary results of the Apollo 17 infrared scanning radiometer. *The Moon* **9**, 97–103.

Montgomery C. G., Saari J. M., Shorthill R. W., and Six N. F., Jr. (1966) Directional characteristics of lunar thermal emission. Boeing Sci. Res. Lab. Dcmt. D1-82-0568.

Schmitt H. H., Trask N. J., and Shoemaker E. M. (1967). Geologic map of the copernicus quadrangle of the moon. U.S. Geol. Surv. Misc. Geol. Inv. Map I-515. Washington, D.C.

Shorthill R. W. and Saari J. M. (1969) Infrared observation on the eclipsed moon. Boeing Sci. Res. Lab. Dcmt. D1-82-0778.

Wildey R. L., Murray B. C., and Westphal J. A. (1967) Reconnaissance of infrared emission from the lunar nighttime surface. *J. Geophys. Res.* **72**, 3743–3749.

Winter D. F. (1969) The infrared moon: Data, interpretations, and implications. Boeing Sci. Res. Lab. Dcmt. D1-82-0900.

24. Infrared Scanning Radiometer

F. J. Low[a†] *and W. W. Mendell*[b]

The infrared scanning radiometer (ISR) is a thermal imaging device capable of mapping lunar surface thermal emission from lunar orbit. The principal experimental objective of the ISR is the measurement of lunar nighttime temperatures and cooling rates for that portion of the Moon overflown by the orbiting command and service module. Such data are related to the physical parameters (density and thermal conductivity) of the local surface layer.

The thermal emission at the surface of the Moon serves to balance the solar radiation absorbed at the surface and the heat flow into or out of the subsurface. Heat conduction through the surface is generally small because the lunar soil is an excellent thermal insulator. Therefore, the daytime temperature regime is dominated by such factors as albedo, Sun angle, and local slope. Conversely, the nighttime emission represents the reradiation of heat stored during the lunar day and is largely dependent on the physical properties of the surface layer.

A simple, one-dimensional model of the soil layer (ref. 24-1) can be used to demonstrate the general behavior of surface temperature. In such a model, families of temperature curves (faired curves in fig. 24-1) can be generated in terms of a single thermal parameter $\gamma = (k\rho c)^{-1/2}$, where k is the thermal conductivity, ρ is the bulk density, and c is the specific heat. This simplified model disregards radiative transfer in the surface layer, but it is still useful to characterize the thermal response in terms of γ. Earth-based measurements of the lunar midnight temperature (ref. 24-2) place $\gamma \approx 850$ cal^{-1} cm^2 K sec$^{1/2}$.

Shorthill and Saari's (ref. 24-3) thermal mapping of the eclipsed Moon from a telescope in Egypt demonstrated a wide variety of thermal behavior on the visible hemisphere. At a spatial resolution of approximately 20 km at the center of the disk, the Moon possessed hundreds of features that remained warm relative to their environs during the eclipse. Studies of these "thermal anomalies" indicated surface rock exposures associated with fresh impact features as an explanation. More recent correlations of the eclipse data with Earth-based radar measurements (ref. 24-4) show that a one-to-one correspondence does not exist between boulder fields and infrared anomalies.

In contrast to the eclipse cooling, which lasts for only a few hours, the lunar nighttime cooling regime lasts for 14 days. The nighttime thermal gradients extend deeper into the subsurface, and the surface temperature distributions are influenced by structure to a depth of a few tens of centimeters. Many observers (refs. 24-5 to 24-9) have attempted to map the nighttime Moon from Earth to take advantage of the improved subsurface resolution. However, the observational difficulties (ref. 24-8) associated with the low level of thermal emission and with the terrestrial atmosphere have precluded substantial success. The ISR provides a solution to the observational problem with an absolute radiometric measurement of lunar nighttime temperatures that represents an order-of-magnitude improvement in spatial and radiometric resolution over Earth-based work.

INSTRUMENT DESCRIPTION

The ISR is a thermal imaging line scanner (ref. 24-10). A schematic diagram of the optical system is shown in figure 24-2. The spherical-spherical Cassegrain optical system has a 17.78-cm (7 in.) aperture. The instantaneous field of view is 20 mrad, which translates to a circular lunar surface resolution element ranging from 2.0 to 2.6 km in diameter during accumulation of data from the spacecraft circularized orbit. This spatial resolution is an order-of-magnitude improvement over Earth-based observations.

[a]The University of Arizona.
[b]NASA Lyndon B. Johnson Space Center.
†Principal Investigator.

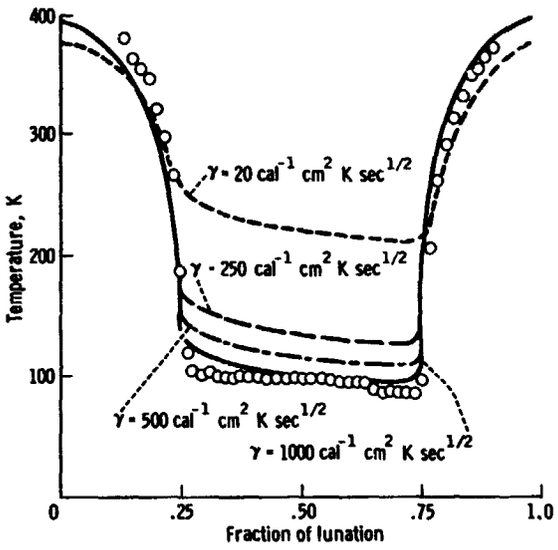

FIGURE 24-1.–Lunar equatorial temperatures (data points) plotted as a function of the lunation coordinate. Theoretical curves for various values of γ are from reference 24-1.

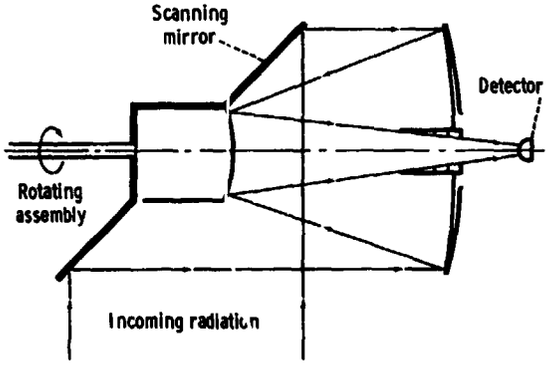

FIGURE 24-2.–Schematic diagram of the optical system for the Apollo 17 infrared scanning radiometer.

The secondary mirror is mounted concentric with the 45° plane scanning mirror, and the entire assembly rotates continuously at 41.7 rpm during ISR operation. An aperture in the casting allows the beam to sweep from horizon to horizon perpendicular to the spacecraft groundtrack. The orbital motion of the command and service module spaces the scans along the groundtrack. The angular velocity of mirror rotation was chosen such that consecutive scans would be contiguous on the lunar surface when the spacecraft altitude was 111 km (60 n. mi.).

The detector assembly, consisting of a thermistor bolometer bonded to a hyperhemispheric silicon immersion lens, is mounted at the Cassegrain focus of the optical system. The spectral response of the radiometer is determined primarily by the lens, the only transmitting element in the optical path. The effective spectral pass band detectable by the ISR ranges from 1.2 to approximately 70 μm. The long-wavelength cut-off is apparently caused by transparency of the detector flake. No filter was found that was capable of filtering out the reflected solar radiation at short wavelengths without compromising the long-wavelength (low temperature) sensitivity.

The ISR measured the full range of lunar temperatures from 80 to 400 K. The instrument output was simultaneously transmitted on three different channels at different gains. In this manner, the low-temperature sensitivity was maintained while the large dynamic range of signal was covered.

A special feature of the ISR radiometric calibration is the space clamping circuit. Once each scan, as the radiometer views deep space before crossing the lunar limb, the detector output is sampled and saved. This stored voltage is electronically subtracted from the detector output for the remainder of the scan. Therefore, each lunar scan is referenced to the radiometric "zero" of deep space. The clamping circuit enhances the absolute accuracy of the measurement while suppressing low-frequency detector noise.

LUNAR SURFACE COVERAGE

The sunrise terminator was located at longitude 28° E, in the eastern part of Mare Serenitatis, at the time of the first ISR scans of the Moon. By the time of transearth injection, the terminator had moved to longitude 46° W, just east of the crater Aristarchus. On the near side of the Moon, the orbit constrained nighttime coverage to the southern portions of Mare Serenitatis and Mare Imbrium, to Oceanus Procellarum, and to the equatorial region at the western limb. On the far side, the nighttime groundtracks passed south of the craters Hertzsprung and Korolev over to the craters Aitken and Van de Graaff.

A horizon-to-horizon scan from an altitude of 111 km includes an arc of 40° on the lunar sphere. Foreshortening seriously degrades surface resolution at the horizon. Good spatial resolution is achieved over a lunar spherical arc of 20° centered on the groundtrack. Somewhat more than 35 percent of the

lunar surface was mapped during the course of the Apollo 17 mission.

DATA QUALITY

During the Apollo 17 mission, the ISR transmitted approximately 97 hr of lunar data containing approximately 1×10^8 independent temperature measurements. Data were received at range stations by way of telemetry from the spacecraft and were recorded on magnetic tape. Samples of the data were available in real time at the Mission Control Center so that instrument performance could be assessed continuously. The available sampling was equivalent to a scan of the lunar surface once every 6° of longitude. The overall impressions and tentative conclusions presented in this section are based on this sparse sampling plus additional, more comprehensive, quick-look displays of full data sets.

The scans in figures 24-3 and 24-4 have not been processed, and the amplitudes are proportional to radiance (instrument output voltage) rather than temperature. The figure legends indicate the approximate temperatures of various features.

In principle, each scan of the lunar surface should be preceded and followed by a short zero signal representing the sweep of the ISR beam through deep space on either side of the Moon. However, examination of the scans showed that the signal from space just past the trailing limb of the Moon (right side of figs. 24-3 and 24-4) was not zero. Scans of deep space during transearth coast were studied for clues to the problem. It was found that each scan contained a small ramp feature, commencing approximately at midscan and increasing linearly until the beam entered the ISR housing. The cause of the feature is not clear, but further work has shown that it can be removed from the data with only a modest increase in noise.

The ISR low-gain channel (channel 3) consistently saturated at the subsolar point. The phenomenon is attributed to the accumulation of error in the estimation of various instrument parameters such as the detector response to reflected sunlight and the wings of the field of view. An underestimation of the relevant quantities on the order of 5 to 15 percent can explain the effect. No scientific objective of the experiment was compromised by this occurrence.

In figure 24-3, two daytime scans received during the mission are compared. The scan centers are separated by only 6° of longitude, but the contrasting effects of topography in the maria and the highlands are quite clear. In figure 24-3(a), the thermal spike to the right of the mare and the dip to the left correspond to the northern and southern rims, respectively, of Mare Crisium. The difference in the thermal signatures of the two scarps demonstrates the dominance of local slope (i.e., local Sun angle) in the daytime thermal regime.

In figure 24-4, three lunar nighttime scans are shown. The scan in figure 24-4(a) comes from Oceanus Procellarum. The center of the scan is dominated by the crater Kepler A. The altitude of the

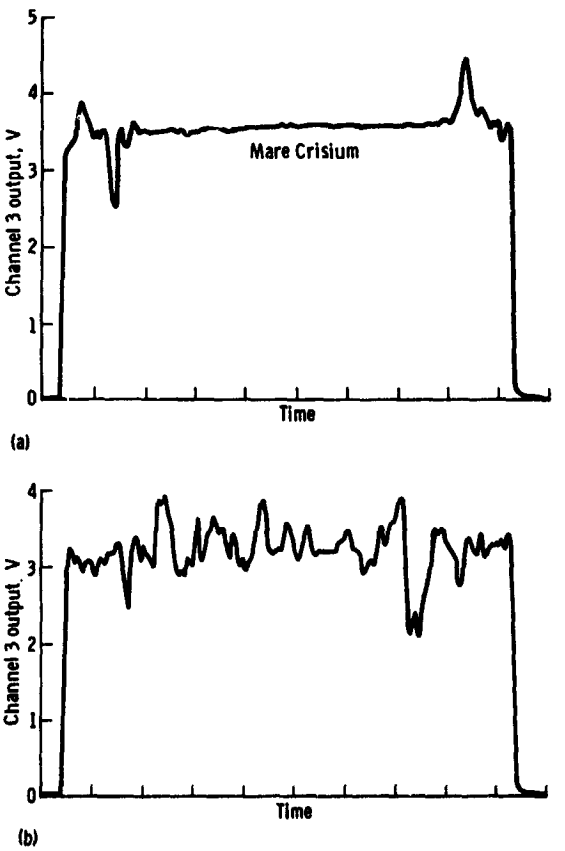

FIGURE 24-3.–Daytime scans of the lunar surface, demonstrating the extreme contrast in the amount of thermal structure in nearby mare and highland terrain. Each division on the ordinates represents 62.5 msec. (a) Mare terrain at a scan center of latitude 17.2° N, longitude 53.0° E, a phase angle of 315.7°, and an altitude of 121.2 km. The temperature in Mare Crisium is approximately 368 K. (b) Highland terrain at a scan center of latitude 18.2° N, longitude 47.7° E, a phase angle of 310.4°, and an altitude of 119.7 km.

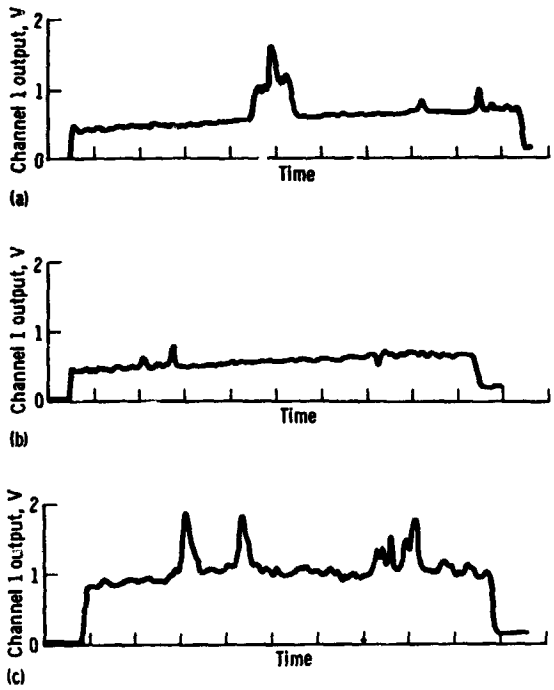

FIGURE 24-4.–Nighttime scans of the lunar surface. Each division on the ordinates represents 62.5 msec. (a) Scan at a scan center of latitude 7.0° N, longitude 35.9° W, a phase angle of 214.1°, and an altitude of 39.7 km. The crater Kepler A is thermally enhanced relative to the 92 K background in Oceanus Procellarum. The temperature in the crater ranges from 112 K on the wall to a maximum of 126 K in the center. (b) Scan at a scan center of latitude 18.9° N, longitude 2.0° E, a phase angle of 264.8°, and an altitude of 109.3 km. A predawn cold spot shows an 8 K contrast to the 90 K background in Montes Apenninus. (c) Scan at a scan center of latitude 22.5° S, longitude 178.4° E, a phase angle of 120.8°, and an altitude of 118.0 km. These large far-side anomalies are enhanced approximately 22 K relative to a 108 K background 2.5 days after lunar sunset.

spacecraft was 39.7 km at the time of the scan, making the ISR resolution element 0.8 km wide on the surface. The width of the broad base of the enhancement is 10 km, coinciding with the crater diameter. The thermal peak in the center is approximately 2 km across. The measured radiance in the central region increases linearly from both sides to the center, implying that the actual temperature at the center has not been fully resolved. The dramatic change of material properties within the crater probably reflects exposure of bedrock. The radial gradient may be caused by a corresponding radial distribution of slump material from the crater walls. Unfortunately, no lunar photographs that contain a good view of the crater bottom have been found.

The scan shown in figure 24-4(b) contains predawn temperatures, the coldest for any given surface region. The scan center is located just north of Mare Vaporum and south of the Apollo 15 landing site. On the right portion of the scan is a negative anomaly, a region having depressed temperatures relative to its environs. In this case, the temperature difference is $\geqslant 8$ K. A lower limit is given because the width of the deflection, only one resolution element, implies that the anomaly may not be fully resolved. The anomalous region lies south of the crater Conon in Montes Apenninus. The magnitude of the temperature contrasts implies that the thermal conductivity of the soil in that region is approximately one-half that of the surrounding material. These underdense regions cannot be impact features. The preservation of the density contrast also implies that the regions are relatively young on a geologic scale. Cold nighttime anomalies are particularly difficult to detect from Earth-based observations. Although such features have been reported previously (refs. 24-8 and 24-11), the ISR results provide the first opportunity to study them in detail.

The scan in figure 24-4(c) includes far-side anomalies. Our abbreviated data survey shows that such features are not common in the nighttime data on the lunar far side (fig. 24-5). A low frequency of occurrence was anticipated because near-side anomalies occur preferentially in the maria, regions which are generally absent in the other hemisphere. The two prominent anomalies on the left side of the

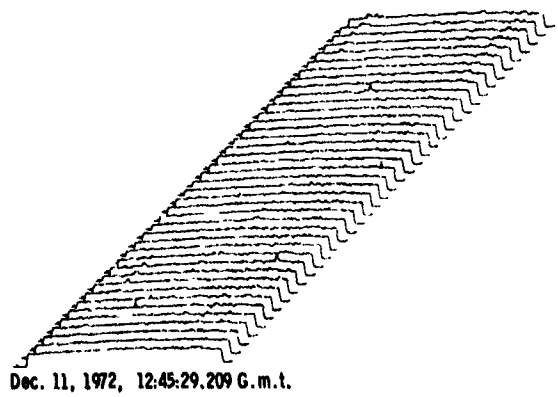

Dec. 11, 1972, 12:45:29.209 G.m.t.

FIGURE 24-5.–Scan sequence of a featureless region northeast of Mare Orientale and South of the crater Hartwig. North is to the left; west is at the top.

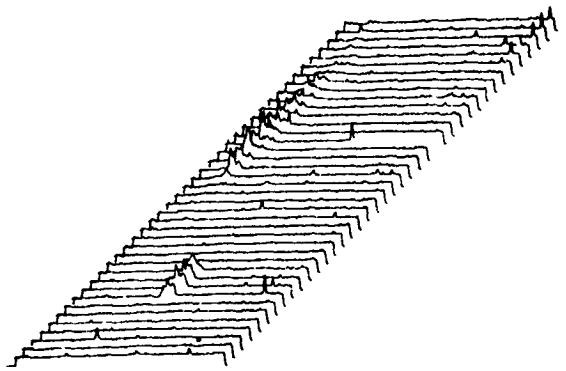

Dec. 11. 1972, 12:31:17.933 G.m.t.

FIGURE 24-6.–This sequence of nighttime scans runs westward approximately between 35° and 38° W longitude at latitude 7° N. The crater in the foreground is Kepler A, and the extended feature in the background is the crater Kepler. North is to the left; west is at the top.

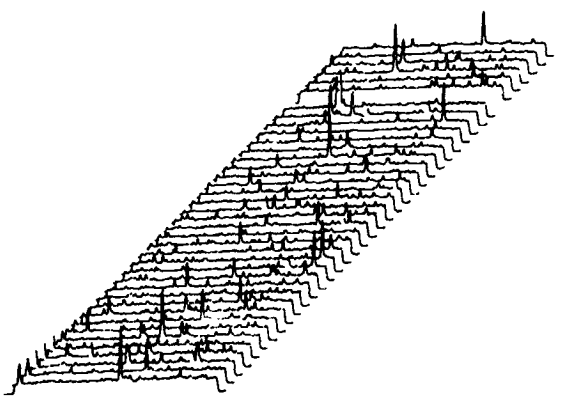

Dec. 11, 1972, 12:36:59.643 G.m.t.

FIGURE 24-7.–This sequence of scans runs from 53° to 56° W longitude just north of the lunar equator. North is to the left; west is at the top.

scan (fig. 24-2(c)) are located between the large craters Aitken and Van de Graaff. The large peak at the right limb corresponds to the crater Birkeland; the smaller structure to its left is in the crater Van de Graaff.

In figure 24-6, the scan in figure 24-4(a) is shown in its full data context. In this sequence of scans, north is to the left and west is upward. The extended feature just past the middle of the sequence is the crater Kepler. An interesting aspect of this set is the general lack of features except for the two major craters. As part of the Kepler ejecta blanket, this region might have been expected to be littered with debris and, consequently, to show considerable thermal structure.

Farther to the west, near the equator south of the crater Reiner, an area in Oceanus Procellarum that is devoid of craters displays many thermal anomalies (fig. 24-7). This structure cannot be attributed to residual, postsunset, topographic cooling differences. Figure 24-5 shows that such structure is entirely absent in a highland region northeast of Mare Orientale and nearer the sunset terminator. It is probable that the amount of thermal structure is associated with the age of the region; older regions have a featureless, soil-like response.

In figure 24-1, lunar temperatures as measured by the ISR are plotted as a function of brightness longitude. The values were taken from scans made by the Apollo 17 spacecraft during revolution 20. An attempt was made to choose a point from each scan on the lunar equator. The spacecraft orbital motion causes the actual sequence of the points to go from right to left on the figure. The first data point of the sequence lies 5.3 days after lunar sunset (abscissa of 0.43 in fig. 24-1) and was measured at 08:26 G.m.t. on December 12, 1972. The final point (at approximately the same lunation coordinate) was measured at 10:25 G.m.t. on the same day. A data gap exists near the subsolar point for this orbit.

The plotted temperatures will change as the ISR values are refined. The error estimate is 3 K for the nighttime measurements; the values probably are systematically low. No correction for albedo or topography has been made.

Theoretical curves for various values of γ are also plotted in figure 24-1. The theoretical calculations represent the cooling behavior at a single point, whereas the measured data are taken over many different types of material. The cooling curve apparently falls below $\gamma \approx 850$ cal^{-1} cm^2 K sec$^{1/2}$, even if the error estimate is taken into account. The elevated temperatures near lunar midnight fall in Oceanus Procellarum, where general thermal enhancement has been noted in eclipse measurements (ref. 24-12).

The data for lunar afternoon temperatures come from the highlands on the far side, and the morning points fall in Mare Fecunditatis and Mare Tranquillitatis. The combined effects of albedo and directionality of emissivity account for the apparent systematic deviations to either side of the theoretical curve.

CONCLUSIONS

This brief survey of the ISR data has confirmed that a variety of thermal behavior exists on the lunar surface. Further work on the measurements will establish the cooling behavior of the major types of lunar regions and the most significant exceptions within each category.

REFERENCES

24-1. Krotikov, V. D.; and Shchuko, O. B.: The Heat Balance of the Lunar Surface Layer During a Lunation. Soviet Astron.–AJ, vol. 7, no. 2, Sept.-Oct. 1963, pp. 228-232.

24-2. Mendell, W. W.; and Low, F. J.: Low-Resolution Differential Drift Scans of the Moon at 22 Microns. J. Geophys. Res., vol. 75, no. 17, June 10, 1970, pp. 3319-3324.

24-3. Shorthill, R. W.; and Saari, J. M.: Infrared Observation of the Eclipsed Moon. Boeing Sci. Res. Lab. Dcmt. AD-689076, D1-82-0778, Jan. 1969.

24-4. Thompson, T. W.; Masursky, H.; Shorthill, R. W.; Zisk, S. H.; and Tyler, G. L.: A Comparison of Infrared, Radar, and Geologic Mapping of Lunar Craters. Contribution 16, Lunar Sci. Inst., Symposium on the Geophysical Interpretation of the Moon (Houston, Tex.), June 1970.

24-5. Wildey, Robert L.; Murray, Bruce C.; and Westphal, James A.: Reconnaissance of Infrared Emission From the Lunar Nighttime Surface. J. Geophys. Res., vol. 72, no. 14, July 15, 1967, pp. 3743-3749.

24-6. Shorthill, Richard W.; and Saari, John M.: Radiometric and Photometric Mapping of the Moon Through a Lunation. Ann. N.Y. Acad. Sci., vol. 123, July 15, 1965, pp. 722-739.

24-7. Allen, David A.: Infrared Studies of the Lunar Terrain. I: The Background Moon. The Moon, vol. 2, no. 3, 1971, pp. 320-337.

24-8. Mendell, Wendell W.; and Low, Frank J.: Lunar Differential Flux Scans at 22 Microns, Final Report. NASA CR-121457, 1971.

24-9. Raine, W. L.: Thermal Mapping of the Lunar Surface. Final Rept. SE-SSL-1649, Contract NAS8-26343, Teledyne Brown Engineering (Huntsville, Ala.), Sept. 1972.

24-10. McIntosh, R. B., Jr.: and Mendell, W. W.: Infrared Scanning Radiometer for Temperature Mapping of the Lunar Surface on the Apollo 17 Flight. Proceedings of the Technical Program, Fourth Annual Electro-Optical Systems Design Conference, Industrial and Scientific Conference Management, Inc. (Chicago), 1972, pp. 356-361.

24-11. Low, Frank J.: Lunar Nighttime Temperatures Measured at 20 Microns. Astrophys. J., vol. 142, no. 2, Aug. 15, 1965, pp. 806-808.

24-12. Saari, J. M.; and Shorthill, R. W.: Thermal Anomalies on the Totally Eclipsed Moon of December 19, 1964. Nature, vol. 205, no. 4975, Mar. 6, 1965, pp. 964-965.

Infrared Scanning Radiometer for Temperature Mapping* of the Lunar Surface on the Apollo 17 Flight

Robert B. McIntosh, Jr.
Barnes Engineering Company
Stamford, Connecticut

and

Wendell W. Mendell
NASA-Manned Space Flight Center
Houston, Texas

*Development Sponsored by NASA Manned Spacecraft Center under contract NAS 9-10845

TABLE OF CONTENTS

LIST OF ILLUSTRATIONS

APOLLO 17 INFRARED SCANNING RADIOMETER

Robert B. McIntosh
Barnes Engineering Company
Stamford, Connecticut 06902

and

Wendell W. Mendell
NASA Manned Space Flight Center
Houston, Texas 77058

Abstract

The Infrared Scanning Radiometer, scheduled to be flown on Apollo 17, was developed to obtain a temperature map of the lunar surface. Variations of night-time temperatures and cooling rates can be correlated with variations in thermal conductivity and density of the lunar soil. Therefore, the radiometer has the potential of identifying anomalously hot or cold regions due to surface features or internal heat sources. The radiometer consists of a 7-inch, f/3.3 cassegrain optical system and a silicon-immersed thermistor bolometer. The radiometer's 20-milliradian instantaneous FOV scans a total angle of 162° using a conventional rotating plane scan mirror. The Noise Equivalent Temperature of the instrument is 1/4°K at 90°K; the temperature typical of the unilluminated side of the moon. The single detector and three overlapping electronic channels provide high-resolution radiometric data for temperatures ranging from deep space to 400°K. The radiometric output is referenced to space once each scan using an integrating type clamp. A low-noise preamplifier and bias filters limit the instrument noise to essentially that of the bolometer. Low frequency compensation reduces signal droop to less than 0.1% during each scan of the lunar surface. Instrument thermal control is achieved by passively exchanging heat with the lunar surface from the nominal 60-mile circular orbit.

INFRARED SCANNING RADIOMETER

I. INTRODUCTION

An Infrared Scanning Radiometer (ISR) has been developed to map the radiant emission of the lunar surface. The radiometer is one of three new orbital experiments that are scheduled to be flown on Apollo 17. The instrument will scan the surface of the Moon, horizon-to-horizon, from a nominal altitude of 60 nautical miles. The combination of a rotating scan mirror and the forward motion of the orbiting spacecraft will produce radiometric data in strip form that can be combined into a continuous thermal map.

Prime scientific data will be obtained from the unilluminated hemisphere of the Moon where the temperatures and cooling rates depend on the thermophysical parameters of the surface. The lunar soil layer is an excellent thermal insulator. Very little heat is conducted into the interior during the lunar day, and daytime surface temperatures are primarily dependent upon the radiative balance established by absorbed solar energy. Nightime cooling rates and temperatures result from energy lost during the two-week lunar night and are very sensitive to local variations of bulk density and effective conductivity of the surface layer.

Earth-based telescopic measurements have established the existence of many features that cool abnormally relative to the general soil background. Most of these thermal anomalies are thought to be either exposed bedrock or extensive boulder fields associated with features too young to have been eroded into soil by micrometeorite bombardment. However, the spatial and thermal resolution of Earth-based data is too poor to rule out the possibility of other heat sources.

The 20-milliradian circular field of view of the ISR collects energy from a 1.2-nautical mile diameter lunar surface element at Nadir and will

improve spatial resolution of lunar thermal data by an order of magnitude. By referencing the ISR radiometric outputs to the effectively zero radiant background of space, the absolute accuracy of the measurements made from lunar orbit will far exceed those made through the atmosphere. The ISR has the ability to detect temperature differences as small as 0.25°K against a 90°K background and therefore provides sufficient sensitivity to map small cooling gradients on the lunar surface. It is anticipated that radiometric data obtained during the Apollo 17 flight, together with other Apollo surface and orbital experimental results, will assist in solving many questions concerning the lunar origin and its evolution.

II. SYSTEM DESCRIPTION

The Radiometer, shown in Figure 1, utilizes a 7-inch, f/3.3 spherical reflecting objective, a hyperhemispheric silicon immersed thermistor bolometer and a flat beryllium scan mirror rotated at 41.7 rpm.

The scan mirror sequentially scans the 20-milliradian field-of-view of the instrument across space, 140° of the lunar surface, space, and a temperature monitored calibration patch that is located within the radiometer housing.

Once each scan revolution, the detector output is clamped when the ISR views deep space just prior to its scanning the lunar surface. Clamping provides d-c restoration of the a-c coupled detector signal by referencing the three scientific data channel outputs of the radiometer to zero. In addition, clamping eliminates errors that are produced by the self-emission of optical elements.

The three outputs are derived from the common detector and differ only in gain. The effective blackbody temperature range of the outputs are 0°K to 165°K, 0°K to 250°K and 0°K to 400°K. The 0° to 165°K high-gain data channel has telemetry-limited resolution of 1°K for a 90°K blackbody source. The 0° to 400°K low-gain channel accommodates the hottest temperature predicted for the illuminated lunar surface.

The radiometer scientific data outputs, shown in Figure 2, were calibrated to an absolute accuracy of ±1°K over a blackbody temperature range of 40°K to 400°K. Calibration was performed in a thermal-vacuum chamber using precision liquid nitrogen and liquid helium cooled sources and shrouds as shown schematically in Figure 3.

In addition to the three prime data output channels, the ISR supplies 5 housekeeping signals. The temperatures of the calibration patch, primary mirror, and detector are measured and transmitted with an accuracy of ±0.5°F.

For diagnostic purposes, outputs from a voltage summation monitor and bias voltage monitor are provided.

At the beginning of each scan cycle, a 4-step electronic calibration pulse is inserted into the analog channel. This pulse provides a zero and a 4-Volt reference level, for 10 milliseconds, in each of the three scientific data outputs. See Figures 4 and 5.

The thermistor bolometer is temperature controlled at 100° F to make the ISR calibration independent of temperature over a temperature operating range of 25° F to 95° F. The 100° F detector set point is placed 5° F above the maximum instrument operating temperature anticipated during a hot-biased orbital mission.

Thermal control of the instrument is achieved passively by radiant heat exchange with the lunar surface and space. The instrument is both conductively and radiatively decoupled from the Scientific Instrument Module and adjacent experiments by an insulated mount and a 3-layer thermal blanket.

III. OPTICAL DESIGN

The ISR optical system, shown in Figure 6, is the most compact configuration for an all reflecting, 7-inch aperture objective, having a 20-milliradian field-of-view. The objective,together with the 45° scanning mirror has an optical length of less than 14 inches. Although the ISR uses only spherical optics, the edge-of-field blur is only 1.2 milliradians.

The 7-inch entrance pupil is located at the primary mirror in order to maximize energy collection within mechanical packaging constraints. Both the 22-inch radius primary and the 16.03-inch radius secondary mirrors are gold-coated spherical surfaces on nickel-plated aluminum. The scan mirror was fabricated by gold plating a sintered beryllium substrate that had been nickel-plated and optically polished. The secondary mirror reflects the focus of the objective two inches behind the primary surface where a 0.464-inch diameter field stop defines the 20-milliradian diameter half-power field-of-view. The secondary mirror and its baffle are mounted to the elliptical, plane-surfaced scan mirror and rotate with it. The scan mirror and its rotating drive assembly were dynamically balanced to avoid possible once-around noise arising from mechanical wobble.

A silicon hyperhemispheric immersion field lens is placed at the field stop so that rays coming to the edge of the field from the exit pupil are refracted into the silicon-selenium detector interface at near critical angle. This insures that the forward hemisphere seen by the detector is filled with energy to the maximum extent possible.

The long-wavelength response of the immersed bolometer resulted in a Noise Equivalent Temperature that was less than half that originally predicted. Significant bolometer responsivity was observed out to approximately 70 microns, the limit of the spectral response measuring instrumentation sensitivity.

IV. MECHANICAL DESIGN

A large section of the radiometer housing, shown in Figure 7, is open to allow the 20-milliradian instantaneous field of view to be scanned through a total angle of 170 degrees. As a result, a heavily ribbed aluminum cast housing was designed to have a high stiffness-to-mass ratio. Two integral bulkheads are located on either side of the entrance aperture to support all the radiometer opto-mechanical components. The scan motor and rotating assembly are mounted to one bulkhead; and the primary mirror, detector assembly, and low-level electronics are mounted to the other. The ISR power supply and the motor logic/drive electronics are mounted in a self-contained removable module.

The 37.5 lb radiometer is mounted to an 'A' frame shelf in the Scientific Instrument Module on six precisely machined mounting pads using thermally insulating washers. Velcro pads are attached to those external surfaces of the housing where the thermal blanket is attached. Bosses, located on the front surface of the housing, are used to measure the alignment between the ISR and the Mapping Camera to improve post flight pointing knowledge.

The ISR scan drive assembly consists of a gear train, an encoder, and a counter-balanced scan mirror assembly. The gear train reduces the 2000-rpm motor speed to drive a ring gear on the scan mirror at the required 41.7 rpm. A combination of single and pre-loaded duplex pair bearings is arranged to minimize the effects of thermal expansion and to produce an axially and radially rigid assembly.

Andox 'C' lubricant was selected to maximize gear life over the required wide range of speeds and operational temperatures. Nylasint lubricant impregnated reservoirs and conventional labyrinth seals at the shaft ends are used to maintain proper lubrication in the space environment.

V. ELECTRONIC DESIGN

Bias Supply and Preamplifier

Both the positive and negative 85-Volt bolometer bias supplies and the preamplifier have noise-equivalent resistances of 10K ohms which is negligible compared to the 125K ohm resistance of the bolometer bridge. A matched-pair FET differential preamplifier is used to provide a high input impedance and to avoid multi-state noise associated with many bipolar transistors. A single 20-second coupling time constant is used in the preamplifier to provide d-c isolation from the detector. Compensation is used in a later stage to reduce the associated droop.

Detector bias voltages are obtained from precision regulators and FET active filters. The opposite polarity regulators use a selected low-noise, temperature-compensated zener diode as a common reference element. Therefore, any temperature variations in bias voltage track and cancel at the detector.

The bias filters were designed to provide low noise N-Channel FETs at both output stages. The effective time constants of the filters approach 200 seconds to limit 1/f noise and low-frequency noise to levels significantly below those of the bolometer.

Clamp Circuit

The angular position of the scan mirror is detected once each revolution by using a rotating aperture, a GaAs emitting diode and a photodiode. The resulting signal is used to activate a clamp circuit and the electronic calibration pulse insertion.

The clamp circuit is used to restore the d-c level of the analog signal once each scan revolution. The clamp period occurs during the 6° of scan prior to scanning the lunar surface.

Simple synchronous clamps reference the radiant signals to the instantaneous noise voltage present at the time of unclamping. If the noise peaks occur when the clamp opens, shifts in the scan-to-scan reference level equal to the peak-to-peak noise will occur. This, in effect, transforms high frequency noise into apparent d-c shifts in the radiometric signal. The ISR electronics minimize this effect using a synchronous clamp followed by a self-integrating clamp. During the first 1.6 milliseconds of the 24 millisecond clamp period, a synchronous clamp provides coarse restoration of scan-to-scan changes of the d-c voltage at the clamp coupling capacitor. For the balance of the clamp period, an integrator and scaling amplifier determine the average value of the bolometer noise. This average is used as the space reference level for the subsequent lunar scan. At the end of the scan cycle, the integrator is dumped and reset to provide a new average during the next clamp interval.

Signal Processing

The ISR analog signal processing is shown in Figure 8. High-frequency boost is used to extend the signal response of the bolometer to 125 Hz. The optimum signal-to-noise ratio, detector time constant, and required boost were obtained when the boosted high-frequency noise was made equal to the low frequency 1/f noise. The 125-Hz bandwidth corresponds to 3.7 system time constants within the dwell time of a single 20-milliradian resolution element.

A 3-pole Butterworth filter is used to sufficiently attenuate noise beyond 400 Hz to prevent aliasing resulting from the 800 Hz telementry sampling.

System droop during the 0.56 second lunar scan was limited to 0.25%. This was achieved by introducing phase lag after the preamplifier to compensate for the input coupling capacitor. The droop associated with this R-C coupling network arises primarily from the phase shift of the low-frequency cutoff. This lag produces some peaking of low frequency noise. However, for a detector having 1/f noise, this effect is cancelled by the large net reduction in low-frequency response required to achieve equivalent droop performance. Most importantly, the size of the high-voltage input coupling capacitor was reduced by a factor of 15.

Power Supply

The ISR utilizes 18 watts of +27.5 Volt d-c spacecraft power along with a 100 pps timing signal. The d-c input supplies a switching regulator that provides ±15 Volt d.c. to a power converter.

The power converter produces precision ±20 Volt d.c. for operating the processing electronics and temperature controlled ±160 Volt d.c. for the bias voltage regulators.

Power is also drawn directly from the switching regulator by the motor drive/logic circuitry. The motor is driven by two-phase 200-Hz square waves generated from the 100 pps timing input.

VI DATA ANALYSIS

The ISR data will be presented as radiance and temperature maps of the lunar surface. Since the ISR has no image motion compensation, the returned "image" must be corrected for spacecraft motion. This is done indirectly by means of a technique of optimal approximation. In this technique, the data is fit in a least squares sense by a set of two-dimensional functionals. The two-dimensional function defined by the fit represents an approximation to the actual thermal scene. The approximation function can then be sampled in any convenient way necessary to produce an image or a contour map.

The thermal map represents a refined data base but the real data reduction only begins there. Cooling curves will be generated for various classes of lunar features. Thermal anomalies will be studied at the highest possible spatial and thermal resolution. The spatial variations and correlations of thermophysical parameters will be derived. The physical properties of the surface layer and lunar geology will be studied in order to correlate the lunar features with their geophysical properties. It is even conceivable that the first lunar volcano may be found.

Acknowledgement

The authors wish to thank R. T. Walter the NASA/MSC Technical Monitor for the Apollo 17 ISR Program; Dr. F. J. Low of the University of Arizona and Rice University, the Principal Investigator for the Apollo 17 ISR Program; and the many people at Barnes Engineering Company and NASA who contributed to the successful development of the Infrared Scanning Radiometer.

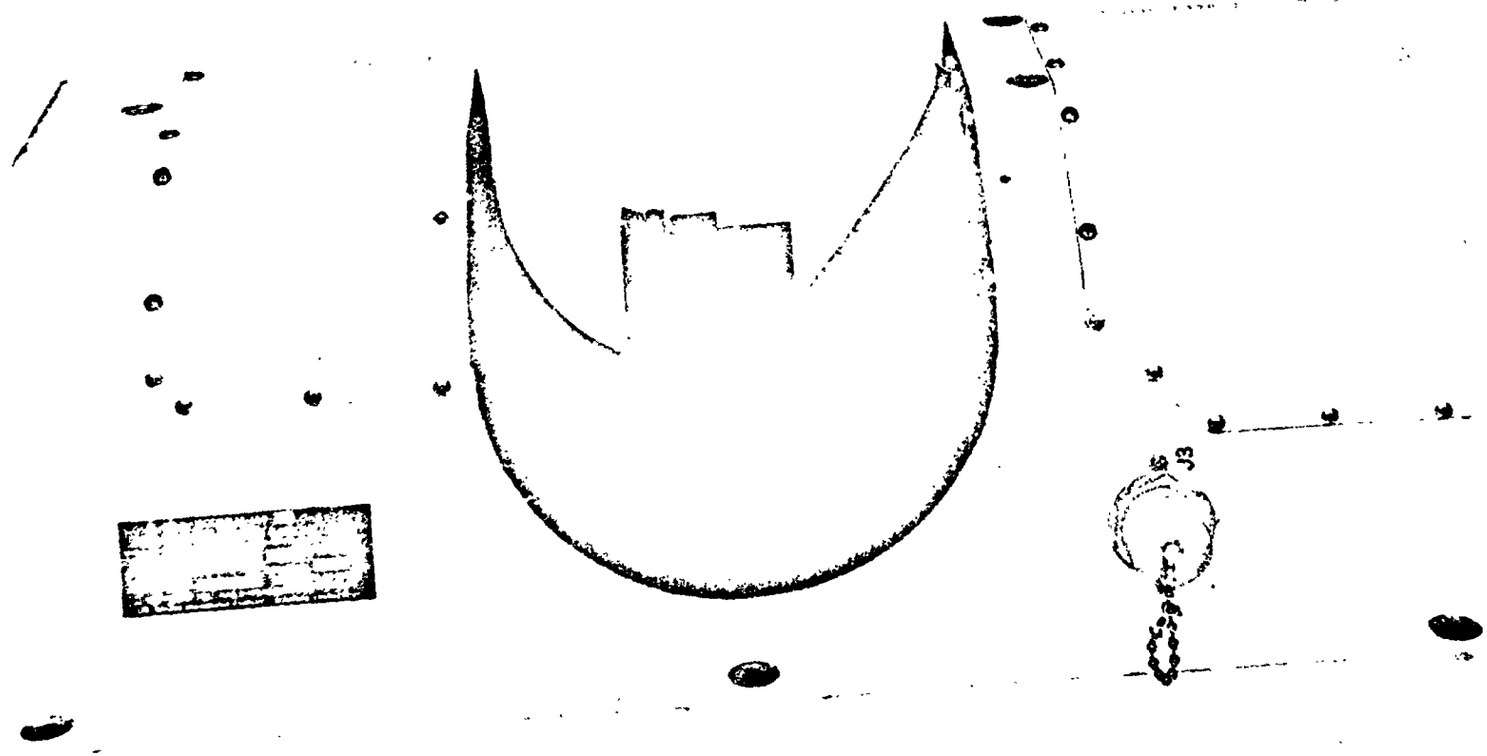

HT23702 A

Figure 1. INFRARED SCANNING RADIOMETER.

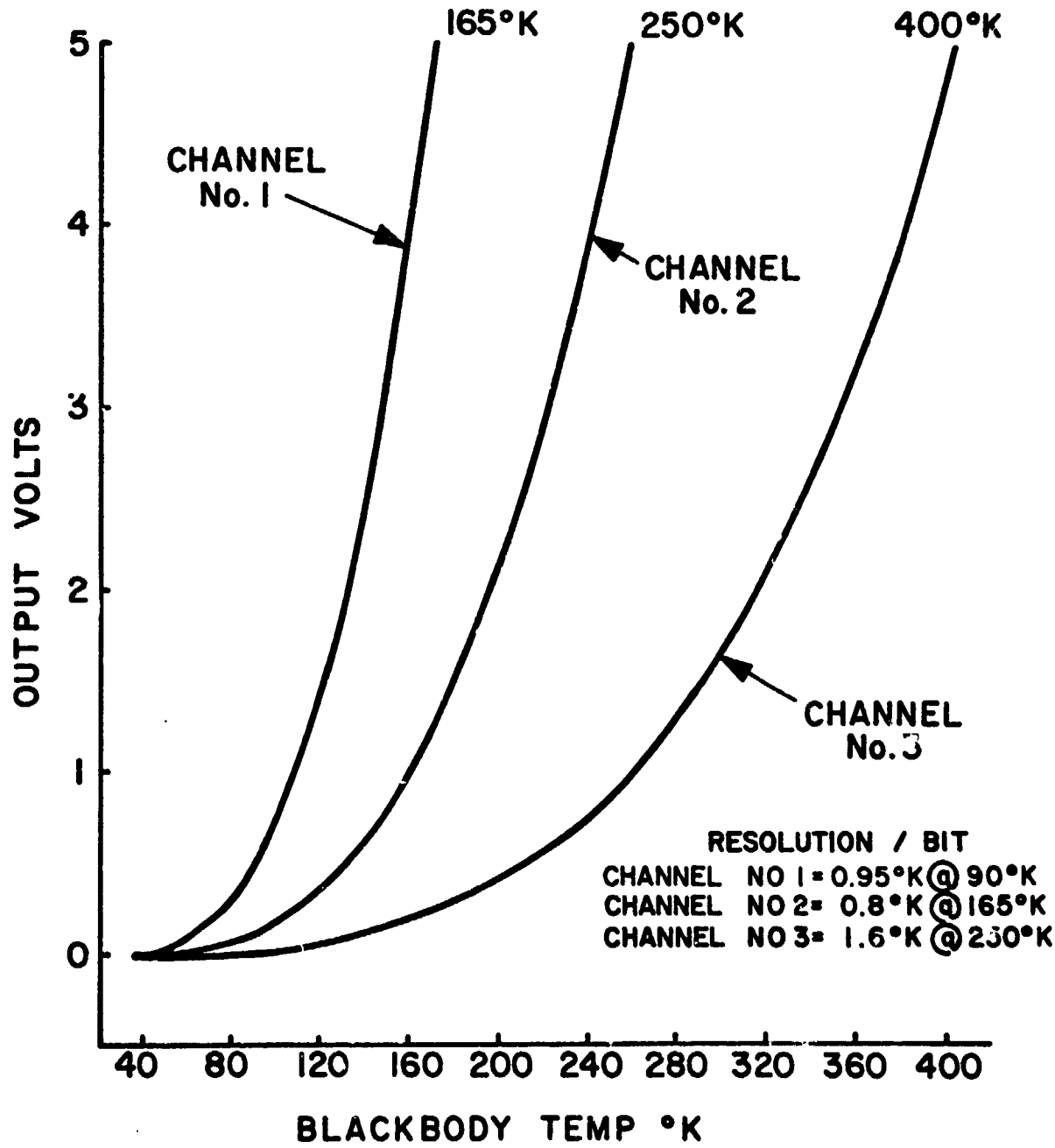

ISR CALIBRATION CURVES

Figure 2

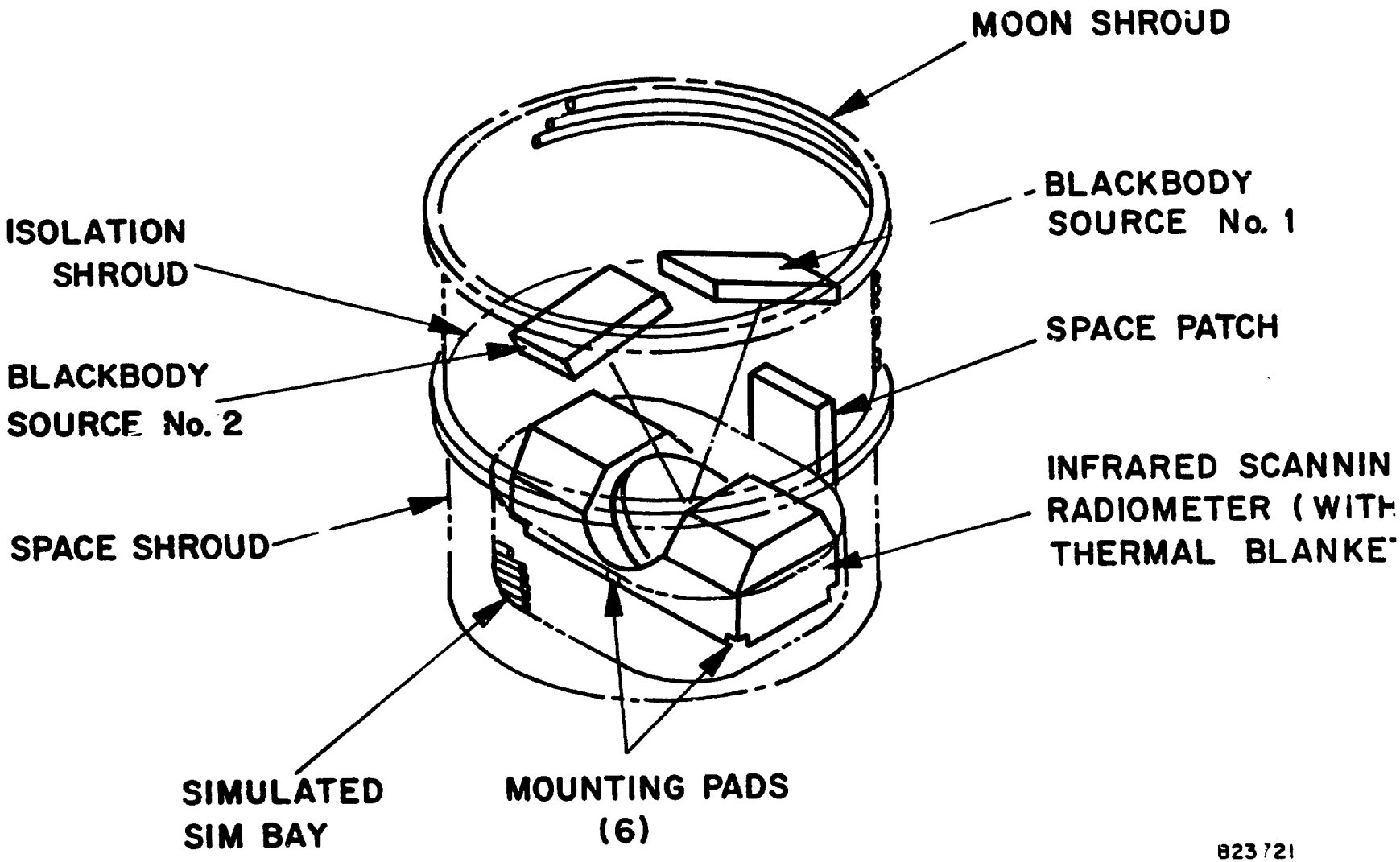

THERMAL VACUUM TEST FIXTURE

Figure 3

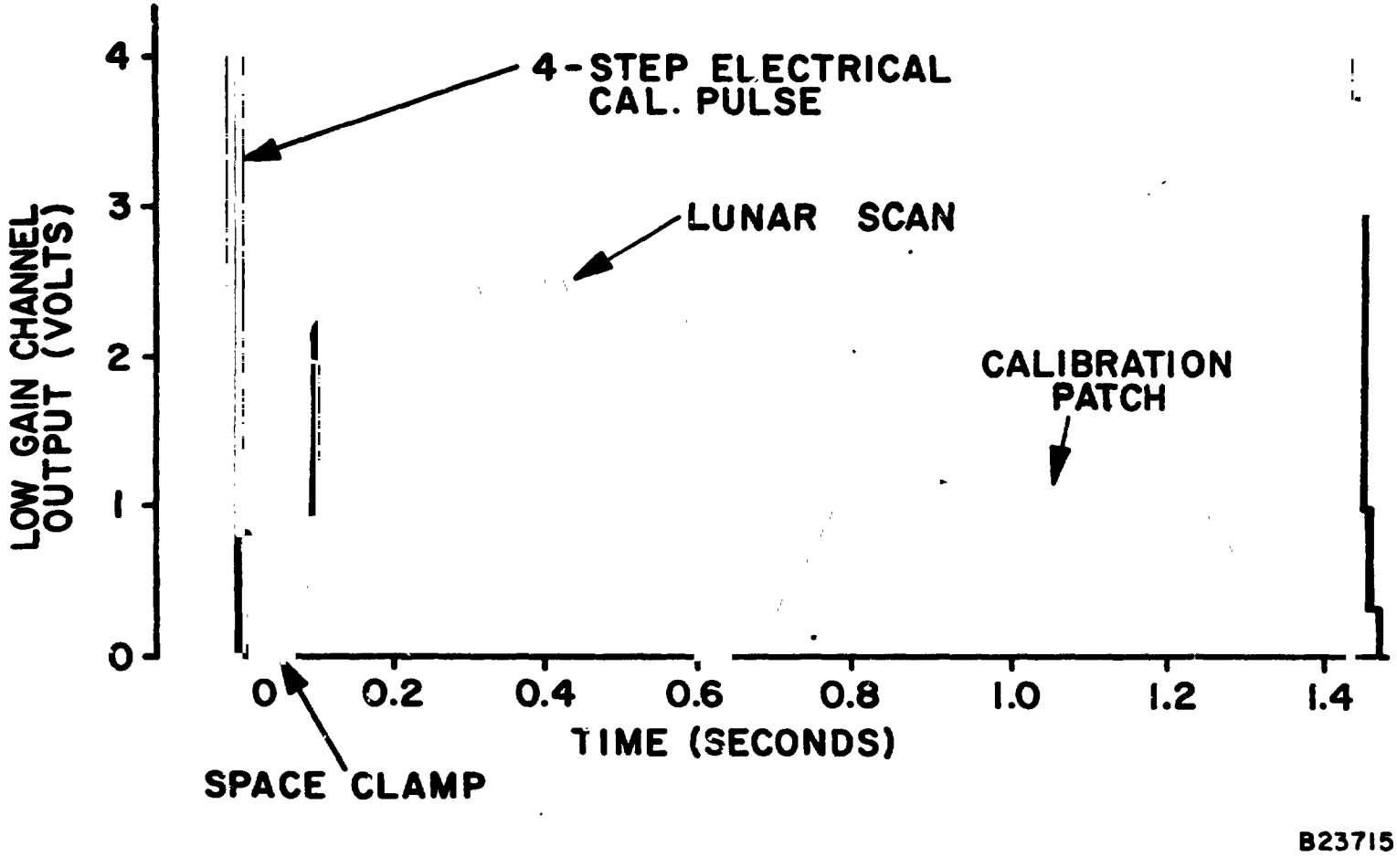

TYPICAL ISR OUTPUT WAVEFORM

Figure 4

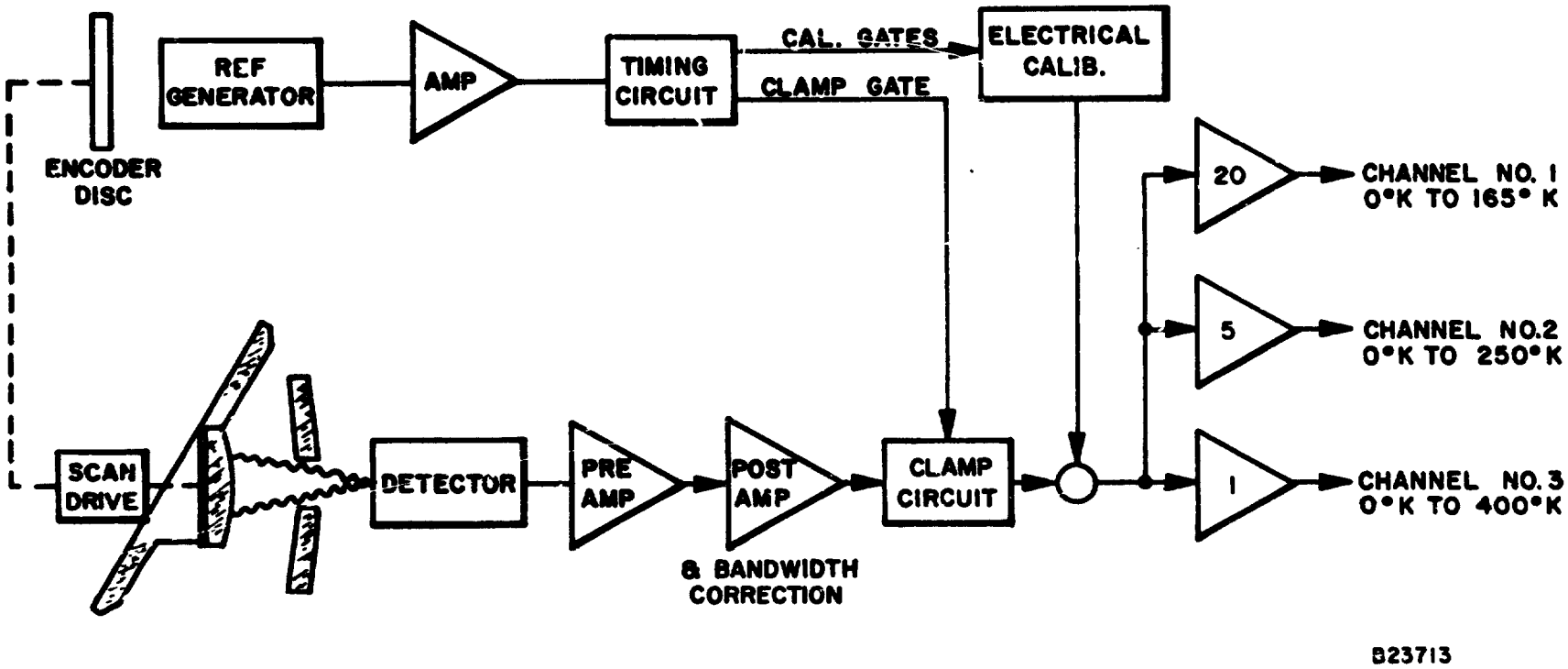

ISR ELECTRONICS BLOCK DIAGRAM

Figure 5

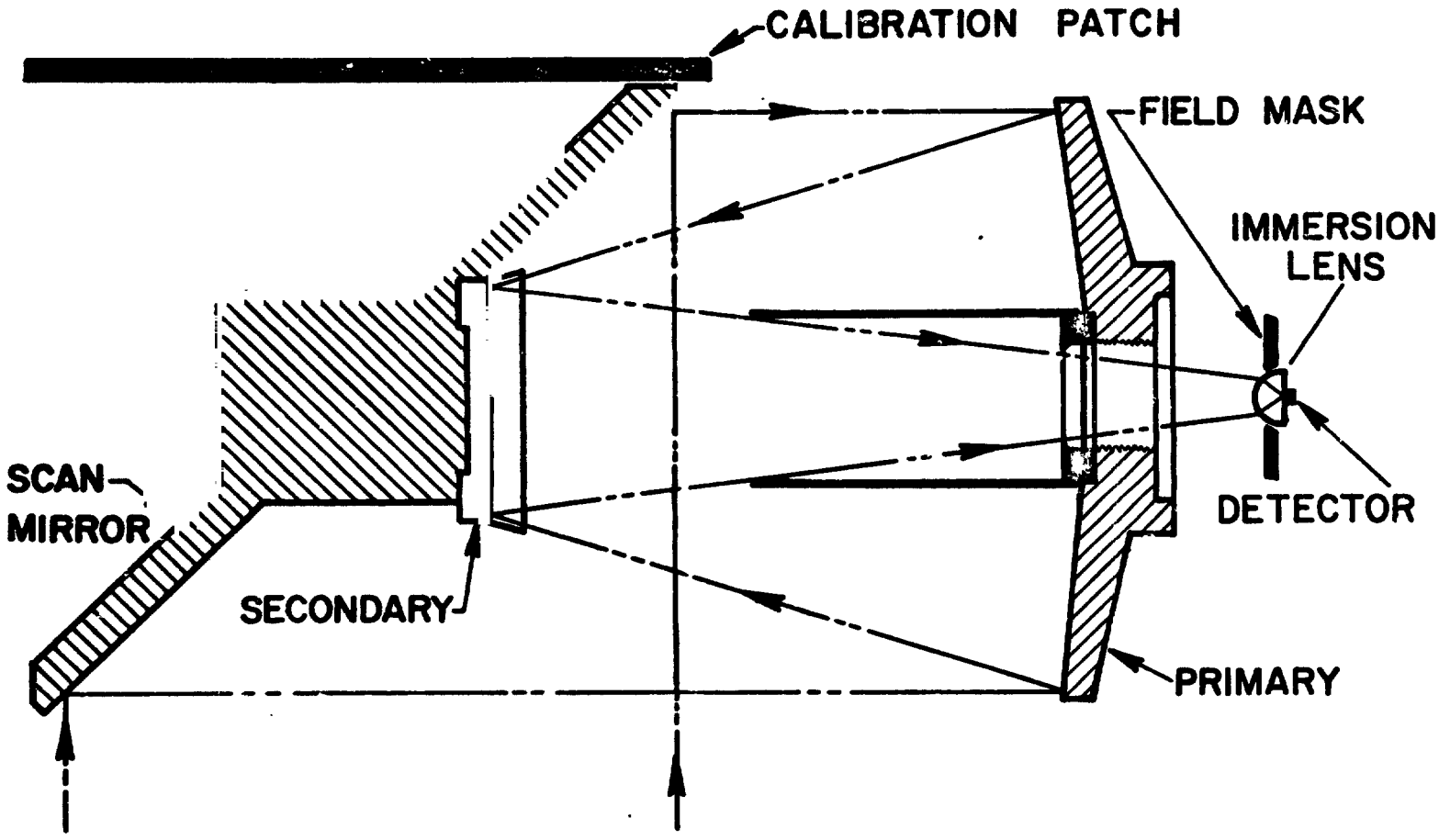

ISR OPTICAL SYSTEM

Figure 6.

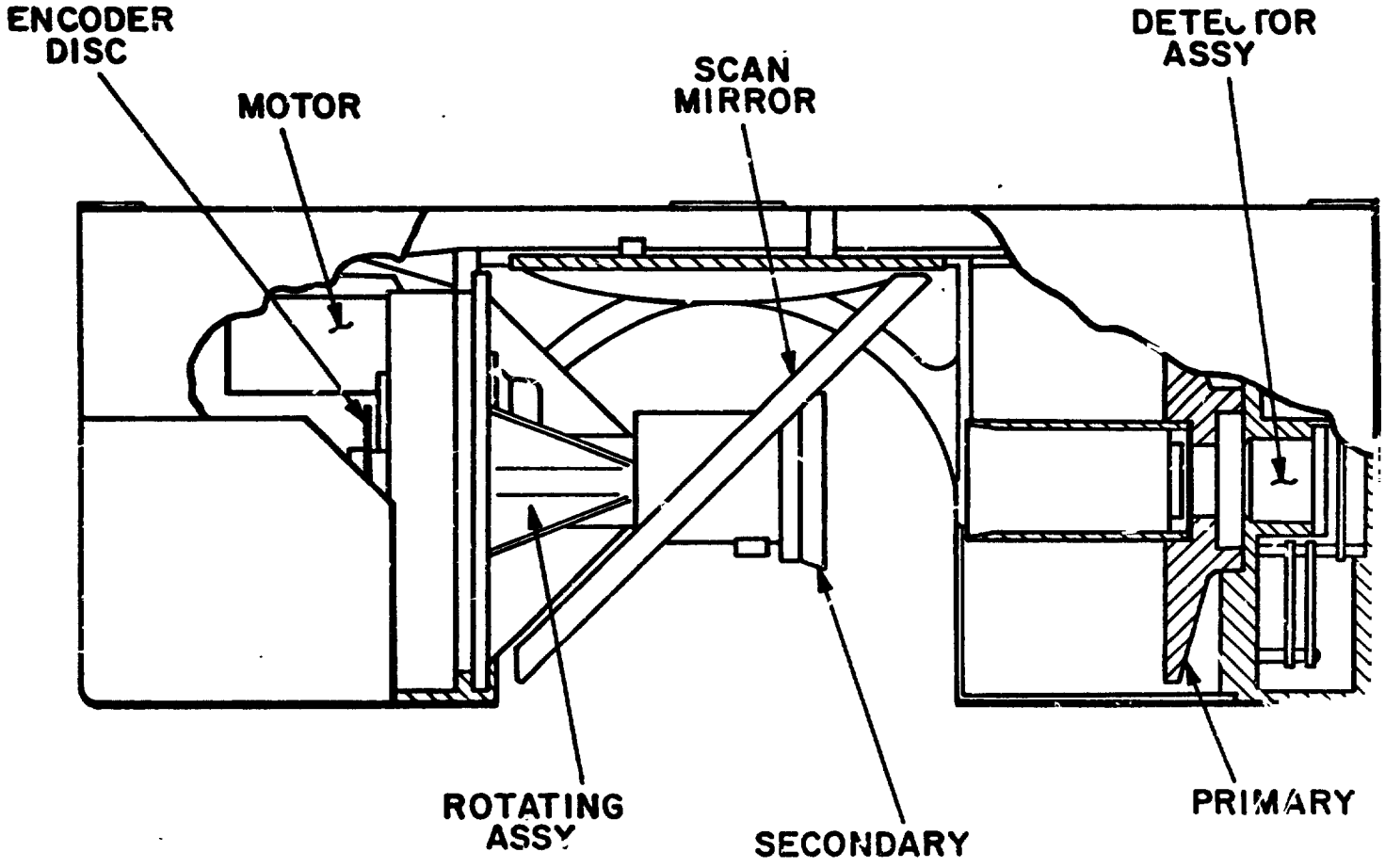

ISR SECTIONAL VIEW
Figure 7.

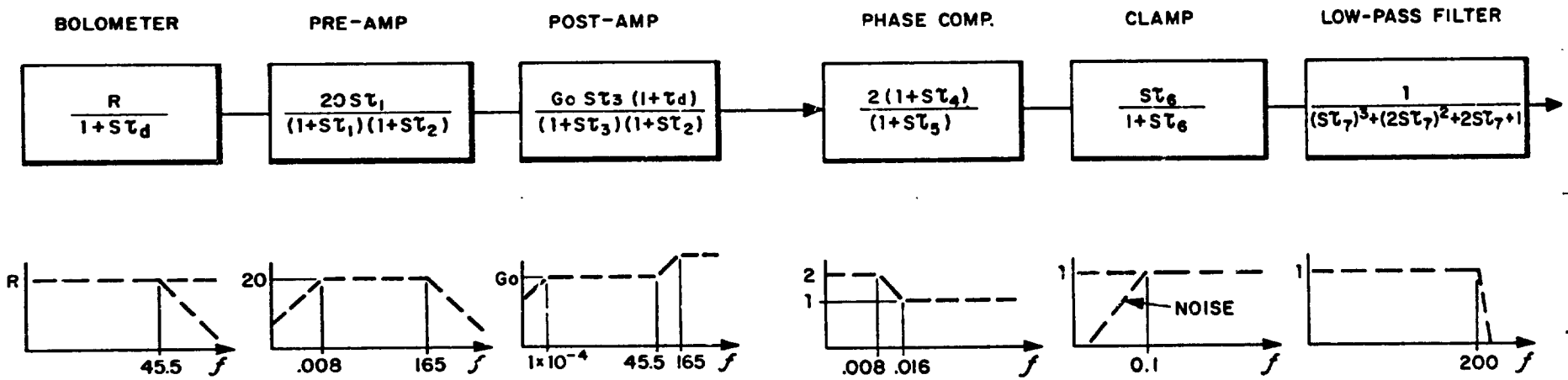

ANALOG PROCESSING

Figure 8